Robert Johnston, B.Sc., M.Sc.

Fundamental insights into the biomechanics of atherosclerotic plaque tissue: Determining possible new diagnostic measures of plaque vulnerability.

_____

Trinity College Dublin, 2022

A thesis submitted to the University of Dublin in partial fulfilment of the requirements for the degree of

Doctor in Philosophy

Supervisor: Prof. Caitriona Lally

Internal Examiner: Prof. Ciaran Simms

External Examiner: Prof. Susan Lessner

Declaration

I declare that this thesis has not been submitted as an exercise for a degree at this or any other university and it is entirely my own work.

I agree to deposit this thesis in the University's open access institutional repository or allow the library to do so on my behalf, subject to Irish Copyright Legislation and Trinity College Library conditions of use and acknowledgement.

Robert Johnston

_____

Summary

Carotid atherosclerotic plaque rupture is known to be a major contributor to ischaemic stroke cases. The development of atherosclerotic plaques within the vessel wall alters both the geometry and mechanical environment of the tissue. However, current diagnostic measures only focus on this change of geometry and not the mechanics of the tissue. Rupture can be observed as a purely mechanical event, whereby the forces exerted on the tissue exceeds its mechanical strength. Therefore, it is of utmost importance to establish a mechanically sensitive indicator that can establish atherosclerotic plaques which are more vulnerable to rupture. The aim of this thesis is to establish possible new diagnostic measures of plaque rupture vulnerability using experimental and computational methods.

In the literature, characterising the location of high stress in the vessel wall has often been proposed as a potential indicator of structural weakness. This work shows that without consideration of the zero-pressure configuration, residual stress and patient specific material parameter there would be an overestimation in the stress calculated. These factors must therefore be included for accurate computational analysis. To understand the mechanics of atherosclerotic plaque tissue and the role collagen has in its mechanical behaviour, atherosclerotic plaque cap samples were pre-screened using small angle light scattering (SALS) to establish the predominant collagen fibre orientation and subsequently uniaxial tensile tests to failure were performed. These results show that when collagen fibres are in the predominantly axial direction they fail at lower stress, higher strain and have lower stiffness while the opposite is observed for tissue with fibres in the predominantly circumferential direction. This is important to note as being able to characterize the strain or establish the collagen fibre orientation, using *in-vivo* imaging techniques, could potentially aid in determining the overall mechanical strength of the tissue. From this mechanical knowledge, patient specific finite element models were created from *in-vivo* MRI images for both healthy volunteers and patients. In order to establish the dominant fibre orientation within these atherosclerotic plaques, *ex-vivo* diffusion tensor imaging (DTI) was performed to give the helical angle which was used to inform the FE models. A novel remodelling metric (RM), dependent on the change of the collagen fibre orientation and the evolution of internal variables that captures the softening that is associated with how far the fibres are from their optimal configuration when the arterial vessel is subjected to load was used to assess the possible vulnerability of atherosclerotic plaques. Overall, this preliminary work has demonstrated the capability of using the RM to possibly characterize plaque vulnerability when being informed with patient specific fibre angles from *ex-vivo* DTI. This is because the remodelling metric observed is higher when the fibres are not in the load bearing configuration. The last aim of this work involved characterizing the strain environment across atherosclerotic plaques using *in-vivo* MRI to establish a sensitive imaging indicator that could possibly aid in determining which

plaques are more vulnerable to rupture and verifying these results using patient specific finite element models. Acquiring images at two cardiac phases using triggering, the circumferential strain and its variability across healthy and diseased carotid bifurcation was calculated. Furthermore, patient specific computational models were created, and the circumferential strain and its variability was again calculated and subsequently compared to the imaging data. Importantly, this study shows that in healthy vessels there is a consistent strain across the bifurcation with small variability however, when plaques are present, higher strains can occur at locations proximal and distal to location of highest stenosis. High strains could suggest that collagen fibres at these locations are disorganised and orientated more axially then in the load bearing circumferential direction. Overall, this study shows that characterizing the strain environment of atherosclerotic plaques *in-vivo* can offer a key mechanical insight into the mechanical integrity of the tissue and that patient specific finite element models can verify the results obtained and allow for further characterization of the vulnerability of atherosclerotic plaques to rupture.

Acknowledgements

First of all, I would like to acknowledge and sincerely thank my supervisor Professor Caitriona Lally for her knowledge, support and guidance over the tenure of my PhD. Her enthusiasm, knowledge, and constant support throughout has been invaluable in the production of this work. I would like to thank the European Research Council and Trinity College Dublin for funding this research, without which none of this research would have been possible.

Throughout my time in Trinity, I have had the fortunate opportunity to meet many great researchers and people who I can safely say have become my friends. A special mention goes to all members of the Lally lab, past and present that helped and supported me throughout the PhD journey, Robbie, Pattie, Emma, Alix, Dave, Orla, Alan, Salman, Celine, Ciara, Sam, Celia and Yasmine. I would like to especially thank both Milad and Brooke for all their help throughout different stages of my PhD and all the joyful moments we had over the years. I will always remember being caught during a long day in the lab listening to music and singing to my heart's content.

I would like to also acknowledge the assistance of Peter O'Reilly, the senior experimental officer of the department of mechanical, manufacturing and biomedical engineering at Trinity College Dublin. Your enthusiasm and willingness to help everyone is a trait I very much admire, and I thoroughly enjoyed all our conversations over the years. I hope you enjoy your retirement.

I would like to than the people closest to me, especially my parents Geraldine and Willie (weird not saying Mom and Dad), all my brothers Sam, Ricky, Kian and Caleb and my sister Niamh as without their constant support and availability to talk about everything going on, this work would not have been achieved, I am eternally grateful and honoured to be your son and brother respectively. Lastly, I would like to also give a shout out to the extended family, all my aunties, uncles and cousins.

List of Publications, Conference Proceedings and Prizes

First – author publications

R.D. Johnston, R.T. Gaul, C. Lally, An investigation into the critical role of fibre orientation in the ultimate tensile strength and stiffness of human carotid plaque caps, Acta Biomaterialia. (2021). https://doi.org/10.1016/j.actbio.2021.02.008.

R.D. Johnston, M. Ghasemi, C. Lally, Inverse material parameter estimation of patient specific finite element models at the carotid bifurcation: The impact of excluding the unloaded zero pressure configuration and residual stress [In preparation]

R.D. Johnston, B. Tornifoglio, C. Lally, Observing the role of fibre orientation in the mechanical strength of atherosclerotic plaques. Verified using patient specific finite element models informed by *ex-vivo* diffusion tensor imaging. [In preparation]

R.D. Johnston, B. Tornifoglio, C. Lally, Characterizing the strain environment of atherosclerotic plaques using magnetic resonance imaging – Determination of a mechanically sensitive plaque rupture vulnerability measure, [In preparation]

Publications not included in this thesis.

B. Tornifoglio, A.J. Stone, R.D. Johnston, S.S. Shahid, C. Kerskens, C. Lally, Diffusion tensor imaging and arterial tissue: establishing the influence of arterial tissue microstructure on fractional anisotropy, mean diffusivity and tractography, Sci. Rep. 10 (2020) 1–12. https://doi.org/10.1038/s41598-020-77675-x.

A.J. Stone, B. Tornifoglio, R.D. Johnston, Quantitative susceptibility mapping of carotid arterial tissue ex vivo: assessing sensitivity to vessel microstructural composition, Magnetic Resonance in Medicine 5327 (2021). https://doi.org/10.1101/2021.02.15.431261

S. Shahid, R.D. Johnston, E. Fitzpatrick, C. Smekens, R.T. Gaul, A.J. Stone, B. Tornifoglio, C. Kerskens, C. Lally, Exploring arterial tissue microstructural organization using diffusion magnetic resonance imaging: prospects and limitations, Sci. Rep. 11 (2021) 1–13. https://doi.org/10.1038/s41598-021-01476-z.

M. Ghasemi, R.D. Johnston, C. Lally, Development of a collagen fibre remodelling rupture risk metric for potentially vulnerable carotid artery atherosclerotic plaques, Frontiers in Physiology section Computational Physiology and Medicine (2021) , Front. Physiol. 12 (2021) 1–17. https://doi.org/10.3389/fphys.2021.718470.

A. Hanly, R.D. Johnston, A. Jose, B. Tornifoglio, C. Lemass, C. Lally, PTA-enhanced 3D micro-computed tomography of porcine carotid arteries and human atherosclerotic plaques preferentially binds to vascular collagen and offers advantages over conventional histology, Atherosclerosis (2021) [In preparation]

Conference Proceedings

R.D Johnston, R.T. Gaul, M. Ghasemi, B. Tornifoglio, C. Lally, Investigating the potential of in-vivo MRI strain measurements to identify carotid plaques at risk of rupture (2021), *26th congress of the European Society of Biomechanics.* July 11-14th, Milan, Italy [Virtual attendance]

R.D Johnston, R.T. Gaul, C. Lally, Collagen fibre orientation, not content, determines the ultimate tensile strength and strain of carotid plaque caps (2020), *Proceedings of the 25th Annual Conference of the Section of Bioengineering of the Royal Academy of Medicine in Ireland.* January 17-19th, Carlow, Ireland

O. McGee, C. Hughes, P. Jamshidi, R.D Johnston, D. Kenny, M. Attallah C. Lally, 3D printing of patient specific stents for paediatric patients (2020) *Proceedings of the 26th Annual Conference of the Section of Bioengineering of the Royal Academy of Medicine in Ireland.* January 17-19th, Carlow, Ireland

R.D Johnston, R.T. Gaul, M. Ghasemi, B. Tornifoglio, C. Lally, (2019) Characterization of circumferential strains from in-vivo MR images- Insight into a possible metric for plaque vulnerability. *European Society of Magnetic Resonance. October 3-5th,* Rotterdam, Netherlands

A.J Stone, B. Tornifoglio, R.D Johnston, C. Kerskens, C. Lally, (2019) Exploring the potential of magnetic susceptibility -based MRI for identifying microstructural degradation in arterial vessels. *European Society of Magnetic Resonance. October 3-5th,* Rotterdam, Netherlands

R.D Johnston, R.T. Gaul, M. Ghasemi, B. Tornifoglio, C. Lally, (2019) Inclusion of residual stresses in patient specific finite element simulations, *Proceedings of the 25th Annual Conference of the Section of Bioengineering of the Royal Academy of Medicine in Ireland.* January 18-19th, Limerick, Ireland

R.D Johnston, M. Ghasemi, Nolan, D.R., C. Lally, (2018) Optimized patient specific finite element models at the carotid bifurcation, *8th World Congress of Biomechanics.* July 8-12, Dublin, Ireland.

R.D Johnston, M. Ghasemi, Nolan, D.R., C. Lally, (2018) Optimization of Magnetic Resonance Imaging (MRI) based patient specific models with mechanical property estimation with inverse

finite element analysis, *16th European Mechanics of Materials Conference*. March 26-28, Nantes, France.

R.D Johnston, M. Ghasemi, Nolan, D.R., C. Lally, (2018) An in-vivo study on the impact of axial resolution on peak stresses at carotid bifurcation, *Proceedings of the 24th Annual Conference of the Section of Bioengineering of the Royal Academy of Medicine in Ireland*. January 25-26, Meath, Ireland

Prizes

Finalist for the Engineers Ireland medal for best biomedical engineering PhD

Contents

List of Figures

Figure 5.6 A schematic presentation of the remodelling process. Once the vector presenting the optimum direction of the fibres was calculated ($\vec{M}_{4op}$) a fraction of the total difference between optimum fibre configuration and the initial configuration ($\tau\Delta\vec{M}$) was added to the initial configuration of the fibres ($\vec{M}^0{}_{4ini}$) resulting in the initial configuration for the next iteration of

List of Tables

Chapter 1 Introduction

1.1 Research Motivation

Cardiovascular disease (CVD) is known to be one of the leading causes of death worldwide and was noted to be responsible for an estimated 17.8 million deaths in 2017, representing 32% of deaths globally and an increase of 21% from 2007 [1]. Due to these high numbers and an increasing trend of CVD development it is predicted a large financial burden can be attributed to CVDs [1–3]. The estimated treatment cost of CVDs and stroke reported by the Americana health Association (AHA) was 316.6 billion dollars, including 193.1 billion dollars being attributed to indirect costs [3–5]. CVDs are a group of diseases that affect the vascular system within the body, which include arteries, veins, and the heart. The two most common CVDs to present themselves in the vasculature are atherosclerosis and aneurysms [6,7]. Atherosclerosis is the build-up of plaque in the arterial wall while an aneurysm is a localized vessel weakness that can expand causing an outward bulging of the arterial wall. Diagnosing vulnerable atherosclerotic plaques at the carotid bifurcation is extremely important, as plaque rupture at this location is known to be a key contributor to ischaemic stroke cases [8]. In diagnosing vulnerable atherosclerotic plaques at risk of rupture, the current geometric diagnostic measure, percent stenosis, does not consider either the mechanical or structural aspects of the tissue and is based on the luminal narrowing of the vessel. Therefore, potential vulnerable plaques are being misdiagnosed as stable. The focus of this research is to understand the mechanics of atherosclerosis and how the development of this disease significantly alters the mechanical properties of the vessel and the tissue response to loading. This understanding would then allow for the establishment of sensitive risk measures that can possibly determine which plaques are vulnerability to rupture. Atherosclerotic plaques by their nature are extremely complex tissues that are composed of a number of structurally dependent components such as fibrous matrix, lipids, and calcifications [9]. Furthermore, changes in the collagen fibre orientation and content are important to characterize, as a lack of remodelling or the absence of fibres in the load bearing configuration at vulnerable locations could contribute to plaque rupture. In order to improve diagnosis, a sensitive mechanical indicator which is determined by the structure of these tissues needs to be established.

Biomechanical modelling of CVDs is becoming a popular tool in the development of risk metrics that could be used for diagnosis and understanding disease progression, with particular focus on estimating the stresses and strains in the vessels as a means to ascertain the areas at greatest risk of rupture. Whilst many numerical studies use constitutive models for the healthy and diseased arteries that incorporate structural details of the vessels, including collagen fibre orientation [10], dispersion [11], remodelling [12–15], and damage [16,17], few studies have included the three-

dimensional nature of the carotid bifurcation with the various plaque components. Some studies also make simplifying assumptions and exclude key aspects such as the zero-pressure configuration [18,19], residual stress [20–22] and patient specific material parameters [23–25], all of which will affect the stress and strain values obtained. Incorporation of these details into a simulation that mimics the behaviour and the geometry of the vessel *in-vivo* can aid physicians in making decisions as to whether an intervention needs to take place and aid the development of new medical devices.

To interpret and inform these biomechanical models, *ex-vivo* mechanical testing or imaging techniques must be performed. Mechanical characterization of excised atherosclerotic plaque tissue has shown that there is a highly variable mechanical response and that each plaque is unique [26]. Furthermore, due to the heterogeneity of the tissue, each component also has its own unique mechanical response [27,28]. Even with this, the particular component in the microstructure that drives this unique mechanical response is yet to be established. *Ex-vivo* imaging techniques have been established as the gold standard for determining the *in-situ* architecture of both arteries and atherosclerotic plaques. These methods can include histology, polarized light microscopy [29,30], multiphoton, second harmonic generation (SHG) [31] and small angle light scattering (SALS) [32–35]. These can provide measures such as collagen fibre orientation, collagen content and cell content but they are restricted to 2D analyses. Using magnetic resonance imaging (MRI) techniques, it is possible to establish the structure of the vessel and atherosclerotic plaques using T1 and T2 weighted contrasts. Furthermore, using more advanced imaging techniques, such as diffusion tensor imaging (DTI), it is possible to map the anisotropy of the tissue and determine the dominant direction of the microstructure [36–39]. Lastly, *in vivo* MRI circumferential strain measurements can be calculated using cardiac gated MRI sequences to acquire images at diastolic and systolic phases. Overall, this may prove to be the sensitive imaging indicator that is related to the mechanics of the tissue which can be interpreted by the insights gained from biomechanical models and experimental testing on plaque tissue.

1.2 Objectives

The overall aim of this thesis is to investigate the role of the collagen fibres in atherosclerotic plaque tissue and how it can determine the tissue's overall mechanical strength. These findings can be incorporated into patient specific computational models that can be used to establish whether certain plaques are potentially more vulnerable to rupture, or not. In turn, this will give another diagnostic tool to the physician in determining whether a clinical intervention needs to take place. To achieve this aim, the following objectives have been met, an overview of which is shown in Figure 1.1:

1. Develop patient specific finite element models from *in-vivo* MRI images and incorporate key methods such as the zero-pressure configuration and residual stress. Furthermore, a method to determine patient specific material properties and the impact excluding the zero-pressure configuration and residual stress has on these estimations is presented.

2. Investigate structurally and mechanically what key component in the arterial microstructure determines the ultimate tensile stress, strain, and stiffness of atherosclerotic plaque caps, and the location in an atherosclerotic plaque where rupture is most likely to occur.

3. Using *ex-vivo* diffusion tensor imaging, determine the collagen fibre angle in atherosclerotic plaque tissue and inform patient specific computational models. Compare healthy fibre structures to diseased fibre structures and determine the collagen fibres' ability to remodel *in vivo*. Establish if the differences between the optimum fibre configuration to the fibre configuration seen in reality may indicate whether a plaque is at risk of rupture.

4. Determine the strain variation across atherosclerotic plaque using *in-vivo* MRI and verifying the results using DTI informed computational models. Observing the strain environment and its variability across the plaque could be the possible mechanical imaging indicator to determine the vulnerability of the plaque to rupture.
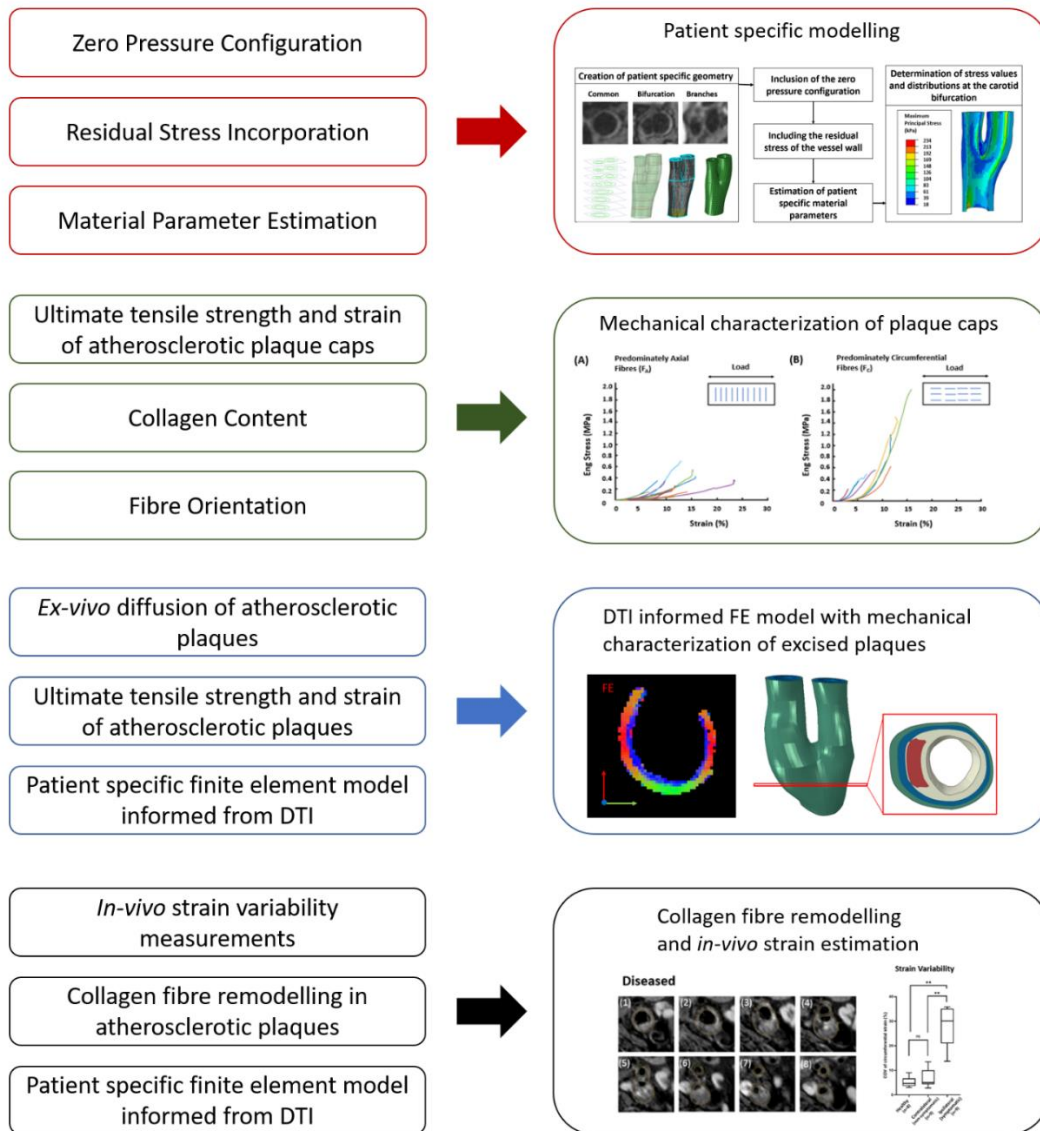
Figure 1.1 Overview of the key research objectives

1.3 Thesis Structure

This thesis consists of seven chapters centred around four studies, which emanate from four separate journal papers (one published, one submitted and two in preparation). A brief description of each chapter can be found below:

Chapter 1: Outlines the motivation behind the work completed as part of this thesis, highlighting the severity of cardiovascular disease, in particular atherosclerotic plaque development at the carotid bifurcation. This chapter outlines the need for patient specific computational models combined with novel imaging strategies which can help establish a sensitive mechanical indicator of vulnerability to plaque rupture.

Chapter 2: Firstly, a general review of the cardiovascular anatomy and physiology with a focus on atherosclerosis is presented. An in-depth review of the mechanical testing of arterial and atherosclerotic plaque tissue along with the development of patient specific computational models is carried out to highlight the key features needed to determine a sensitive mechanical plaque rupture indicator. Lastly, the relevant structural imaging techniques that are able to characterise the microstructure of the vessel and plaques are outlined.

Chapter 3: Outlines the development of patient specific finite element models from *in-vivo* MRI and implementation of key methods needed, such as the zero-pressure configuration, residual stress and patient specific material parameters for robust patient specific stress-strain analysis in arterial geometries.

Chapter 4: Presents an investigation into the critical role of fibre orientation in the ultimate tensile strength and stiffness of human carotid plaque caps. Carotid plaque caps are known to be the location at highest risk of rupture and therefore determining their mechanical behaviour with respect to their structure is critical in establishing a relevant mechanical rupture indicator.

Chapter 5: Involves observing the role of fibre orientation in the mechanical strength of atherosclerotic plaques by using ex-vivo diffusion tensor imaging to establish the fibre orientation and inform patient specific finite element models of the carotid bifurcation and atherosclerotic plaque. A mechanically sensitive remodelling metric is presented and used to establish which plaques are more vulnerable to rupture.

Chapter 6: Demonstrates a method which uses *in-vivo* MRI to determine the strain variability across atherosclerotic plaques and compares these results with patient specific ex-vivo DTI informed biomechanical models.

Chapter 7 and 8: Concludes with a final discussion to unify the key findings from Chapters 3-6 and highlights the contribution of this work to the area of atherosclerotic plaque biomechanics. Furthermore, recommendations for future work are also presented.

Chapter 2 Literature Review

2.1 Cardiovascular System

The cardiovascular system consists of the heart, blood vessels and circulating blood and is responsible for many vital functions in the body. The circulating blood provides oxygen and nutrients for many important functions in the body such as supplying nutrients and removing carbon dioxide and waste products from the cells. The cardiovascular system can be split into two distinct circuits which depict their blood flow pathways; (i) the pulmonary circuit, which carries oxygen depleted blood from the heart to the lungs where oxygenated blood is then circulated back to the heart, and (ii) the systemic circuit which carries oxygenated blood to the rest of the body and this oxygen depleted blood is then circulated back to the heart [40]. These circuits are illustrated in figure 2.1.
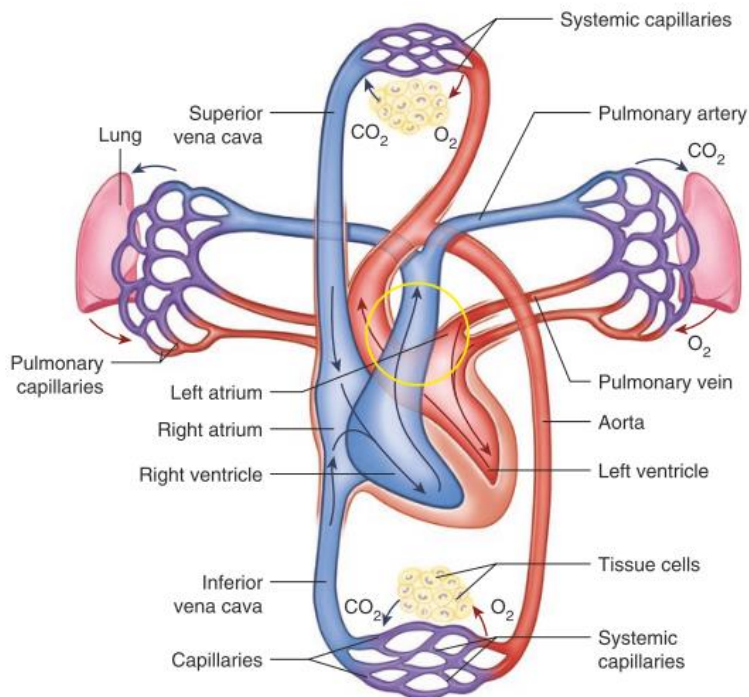
Figure 2.1 Pulmonary and systemic circuits with the heart located in the centre [40]

At the centre of these circuits is the heart. A muscular organ, the heart consists of four chambers. The heart receives deoxygenated blood from the systemic circuit into the right atrium and from this location, the blood is passed onto the pulmonary circuit to become oxygenated by the lungs before returning to the left atrium. The blood passes through the mitral valve to the left ventricle which pumps the oxygenated blood through the aorta and around the body via the systemic circuit [40].
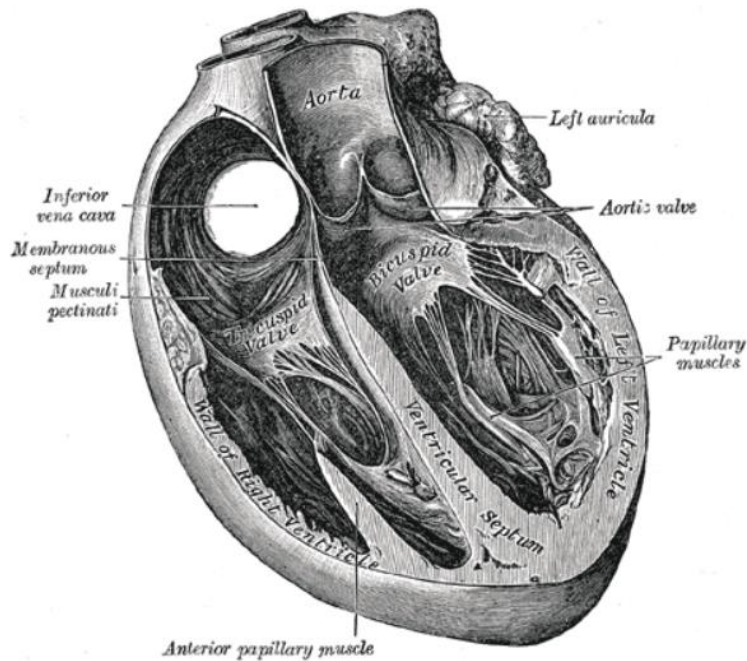
Figure 2.2 Schematic of the heart anatomy depicting its four chambers and the ventricular septum [41,42]

Considerable research has been done to understand the structure and mechanics of the cardiovascular system. However, in order to develop specific treatments and diagnostic metrics for cardiovascular diseases that relate to its structural and mechanical function, more research is required.

2.2 Carotid Arteries

The carotid arteries are located in the upper body, neck and head and are the primary blood suppliers of oxygenated blood to these locations. They are classed as large to medium arteries that experience different blood pressure in both the systolic (peak pressure during heart contraction) and diastolic (minimum pressure in which the heart expands and refills) phases in the cardiac cycle. The carotid arteries on the right and left originate from the brachiocephalic trunk and the aortic arch, respectively. Although the origins of the left and right carotid are different, both arteries diverge to create the internal and external carotid arteries at a location known as the carotid bifurcation. The external carotid arteries, which are generally smaller in size then the internal carotids, have more branches which supply blood to the face, scalp and meninges; meanwhile the internal carotid arteries are arteries with many branches diverting off them and supplying blood to the brain (via the circle of Willis) and eyes. The carotid bifurcation experiences a complex hemodynamic environment due to its structure and therefore

atherosclerotic plaques commonly develop at this location. The development of atherosclerotic plaques compromises the structure and stability of the vessel [40,41].
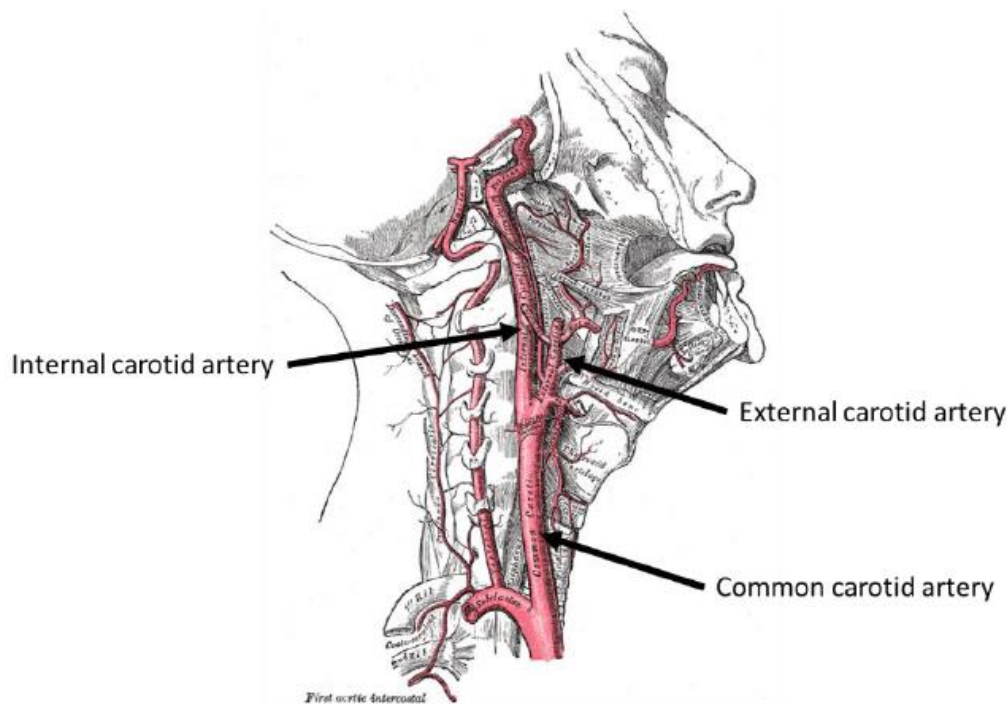
Figure 2.3 Modified image to show the location of the right common carotid artery (CCA) in the neck with branching into internal (ICA) and external (ECA) carotid arteries. [41]

2.2.1 Arterial Structure

The carotid artery is a heterogenous structure and comprises of three main layers which determine its mechanical behaviour, these are the tunica intima, tunica media and the tunica adventitia [10,43]. All these constituents contribute to the biomechanical behaviour of the artery. The outermost layer, the tunica adventitia, is composed of connective tissue with both collagen and elastin fibres [43]. The collagen and elastin fibres are vitally important for maintaining the mechanical integrity of the tissue whereby the collagen provides the strength and prevents failure at high pressures and elastin provides reversible extensibility during cyclic loading of the cardiac cycle. The middle layer of the artery, the tunica media, is the thickest of all the vessels layers and is comprised of collagen, elastin, smooth muscle cells and proteoglycans arranged helically [43]. The adventitia and media together are known to be the most dominant contributors to the mechanical behaviour of healthy arteries [10]. The innermost layer, the tunica intima, is an extremely thin layer that consists of longitudinally orientated endothelial cells on a thin basal lamina [43]. The intima has little mechanical contribution in arterial tissue in younger people but is the layer most impacted by the development of atherosclerosis [44]. The development of atherosclerosis in the vessel stiffens and thickens the subendothelial layer, impacting the intima

and results in it becoming more mechanically important in the vessel. The width of the layer between the tunica intima and the external elastic membrane is called the intima-media thickness (IMT). The quantification of the IMT is often used as an indicator of atherosclerosis [45,46].
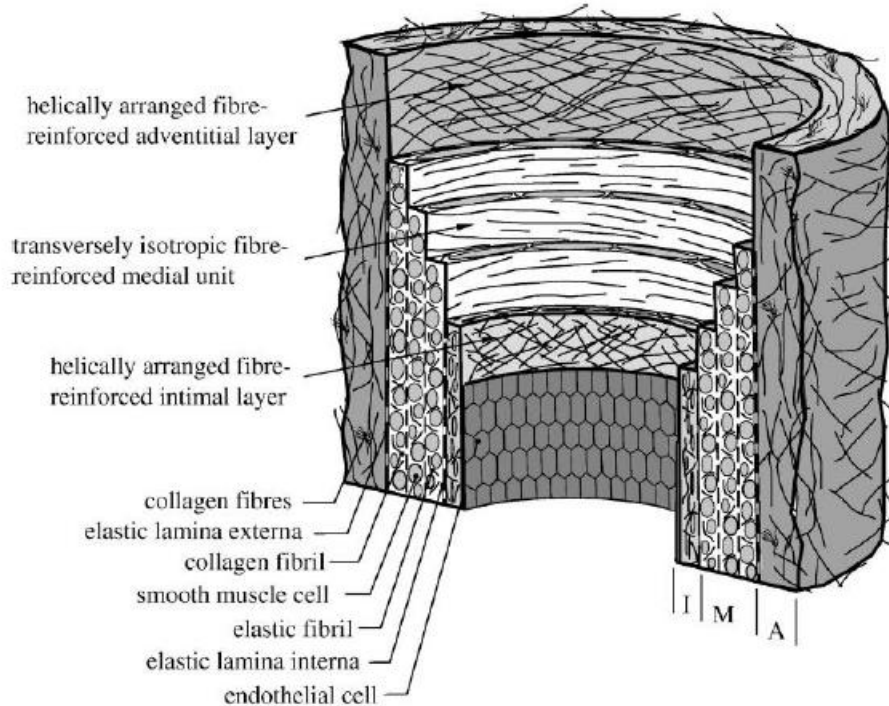
Figure 2.4 Structure of the healthy arterial wall depicting its layers and microstructure. The tunica intima (I), the tunica media (M) and the tunica adventitia (A) [10].

2.2.2 Artery Types

Arteries can be divided into three categories, (i) elastic arteries, (ii) muscular arteries and (iii) arterioles and categorization generally depends on their size, location, and function [47]. Elastic arteries are generally the largest in the body and are involved in transporting the largest volumes of blood at high pressures away from the heart. This is to facilitate this high-pressure fluctuation from diastole to systole and large volumes of blood involved. The tunica media in elastic arteries has a higher elastin content and lumen diameter compared to muscular arteries and arterioles. The carotid arteries, those of interest in this thesis, are classified as elastic arteries [47,48]. In a localised region in the vasculature such as the carotid artery, it has been observed that this elastic artery classification may not be true as there a transition from elastic (more elastin less cells) to muscular (less elastin more cells) when comparing proximal and distal regions

Muscular arteries differ from elastic arteries as they have smaller lumen diameters and more smooth muscle cells in the media, rather than elastin or collagen fibres. Muscular arteries are located distally to elastic arteries and are responsible for the distribution of blood to skeletal muscles and internal organs [47]. Cerebral vessels are known to be muscular arteries [49].

Arterioles are the smallest of all vessel types mentioned here. They are located distally of muscular arteries and are the most distal vessels from the heart. The tunica media in these vessels contain a few layers of smooth muscle cells while the adventitia is almost completely absent. The blood flow rate in the arterioles is constant. The greater percentage of smooth muscle cells in muscular arteries and arterioles is vitally important for controlling blood flow in response to certain stimuli. Smooth muscles cells enable contractility of the vessel wall allowing it to relax and dilate to reduce resistance and increase blood flow rate accordingly [47].
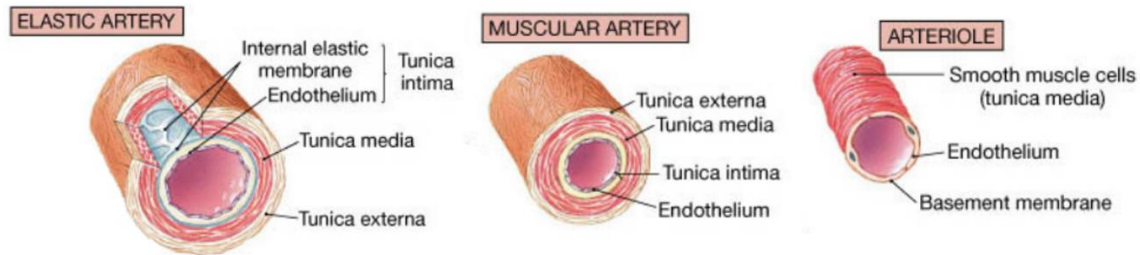
Figure 2.5 Comparing the structure of elastic, muscular and arteriole arteries.

The relative amounts of elastin and smooth muscle cells are optimized in each artery in order to perform the artery's role while expending minimal energy. It could be suggested that the arteries only require smooth muscle cells, and no elastin would give more blood flow control while still resisting pressure and reducing flow fluctuations. However, under this circumstance, the smooth muscle cells would require a constant supply of energy to continually contract and resist pressure. In arteries, the pressure is resisted by the deformation of the elastin and collagen fibres and thus uses minimal energy. This leaves the smooth muscle cells to control the contractility of the artery and the blood flow rate [47].

2.3 Mechanical Behaviour of Arteries

The mechanical behaviour of the arterial wall is determined by the composition of the artery (endothelial cells, smooth muscle cells, elastin and collagen). Due to the highly heterogenous and anisotropic nature of the arterial wall, these components are not distributed or orientated in a structured fashioned and are sample dependent. The mechanical behaviour tends to be similar in healthy arterial vessels. A comprehensive review on the physiological performance of arteries is provided by Burton et al (1968) and considerable work has looked at characterizing their non-linear anisotropic mechanical response [49].

Uniaxial tensile testing of arterial tissue is well documented in the literature [26,50]. In all cases, the tensile testing of arterial tissue produces the characteristic "J-shaped" curve, where large levels of strain are observed at low loads until a stiffening response is initiated [26,50,51]. The elastin and ground matrix of the tissue dominates the initial linear region of the curve, where low

loads equate to high deformations in the tissue [51]. At this initial uptake, the collagen fibres are wavy in nature and do not bear the load until the tissue deforms to a certain level. After this initial uptake, the collagen fibres are recruited to bear the load. To do this, the collagen fibres straighten and align accordingly [52]. What is important to realise is that the layers of the artery respond differently when loaded [53]. Holzapfel et al (2005), looked at the mean response of 13 human left anterior descending coronary arteries separated into their individual layers in the longitudinal and circumferential directions as illustrated by figure 2.6. This varied mechanical response can solely be attributed to the varied microstructural organisation in these layers, in particular the distribution of the collagen fibres [53].
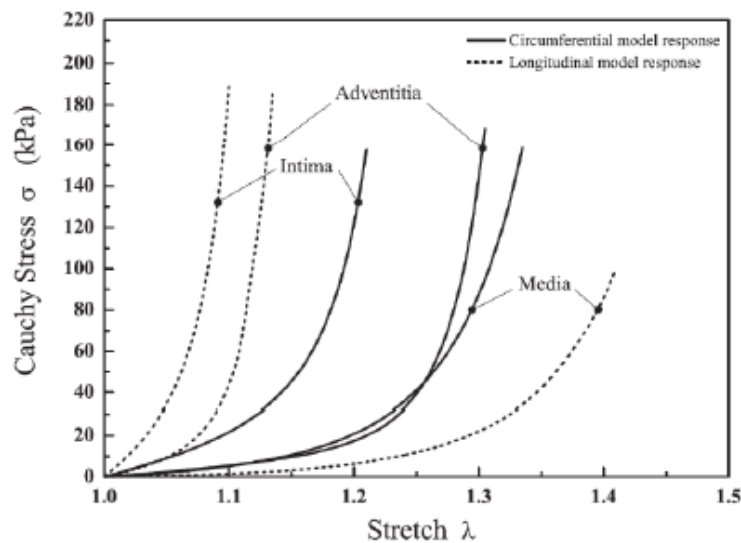
Figure 2.6 Mean Cauchy stress-stretch showing layer specific response (intima, media and adventitia) for the coronary artery in the circumferential and axial directions [53]

Arteries behave viscoelastically, this can be shown when creep is induced at constant strain and stress relaxation under constant load and hysteresis in cyclic loading. Arteries are relatively insensitive to strain rates and can be preconditioned to reduce hysteresis [54]. For this reason, preconditioning of arterial vessels in mechanical testing is important in order to capture the true mechanical behaviour of the tissue.

It has been established that the arterial wall has residual stresses that reside in the wall to homogenise the stress through the vessel wall *in-vivo* [21,55,56]. Similar to having different mechanical behaviours, the vessel layers also exhibit different residual stresses due to their microstructure, to homogenise the stress distribution [57,58]. Holzapfel et al (2007) demonstrated this layer specific residual stress response experimentally in human aorta samples. To do this, they delineated the artery into its respective layers (intima, media, and adventitia) and cut them open as illustrated in figure 2.7. They established that after separation, the adventitia from the

ring sprang open by about 180° on average, becoming flat, the intima opened only slightly, but the media sprang open by more than 180° (as did the intact strip) [58]. Most importantly, they found that residual deformations are three dimensional and cannot be described by a single parameter such as the opening angle [58].
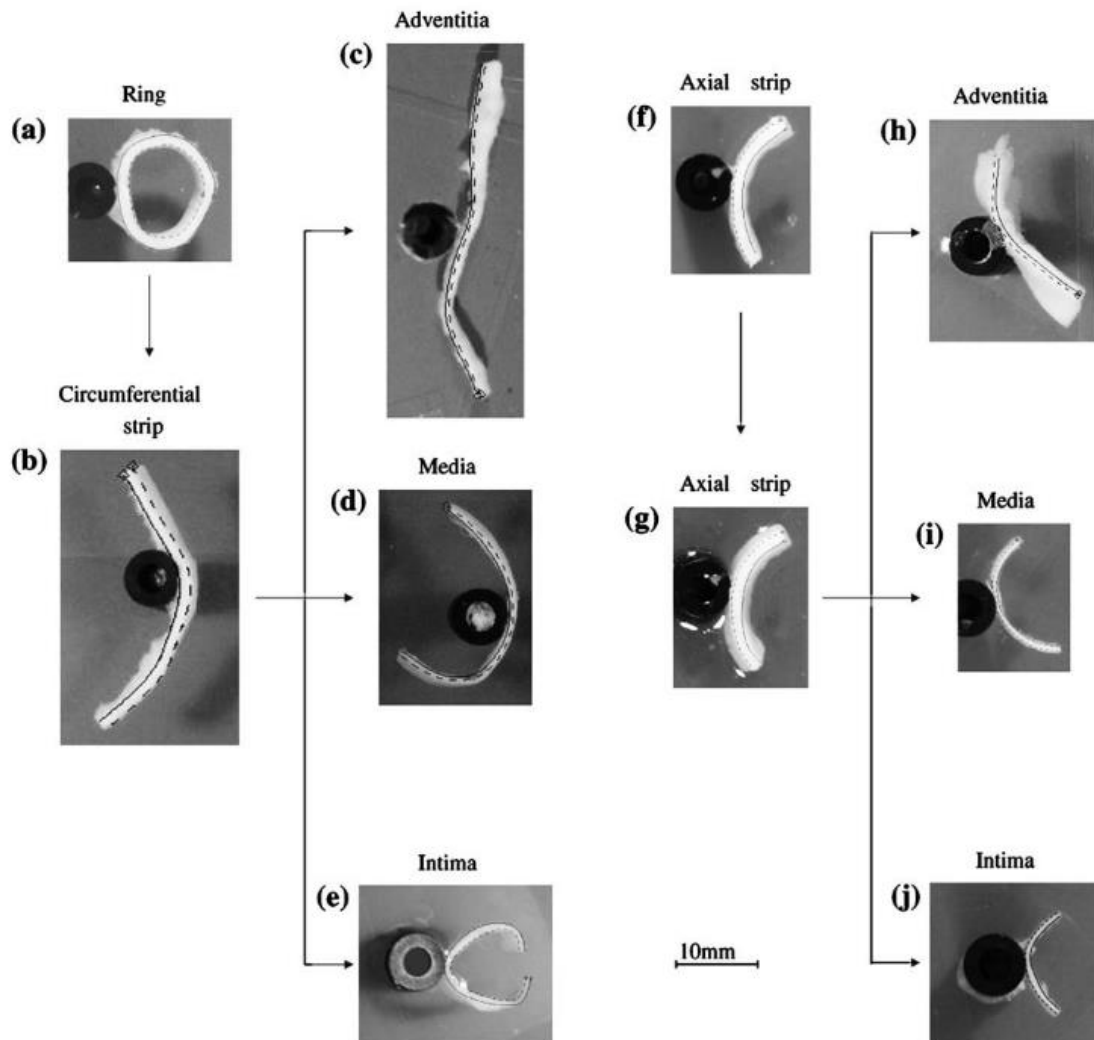
Figure 2.7 Circumferential (a, b) and axial (f, g) strip response after 16hrs of equilibration for the adventitia (c, h), media (d, i), and intima (e, j). Observed here is that each layer exhibits different opening angles indicating a layer specific residual stress response

Further mechanical testing has been performed to characterise the behaviour of arteries under more physiological conditions such as biaxial and pressure inflation testing. Biaxial testing is performed to observe the contribution of collagen fibres with respect to their orientation when loaded [54,59,60]. Sommer et al (2009) established the biaxial mechanical properties of intact and layer dissected human carotid arteries at both physiological and supraphysiological loading conditions highlighting that the level of axial stretch imposed on the tissue effects the overall mechanical response of the tissue. Pressure inflation testing is becoming more common in the

testing of arterial tissue as it mimics *in-vivo* loading conditions and facilitates *ex-vivo* imaging of the samples [61,62]. Therefore, using experimental methods that mimic *in-vivo* conditions allows for a more in depth understanding of the stress strain environment of the tissue, what it is experiencing *in-vivo* and offer the capability to translate established methods to a clinical setting.

2.4 Cardiovascular Diseases

CVDs are known to be the one of the leading causes of death worldwide [6]. Due to an aging world population and the prevention of infectious diseases in developing countries, it is expected that the number of people dying due to CVDs is expected to increase [63]. CVDs encompass a number of different diseases that all effect the vasculature of the body, and in which the development of these diseases generally leads to fatal events such as stroke or myocardial infarction.

2.4.1 Atherosclerosis

The main reason for stroke occurrence is due to the presence of atherosclerotic plaques in the vasculature. Atherosclerosis is a systemic disease of the artery, caused by the accumulation of inflammatory cells and lipids inside the arterial wall. Classed as an intima-media disease, this accumulation often leads to a thickening and stiffening of the arterial wall [63]. Locations with a complex hemodynamic environment, such as the carotid bifurcation, often experience accelerated atherosclerotic plaque development [64], as shown in figure 2.8. Due to the carotid's proximity to the smaller muscular arteries that supply blood to the face and brain, detection of vulnerable carotid plaques that could possibly rupture at this location is of vital importance.
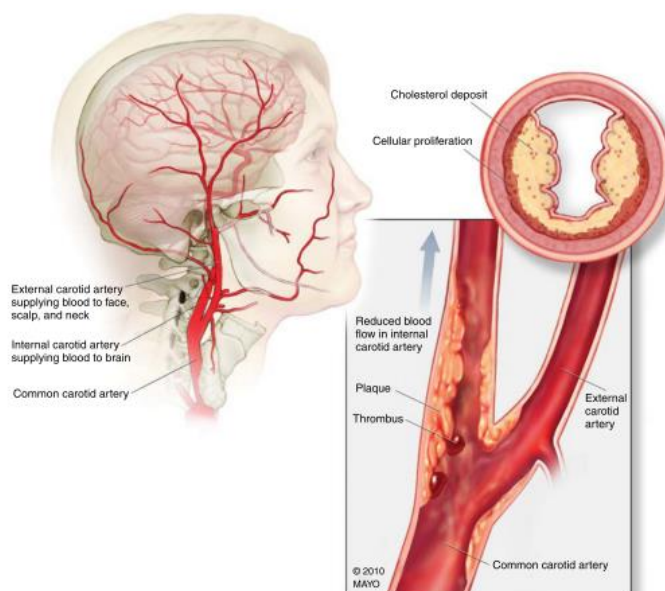
Figure 2.8 Development of an atherosclerotic plaque at the carotid bifurcation. Plaque, a result of cholesterol deposit and cellular proliferations reduces the arterial lumen and alters blood flow [52].

In order to understand the development of atherosclerosis in at the arterial wall, the American Heart Association (AHA) has developed a classification system which categorizes the plaque into eight categories depending on the stage of its development [65,66]. Type I and II lesions depict the early developments of atherosclerosis and can be seen as early as infancy. More specifically, Type I shows the adaptive thickening of the vessel where lipid laden foam cells infiltrate the intima whereas Type II shows macrophage foam cells distributed throughout the intimal layer of the artery at highly susceptible locations. Type III lesions progress from the aforementioned Type II lesions by developing extracellular lipid pools along with smooth muscle cell disruption. Type III lesions are classified as the intermediate stage of atherosclerosis development [65,66].

Type IV, V and VI lesions are classified as the latest stages of atherosclerosis development. Type IV lesions develop a core of extracellular lipid (also called the necrotic core) within the wall. This signals the development of a clinically relevant atheroma but is absent from both calcified and fibrous tissue seen in V and VI lesions. The inclusion of this extracellular lipid significantly alters the intima microstructure which impacts the effect it has when reacting to a mechanical stimulus. The inability for the collagen and SMCs to remodel and distribute new collagen increase the risk [65,66].
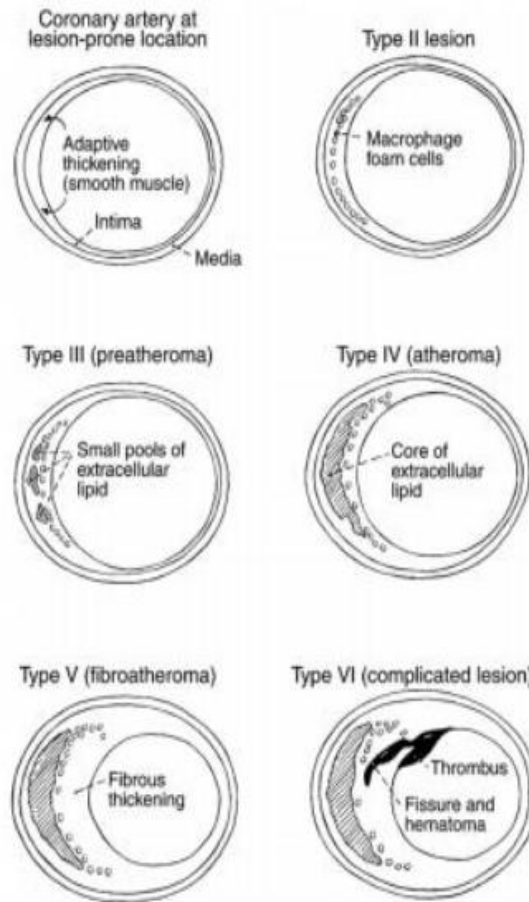
Figure 2.9 Schematic depicting the progression of a coronary plaque [67]

Type IV lesions can take several development paths depending on their growth mechanism. Type IV lesions can accelerate their progression to become complicated type VI lesions which present fissures and hematoma along with surface haemorrhage in the form of thrombus formation. Successive type VI lesions may lead to complete occlusion of the artery, which in some cases is seen as structurally stable. Healing at stage VI can cause the development of fibrous tissue (fibroatheroma) and is then called a type V lesion. The flowchart shown in figure 2.10 illustrates that the development of fibrous tissue can lead to a runaway development of thrombosis and atheroma. Regression or change in the lipid of lesion types IV, V and VI can result in the development of type VII lesions where calcifications are present or type VIII lesions where fibrous tissue dominates. These lesions are more mechanically stable than the type IV, V and VI lesions but can regress towards these higher risk plaques [65–67]

```
┌────────────────────────────────────┐   ┌────────────────────────────────────────┐
│ Intima at highly susceptible sites │   │ Intima at moderately susceptible sites  │
│          of arteries               │   │            of arteries                  │
└────────────────────────────────────┘   └────────────────────────────────────────┘

            ┌──────────────────────────────────────────┐
            │      I. Isolated macrophage foam cells     │
            └──────────────────────────────────────────┘

            ┌──────────────────────────────────────────┐
            │      II. Multiple foam cell layers formed  │
            └──────────────────────────────────────────┘

            ┌──────────────────────────────────────────┐
            │   III. Isolated extracellular lipid pools added │
            └──────────────────────────────────────────┘

            ┌──────────────────────────────────────────┐
            │  IV. Confluent extracellular lipid core formed  │
            └──────────────────────────────────────────┘

            ┌──────────────────────────────────────────┐
            │   V. Fibromuscular tissue layers produced  │
            └──────────────────────────────────────────┘

            ┌──────────────────────────────────────────┐
            │   VI. Surface defect, hematoma, thrombosis │
            └──────────────────────────────────────────┘

            ┌──────────────────────────────────────────┐
            │      VII. Calcification predominates        │
            └──────────────────────────────────────────┘

            ┌──────────────────────────────────────────┐
            │  VIII. Fibrous tissue changes predominate  │
            └──────────────────────────────────────────┘
```

Lipid and cells accumulate faster and advanced lesions develop first at highly susceptible rather than moderately susceptible sites

Regression of type I-III changes to normal is possible

Fibrosis of type VI change adds to type V thickness and stiffness and leads to loss of lumen

Successive type IV episodes may quickly lead to occlusion

Regression or change of lipid in lesion types IV-VI may result in lesion types VII-VIII

Figure 2.10 Flowchart depicting plaque types and progression mechanisms [65]

Table 2.1 Summary of histopathological features of atheromatous plaques [68].

AHA Plaque Type	Histopathological Findings	Symptomatic Status
Type I	Isolated deposition of macrophages & foam cells.	Asymptomatic
Type II	Fatty streak lesion w/ mainly intracellular lipid accumulation.	Asymptomatic
Type III	Deposition of intracellular lipids w/in the plaque.	Asymptomatic
Type IV	Dense accumulation of extracellular lipid (i.e., lipid core). Inflammatory cell infiltration. No fibrous tissue formation, no surface defects or thrombosis.	Possibly symptomatic
Type V	Fibrous cap overlying necrotic lipid core. Inflammation w/in plaque & in the vasa vasorum of the artery wall. Prone to hematoma, thrombus formation, & fissuring.	Possibly symptomatic
Type VI	Fissuring & ulceration of plaque. Necrotic lipid core. Intraplaque hemorrhage & thrombus. Inflammation w/in the plaque.	Probably symptomatic

Atherosclerotic plaques can be categorized as either (i) stable or (ii) vulnerable. Vulnerable plaques can develop when a plaque has a lipid rich necrotic core covered by a thin fibrous cap. Failure is most commonly observed at the location of the fibrous plaque cap, whereby the stress exerted on this location exceeds it overall mechanical strength [68]. Type I – III plaques are

categorized as asymptomatic plaques; however, these plaques can still be vulnerable to rupture. There is currently a lack of understanding of what in the microstructure of atherosclerotic plaques drives its overall mechanical behaviour [69].

Naghavi et al (2003) established the many different forms of the vulnerable atherosclerotic plaque [69]. By extending on the initial AHA classifications, Naghavi et al (2003) looked to quantify what constitutes not only a vulnerable plaque but a "vulnerable patient". This new term encompasses a number of different aspects such as the vulnerability of the plaque, blood flow and the myocardium condition in order to diagnose patients [68]. Potentially vulnerable plaque types based on these criteria are illustrated in figure 2.11. Altogether, 5 major criteria have been established to aid in the identification of plaque vulnerability. These are (i) active inflammation, (ii) thin fibrous cap, (iii) large lipid core, (iv) endothelial denudation (v) platelet aggregation as well as a number of potential intravascular diagnostic measures. A closer look at plaque pathogenesis has identified factors behind plaque stabilization, which has been observed to occur post rupture, however no clear means for achieving this has been suggested. Despite the substantial volume of work to date investigating plaque development, progression, and vulnerability, the mechanobiological cues driving atherosclerosis is still unclear. Furthermore, determining whether a plaque can be stable or less vulnerable than others is still yet to be fully established.
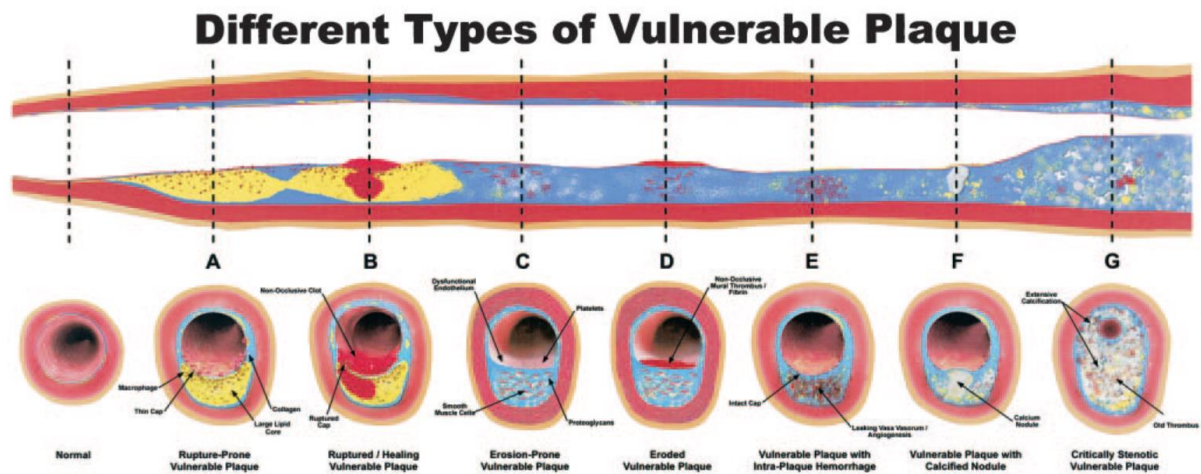
Figure 2.11 Forms of vulnerable plaque (A) Rupture prone plaque with large lipid core and thin fibrous cap infiltrated by macrophages (B) Ruptured plaque with subocclusive thrombus (C) Erosion prone plaque with proteoglycan matrix in a smooth muscle cell rich plaque (D) Eroded plaque with subocclusive thrombus (E) Intraplaque haemorrhage (F) Vulnerable plaque with calcified nodule (G) Critically stenotic vulnerable plaque [68]

2.5 Current Diagnosis and Treatments of Vulnerable Atherosclerotic Plaques

The current method to diagnose plaque vulnerability to rupture is a combination of both clinical examination and cardiovascular imaging to determine the degree of percent stenosis. The cardiovascular imaging aspect will be explained later in the literature review. Traditionally, only diametric measurements are used for the evaluation of stenosis [70], whereby a normal region proximal or distal to the lesion serves as the reference and the minimum luminal diameter is the target, see figure 2.12a. The percentage of stenosis is then calculated from these measurements. There are now two established methods for the grading of the percent stenosis in the carotid. These are (i) The North American Symptomatic Carotid Endarterectomy Trial (NASCET) [71] and (ii) European Carotid Surgical Trial (ECST) [71]. These metrics are defined by the narrowed lumen diameter (a in figure 2.12b), the diameter of the outer wall (b in figure 2.12b) and the diameter of the normal lumen (c in figure 2.12b). The relationship between NASCET and ECST is shown in figure 2.12b.
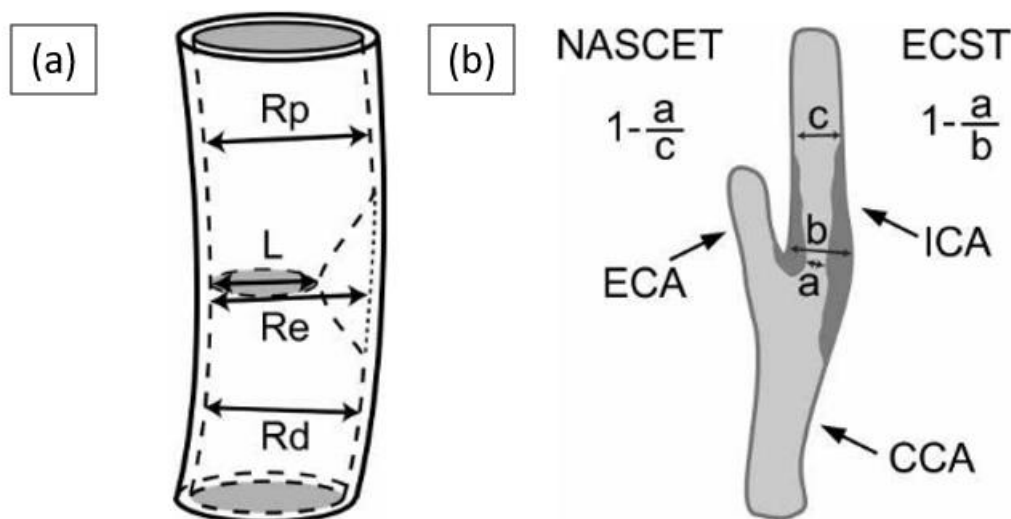
Figure 2.12 (a) Measurements used to determine the degree of stenosis. R_p, R_e and R_d can serve as the reference value. Percent stenosis is calculated as (1-L/R)x100, where L = lesion diameter and R = diameter at reference site. (b) How to establish the degree of stenosis in the internal carotid artery using either ECST or NASCET criteria [70].

Another important measure is plaque burden, which is the percentage of wall volume of the plaque relative to the whole wall volume of the vessel (i.e., wall and lumen volume inclusive). Stork et al (2004) specifically showed that plaque burden was a reliable predictor for the presence of atherosclerotic plaques in elderly cases [72]. The artery is known to actively remodel when a plaque is developing and the thickness of the intima and media increases [72]. As stated previously, it is for this reason the intima-media thickness (IMT) has been used as a predictor of early onset atherosclerosis [73].

For clinical examinations, the major symptoms include changes in vision, headaches, speech, or facial and extremity weakness. Patients with a prior history of stroke or transient ischaemic attack (TIA) are especially susceptible to plaque accumulation and are deemed a "risky" group. Furthermore, a high-pitched bruit at the carotid artery along with an increase in pulsations of the vessel symbolizes turbulent blood flow and is known to be a possible indicator of carotid artery disease. Once a vessel has been identified as vulnerable, depending on the severity and location of the condition, three methods can be used to treat carotid artery disease.

1. Medical Treatment

For the early stages of plaque formation and less vulnerable cases, the physician may recommend treatments that encompass a combination of non-invasive treatments directed at correcting modifiable risk factors. Management of the risk factors include the support of healthy lifestyle choices including diet modification, exercise, and smoking cessation along with antithrombotic, antihypertensive, dyslipidaemic, antiarrhythmic and diabetic treatments [6].

2. Surgical Treatment

For more vulnerable cases, surgical intervention can be carried out in the form of a carotid endarterectomy (CEA). CEAs are the well-established method for the removal of atherosclerotic plaques. Endarterectomies are of greatest benefit to patients with a stenosis of greater than 70% and a marginal benefit in symptomatic cases ranging in 50-69% stenosis. Patients that exhibit a percent stenosis of <50% showed no significant benefit from endarterectomy procedures [40]. For this reason, medical and endovascular treatments could be used for this cohort of patients.

The carotid endarterectomy procedure, illustrated in figure 2.13, involves several key steps. Firstly, an incision is made to locate the carotid artery and the plaque, and then cross clamping is done on the common carotid to ensure no blood flow in the region. Once clamped, the lumen of the artery is opened up via a small excision into the vessel wall and the plaque is subsequently removed. Plaques can be removed both completely intact or with an axial incision, subject to surgeon preference. The artery is then sutured closed, and a patch is placed to ensure the lumen does not decrease in size. Use of the patch is optional but is more common than not. Homeostasis is then achieved by releasing the clamps and allowing for blood flow to perfuse through the vessel once again.
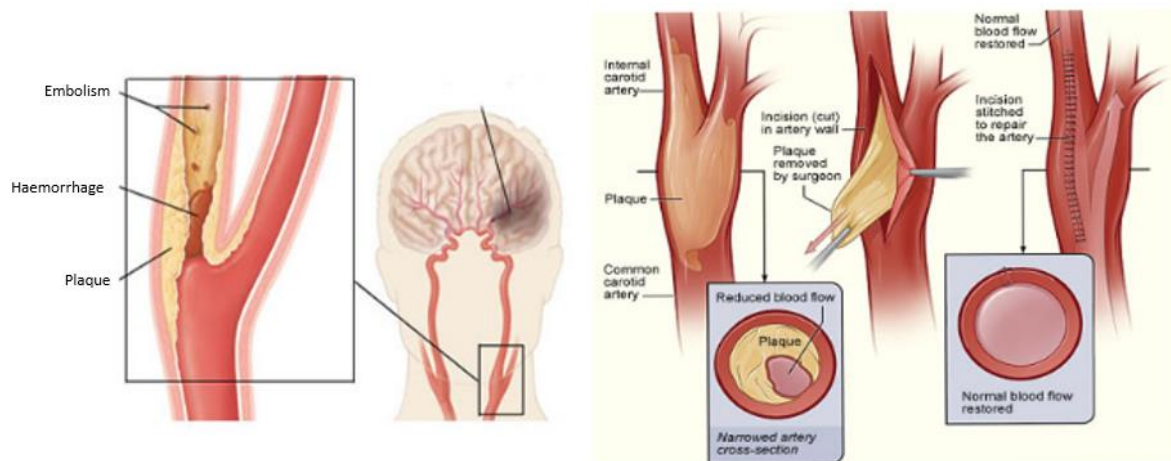
Figure 2.13 The carotid endarterectomy procedure.

3. Endovascular Treatment

Endovascular carotid artery angioplasty and stenting is becoming more common in the treatment of atherosclerosis. The procedure is illustrated in figure 2.14 and involves the introduction of a catheter via a guidewire and the deployment of a balloon, with or without a stent, to expand the lumen of the artery which has been blocked. A stent deployment at this location can also help prop open the artery and decrease the possibility of the vessel narrowing again. Once the lumen is opened up sufficiently, the device is withdrawn [52].
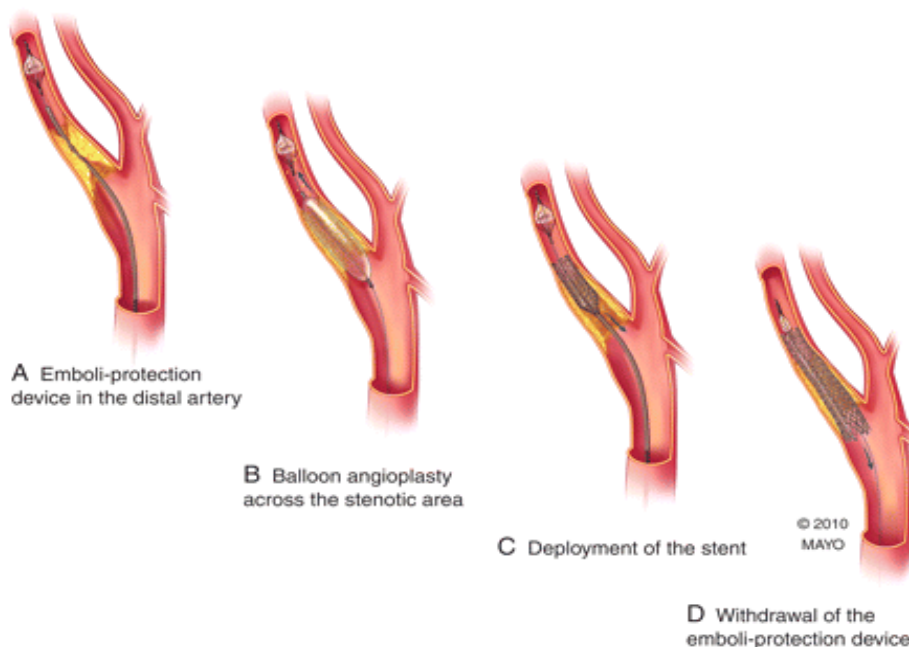
Figure 2.14 Illustration of the steps performed in a carotid angioplasty and stenting (a) Emboli protection filter is placed to capture any fragments (b) Balloon angioplasty to increase lumen diameter (c) Deployment of stent (d) Withdrawal of the emboli-protection filter [52]

Uptake of stenting and angioplasty in the treatment of carotid artery disease was initially poor due to the low long-term patency of the carotid artery and the risk of embolization of debris causing neurological deficits. The development of stents (intraluminal and crush resistant nickel-titanium) with long patency and double balloon or emboli-protection devices improved results. However, compared to the success of the CEA it is still not as popular a form of treatment for carotid artery disease and is more suited to locations such as the coronary artery.

2.6 Mechanical stresses within atherosclerotic plaque tissue

To fully establish what experimental methods are required to characterize the mechanical properties of atherosclerotic plaque tissue, it is important to fully understand the forces that the tissue is subjected to *in-vivo*. Force is known to be a vector that has both a magnitude and direction and has the capacity to change an object's motion. If all forces acting in all directions are equal, then no change in motion will occur. Forces influence the mechanics and fluid dynamics in arterial tissue and the forces experienced by these tissues have the capacity to alter the motion and therefore cause internal stresses [74]. Atherosclerotic plaques are subjected to mechanical stresses due to the presence of blood pressure and blood flow. As shown in figure 2.15, several types of stress are present in atherosclerotic plaques. Firstly, mechanical contributions in the form of circumferential, radial, and axial stresses are due to the presence of luminal pressure and axial strain. Secondly, fluid forces contribute to the overall force exerted on the tissue in the form of shear stress. Shear stress is present due to the frictional forces from blood flow across the plaque.
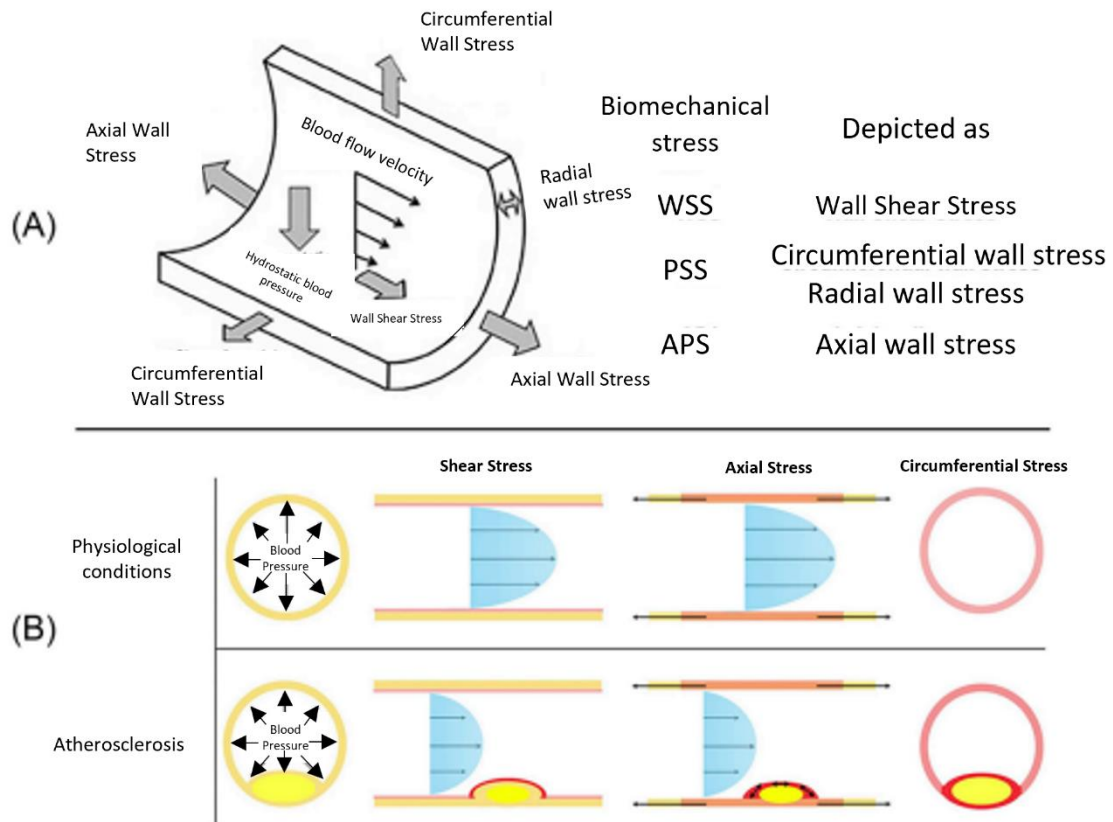
Figure 2.15: Illustrative summary of the biomechanical wall stresses present in the vessel wall and atherosclerotic plaque. (A) Stresses exhibited in the vessel wall and atherosclerotic plaque which are wall shear stress (WSS), peak structural stress (PSS) and axial plaque stress (APS) (B) Comparative representation of the stresses and their magnitude (shade of red) in normal and atherosclerotic arteries [74]

Lastly, there is an active force contribution due to the presence of vascular smooth muscle cells (VSMCs) in the vessel wall and atherosclerotic plaque which contributes to the overall stress experienced by the tissue *in-vivo* [75]. VMSCs are present at all stages of atherosclerotic plaque development and are responsible for contraction and production of extracellular matrix (ECM) within the tissue.

2.7 Mechanical characterisation of atherosclerotic plaque tissue

To establish possible new metrics to determine a vulnerable plaque to rupture, understanding the mechanics of the tissue and the many structural components is crucial. Like the artery, the mechanical behaviour of atherosclerotic plaques is also defined by its composition. Due to there being many different types and stages of atherosclerotic plaque development, as stated in section 2.4, the distribution of structural components being different would lead to a unique mechanical response of each plaque in each respective patient.

Uniaxial tensile testing has been the most common testing method for determining the mechanical behaviour of the atherosclerotic plaque tissue from different locations in the vasculature. Each method in the literature has varying test protocols ranging from specimen retrieval, storage, component testing and length to width ratio of samples [26,76–79], making it more difficult to standardise the testing protocols. Walsh et al (2014) reviewed a number of studies that looked into the uniaxial tensile testing of atherosclerotic plaques and summarized their findings. A brief review of the carotid plaque results and more recent publications will be discussed here. Maher et al (2009) performed uniaxial tensile tests of carotid plaques in the circumferential direction with samples classified pre-operatively by using duplex ultrasound; 8 samples were calcified, 4 samples were echolucent and 4 samples were mixed. No significant difference was observed in the mechanical responses of these plaques based on these groupings [76]. Teng et al (2009) tested diseased carotid arteries in both axial and circumferential directions in each vessel and diseased media strips. Teng observed a stiffer response than the previous study because the media and adventitial layers of the vessel were also included [79]. Lawlor et al (2011) performed uniaxial tension on plaques in the circumferential direction and also classified the plaque specimens using duplex ultrasound. In grouping the samples, 5 were calcified, 2 echolucent and 6 were mixed [77]. Similar to the results shown in Maher et al (2009), no significant difference was seen in the mechanical responses of the tissue. Mulvihill et al (2013) performed biaxial extension test of strips of carotid plaque samples in the circumferential direction and similar to Maher and Lawlor classified the samples using duplex ultrasound with 5 calcified, 12 echolucent and 7 mixed. Similar results again were observed as in previous studies [80]. An overview of the experimental data from these studies are illustrated in figure 2.16a. Furthermore, these plaques have different mechanical responses based on their classification from duplex ultrasound, as shown in figure 2.16b, c,d. hereby, calcified plaques exhibited a stiffer response to plaques that were lipid rich, highlighting the mechanical and structural variability in the tissue.
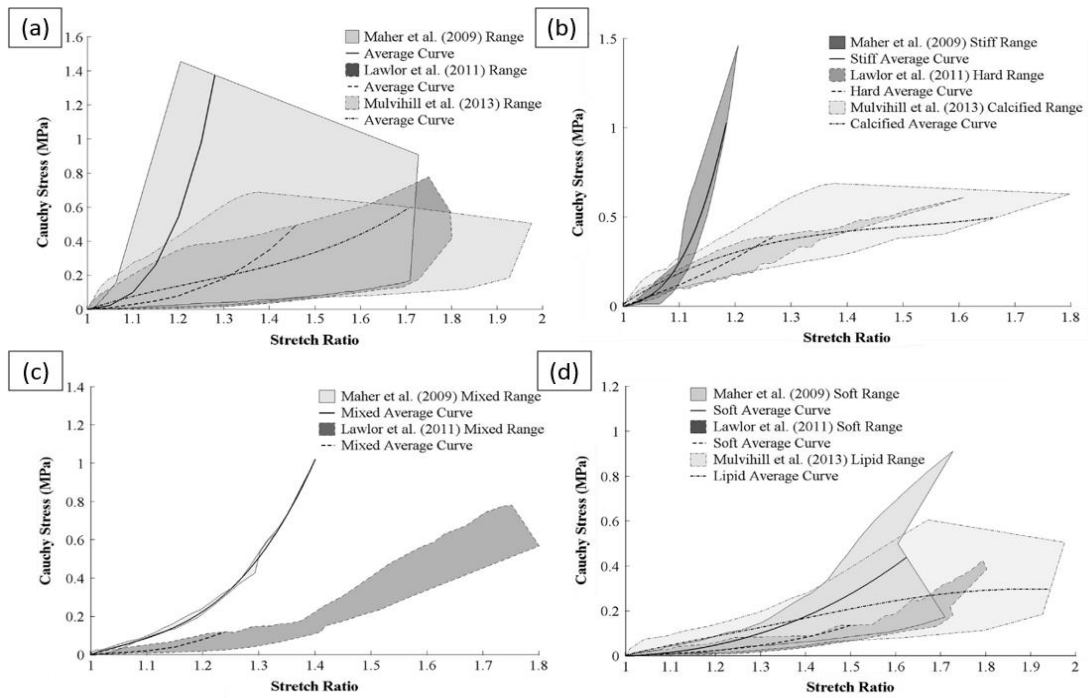
Figure 2.16 (A) Cauchy stress vs stretch ratio data for human atherosclerotic carotid plaques undergoing uniaxial tension. Cauchy stress vs stretch ratio data for human atherosclerotic carotid plaques based on their classification. (B) Calcified / Hard / Stiff (C) Mixed (D) Soft / Lipid rich plaques [26]

Selective testing of individual plaque components has also been performed in a number of studies not mentioned in the review by Walsh et al (2014). Teng et al (2014) performed uniaxial tensile tests on strip samples of the media, fibrous cap, lipid and intraplaque haemorrhage / thrombus (IPH/T) and demonstrated the highly variable mechanical response of each component showing that the fibrous cap and media are stiffer than either lipid or IPH/T in all cases [28]. Davis et al (2016) performed uniaxial tensile tests specifically on the fibrous plaque cap with an aim to characterize the fracture behaviour of this tissue. Observing the various mechanical responses from atherosclerotic plaque samples, seen in figure 2.17, Davis et al (2016) established that crack tip opening displacement (CTOD) could be used as a comparative metric for fracture toughness [27]. Furthermore, it was stated here that plaques with high collagen content are able to withstand high stresses, though they may still be vulnerable to a strain-based fracture of the fibrous cap [27] and that information on the underlying collagen fibre orientation could provide insights into what is causing this highly variable mechanical response.
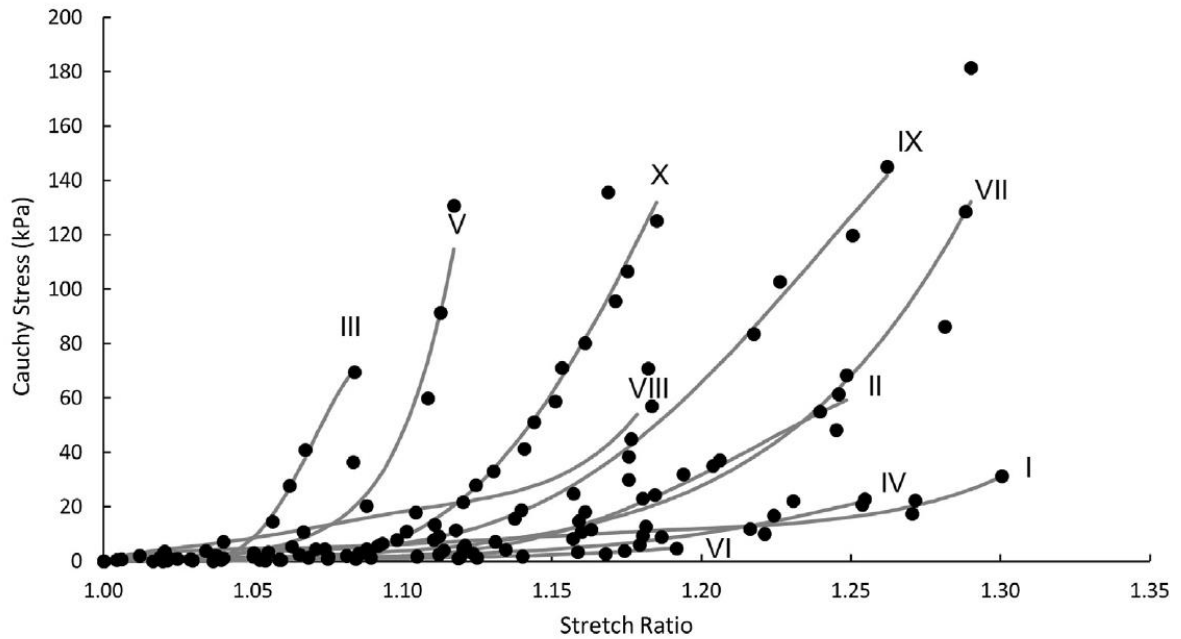
Figure 2.17 Stress-strain response of several fibrous caps. The dots represent experimental data points. Highly variable mechanical response observed across samples [27]

Compression testing of carotid atherosclerotic plaques and its components has also been performed to determine their stiffness properties [76,81–83]. Similar to the uniaxial tension tests, these compression methods are different from each other in terms of sample retrieval, storage, layers, components tested and variable length to width ratios. Akyildiz et al (2014) summarized the testing methods and results for compressions testing for atherosclerotic plaque tissue. A brief review of the carotid plaque results in this review and more recent publications will be discussed here.

Maher et al (2009, 2011) performed cyclic dynamic compression tests and compression test up to 10% strain for samples taken in the radial directions [76,84]. These experiments showed that the plaque has high radial compressive properties even when compared to the study by Barrett et al (2009). Variation in this stiffness can be attributed to the sample heterogeneity and the large biological variation in the tissue. Chai et al (2013) reported similar stiffness values seen in Barrett et al (2009) but the samples were taken in the axial direction. This is important to note as the collagen fibres in atherosclerotic plaque tissue can be more disperse and contribute to the loading in the radial, circumferential, and axial directions [83,85]. Furthermore, it must be stated that the different experimental procedures being used in these examinations contribute to the different stiffness responses observed in the tissue. Preconditioning, sample storage, specimen direction and collagen fibre orientation all play a significant role in the mechanical behaviour of the tissue and must be considered in the testing protocol for full understanding what is happening mechanically.

2.8 Computational modelling of arteries and atherosclerotic plaques

As stated in section 2.4, the indication for elective surgery of carotid artery disease is determined mainly by the percent stenosis. It is generally suggested that a percent stenosis greater than 50% should be used as the threshold for determining when a surgery should take place. Plaque rupture however can occur below this set threshold and therefore patients are at risk of being missed in diagnosis. Rupture of atherosclerotic plaque tissue can be observed as a purely mechanical event, whereby the stresses exerted on the plaque tissue exceeds its overall mechanical strength [86–88]. A particular location of interest for these computational simulations of atherosclerotic plaques is the fibrous plaque cap, where the stress is often the highest and where rupture is deemed most likely to occur [89,90]. Finite element (FE) analysis has been used as a tool to estimate the stresses experienced by the artery and plaque by using constitutive equations that describe the arterial microstructure in patient specific geometries making it a possible method to diagnose vulnerable plaques at risk of rupture in the clinic. However, due to the complexity of this simulation, many studies simplify the problem (constitutive equation, geometry extraction, meshing technique, exclusion of residual stress) to ensure convergence of the solution and gain insight into the behaviour of the tissue. However, these simplifications should not be performed if accurate quantification of the stress and strain observed in the simulation is desired as it is not truly representative of the *in-vivo* conditions.

Previous work has demonstrated the capability of using FE to predict rupture risk in patient specific models of abdominal aortic aneurysm (AAA) [91–94]. Fillinger et al (2002) and Heng et al (2008) showed that the peak wall stress (PWS) estimated the risk of rupture more reliably than standard geometric measures [92,94]. Using this knowledge, Gasser et al (2010) looked at determining the feasibility of using PWS and peak wall rupture risk (PWRR) as metrics of rupture for AAAs and established that these measurements correlated positively with both maximum diameter and intra-luminal thrombus (ILT) volume, see figure 2.18. It is observed that without the inclusion of ILT, these metrics are unable to determine rupture and non-rupture accurately. This limitation details the need to specify the geometries further for increased prediction accuracy [91].
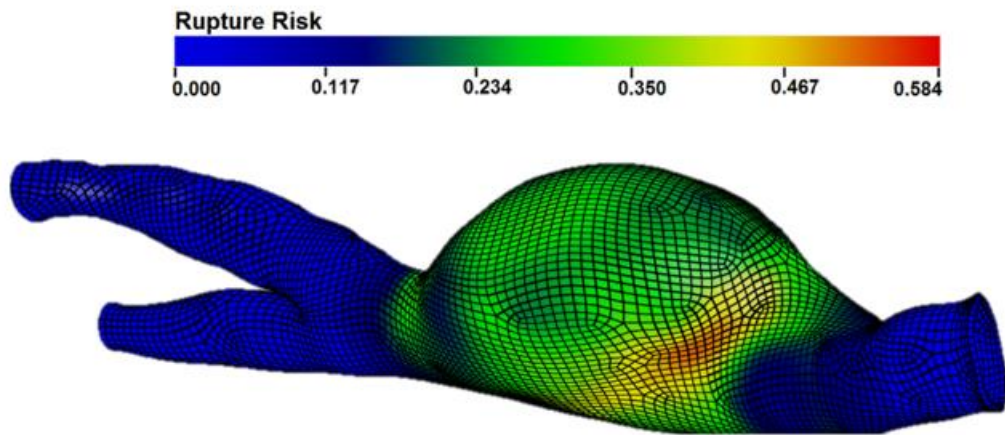
Figure 2.18 Predicted rupture risk of an aortic aneurysm model [91]

Creane et al (2011) looked at the possibility of developing a vulnerability measure to determine vessels at risk of plaque rupture by observing the fibre remodelling of the vessel when subjected to different levels of plaque burden [12]. It was established that when the plaque thickness increased, so did the remodelling metric developed, indicating that the vessel remodels accordingly to accommodate the plaque. Furthermore, a measure of the total predicted fibre remodelling (TRM) and total plaque burden (TPB) was found to be higher in the symptomatic rather than asymptomatic cases, delivering a possible plaque rupture metric [12]. Overall, this suggests that the arteries and atherosclerotic plaque in particular may have an inability to remodel and that this inability may be an indicator to plaque rupture vulnerability.

2.8.1 Constitutive modelling of arteries and atherosclerotic plaques

When determining the appropriate constitutive law for the computational modelling of arterial vessels, it is of vital importance to consider its biological complexity. The arterial wall is defined by three layers (. i.e., intima, media, and adventitia) as discussed previously. All these layers contain anisotropic components (collagen fibres with given dispersion and orientation) immersed in an isotropic ground matrix (elastin dominated). The structural complexity of arterial tissue gives it a non-trivial mechanical behaviour; which can be described by the following main aspects: (i) non-linear response; (ii) anisotropy, (iii) hysteresis and (iv) non-linear stiffening, especially at high levels of strain, due to recruitment of collagen fibres and exhibits the characteristic j-shape curve that has been associated with arterial tissue.

Several constitutive models have been described in the literature to describe the complex nature of arterial tissue. These models were firstly characterized by using stress strain data obtained from mechanical tests and the appropriate strain energy density function (SEDF) was formulated to capture the response. One of the first studies done by Delfino et al, 1997 proposed an

exponential isotopic strain energy function for the carotid arteries which predicted the stiffening effects at high pressures [21]. In this formulation, I_1 is the first invariant of the strain tensor and *a. b* are the material constants.

$$W = \frac{a}{b}\left\{\exp\left[\frac{b}{2}(I_1 - 3)\right] - 1\right\}$$

(2.1)

Mooney-Rivlin (1948) model proposed an isotropic hyperelastic constitutive equation where the strain energy density function is a linear combination of two invariants of the left Cauchy-Green deformation tensor B.

$$B = FF^T$$

(2.2)

$$W = C_{10}(\bar{I}_1 - 3) + C_{01}(\bar{I}_2 - 3) + C_{20}(\bar{I}_1 - 3)^2$$
$$+ C_{11}(\bar{I}_1 - 3)(\bar{I}_2 - 3) + C_{30}(\bar{I}_2 - 3)^3$$

(2.3)

Tang et al (2005,2009) and Teng et al (2009) extended this to describe the material properties of the vessel wall as well as the plaque component for steady flow in both thin wall and thick-walled distensible vessels [79,87,95] .

$$W = C_1(\bar{I}_1 - 3) + C_1(\bar{I}_2 - 3) + D_1\{\exp[D_2(I_1 - 3)] - 1\}$$

(2.4)

Ogden (1997) proposed an isotropic; hyperelastic constitutive equation that incorporates 6 material parameters (three dimensional μ_1, μ_2, μ_3 and three non-dimensional a$_1$, a$_2$, a$_3$) which are a function of the principal stretch ratios λ_1, λ_2, λ_3)

$$W = \sum_{i=1}^{3} \frac{\mu_i}{a_1}(\lambda_1^{a^i} + \lambda_2^{a^i} + \lambda_3^{a^i}) - 3$$

(2.5)

For these models, W is the strain energy function, I$_1$ and I$_2$ are the first and second invariants of the left Cauchy-Green deformation tensor and a,b, C$_i$ and D$_i$ are constants fitted to match experimental data. D introduces the material compressibility of the tissue.

To include the microstructure of the arterial wall, Holzapfel et al (2000) developed constitutive equations that incorporate different strain energy density functions for each of the arterial layers. Media and adventitia are considered the main contributors to the mechanical properties of the arterial wall [10]. The HGO model incorporates the anisotropic collagen fibres with a mean orientation, embedded in an isotopic ground matrix (elastin).

$$W = \frac{1}{2}\mu(\bar{I}_1 - 3) + \frac{k_1}{2k_2}\sum_{i=4,6}\left\{\exp\left[k_2(\bar{I}_i - 1)^2\right] - 1\right\}$$

(2.6)

The isotropic term consists of a shear modulus, μ and the first invariant of the deviatoric right Cauchy-Green tensor, I_1 and the anisotropic term consists of material constants k_1 and k_2. The HGO model here assumes incompressibility, a common assumption for arterial tissue and is enforced by a Lagrange multiplier in the volumetric component, please refer to Holzapfel et al (2000) [10] for further mathematical detail. This however may not be strictly true for arterial tissue [96]

This model was further developed to include the collagen fibre dispersion seen histologically. Gasser et al (2006) updated the structural tensor, H_{fami} to include a fibre dispersion parameter κ, to replicate the anisotropy of the tissue due to the collagen fibres. The dispersion term, κ, controls the 3D conic splay of fibres with $\kappa = 0$ depicting an anisotropic response and $\kappa = 0.33$ an isotropic response [11]

$$W = C_1(\bar{I}_1 - 3) + \frac{k_1}{2k_2} \sum \{\exp[k_2(\kappa I_1 + (1 - 3\kappa)I_4 - 1)^2] - 1\} \tag{2.7}$$

To accurately predict the stresses and strains, a constitutive model that incorporates the structure of the vessel wall is vitally important.

To add to the complexity of arterial constitutive modelling, the inclusion of atherosclerotic plaques adds to the biological complexity that is being simulated. Atherosclerotic plaques as stated before are heterogenous tissues that comprise of different components that if included in computational simulations need their own separate constitutive law and material parameters to describe their mechanical behaviour. Constitutive parameters are often established by experimental means, with each component showing a distinct mechanical response. Therefore for effective and accurate simulation, it is of utmost importance to determine the best material model to characterize the behaviour of atherosclerotic plaque components [97,98].

Teng et al (2015) explored and reviewed several strain energy density functions (SEDFs) to characterize the behaviour of atherosclerotic plaque tissue under uniaxial tensile loading conditions [97]. The models that have been used in this study are Neo Hookean [99], one term Ogden [83] , two term Ogden [100,101], Yeoh [77], Mooney-Rivlin [76], Demiray and a modified Mooney-Rivlin [102]. Experimental results are fitted to establish material parameters for each constitutive model as shown in figure 2.19.
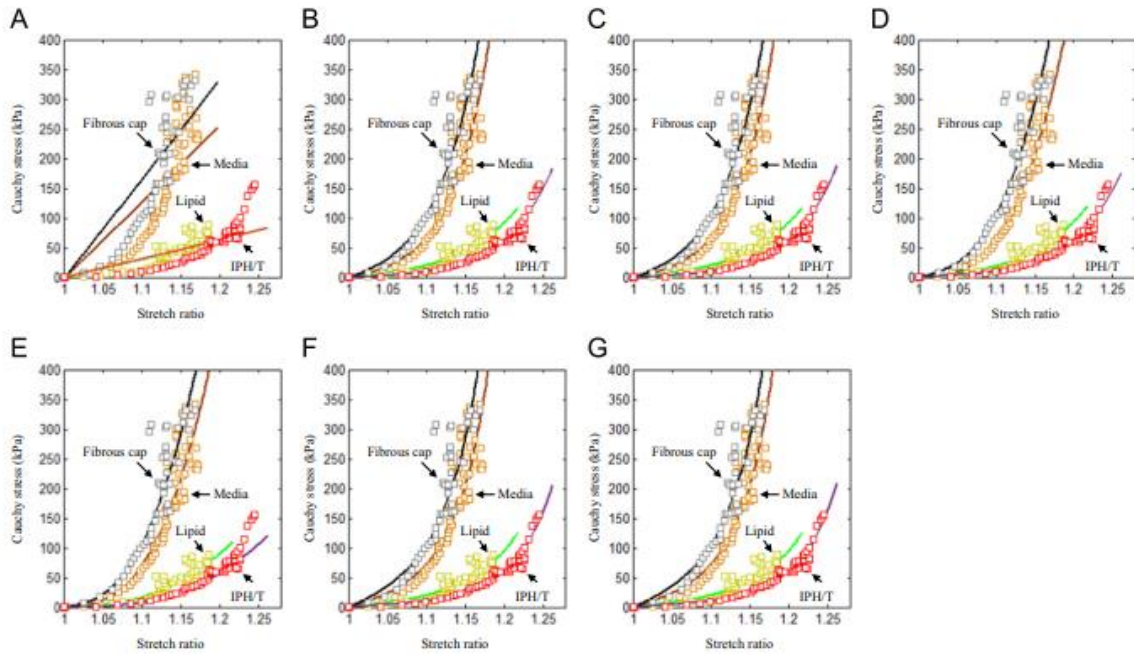
Figure 2.19 Stress stretch data obtained from 21 carotid plaque specimens (A) Neo-Hookean (B) One-term Ogden (C) Two-term Ogden (D) Yeoh € Mooney-Rivlin (F) Demiray (G) Modified Mooney-Rivlin [97]

No constitutive model has specifically been tailored to modelling atherosclerotic plaques due to the heterogenous nature of the tissue [97]. Teng et al (2015) determined that a modified Mooney-Rivlin model is enough to capture the stress-stretch responses for the plaque components if one constitutive equation was to be used. Simpler models, such as the Neo-Hookean is insufficient in modelling plaque components due to its inability to capture the non-linear mechanical response of the tissue. Ideally, a mixture of constitutive equations should be used in computational simulation of atherosclerotic plaques, with the independent behaviour of each component described by its own constitutive equation and material parameters.

2.8.2 Creation of patient specific finite element models from clinical images

Patient specific finite element models are becoming more commonly used in bioengineering to investigate both the local hemodynamics and the stress strain environment within realistic geometries in order to better understand the mechanical behaviour of the tissue. Initially, geometries took a more idealized approach and were often simplified to represent the artery or atherosclerotic plaque [99,103,104]. For example, Akyildiz et al (2011) used idealized computational models as shown by figure 2.20, to observe the effects of intima stiffness and plaque morphology on the peak cap stress by varying the material properties attributed to the fibrotic media. These geometries although simplified, gave key insights into the impact of plaque progression throughout the arterial wall such that for soft plaque models, necrotic core thickness and angle had the biggest influence on the peak cap stress [99].
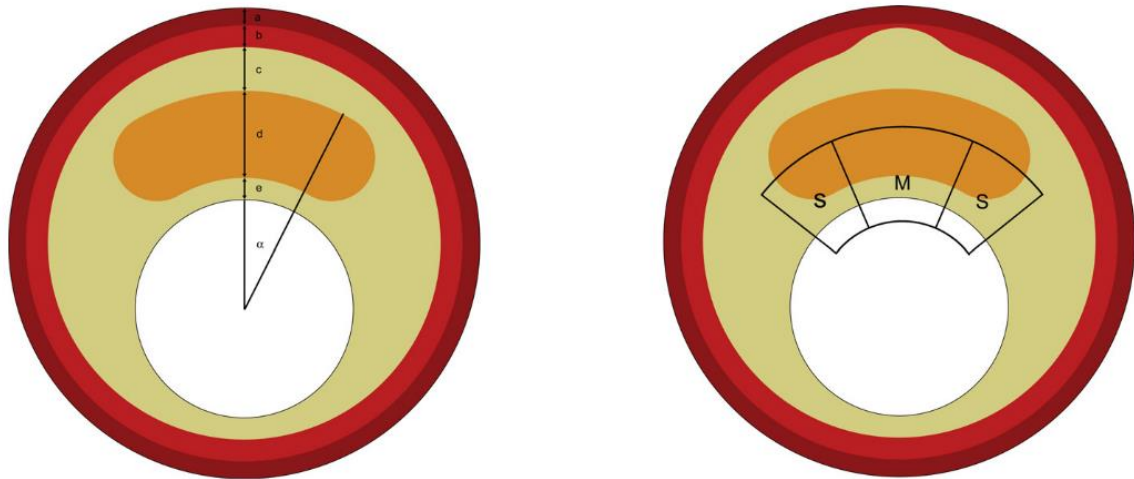
Figure 2.20 Idealized plaque model showing different arterial layers (media, adventitia), fibrotic media and lipid core, Brown = Adventitia, Red = Media, Yellow = Fibrotic intima and Orange = Necrotic Core. Geometry on left denotes geometric features: α = necrotic core angle, a = adventitia thickness, b=media thickness, c= intima thickness behind necrotic core, d= core thickness, e = cap thickness. Geometry on the right denotes the shoulder region (s) and the midcap region (m) [99]

To increase the specificity of the developed computational model and to deliver a more patient specific response, more complex geometries have been created by segmenting the plaque structure from histological images which were retrospectively verified with images taken from MRI [100,105]. Due to the histological processing, these models neglect the arterial wall and only include the plaque components and looked at peak stresses in the plaque. Similar to the simplified models, these models established that in the region denoted as the fibrous plaque cap and in particular at plaque shoulders, high stresses are observed. The peak values however are now different due to the specificity of the created geometry.

Figure 2.21 Example of plaque component geometry in 2D computational models. Informed by (a) in-vivo T2 MRI (b) Histological cross-section showing extensive lipid core region (green star) (c) Geometry for FE simulation [100]

Geometries that incorporate the many components of atherosclerotic plaques in three dimensions have also been developed from CT and MRI images. Huang et al (2010) developed 3D geometries of the arterial wall and plaque components for fluid structure analysis [106]. These geometries were created using an in-house created software called CASCADE, which is now a commercially available software called MRI-PlaqueVIEW. This software receives input of 2D axial cross section images of a specific contrast and segments the components based on the signal intensities displayed in the images. A 3D reconstruction is then performed as an interpolation between the slices with all the components included. This method has been used in a number of studies, however the issue with this methodology is that they only use one contrast (T1W, T2W or PDW) for their segmentation process [107,108]. MRI contrast weightings are sensitive to certain plaque components, therefore a co-registration of multiple image contrasts (T1W, T2W or PDW) and verification with initial models from *in-vivo* MRI, *ex-vivo* MRI and histological images would provide highly specific models of the plaque and vessel wall.
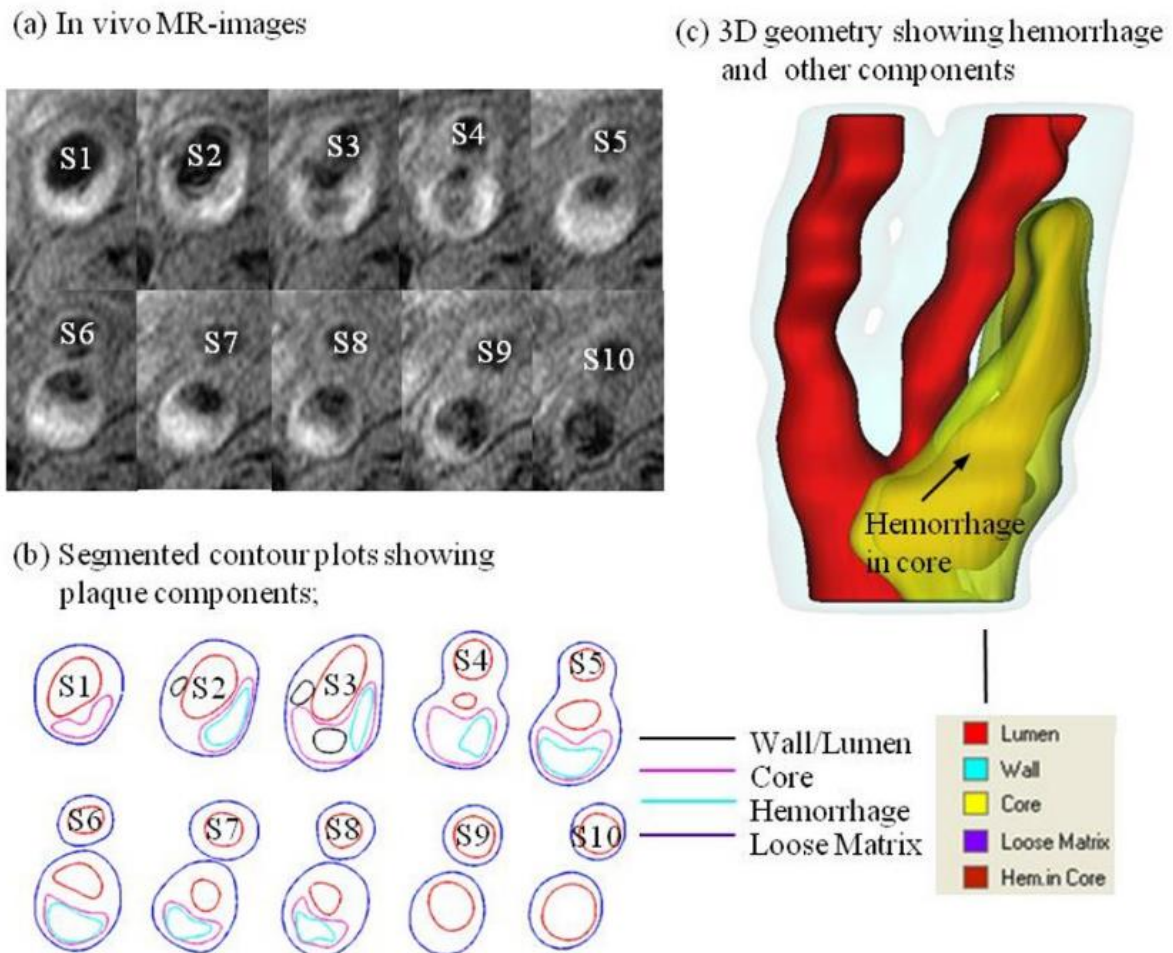
Figure 2.22 3D geometry creation from MRI images including plaque components (a) In-vivo MRI images (b) Segmented contours plots showing plaque components (c) 3D geometry [109]

2.8.2.1 Hexahedral meshing of arterial bifurcations and atherosclerotic plaques

In finite element analysis, establishing the most suitable element type is also important as it is these elements and their respective integration points which calculates the stress and strain experienced in the model. Tetrahedral elements may not be the best method of meshing when determining a patient specific stress strain response. Although tetrahedral elements are highly conformable to tortuous geometries, tetrahedral elements are stiffer than hexahedral based elements and therefore any stress strain predictions may be overestimated. Furthermore, the increase in mesh density when using tetrahedral elements significantly increases the computational time, making these non-viable in a clinical setting. Therefore, the creation of finite element models with hexahedral elements are more desirable, but without tailored pre-processing methods, meshing of tortuous geometries can lead to sharp edges in the model.

Many approaches to hexahedral meshing of arterial geometry are from blood flow images either from CTA or MRI [110–113]. Lee et al (2000), first demonstrated the ability to create automated hexahedral meshes from MRA and CTA images to study the complex hemodynamic environment of patients with arterial disease development at the carotid bifurcation [111]. Implemented in MATLAB, the method for mesh generation has two main steps, (i): axial images of bifurcation lumen were converted into 3D geometry and (ii) geometry created was used to generate vertices and connectivity of mesh. The meshing technique separates the bifurcation into a bottom, top left and top right segments and is meshed as separate blocks with interior points evenly spaced in the vertical direction. The number of points is kept the consistent in each segment in order to ensure mesh connectivity. Outline vertices are created, and a quadrilateral surface mesh is applied and subsequently joined to create hexahedral elements [111]. This is illustrated in figure 2.23.
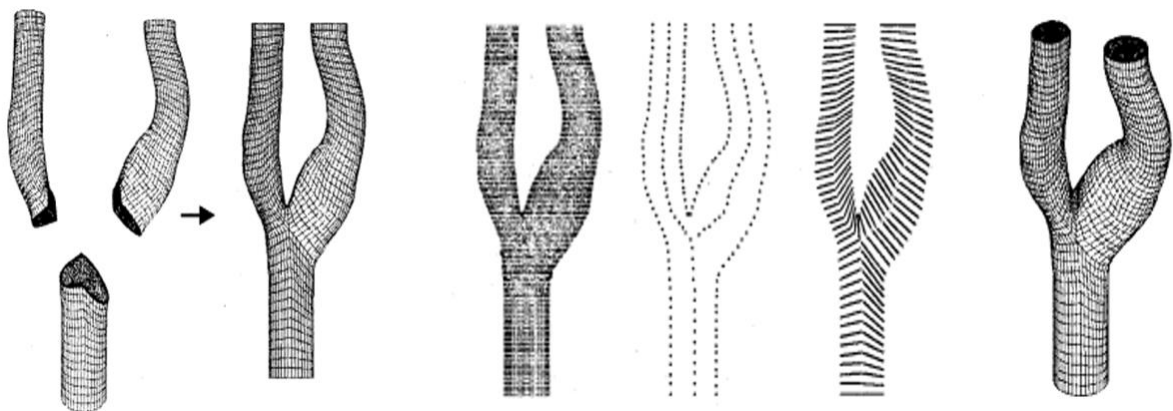
Figure 2.23 Segmented tubes with two angled surfaces joined to create 3D bifurcation. Four points define separation line followed by vertices and centreline detection. Lastly, angled sections for mesh creation and final created mesh [111]

Wolters et al (2005) developed a process to create hexahedral meshed patient specific fluid structure interaction (FSI) models of abdominal aortic aneurysms. To do this, they extracted

centrelines by specifying end points using a semi-automated minimum cost path approach and segmentation using a 3D active object (3DAO). The 3DAO is initialized as a tubular structure around the centrelines and is inflated until it matches lumen boundary. Meshing of this geometry is done using these created centrelines and transformation of the centrelines into the patient specific configuration to create a triangulated boundary surface. Discrete points are then projected to create hexahedral elements in the fluid domain [114]. Creane et al (2010) developed an automated MATLAB algorithm to create structured hexahedral meshes of the carotid bifurcation from CTA scans as shown by figure 2.24. Segmentation of the CTA images are done by flood-fill and morphological operations to extract curves of the geometry. To ensure that the mapping of elements is not distorted at the bifurcation, the Wolters method was adapted by adding an extra segment (green region) that traverses the bifurcation axially [115].
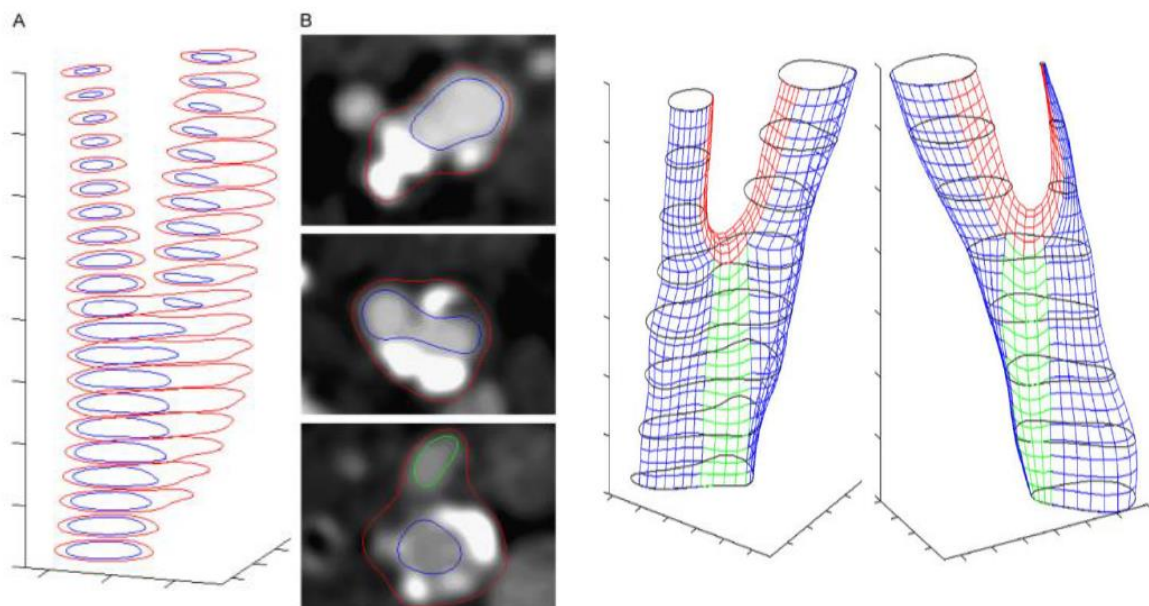
Figure 2.24 Segmentation of contours from carotid artery CTA scan and geometries created for two patients (a) Segmented contours of lumen and outer wall (b) Contours on CT scan [115]

De Santis et al (2010) used pyFormex, a python-based software designed to handle large geometrical models and process CT files to generate a structured hexahedral mesh of the coronary artery. Using the same process, it has also been used to create patient specific models of the carotid bifurcation [112]. The methodological framework in PyFormex involves three stages to create hexahedral meshes of patient specific geometries and these are (i) topological partitioning, (ii) surface reconstruction and (iii) meshing. Topological partitioning separated the geometry into three segments (CCA, ECA and ICA) and the surface was reconstructed using Bezier splines creating tube like structures. For meshing, parabolic and cubic curves are fitted to the transformed topological partitions, allowing for a smooth transition between partitions. Mesh blocks are then applied to create the hexahedral mesh structure [112]. Tarjuelo-Gutierrez et al (2014), used MRI

images as their input for hexahedral created geometries of abdominal aortic aneurysms. Using similar approaches as previously discussed, they divided the geometry into three segments (CCA, ECA and ICA), built quadrilateral surface meshes of each section and defined the centrelines. Then to build hexahedral meshes, points along the lumen centreline are mapped to the quadrilateral mesh and axial contours are joined together creating the desired hexahedral structure. Distortion of elements is controlled by early mesh refinement of the quadrilateral surface mesh [116].

For structural FE analysis, these methods have not been optimized for the segmentation of the vessel wall and plaque components together and a major limitation to these methods is that layers of elements are added at a fixed thickness to represent the wall thickness. This approximation is inaccurate for patient specific analysis as the vessel wall thickness can differ from one location to another in the same vessel in both healthy and diseased cases. Therefore, it is important to develop a geometry creation and meshing strategy to accurately segment the altering wall thickness in arterial geometries, the components within atherosclerotic plaque tissue and a robust hexahedral meshing process to accurately characterize the stresses and strains observed in patient specific geometries.

2.8.3 Determination of the zero pressure / unloaded configuration of arteries

Establishment of the zero-pressure configuration is important for the correct characterization of the stress strain distribution in patient specific analysis. It is observed during image acquisition, a physiological pressure is present in the arterial system, therefore creation of geometries at this stage will lead to the creation of the geometry in an already loaded configuration. Furthermore, loading these geometries created at this "loaded" configuration with *in-vivo* pressure conditions would be incorrect as the vessel has now deformed more then what it would have *in-vivo*. It is not possible to accurately measure the undeformed configuration from MRI; however, it is possible to image the vascular geometry at certain cardiac phases by the use of cardiac triggering. Creating geometries from these known configurations, it is possible to estimate the initial zero pressure configuration by computational means [18]. The majority of studies have looked at determining the zero-pressure configuration for AAAs due to the significant level of deformation it experiences *in-vivo*. In order to estimate the zero-pressure configuration, a number of assumptions need to be taken such as (i) the *in-vivo* geometry is known at a certain phase and (ii) the residual stress of the vessel is not included.

Raghavan et al (2006) developed an optimization framework for estimating the zero-pressure configuration for abdominal aortic aneurysms. In this framework, they assume that the initial *in-vivo* MRI configuration is the zero-pressure configuration, and a forward analysis is done by loading this geometry with the known pressure experienced *in-vivo* and a backwards calculation

is performed to get the "actual" zero pressure geometry guess. A scaling parameter k is introduced and needs to be optimized so the geometry coordinates can lead to a better estimation of the optimized zero pressure geometry. This optimization of the scaling parameter k ensures that the "actual" zero pressure configuration, once reloaded with the required pressure, results in the original MRI geometry as shown by figure 2.25 [18].
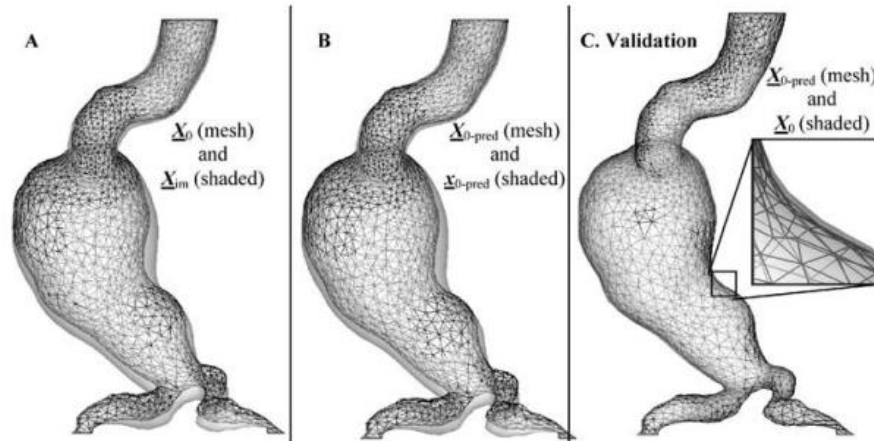
Figure 2.25 Zero pressure configuration determined for abdominal aortic aneurysm. The difference between the recovered and true zero pressure geometry [18]

De Putter et al (2007) established a backward incremental (BI) method to estimate the equilibrium configuration. This method involves incrementally increasing the pressure and updating the deformation gradient to the *in vivo* pressure experienced, after which a pre-stressed and pre-strained configuration is obtained. Once obtained, the zero-pressure geometry can be constructed by reducing the luminal pressure to 0 Pa as shown in figure 2.26. [19]. Riveros et al (2013) used a pullback algorithm similar to Raghavan et al (2006) except they continuously updated the guess for the zero-pressure configuration after each iteration [117]. This is further validated by Chandra et al (2016) by experimental methods [118].
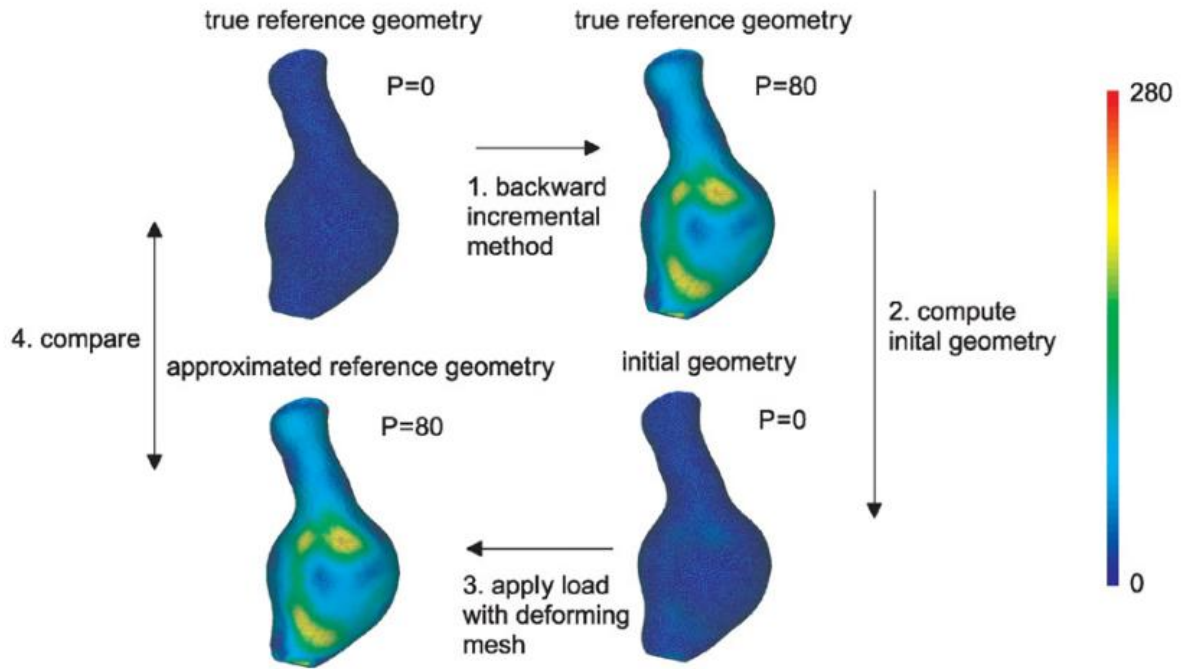
Figure 2.26 Approximation of the zero-pressure configuration of an AAA. Contours represent the von mises stress in kPa. The pressures (P) are in mmHg [19].

Bols et al (2013), developed a backward displacement method based on a fixed-point algorithm to determine the zero-pressure configuration not only for an idealized cylinder geometry but also in the geometry of a mouse abdominal aorta segmented from CT scans. Again, the original image-based geometry is used as an initial guess and a fixed point-based iteration is performed until convergence is reached. An equilibrium configuration is calculated from the intermediate configuration loaded with the known pressure. The displacements are calculated from this forward analysis and subtracted from the initial MRI geometry coordinates to give the zero-geometry configuration. The mesh is also updated at this stage. Convergence is reached when the residual vector is smaller than a set convergence criterion [119]. To speed up this convergence, Bols et al (2013) also developed a quasi-newton (QN-LS) algorithm to estimate the zero-pressure configuration by estimating the jacobian from a least squares model [119]. Overall, these both achieved the same result by estimating the zero-pressure configuration, however the time of estimation was improved.

2.8.4 Inclusion of the residual stress in computational modelling

Studies have demonstrated the importance of including the residual stresses in computational models to get an accurate calculation of the stress distribution throughout the wall [21,22,120,121]. Estimating the residual stresses in arterial tissue is often achieved by doing an opening angle experiment whereby a ring sample of the tissue is cut longitudinally to release the residual stress. Quantification of this "opening" and its corresponding angle can be related to the

residual stress, but it is important to know that cutting at different locations gives different opening angles. Even with this pitfall, the use of the opening angle is the most common method for inclusion of residual stresses.

Computationally, to incorporate the residual stress the model should start in its stress-free open state, with displacement boundary conditions imposed to close the artery to its unloaded state, as shown in figure 2.27. This closing of the angle will incorporate the residual stress into the FE simulation and can then be loaded with a pressure force for accurate prediction of the stress distribution through the wall. It is important to note that exclusion of the residual stress, a common assumption in many computational simulations has far reaching consequences on the stress state in the vessel wall. If no residual stress is present, the inner wall would be subjected to significantly higher stress and stretch when compared to the outer part of the wall. The incorporation of the residual stress homogenises the gradient of stress throughout the vessel wall. Fung et al (1991) proposed that this is because the artery grows and remodels itself accordingly that the circumferential strain and stress are transmurally uniform at mean arterial pressure (MAP) [122].
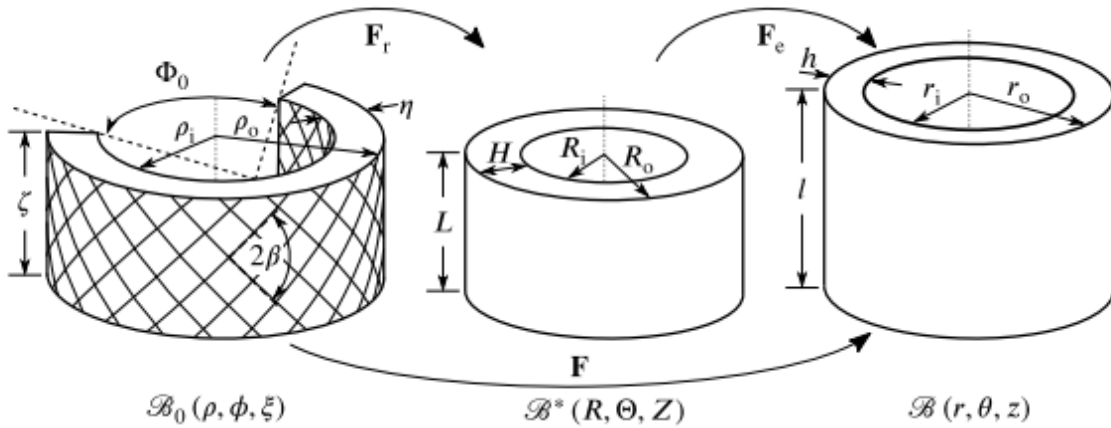
Figure 2.27 Opening angle experiment for determination of residual stresses. Stress-free (β_0), unloaded (β^*) and deformed configuration (β) of an arterial segment. The coordinates (ρ,ϕ,ξ), (R,Θ,Z) and (r,θ,z) are associated with the radial, circumferential, and axial directions of the respective domains.

Delfino et al (1997) introduced residual strain in a bifurcation artery model via an opening angle approach and compared the results to what would be expected if this stress gradient was not introduced. They showed that the inclusion of residual strain, particularly at the apex of the bifurcation, decreases the maximum principal stress and makes the stress field more uniformly distributed throughout the bifurcation as shown in figure 2.28 [21].
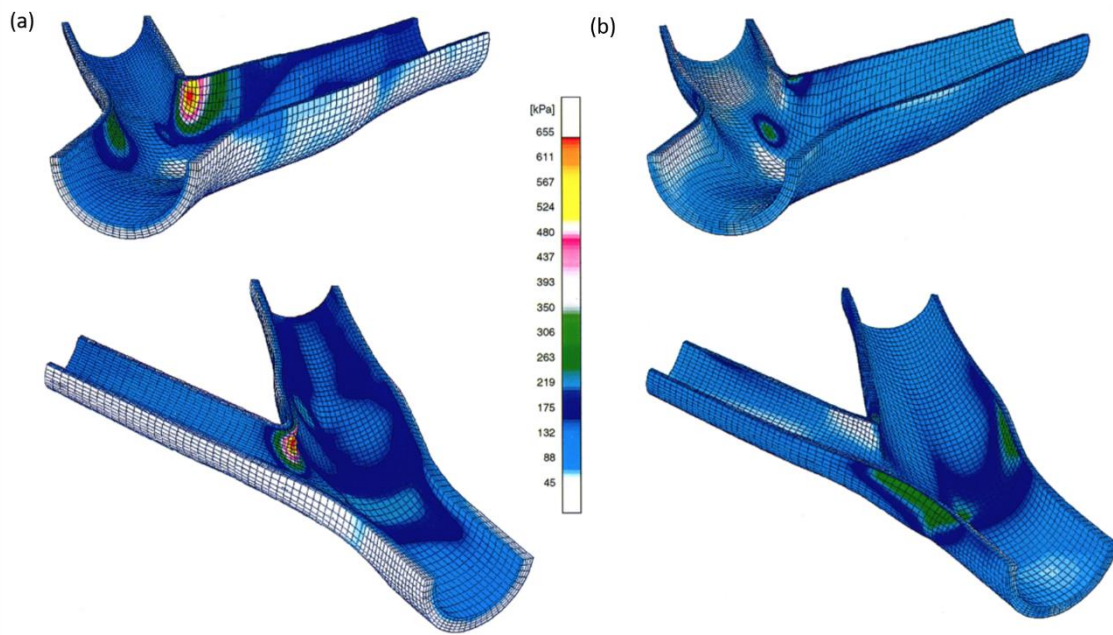
Figure 2.28 Effect of the inclusion of residual strain on the stress field at the carotid bifurcation (a) without residual strain (b) with residual strain [21]

Raghavan et al (2004) looked at how the residual strain is introduced into computational models and compared an idealized cylinder geometry and non-circular geometry to predict the residual stresses. It was observed that the distribution of the residual stress differed when the geometry was non-uniform, as the residual stress differs in certain locations [56]. This may be more representative of what is happening *in-vivo* due to the variable thickness of the vessel wall. Alustrue et al (2007) assessed the use of the opening angle method when enforcing residual stresses in patient specific arteries using an anisotropic material model. To do this, they assume that the total deformation gradient tensor can by multiplicatively decomposed into an initial non-compatible part composed of the opening angle experiment deformation gradient and a part produced a compatibility enforcement deformation gradient and showed similar results to Delfino and Raghavan [123]. For cylindrical example, they observed a stress gradient through the wall that normalized the stress field once loaded and a different circumferential stress when the geometry was non-uniform. They also demonstrated different residual stresses for the media and adventitia, where they observed compressive stress in the media at the luminal side and tensile stress near the adventitia. Overall, they concluded that the residual stress must be accounted for in the analysis of stresses for tissues that exhibit a non-linear behaviour [123]. Schroder et al (2014) developed a novel method to determine the residual stress directly from the current stress state within the arterial wall and that the gradient seen must be smoothed between inner and outer layers of the vessel. Circumferential residual stresses are compressive on the inner part of a ring and tensile on the outer part. To simulate this behaviour, they focused on the

distribution of fibre stresses in the radial direction. As an underlying optimization, the deviations of suitable stress invariants from their volumetric mean values in segmented sections are smoothed between inner and outer margins of the individual vessel layers [22]. To verify these results, simulations were carried out on a simple cylinder model and a cross section of a diseased artery, which showed a smoothing of stress gradient in the models and stress responses once loaded similar to previous studies. Furthermore, a demonstration of the release of residual stress was also shown when a radial cut was simulated and shown by figure 2.29.
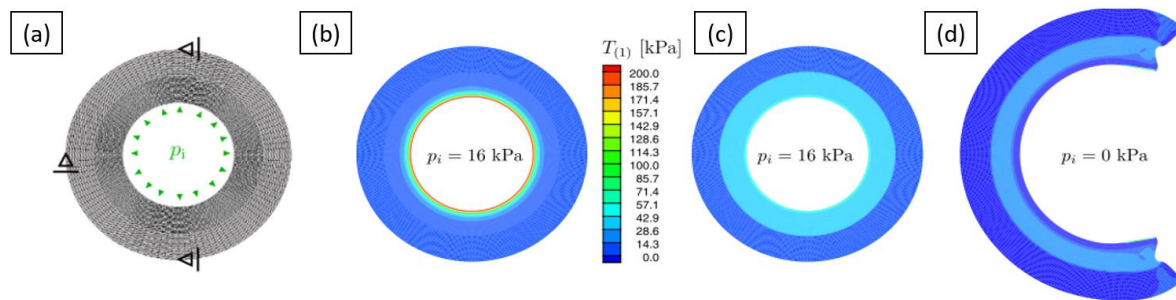
Figure 2.29 (a) Two-dimensional circular ring consisting of media and adventitia. Distribution of fibre stress (b) without residual stresses (c) with residual stresses (d) simulated opening angle releasing residual stresses [22]

The inclusion of residual stress in arteries for computational stress simulations led to a substantial reduction in the circumferential and axial stress in the arterial wall. The opening angle, which is usually used for calculation of the residual stress distribution through the arterial wall cannot be obtained directly *in-vivo*. Methods like the one established by Schroder et al (2014), that introduces a stress gradient throughout the wall, without direct input from opening angle measurements seems to be the most applicable for a clinical setting.

2.8.5 Constitutive material parameter estimation

Determination of the material parameters used in the constitutive models are vitally important in establishing the actual material behaviour of the tissue *in-vivo*. Inclusion of a patient specific material response along with the input of a patient specific geometry and the *in-vivo* loading and boundary conditions would create highly specific models to determine the stress strain response. Common methods for determining material parameters are by fitting to experimental data and extrapolating the parameters via an inverse finite element approach. Kroon and Holzapfel (2009) demonstrated the ability to estimate material properties based in boundary conditions and displacement/ strain fields measured experimentally for vascular membranes [124]. Avril et al (2010) and Genovese et al (2013) used the virtual field method for extracting both homogenous and heterogenous constitutive parameters from *in-vitro* measurements of blood vessels (mouse aorta) and in an unloaded configuration [125,126]. However, these *ex-vivo* techniques often exclude *in-vivo* characteristics of the blood vessels such as the pulsatile loading and unloading

of the vessel, axial stretching and residual stresses. Making these determined material parameters inaccurate for *in-vivo* stress strain analysis.

Estimation of material properties from in-vivo images and inverse finite element analysis often involves three key steps: (1): Estimation of the zero-pressure configuration. (2) deforming this geometry with in-vivo loading conditions with estimated initial input material parameters and (3) using optimization techniques and applying appropriate boundary and loading conditions. The estimated material parameters are adjusted through minimization of some physical measurement (stress/strain/displacement) of the deformed configuration and the *in-vivo* loaded configuration. Wittek et al (2013, 2016) developed two methods for estimation of the material properties of the Gasser-Ogden-Holzapfel (GOH) model by using 4D ultrasound and minimizing the strain differences [23,24]. A limitation of this process is that the computational workload was expensive and therefore made it inapplicable for clinical use. Liu et al (2017) determined material parameters for the aortic wall by using two main steps: (i) computation of an "almost true" stress field from the geometry in-vivo loading conditions and (ii) building of an objective function based on this "almost true" stress state and "true" stress state experienced using desired constitutive equations and deformation relations, estimating the material parameters by minimization of this objective function. To compute this "almost true" stress field, very stiff material properties were applied to the vessel wall, making the deformation infinitesimal and yet the stress calculated should be close to the true stress of the wall [25]. The unloaded configuration is then attributed material parameters and the deformation established between the systolic and diastolic phases. Optimization methods are then used to find the "true" material parameters such that differences between the actual and "almost true" stress states are minimized. This method was not very computationally expensive as multiple iterations of FE simulations were not required and furthermore optimized material parameters were achieved quickly [25].
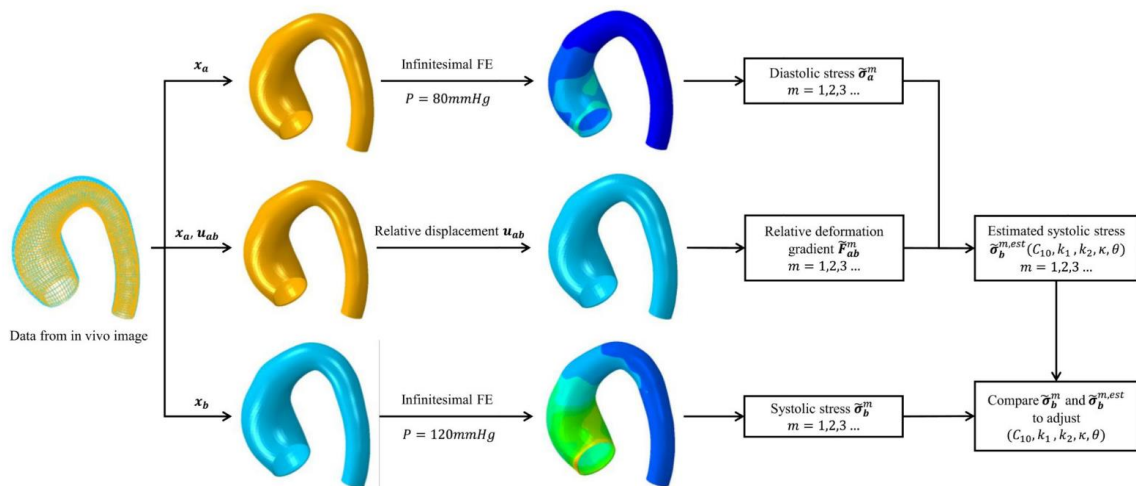
Figure 2.30 Flowchart of material parameter estimation process in Liu et al (2017) [25]

Akyildiz et al (2016) developed an *ex-vivo* framework on pressurized porcine iliac arteries imaged with ultrasound, simulated with FE and inverse finite element analysis to estimate the material parameters based on a minimization of the displacements between the two. To quantify this displacement, a grid procedure was used to accurately correspond to the element sizes to ensure accuracy [127]. Chen-Ket Chai et al (2015) also determined local anisotropic properties from atherosclerotic plaques using nano-indentation and FE to determine fibre stiffness [128].
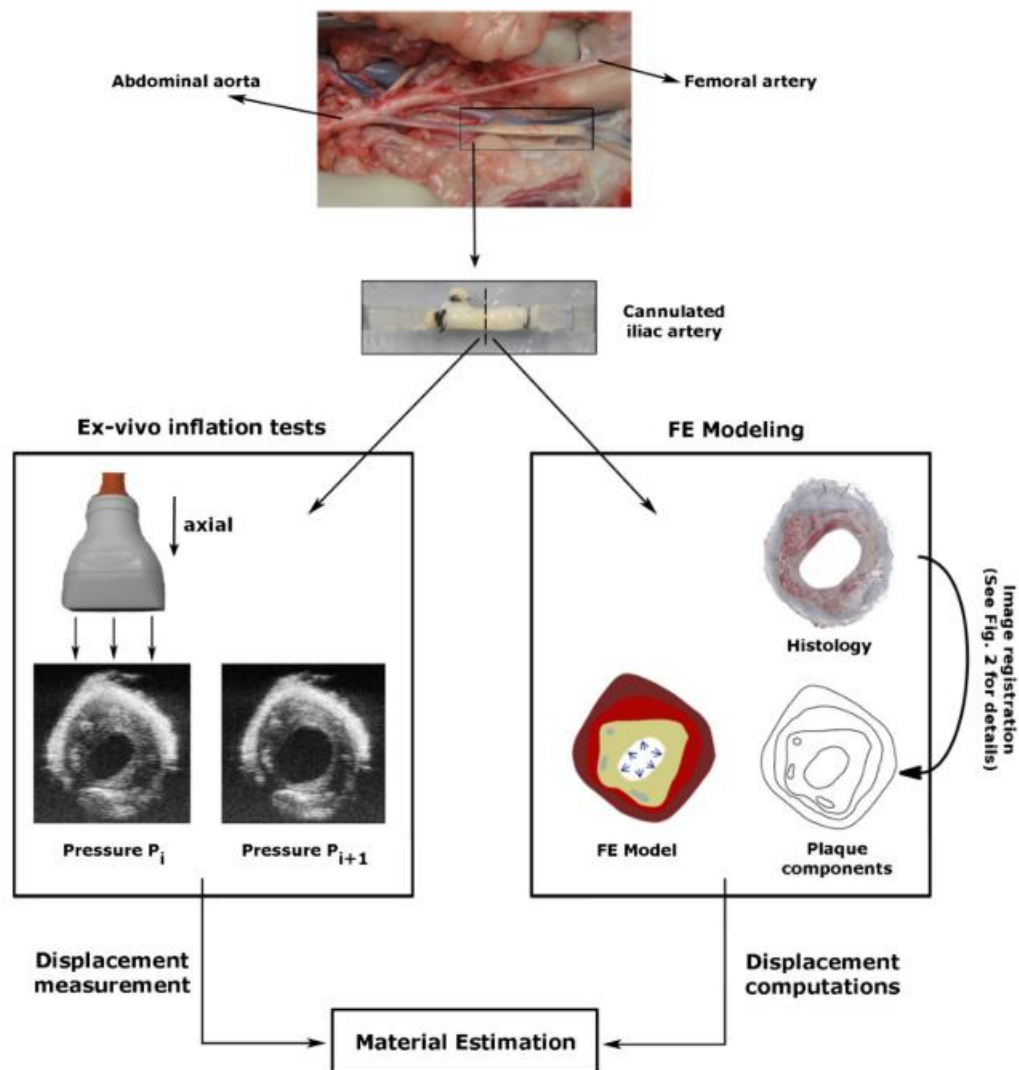
Figure 2.31 Methodology imposed for the estimation of material parameters from displacement measurements from ex-vivo ultrasound images and FE simulation [127]

The carotid artery experiences dynamic loads *in-vivo* and displays two different configurations at both its systolic and diastolic phases. It is possible to recover these geometries in MRI by cardiac triggering based on the patient's heartbeat and estimate material parameters using similar methods discussed here. Inclusion of patient specific estimated material parameters would give

real stress strain information that is experienced *in-vivo* and possible mechanical indicators of plaque rupture risk.

2.8.6 Arterial remodelling algorithms

To characterize the microstructure of the artery and accurately predict the *in vivo* vessel response, remodelling algorithms have been implemented by a number of studies to simulate the collagen fibre dispersion and orientation in the artery when subjected to different loading conditions due to disease development. Remodelling algorithms are classified on how they determine the optimum fibre distribution; in the literature the most common are (i) stretch [129,130] (ii) strain [131] and (iii) stress [15,132]. It is important to mention that geometric measures have also been used to determine the optimum fibre orientation [133,134].

Driessen et al (2003) proposed a remodelling algorithm that is governed by the principal stretch directions. In this implementation, it is assumed that the angle of fibres is between the first and second principal stretches. The extent of the angle is determined by a ratio of these principal stretches. Fibre dispersion was also included. Results from this implementation of fibre remodelling was verified experimentally and was found to mimic the collagen fibre architecture of arterial tissue [130]. Creane et al (2010) developed a robust fibre remodelling algorithm to determine the optimum fibre directions at the carotid bifurcation for healthy volunteers and demonstrated the capability of collagen to remodel to accommodate atherosclerotic plaques [131]. This remodelling algorithm based on principal strains experienced *in-vivo* uses the max and intermediate principal strains as a ratio to determine the mean fibre angle and dispersion. For healthy cases, the fibres are observed to be highly aligned at the apex (rectangle region in figure 2.32) to accommodate the highest load while low alignment is observed at regions proximal to the apex (triangular region in figure 2.32). Fibres are shown to actively remodel in the vessel to accommodate the plaque in order to sufficiently bear the load [131].
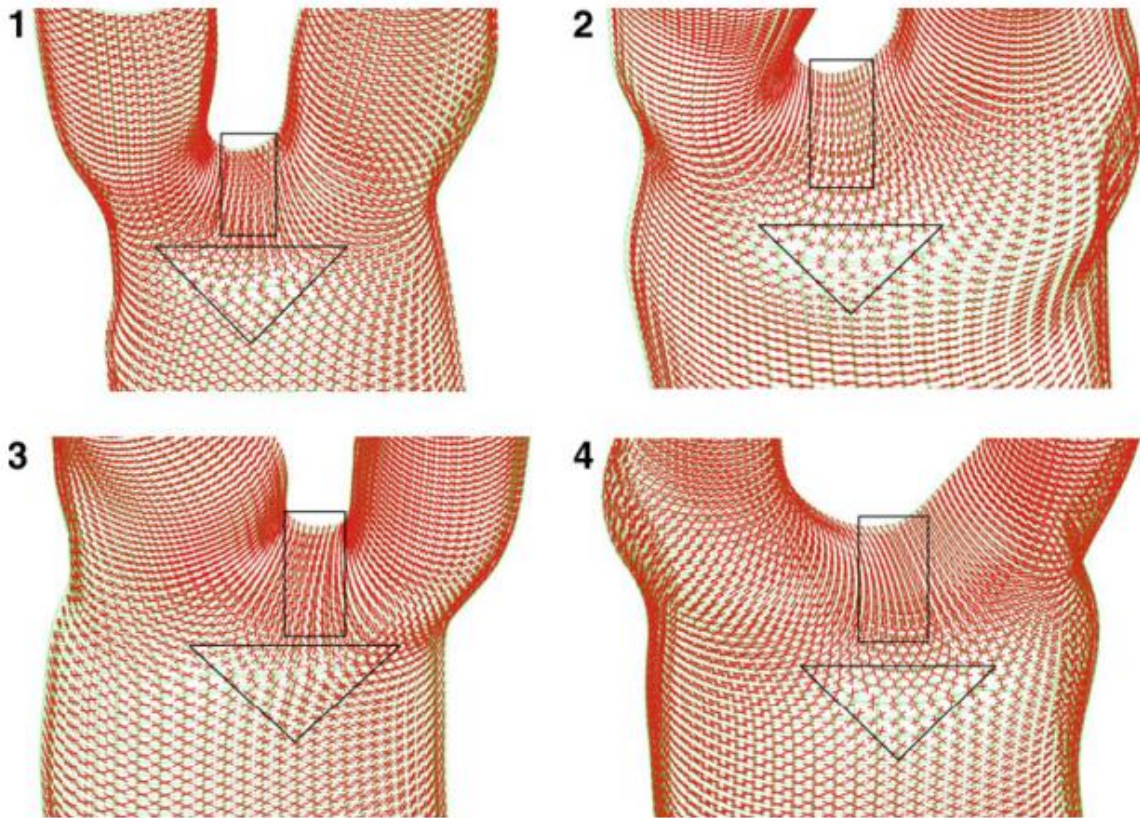
Figure 2.32 Healthy fibre architecture in second layer of healthy wall elements of a carotid bifurcation model for four volunteers. Square indicates unidirectional region at the apex (high alignment), triangle indicates multidirectional region (low alignment) [131].

Hariton et al (2007) also demonstrated the capability to predict fibre patterns by using the max and intermediate principal stresses. To determine these stresses an iterative simulation of the remodelling process was proposed that initially used an isotropic constitutive law to determine principal stresses in an FE model. After this, if convergence of stress field is not met after implementation of the anisotropic constituent law, the fibre directions are modified until they meet it, see figure 2.33 [132]. The fibre directions determined at the bifurcation in this study were similar to the fibre directions seen in Creane et al (2010), see figure 2.34, whereby, the apex of the bifurcation showed high alignment while locations proximal to the apex showed low alignment [131,132].
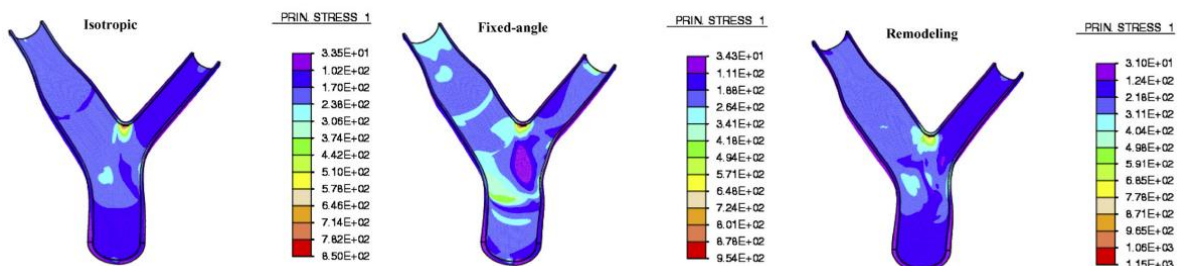
Figure 2.33 Distribution of maximal principal stresses for the isotropic, fixed angle and remodelling models [132]

Figure 2.34 Principal stress segments (black) and collagen fibre orientation (red) at the carotid bifurcation. High alignment observed at the bifurcation apex [132]

Geometric systems for defining the fibre directions have been used by Kiousis et al (2009) and Mortier et al (2010). To do this, they create a local basis in the elements of the FE mesh and the fibre directions are set at an angle between the circumferential and axial directions [133,134]. The method here is further illustrated by figure 2.35
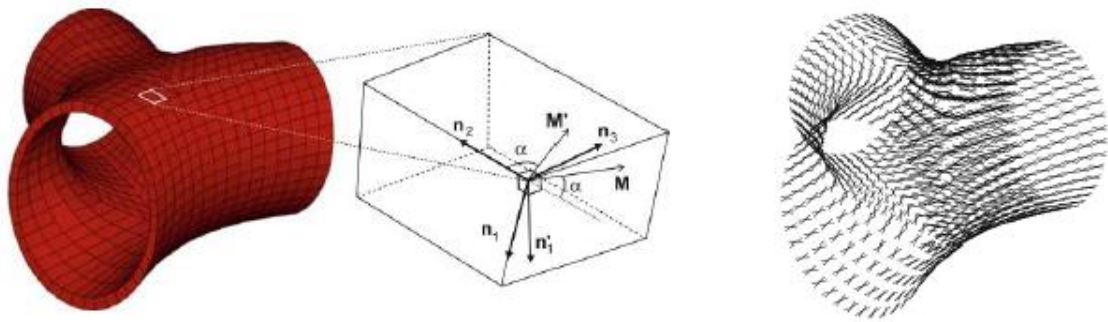
Figure 2.35 Outermost layer of the bifurcation mesh. Assigned fibre orientations and illustration of the mean fibre directions (M and M') for finite elements [133].

More recently, Ghasemi et al (2021) has established a sensitive remodelling metric to determine plaque vulnerability to rupture [135]. Using a previously developed continuum damage model (CDM), in which the influence of collagen fibres in the mechanical response of arterial tissue to physiological and supraphysiological loads was captured [16], the ability to characterise the lack of remodelling to the optimum fibre configuration in atherosclerotic plaques could be determined. It was observed that the further away the fibres from this optimum configuration (optimum configuration measured according to the ratio of maximum and intermediate Cauchy stresses [15,132]), the stiffness of the tissue is reduced, resulting in higher strains in these high-risk atherosclerotic plaques [135].

Inclusion of the arterial fibre orientation and dispersion is important for determining the correct response of the microstructure to high loading conditions. Incorporating the residual stress would alter these predictions of the highly aligned fibre structure as more uniform stress distributions are seen, particularly at the bifurcation apex. These models can be informed by magnetic resonance imaging (MRI) and diffusion tensor imaging (DTI) measurements *in-vivo or ex-vivo* to characterize the actual microstructural nature of the vessel and atherosclerotic plaque, giving a more patient specific response.

2.9 Ex-vivo imaging techniques of arteries and atherosclerotic plaque tissue

Many imaging techniques have been used to establish the characteristics of arterial and atherosclerotic plaque tissues *ex-vivo*. The translation of these techniques to be clinically applicable has been difficult as these techniques often need extraction of the tissue followed by destruction of the sample. These destructive methods will be discussed as they provide the fundamental understanding of what is expected *in-vivo*. Clinically, the imaging modalities used for diagnosis can be ultrasound, CT, and MRI.

2.9.1 Bright field light microscopy

Optical light microscopy is the most popular method for viewing and characterising the structure of tissue samples. By using histological stains such as Haematoxylin and Eosin (H&E), Verhoeff van Gieson (VVG), Picro-Sirius Red (PS-Red), and Masson's trichrome or Movat pentachrome, different microstructural components can be differentiated from each other. Image processing techniques can then be used to more quantitively analyse the tissue microstructure.
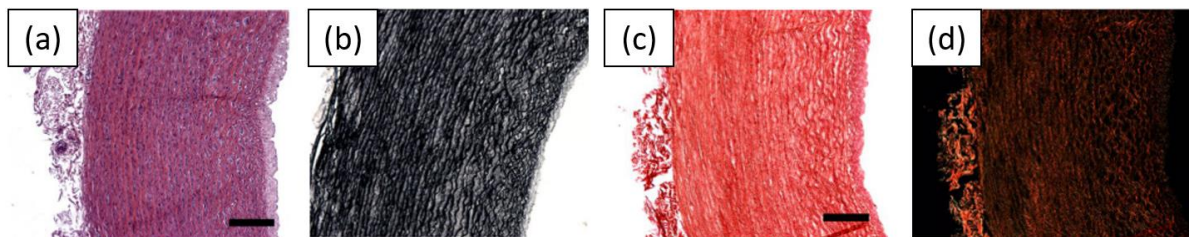
Figure 2.36 Histological images of arterial tissue (a) Haematoxylin and Eosin (H&E) (b) Amended Verhoeff van Gieson (c) Picro-Sirius Red (PS-Red) (d) Polarized light (PLM). Scale bar 250µm [39]

Studies that have used histological approaches characterise the structure of arteries and determine key attributes such as collagen content, dispersion and orientation [29,30,136–138]. Douglas et al (2017) demonstrated the ability to determine fibre orientation and dispersion of atherosclerotic plaque tissue from standard histological images obtained as shown figure 2.37**.**
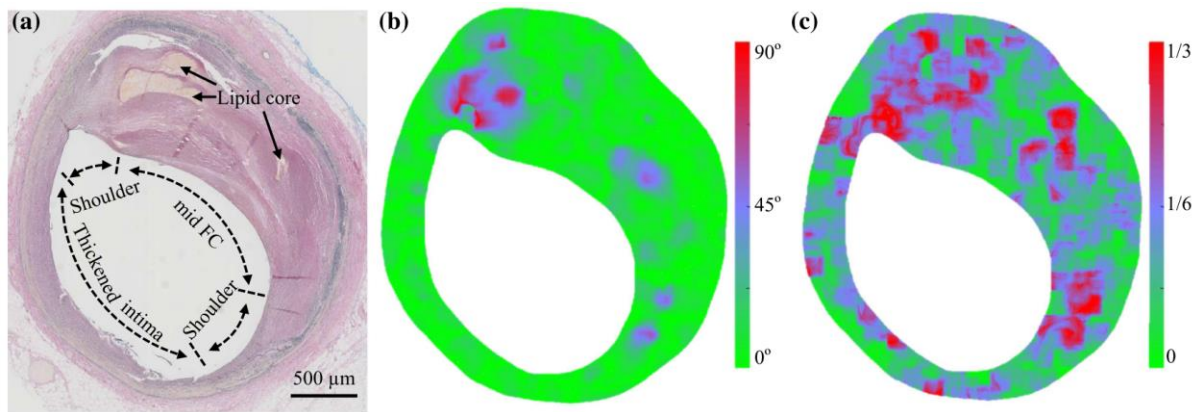
Figure 2.37 (a) Representative Elastin Van Gieson (EVG) image of atherosclerotic plaque (b) Map of fibre orientation (green - better alignment with lumen) (c) Map of fibre dispersion (green - less fibre dispersion) [30]

Histology is still the most commonly used validation tool of more advanced imaging modalities and experimental results of tissue. However, for *in-vivo* analysis, it is not a viable option as the plaque needs to be excised and destroyed before analysis can be performed.

2.9.2 Polarized light microscopy

Polarized light microscopy (PLM) is an extension of bright field microscopy and takes advantage of the birefringent properties exhibited by tissues [137,138]. Using the same setup as the bright-field microscope, polarized lenses are placed before and after the light passes through the tissue sample. The first polarizer lens polarizes the antagonistic light before it interacts with the sample, the disturbed light then passes through the second polarizer lens, known as an analyser.

Gasser et al (2012) used PLM and Picro-Sirius red to identify structural differences in healthy and aneurysmal human aortic tissue. Both the in-plane and out-of-plane fibre angles were measured through each vessel layer. Diseased tissue was identified as having large levels of fibre disorganisation identified by a high level of dispersion when compared to healthy tissue [138]. These findings suggest that maladaptive remodelling occurs in diseased vessels which may potentially lead to a fatal event occurring. Schriefl et al (2012) employed PLM in conjunction with Picro-Sirius red to identify structural differences between the intima, media and adventitia of the human thoracic and abdominal aorta as well as common iliac arteries. PLM identified layer specific and location specific fibre architecture across each vessel. Two helically wound fibre families were present in the intima, media, and adventitia in thoracic and abdominal aortic arteries with often a 3rd or even 4th presenting in the intima. Fibre orientation was found to be symmetrically arranged across each vessel layer with a more axial direction in the adventitia and circumferential direction in the media [137]. The orientation of fibres in the intima were found to be in between that of the media and adventitia, as illustrated in figure 2.38.
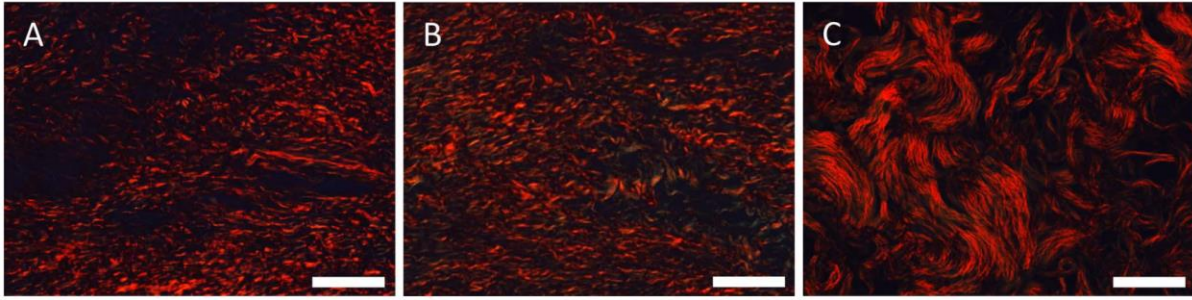
Figure 2.38 Polarized light images of (A) intima, (B) media and (C) adventitia showing layer specific fibre architecture. Scale bar = 50μm [32]

2.9.3 Confocal, Multiphoton and Second Harmonic Generation (SHG) microscopy

Confocal microscopy achieves a higher level of focus than standard brightfield microscopy techniques. It achieves this by passing the light source through a sample and only collecting the in-focus light via a pin-hole aperture in the same focal plane as the sample. Rezakhaniha et al (2012) tagged the collagen with CNA35 probe which fluoresces when illuminated by a light source of a certain wavelength [139].
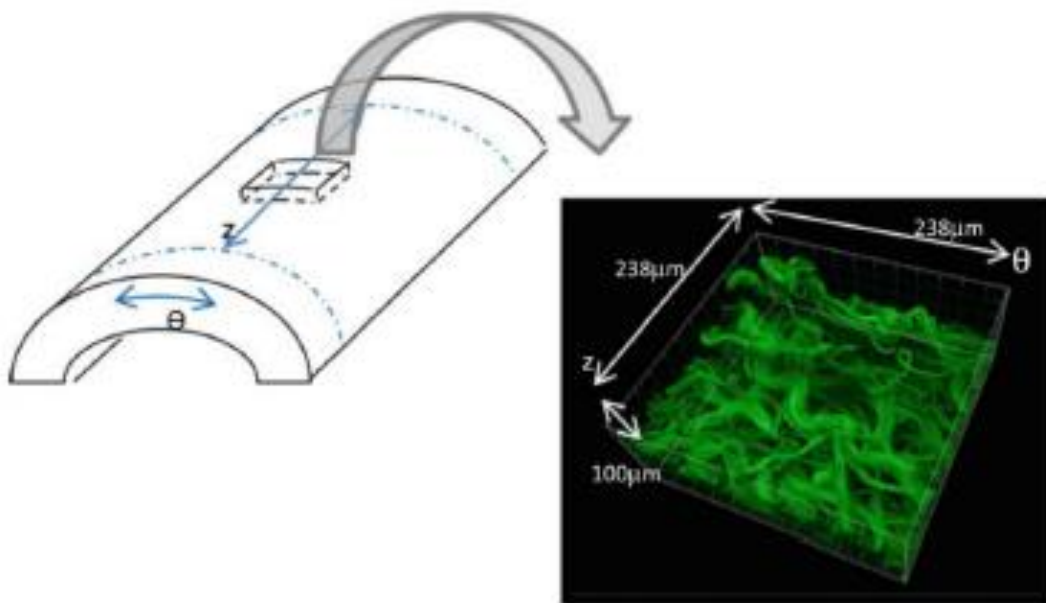
Figure 2.39 Confocal microscopy visualizing the adventitial collagen fibres tagged with CNA35 probe [139]

Multiphoton microscopy uses the material's non-linear optical properties to excite fluorophores through the absorption of energy from photons. This imaging technique involves minimal sample preparation and thick samples can be imaged so a 3D image can be constructed [140]. Multiphoton microscopy has been used as a source of real time imaging that can view remodelling of collagen subject to loading as shown by figure 2.40.
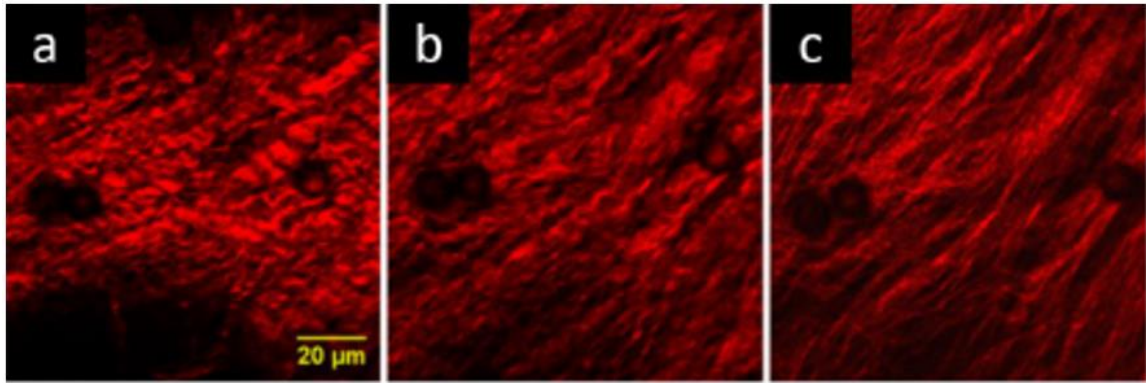
Figure 2.40 Multiphoton images of collagen in the coronary artery under increased loading [140].

Second Harmonic Generation (SHG) uses the fluorescent properties exhibited by collagen and its non-symmetric nature to visualise its structure. Collagen exhibits an SHG response when two photons of light of the same frequency are absorbed by the collagen and effectively combined to emit a photon of twice the frequency and half the wavelength [141].

2.9.4 Small Angle Light Scattering (SALS)

Small angle light scattering (SALS) is an imaging technique that uses light scattering principles to determine structural information from the sample such as the orientation of collagen fibres. To do this, incident light passed through the sample and is scattered orthogonally to the central axis of a sample's constituent fibres [32–35]. SALS also offers the possibility to determine real-time structural changes of intact tissue in response to load. Gaul et al (2017) demonstrated that SALS can be used to quickly determine the orientation of collagen fibres in arterial tissue and verified this with a histological orientation analysis on polarized light images. The fibre orientation is determined by a metric called eccentricity, where a more eccentric profile with value of 1 is anisotropic (has a principal direction) and less eccentric profile with value of 0 is isotropic (directions all the same) [32].
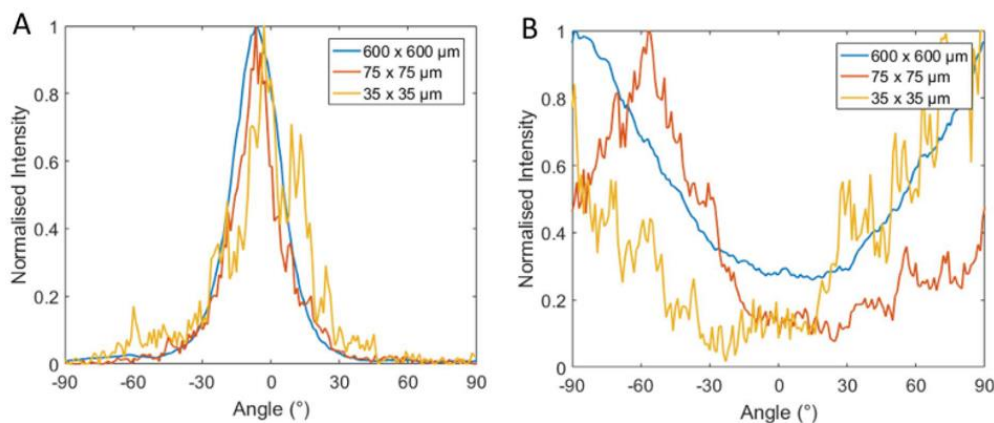
Figure 2.41 Histological orientation analysis (HOA) of fibre orientations for (A) Media and (B) Adventitia [32]
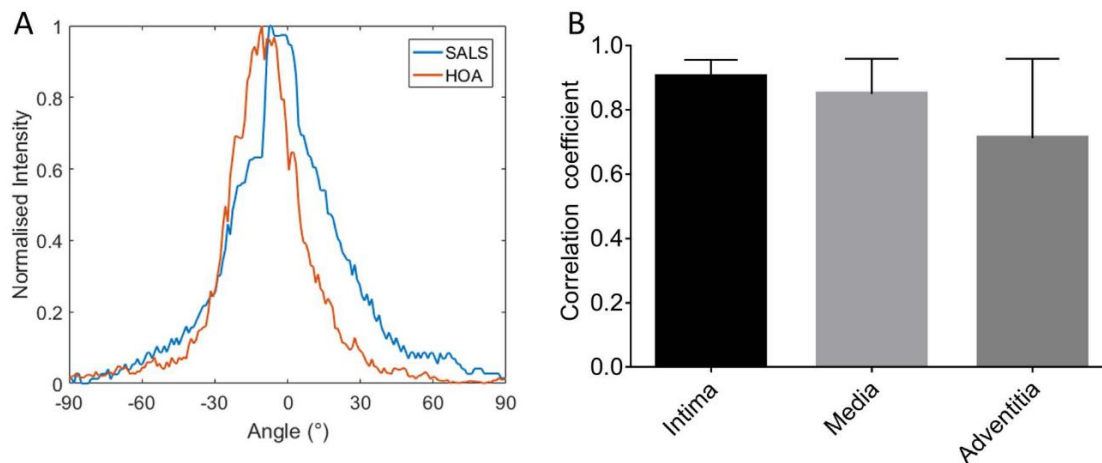
Figure 2.42 (A) Medial fibre distribution determined using SALS and HOA. (B) Correlation coefficients between SALS and HOA for each layer, n=10 [32]

Although these methods have helped ascertain the structure of arterial tissues and atherosclerotic plaques, due to the dynamic loading conditions experienced by the tissue *in-vivo*, determining the structure of the vessel wall and how the tissue can actively remodel the collagen fibre structure is of utmost importance. An inability to remodel during the onset of disease may lead to an indicator of possible plaque rupture.

2.9.5 Ultrasound

Carotid Duplex Ultrasound (CDUS) is a non-ionizing imaging modality used in the determination of percent stenosis and flow rates for evaluation of the carotid arteries [142–145]. The principle here is based in reflection and transmission of high frequency sound waves, where the waves are reflected or absorbed as they transmit through the tissue. Depending on the tissue composition, these sound waves are attenuated and reflected via echoes. Due to the duplex effect, sound waves that are attenuated for a moving target (e.g., blood flow) that has velocity cause a shift in frequency in the sound wave reflected and can be used for velocity estimation and visualization of blood flow. Ultrasound is useful as it can determine the composition of atherosclerotic plaque due to the different attenuations from components in the tissue. Furthermore, using more advanced techniques such as elastography, it is possible to establish the stiffness and strain environment in a diseased vessel. Huang et al (2016) established the capability of differentiating between vulnerable and stable plaques using the maximum amplitude strain rate (MASR), showing that a sensitive mechanical measure via imaging is possible [146].
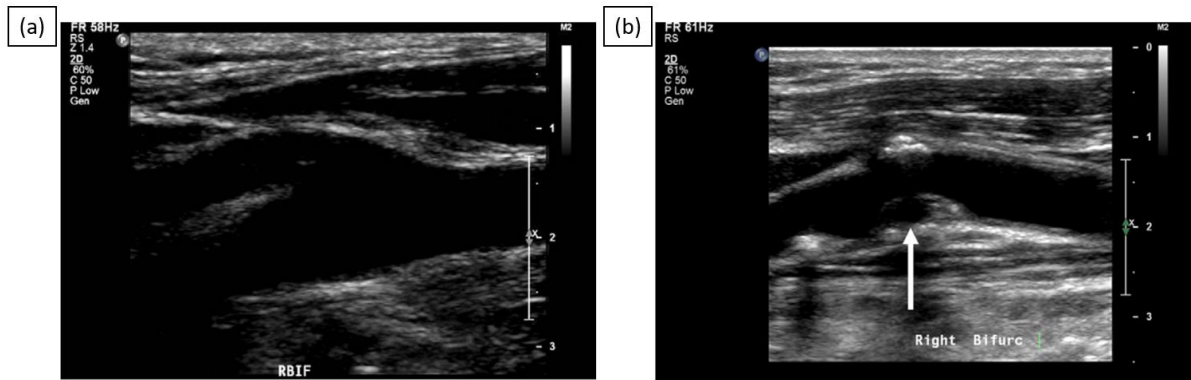
Figure 2.43 Ultrasound Images of the Carotid Bifurcation (a) Healthy (b) Proximal ICA plaque [144]

A major limitation of ultrasound is the scanning depth it can achieve, making it only useful for more superficial vessels such as the carotid artery. However, due to the presence of the jaw (bone cannot be penetrated by sound wave), only a small section of the carotid can be scanned. Furthermore, it suffers from poor resolution as echoes are reflected from all tissues in the region that is being scanned. It can therefore be difficult to determine the correct dimensions and size of plaque components in the vessel wall.

2.9.6 Computed Tomography (CT)

The fundamental concept behind CT is very similar to conventional x-ray that is used in medical diagnostics. The patient is placed inside the CT bore and an x-ray source is rotated around the patient at high RPM (rotations per minute). The x-ray source emits x-rays that pass through the patient and is attenuated by the tissue depending on the tissue's absorption capabilities. These attenuated x-ray photons are then collected via photomultiplier tubes and the intensities are reconstructed by filtered back projection to create 3D reconstructions. Computed Tomography Angiography (CTA) is one of the gold standard techniques in determining the degree of stenosis and location / size of the plaque [147–149]. A contrast agent is often used to increase the x-ray attenuation of the blood flow and allow for visualization of the carotid bifurcation as shown in figure 2.44a. Geometric measures are taken following either NASCET or ESCT schemes to determine the percent stenosis.

Koelemay et al, 2004 showed that CTA is highly sensitive and specific in determining carotid artery stenosis, with an 85% sensitivity and 93% specificity for stenosis of 70%-99% [149]. A comparative study by Wardlaw et al, 2006 showed that CTA had the highest specificity at 95% among all non-invasive imaging modalities for determining plaques with 70%-99% stenosis. However, in determining stenosis less than 70%, CTA proves to be less efficient .

2.9.6.1 Micro CT (μCT)

Micro CT offers the capability to image *ex-vivo* samples of atherosclerotic plaques at significantly higher resolution then any imaging modality to date. Furthermore, it offers significant advantage over conventional histology as it does not involve destruction of the sample. Imaging the structure of soft tissue requires the use of a heavy ion contrast agent, such as iodine, phosphotungstic acid (PTA) or phosphomolybdic acid (PMA) [150–154]. Some of these particular contrast agents are more preferable in certain soft tissues as the molecules are variable in size and have different diffusion capabilities through the tissue. Nierenberger et al, (2015) established the relevant contrast agents for the MicroCT of porcine iliac veins, stating that both PTA and PMA are effective in terms of differentiating the layers of the vein and observing the microscopic collagen networks, see figure 2.44b [153]. More recently, Robinson et al, (2021), stained cadaveric specimens with iodine contrast agent to demonstrate the capability of visualizing the spatial distribution of features in three dimensions and guide histologic analysis [154]. However, quantitative measurement on collagen content and collagen fibre orientation in arterial vessels directly from MicroCT is still yet to be established.
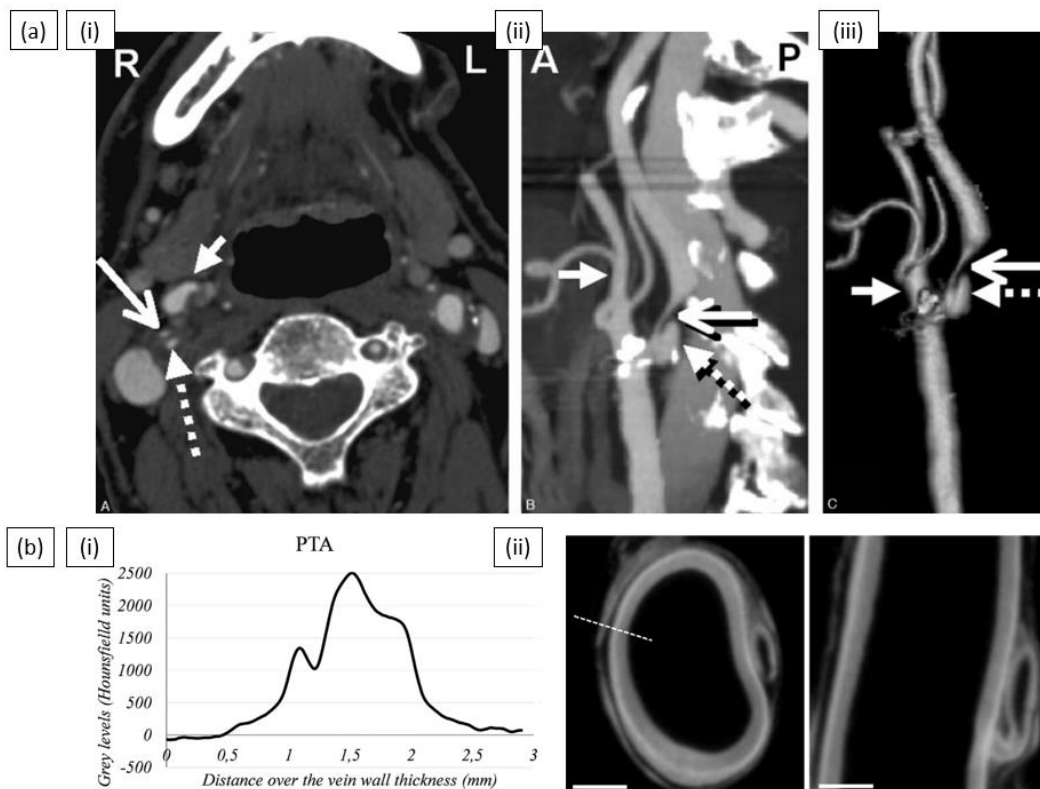
Figure 2.44 (a) Clinical CTA showing severe carotid stenosis with deep plaque ulceration (i) axial image (ii) sagittal image (iii) 3D rendered image [155] (b) Contrast enhanced MicroCT of porcine iliac vein (i) Grey level profile in Hounsfield units along the thickness of the vein wall showing contrast obtained. (ii) PTA staining raw data. Scale bars = 2mm [153]

2.9.7 Magnetic Resonance Imaging (MRI)

MRI operates via a completely different principle than what is used in either ultrasound or CT. Key to the understanding of the mechanisms behind MRI is the behaviour of hydrogen atoms within a biological material in a strong magnetic field B0. The nucleus of the hydrogen atom contains one proton that exhibits the property called spin. Under a magnetic field, the spins associated with the protons align in a certain direction with the main magnetic field. The sum of all these spins vectors in this area is called the net magnetization vector. The magnitude of the net magnetization vector is recorded for each voxel representing the tissue and is presented as an image after signal reconstruction. MRI offers the ability to structural visualize the vessel wall and plaque components at high resolution, a significant advantage over CT and ultrasound. Furthermore, MRI can be used to determine blood flow measurements similar to duplex ultrasound and determine percent stenosis via magnetic resonance angiography (MRA) [156–158].

The most common weightings used in MRI for added contrast are T1, T2 and proton density. These are commonly used to visualize structural information of the arterial wall and plaque. T1 (spin lattice relaxation) contrast is achieved by the longitudinal relaxation of the tissue's net magnetization vector. Aligned spins in a strong magnetic field B0 are put in the transverse plane by a radiofrequency (RF) pulse and left to relax to equilibrium at B0. T1 weighting often has short echo (TE) and repetition times (TR). Contrast agents are more commonly used for T1 weighted images to prolong this relaxation. T2 (spin-spin relaxation) contrast is achieved by capturing the decaying spins from their aligned precession in the transverse plane. T2 weighting often has a long TE and TR. Proton density weighting is an intermediate sequence that shares both features of T1 and T2 and is weighted to reflect the actual density of protons [158,159].
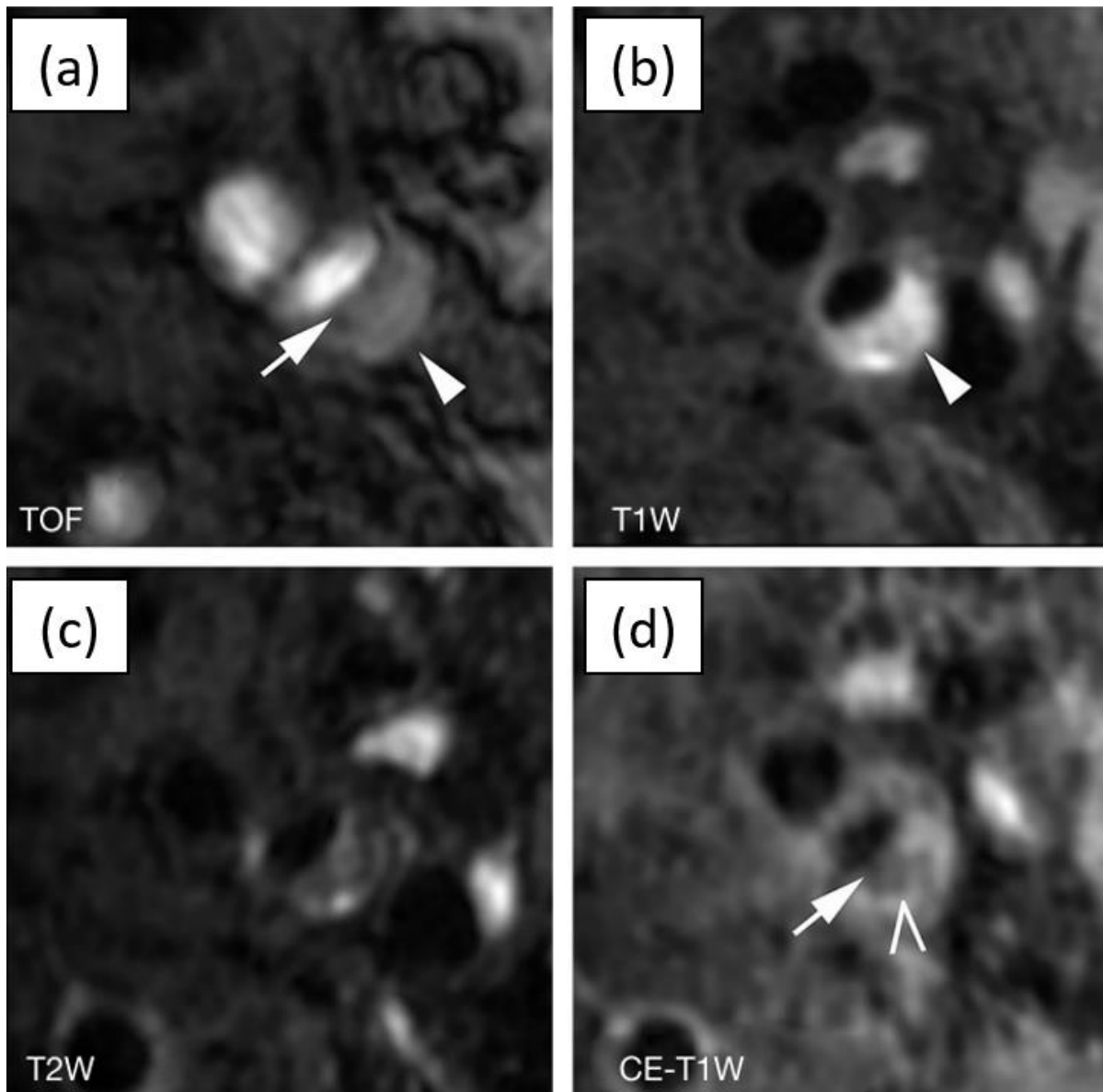
Figure 2.45 Contrast weightings from the different MRI sequences at the bifurcations (a) Time of flight (TOF) angiogram – disrupted dark band (arrow) shows presence of fibrous cap (b) T1 weighted image – high intensity region denotes the presence of haemorrhage (c) T2 weighted image – Low intensity denotes lipid rich necrotic core (d) Contrast enhanced T1 weighted image [160].

Clinically, current techniques to evaluate carotid stenosis using MRI often use 2D time of flight (TOF) or multiple overlapping thin slab acquisition (MOTSA) sequences to visualise the blood flow through the artery. Slow, turbulent, and absent blood flows are poorly distinguished by magnetic resonance angiography (MRA) techniques, including when contrast enhancement agents are used.
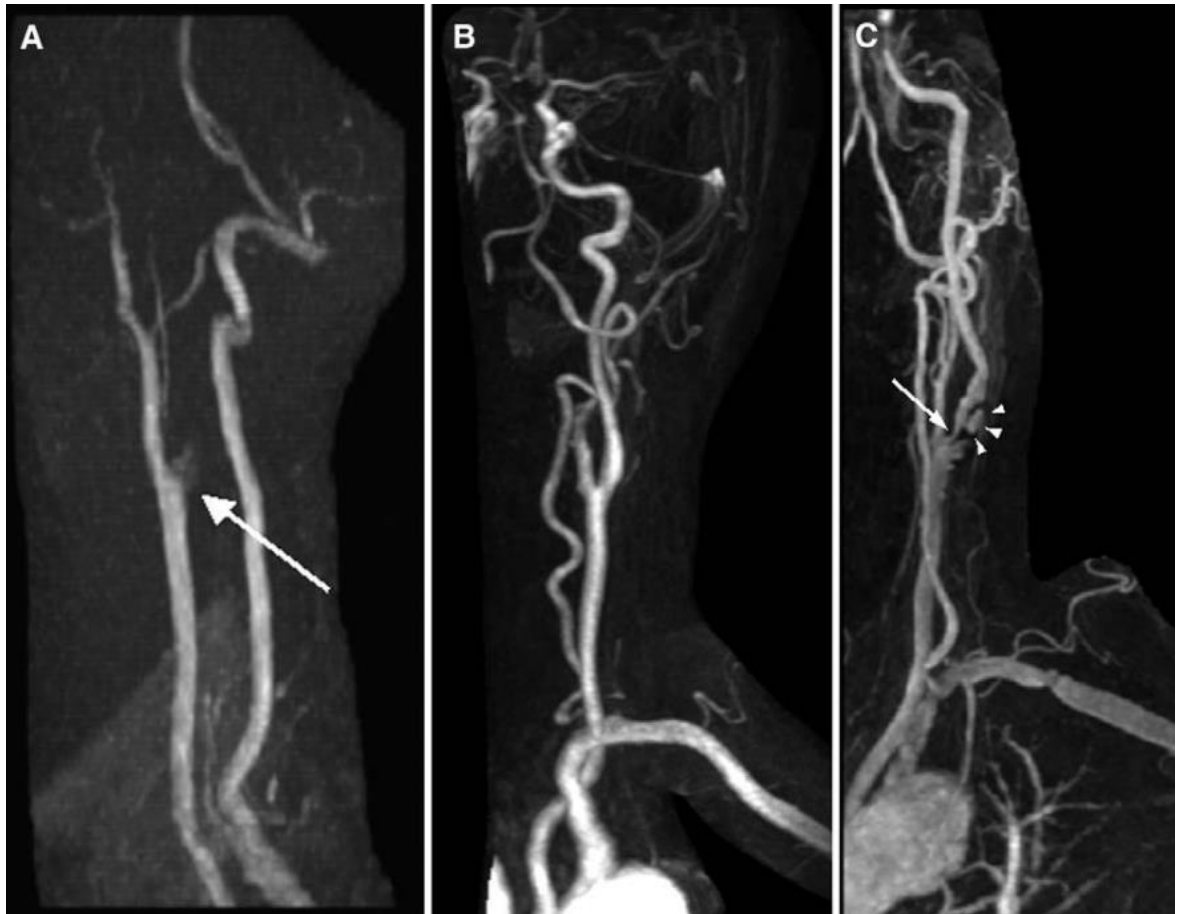
Figure 2.46 MRA of the carotid arteries. (A) 2D TOF showing signal drop-off at ICA (arrow) (B) Gadolinium contrast enhanced MRA of normal carotid bifurcation (C) Gadolinium contrast enhanced MRA showing severe stenosis in the ICA (arrow) – ulcerated carotid plaque observed (arrowheads) [144]

High resolution MRI has been used extensively in the imaging of the carotid artery and classifications have been established to correspond to plaque types discussed by the AHA [157]. Cai et al (2005) used TOF, T1W, T2W and PDW images to classify the plaque types and validated this by means of histological staining. A limitation of this study is that the plaques taken here are from patients undergoing endarterectomy. Thus, the majority of specimens were in the advanced stages of atherosclerosis. Studies by Saam et al (2005,2007) also used high resolution MRI and multiple imaging contrasts to determine the composition of the plaque and its components [158,159]. As shown in figure 2.47, results reveal good agreement between the in-vivo MRI and histology for quantitative measurements of the plaque components such as fibrous tissue, lipid core, calcification, and loose matrix.

Plaque Composition
[as percentage of the wall]
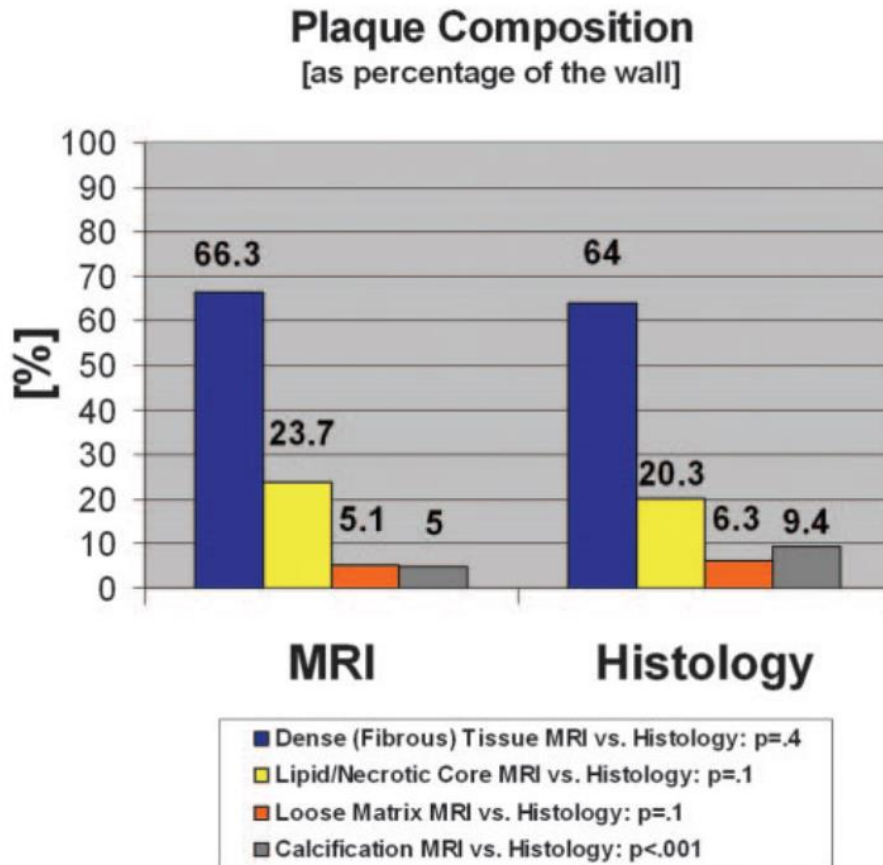
Figure 2.47 Plaque composition calculated as the percentage of vessel wall area for 31 samples
[158]

Atherosclerotic plaque characterization in all of these studies are based on the signal intensities
and the morphological appearances of the plaque on T1W, T2W, proton density weighted (PDW)
and TOF images as summarized by table 2.2 [161]. Lipid rich necrotic cores (LR/NC) appear
hyperintense in TOF, T1W, PDW and T2W images while haemorrhage is hyperintense on T1W,
T2W and TOF, but receives heterogenous signal for PDW. Fibrous caps, which can be difficult
to differentiate from fibrotic media in in-vivo images appear as isointense in all images and
calcifications are defined as hypointense regions within the plaque for TOF, T1W, PDW and
T2W images. Fibrosis changes from isointense to hyperintense in T1W, PDW and T2W but
hypointense in TOF [161,162].

Table 2.2 Plaque imaging characteristics for different imaging contrasts [161]

	Time-of-flight image	T1-weighted image	Proton density image	T2-weighted image
Lipid/necrotic core	Isointense to slightly hyperintense	Hyperintense	Hyperintense	Hyperintense
Hemorrhage	Hyperintense	Hyperintense to isointense	Heterogeneous	Hyperintense
Fibrous cap	Hypointense band		Isointense to slightly hyperintense	Isointense to slightly hyperintense
Calcium	Hypointense	Hypointense	Very hypointense	Very hypointense
Fibrosis	Hypointense to isointense	Isointense to slightly hyperintense	Isointense to slightly hyperintense	Isointense to slightly hyperintense

2.9.7.1 Diffusion Weighted Imaging (DWI) and Diffusion Tensor Imaging (DTI)

Diffusion weighted imaging (DWI) is an alternative to T1 and T2 and has primarily been used to investigate neurological disorders, such as patients suffering from white matter disorders or stroke. For DWI to work, the signal needs to be sensitized to diffusion in a certain direction by using strong magnetic field gradient pulses. This degree of diffusion is controlled by the b-value (b), a factor determined by the gyromagnetic ratio (γ), gradient strength (G), gradient duration (δ) and time spacing (Δ):

$$b = \gamma^2 G^2 \delta^2 (\Delta - \delta/3) \tag{2.8}$$

The optimum choice of b-value changes depending on the anatomical structure, number of signals averaged and field strength. Routine DWI uses b-values from 0 to 1000. For arterial tissue *ex-vivo*, a b-value of 800 s/mm^2 was deemed to be sensitive to measure diffusion [36,37]. Diffusion tensor imaging (DTI) is an extension of diffusion weighted imaging (DWI) and has been used as a sensitive probe to the structure of tissues by measuring the diffusion of water molecules to obtain sensitive microstructural measurements such as the fractional anisotropy (FA), mean diffusivity (MD) and helical angle (HA).

Ex-vivo MRI studies looking into arterial tissue have looked at determining the feasibility of applying this technique to arterial tissue to determine the collagen fibre orientation and reorganization in response to loading conditions. Flamini et al (2010) first demonstrated the ability to use DTI to determine fibre structure of porcine aortic artery [36]. Here, it was determined that the optimal b-value for arterial tissues was approximately 800 s/mm^2, as this is the value that there is a balance between the eigenvector angles in tensor maps produced and the fibre data obtained by the fibre tracking procedure used [36]. Ghazanfari et al (2012) detailed the fibre structure of porcine carotid arteries using DTI and fibre tractography. In the DTI analysis, it was seen that the carotid artery exhibited a predominant circumferential orientation. This was then validated using SHG with strong agreements [31]. Further *ex-vivo* studies by Tornifoglio et al (2020) have determined the diffusion responses from porcine artery when structural components such as collagen, elastin and smooth muscle cells have been selectively taken out by use of purified collagenase solutions, purified elastase solution and decellularization protocols.

The common belief in diffusion MRI of arterial tissues is that the collagen fibre alignment dictates the water diffusion in the tissue to be anisotropic. However, when the collagen was selectively degraded using purified collagenase solution, some anisotropic behaviour is still observed whilst when the tissue is decellularized, a dominant isotropic response is observed, see figure 2.48. This indicates that it is actually the cells that predominantly determine this anisotropy [39]. This misconception could be from the fact that cells and collagen are aligned in the same direction in arterial tissue and is generally only validated by histological means [39].
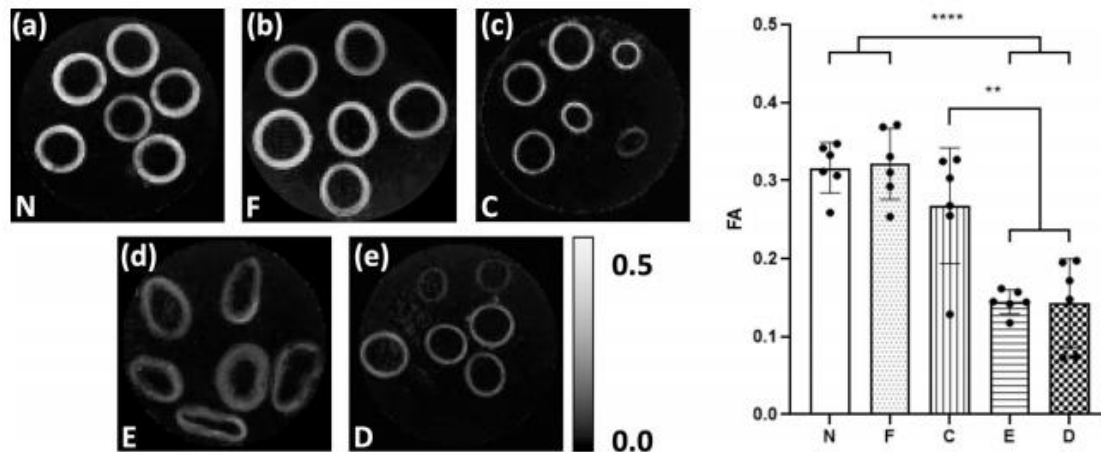
Figure 2.48 Parametric maps of fractional anisotropy (FA) in a representative slice for each of the tissue models. Measured in the vessel media, both (a) native (N) and (b) fixed native (F) porcine carotid artery (PCaA) showed significantly higher FA than both the (d) elastin degraded (E) and (e) decellularized (D) tissue models. Collagen degraded PCaA also showed a significantly higher FA than both elastin degraded and decellularized PCaA. FA maps scaled to show 0 to 0.5 (**p=0.0018 (C vs. E), **p=0.0016 (C vs. D), ****p<0.0001) [39].

Studies by Akyildiz et al (2017) showed the fibre orientation for an entire plaque specimen using a DTI sequence in a 9.7 Tesla scanner. They determined that the most dominant fibre orientation in this case was in the circumferential direction (52%), but fibres can be orientated in the axial and radial directions throughout the plaque and at risky locations such as the fibrous plaque cap, as shown in figure 2.49 [38], demonstrating that the fibre orientation is highly variable throughout the plaque.
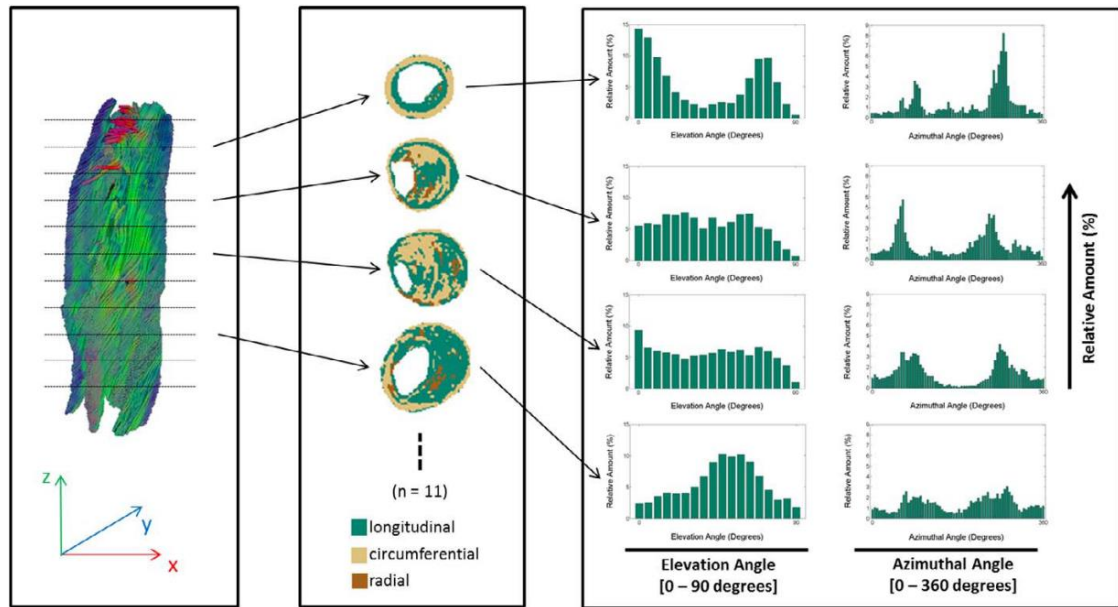
Figure 2.49 Fibre orientations of a 3D plaque sample (left panel) and principal predominant fibre orientation in four selected cross-sections (mid panel), together with elevation and azimuthal angle histograms (right panel) [38]

Oppreisnig et al (2018), have shown in a cadaveric specimen the fibre orientation of the common carotid artery with an atherosclerotic plaque, see figure 2.50. They determined from these initial results that the fibrous cap fibre orientation must be aligned circumferential to have mechanical integrity [163], which would be in agreement with mechanical assessments [164].
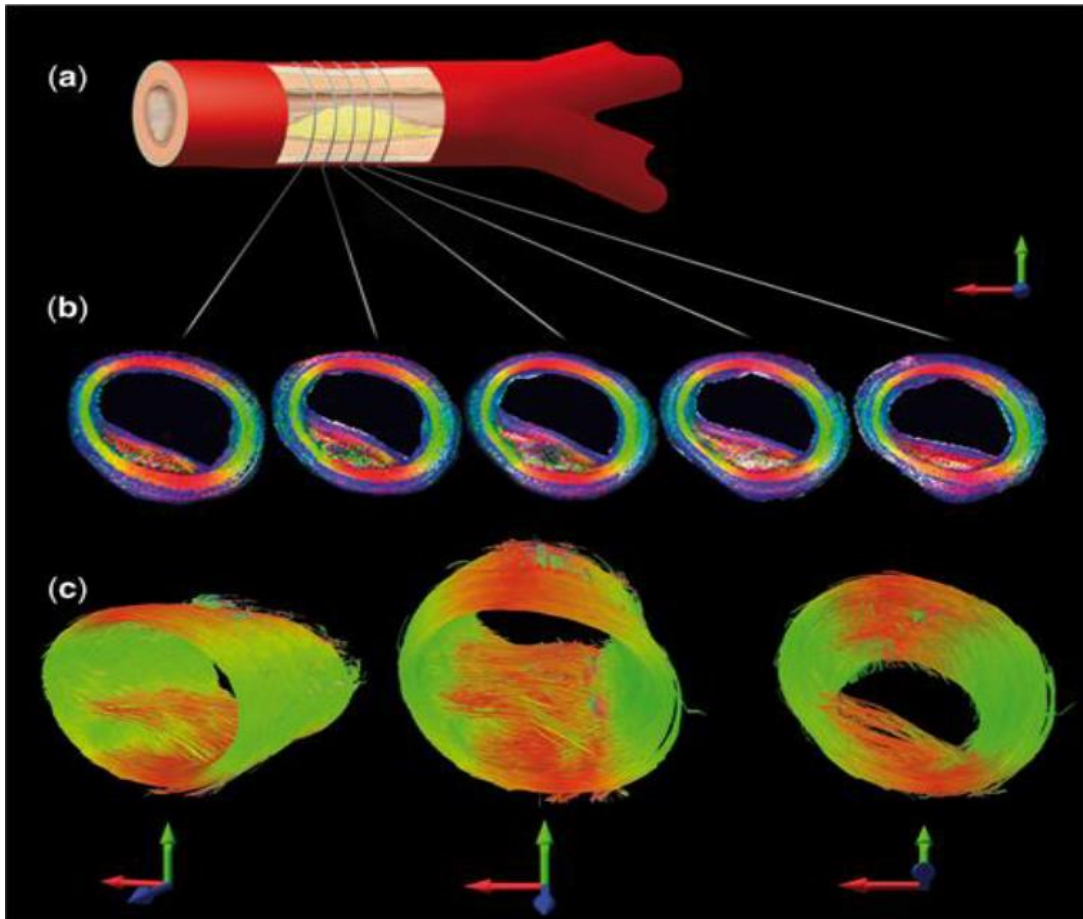
Figure 2.50 2D Fibre Orientation of vessel and atherosclerotic plaque from cadaveric specimen (a) Specimen schematic (b) Fractional anisotropy (FA) maps (c) Fibre tractography [163]

Further ex-vivo studies of the vessel and plaque should be done to determine optimum b-values to be used in analysis as the suggested value of b = 800 s/mm2 may not be suitable *in -vivo*. Furthermore, DTI of the arterial vessel in a longitudinally tethered state and loaded with pulsatile motion could aid possible translation to in-vivo settings and possibly give insights into the remodelling of arterial tissue. There has only been one study to date that has demonstrated the ability to do DTI of the carotid artery in-vivo. Oppreisnig et al (2017) used a Siemens 3T Prisma and a 2D DTI read-out segmented EPI sequence using four b-values (0 – 600 s/mm2) and 18 diffusion directions. In this study, it was determined that the principal direction of diffusion was tangential to the applied diffusion direction which shows that healthy vessels have a dominant circumferential orientation [165].

2.10 Summary

Extensive research has been performed to investigate the structure and function of the arterial wall, atherosclerotic plaques and their many components. The collagen fibre architecture has been the primary focus of much of this work, due to the fact that it is the major load bearing component of the tissue. Remodelling of this collagen fibre architecture is critical in order to

maintain healthy arterial function. An inability for the fibres to remodel to the optimum load bearing configuration in atherosclerotic plaques may increase the vulnerability of the plaque to rupture. To fully understand the mechanisms behind plaque rupture, a greater understanding of the atherosclerotic plaque microstructure and its response to loading needs to be established. Studies to date have tested atherosclerotic plaques and their components (see section 2.6) depicting a highly variable mechanical response. However, the relationship between the mechanical strength and collagen fibre orientation in the plaque and its fibrous cap is yet to be quantified. By pre-screening the tissue before testing with a non-destructive imaging technique such as SALS, it may be possible to answer this question.

To investigate the varying number of different cases of CVDs, numerous biomechanical models have been developed in an effort to determine relevant measures that can quantify the risk of vessel or plaque rupture (see section 2.7). However, certain limitations can be associated with these techniques mentioned, as they use peak stress as their sensitive indicator to rupture. Firstly, extracted geometries are already in a loaded configuration, and estimation of the zero-pressure configuration is not determined. This may lead to an incorrect deformation being imposed on the vessel as is not mimicking *in-vivo* conditions. Secondly, the residual stress of the vessel is generally excluded from the simulations. Residual stress is known to homogenise the gradient of stress through the vessel wall. Furthermore, simplified constitutive laws and material parameters from literature are not able to characterize the individual mechanical response of the tissue. To have a fully specified biomechanical model and more importantly robust stress strain results, these aspects need to be considered.

Lastly, the clinical technique for assessing the risk of plaque rupture using ultrasound or CT is insufficient as percent stenosis is based purely on the geometric measures and not mechanical or structural aspects. Furthermore, studies have shown that there is not a direct correlation between plaque rupture and percent stenosis. Characterizing the strain environment these plaques are subjected to *in-vivo* has shown promise in determining the difference between vulnerable and stable plaques. Such a measure can then be used in combination with patient specific finite element models informed from other established imaging techniques such as DTI to possibly determine the vulnerability of plaque rupture on an individual basis. Furthermore, it is hypothesised in this thesis that knowing the optimum configuration of the collagen fibres and comparing this with the real distribution of the fibres in the tissue, it may be possible to identify the lack of remodelling in atherosclerotic plaque tissue computationally, establishing which atherosclerotic plaques are vulnerable to rupture.

Chapter 3 Inverse material parameter estimation of patient specific finite element models at the carotid bifurcation: The impact of excluding the unloaded zero pressure configuration and residual stress

3.1 Introduction

The carotid bifurcation experiences a complex loading environment due to its anatomical structure. Previous *in-vivo* material parameter estimation methods often use simplified model geometries, isotropic hyperelastic constitutive equations or neglect key aspects of the vessel, such as the zero-pressure configuration or residual stress. These factors have independently been shown to alter the stress environment of the vessel wall. Characterising the location of high stress in the vessel wall has often been proposed as a potential indicator of structural weakness. However, excluding the afore-mentioned zero-pressure configuration, residual stress and patient specific material parameters can lead to an incorrect estimation of the true stress values observed, meaning stress alone as a risk indicator of rupture is insufficient. In this study, a computational investigation is performed to see how the estimated material parameters and overall stress distributions in geometries of carotid bifurcations, extracted from *in-vivo* MR images, alter with the inclusion of the zero-pressure configuration and residual stress.

This approach consists of the following steps: (1) geometry segmentation and hexahedral meshing from *in-vivo* MRI images at two known phases; (2) computation of the zero-pressure configuration and the associated residual stresses; (3) minimisation of an objective function built on the difference between the stress states of an " almost true" stress field at two known phases and a "deformed" stress field by altering the input material parameters to determine patient specific material properties; and (4) comparison of the stress distributions throughout these carotid bifurcations for all cases with estimated material parameters. This numerical approach provides insights into the need for estimation of both the zero-pressure configuration and residual stress for accurate material property estimation and stress analysis for the carotid bifurcation, establishing the limitations of stress as a rupture risk metric.

3.2 Methods

3.2.1   In-vivo MRI imaging protocol

In Vivo MRI scans of the carotid arteries were obtained from healthy volunteers using a 3T whole body MRI scanner (Achieva, Phillips Medical Systems, Best, Netherlands) combined with an 8-channel dedicated bilateral carotid artery coil (Shanghai Chenguang Medical Technologies,

Shanghai, China). For each volunteer, cuff diastolic and systolic pressures were recorded as shown in Table 3.1 and used as loading conditions in these finite element simulations. The imaging parameters used for the creation of the geometries are stated in Table 3.2 with the field of view (FOV) centred on the carotid bifurcation after localization using the time of flight (TOF) sequence. A triggering time was imposed so imaging could be performed at both diastolic and systolic phases of the cardiac cycle. This changed the overall scan time for each patient as it was dependent on their heart rate.

Table 3.1: Information acquired from volunteers during scanning

Acquired Information	Volunteer #1	Volunteer #2	Volunteer #3
Age (Years)	25	30	42
Diastolic Pressure (mmHg)	75	68	82
Systolic Pressure (mmHg)	112	107	120

Table 3.2: *In-vivo* image acquisition parameters used for visualisation of the carotid bifurcation

Acquisition Parameters	Time of flight (TOF)	T1 weighted	T2 weighted	Turbo spin echo (TSE)
Number of slices	48	8	8	8
TE (ms)	25	984	3000	2 R-R intervals
TR (ms)	3	11	38	38
Resolution (mm)	0.5 x 0.5	0.5 x 0.5	0.5 x 0.5	0.5 x 0.5
Slice thickness (mm)	3	3	3	3
Number of echoes	1	1	1	6
Scan time (mins)	2:06	6:30	6:38	6:38

To test the impact of image axial resolution on the stress results obtained from the computational models, the FOV was translated by 1mm in the z-direction and then shifted 1mm again with acquisitions being taken at both stages. This allowed for the creation of a higher resolution with an "apparent" slice thickness of 1mm by reallocating respective slices into the imaging stack, with a registration landmark set at the centre of the lumen to ensure images were correctly aligned and accurate segmentation could be performed.

3.2.2 Segmentation, preparation and hexahedral meshing of arterial bifurcations

3.2.2.1 Segmentation

After image acquisition, the DICOM stacks were input into Simpleware ScanIP (Synopsys, Inc., Mountain View, USA) for segmentation. The stack was first cropped to the region of interest and a mask was defined to perform the segmentation. Curves were delineated and arteries were then segmented manually from T2 weighted images of the carotid artery due to the high contrast of the vessel wall compared to the lumen and the surrounding tissue, see figure 3.1A. Each slice was analysed independently to ensure that the segmentation was as accurate as possible. This method accounted for the variable wall thickness of the vessel wall.

3.2.2.2 Geometry preparation

Once created, the segmented geometries needed to be smoothed further to avoid sharp edges in the reconstructed artery. This was especially important at the location of bifurcations, where an un-smoothed geometry could result in sharp elements that cause not only numerical convergence issues but locations of high stress. Using ANSYS Spaceclaim (ANSYS Inc, USA), the geometry was imported and the STL facets were checked using the inspect function. Sharp edges, as shown in figure 3.1B, were highlighted and subsequently smoothed using the fix sharps tool. After all sharp edges were removed, curves were extracted from the boundaries of the vessel wall by obtaining cross sections of the geometry using a series of parallel planes, see figure 3.1C. These curves were then connected to construct the inner and outer surfaces of the arterial wall. The geometry was then stitched together to ensure there were no gaps between surface interfaces in the next step. The blend function was then applied to connect the inner and outer vessel wall to ensure a connected geometry. These smoothed surfaces were then saved as STL meshes to export to ANSA pre-processor software.

3.2.2.3 Hexahedral meshing

After importing the new processed STL geometry, hexahedral meshing was performed using ANSA pre-processor software (v17.0, BETA CAE Systems, Thessaloniki, Greece). Using the *Hexa Block* module, the volume of the STL was defined initially in the form of a box, see figure 3.1D. This box was first split into four sections and the outside perimeters of the boxes were then moved to fit to the curvature of the geometry. Crosshatch faces, which are the intersecting planes between adjacent boxes, were then selected to separate the joined boxes in order to fit three independent boxes defining the three different sections of the carotid artery, more specifically, the common carotid, internal and external carotid. The perimeters of each defined box were then assigned to the outer wall of the geometry using the *project to surfaces* tool while the edges at proximal and distal were assigned using the *project to edges* tool. To include the inner wall, the

O-Grid function was used, whereby inner perimeters were created and assigned to the interior wall using the project to surfaces and project to edges tools. To complete meshing, the connecting hatches in the lumen of the model were removed leaving just the assigned boxes to the vessel wall. This step is not necessary if fluid-based models are desired. Lastly, the *Pure Hexa* module was applied to automatically generate a structured hexahedral mesh of the bifurcation with the desired mesh density. This mesh density could be set by setting the desired number of elements on the perimeters of assigned boxes.
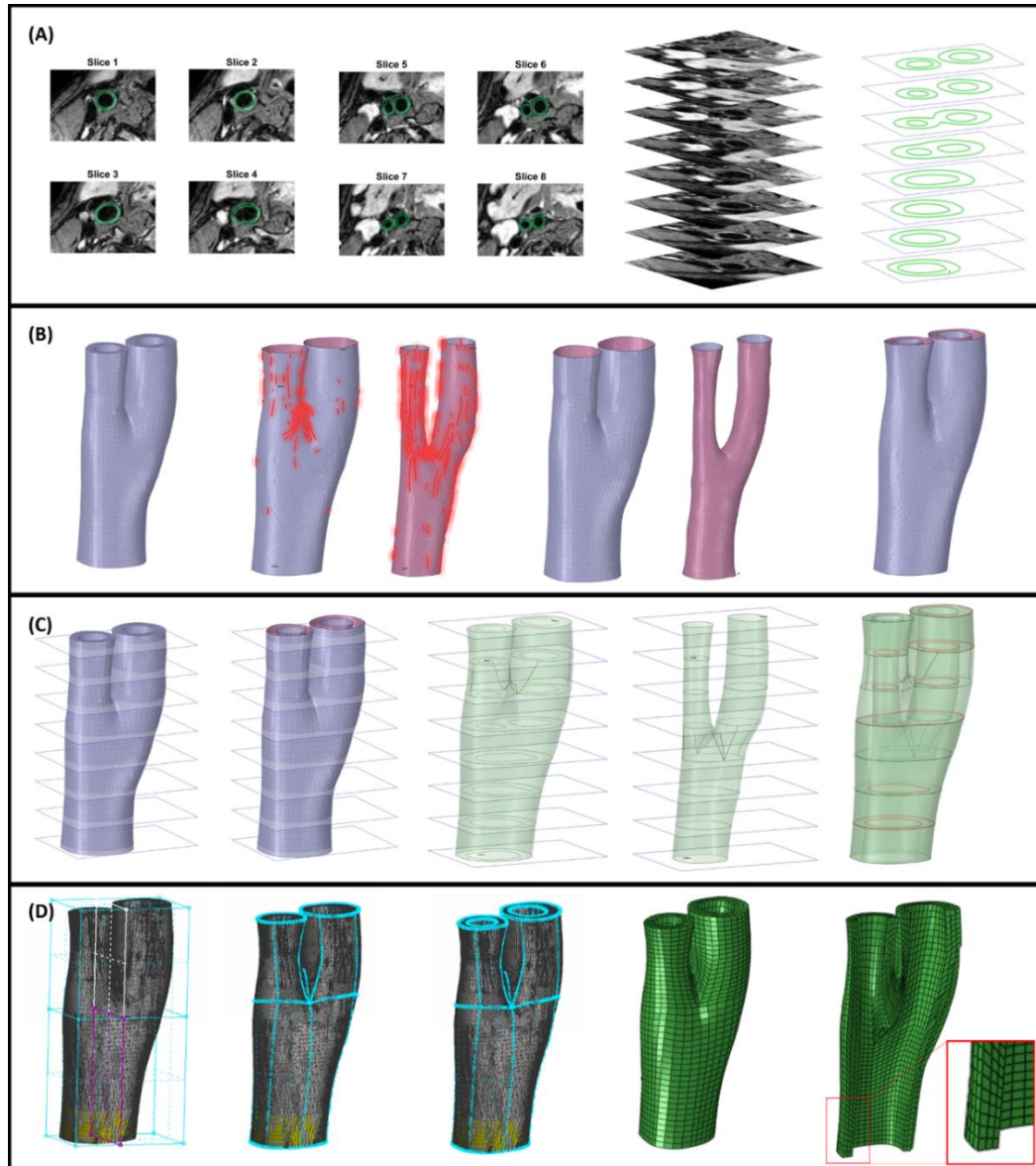
Figure 3.1: (A) Delineation of vessel from T2 weighted MRI images and creation of 3D stack (B) Initial model created – determining the location of sharp edges and smoothing the geometry (C) Surfaces of new smoothed surface are extracted and volume model is created for export into mesh pre-processor (D) Hexa-block tool used to define the geometry and create hexahedral finite element meshes of the bifurcation.

3.2.3 Constitutive equation

For implementation in all models, the fibre reinforced HGO hyperelastic material model was used [10]. This model assumes that the tissue is composed of a matrix material that is embedded with two families of fibres, each has a preferred fibre direction. Mathematically, the model can be expressed by the strain energy function **W**:

$$W = C_{10}(\bar{I}_1 - 3) + \frac{k_1}{2k_2} \sum_{i=4,6} \{e[k_2(\bar{I}_i - 1)^2] - 1\} \tag{3.1}$$

$$\textbf{\textit{Where}} \; \kappa = \int_0^\pi \varphi(\theta)sin^3\theta d\theta$$

Where C_{10} is used to describe the isotropic matrix material along with the deviatoric strain invariant $\bar{I}_1$. k_1 is a positive material parameter with the units of kPa while k_2 is a dimensionless parameter. The deviatoric strain invariant $\bar{I}_i$ is used to characterize each fibre family and κ is used as a dispersion parameter describing the fibre distribution, whereby $\kappa = 0$ describes high alignment while $\kappa = 0.33$ means the fibres are isotopically distributed. Θ is defined as the angle between the fibre direction and the circumferential axis. For further mathematical background, the reader is referred to Holzapfel et al 2000 [10] and the Abaqus documentation. Five material parameters are therefore required to be input for the models and the values used are those in Balzani et al (2012) and are reported in Table 3.3.

Table 3.3: Material parameters taken from Balzani et al (2012) implemented in computational models [17]

C_{10} (kPa)	k_1 (kPa)	k_2	κ	θ (deg)
6.56	1482	561	0.16	37

3.2.4 Determining the zero-pressure configuration of arterial bifurcations

The method for estimation of the zero pressure configuration is detailed in the schematic figure 3.2, the workflow in figure 3.3 and is adapted from Raghavan et al, 2006 [18]. In this adaptation, the initial "loaded" *in-vivo* geometry is assumed to be stress free and to be at a known pressure. From this configuration, the displacement between the deformed and *in-vivo* geometry is calculated. The subtraction of this calculated displacement from the *in-vivo* geometry gives the first guess of the estimated zero pressure configuration. To ensure this is correct, the estimated configuration is loaded again to give a new configuration that should equal the *in-vivo* geometry. This is further optimized using the scaling parameter K to ensure the comparison between these configurations is sufficient. Once optimized, the estimated zero configuration is then determined.
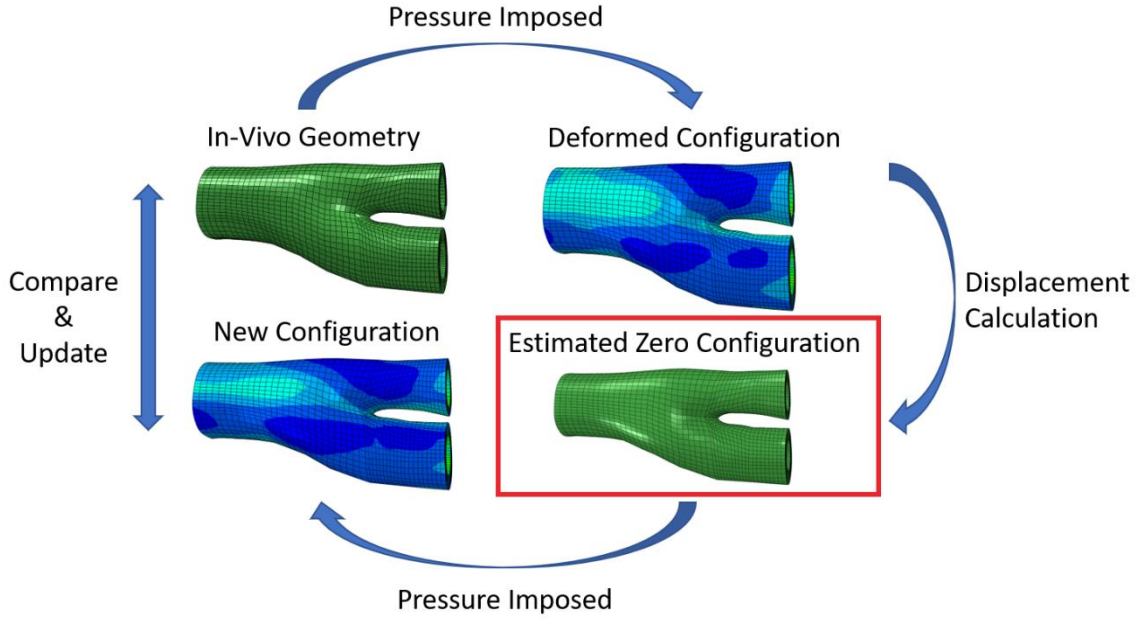
Figure 3.2: Schematic illustration for estimating the zero-pressure configuration from an in-vivo geometry segmented at a known pressure state.

The process of estimating the zero-pressure configuration stated previously is implemented in MATLAB (MATLAB 2019a, The MathWorks, Inc., Natick, Massachusetts, United States). Here, X is the N x 3 array that describes the original undeformed nodal coordinate positions (x, y and z) and x is denoted to represent the deformed configuration after pressure loading. Element connectivity is kept constant throughout ensuring that no errors were incurred between initial and deformed configurations. Illustrated by the algorithmic workflow in figure 3.3, the *in-vivo* geometry was extracted using the protocols described in Section 3.2.1 and 3.2.2. This initial in-vivo geometry $(\mathbf{X_1})$ is initially assumed to be stress free and loaded with in-vivo pressure conditions $(\mathbf{P_1})$. To create the candidate zero pressure configuration, the displacement vector field $(\mathbf{U_1})$ was calculated. This displacement field vector is a subtraction of the initial in-vivo geometry and the deformed configuration $(\mathbf{x_1})$.

$$\mathbf{U_1 = X_1 - x_1} \tag{3.2}$$

Once calculated, the displacement field is scaled using a parameter **K** and subtracted from the in-vivo geometry to obtain the first estimate of the zero-pressure configuration $(\mathbf{X_2})$.

$$\mathbf{X_2 = X_1 - K.U_1} \tag{3.3}$$

Here, it is again assumed that this first estimate of the zero-pressure configuration is stress free. The same pressure condition $(\mathbf{P_1})$ is imposed as in the previous step to obtain a new deformed configuration $(\mathbf{X_3})$.

$$\mathbf{U_{obj}} = [(\mathbf{X_1} - \mathbf{x_3})^2] \tag{3.4}$$

Theoretically, this new deformed configuration $(\mathbf{x_3})$ should be equal to the *in-vivo* geometry $(\mathbf{X_1})$ from the initial step. However, due to the mechanical properties, the deformation of the geometry will be different. Therefore, to improve accuracy of the geometry estimated, an objective function of the displacement $(\mathbf{U_{obj}})$ between the initial *in-vivo* geometry $(\mathbf{X_1})$ and the deformed zero-pressure $(\mathbf{x_3})$ configuration is implemented.

$\mathbf{U_{obj}}$ is then minimised until it reaches a set tolerance of less than 0.05 mm. If the geometry is not deemed optimised after a pre-set criterion of 50 iterations, a new value of K is implemented by incrementing the previous value by 0.05.
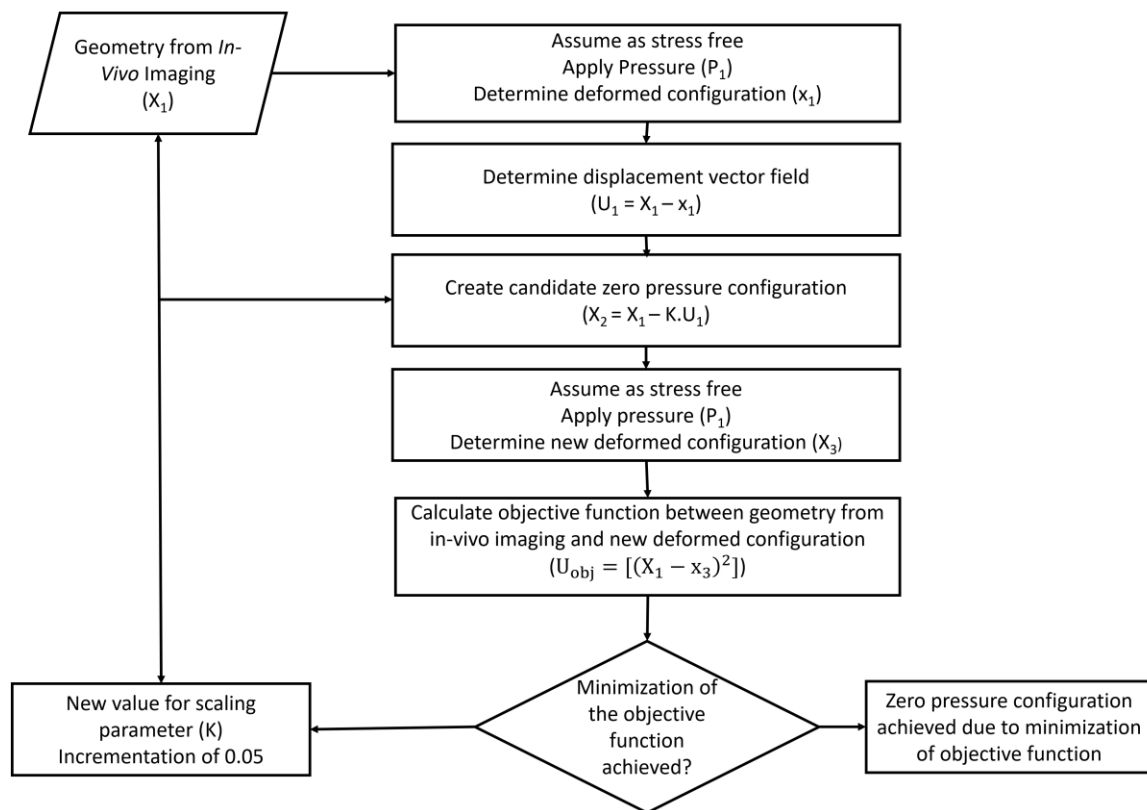
Figure 3.3: Algorithmic workflow for extracting the zero-pressure configuration from an in-vivo arterial bifurcation geometry with known pressure conditions.

3.2.5   Incorporation of the residual stress in arterial bifurcations

For the entire mathematical derivation, the reader is directed to Schroder et al, 2014 [22]. Details included here are a summary of the algorithm implemented in that publication. Firstly, for

implementation into the computational models, it is assumed that arterial tissue is an incompressible material. Secondly, for fibre reinforced tissues such as arteries, the Cauchy stress tensor $\boldsymbol{\sigma}$ **is** additively decomposed into deviatoric ground stresses $\boldsymbol{\sigma}^*$ and reaction stresses $\boldsymbol{\sigma}^{\text{reaction}}$, which represent the influence of the fibre stress state.

$$\boldsymbol{\sigma} = \boldsymbol{\sigma}^* + \boldsymbol{\sigma}^{\text{reaction}} \tag{3.5}$$

It is then assumed that this reaction stress is composed of the hydrostatic pressure imposed, the fibre tensions $\mathbf{T_1}$ and $\mathbf{T_2}$ and the structural tensors $\mathbf{m_1}$ and $\mathbf{m_2}$ which incorporate the preferred fibre directions $\mathbf{a_1}$ and $\mathbf{a_2}$.

$$\boldsymbol{\sigma}^{\text{reaction}} = \mathbf{T_1}\bar{\mathbf{m}}_1 + \mathbf{T_2}\bar{\mathbf{m}}_2 \tag{3.6}$$

$$\bar{\mathbf{m}}_a = \bar{\mathbf{a}}_{(a)} \otimes \bar{\mathbf{a}}_{(a)} \ \textbf{with a=1,2} \tag{3.7}$$

For the fibre tensions, $\mathbf{T_1}$ and $\mathbf{T_2}$, these can be obtained by using equation 3.8 and 3.9 respectively. Here the abbreviations $\boldsymbol{\xi} = \bar{\mathbf{m}}_1 : \bar{\mathbf{m}}_2 = \cos^2\emptyset$, where $\emptyset$ is the inclination angle between the two fibre directions.

$$\mathbf{T_1} = \frac{\boldsymbol{\sigma} : \bar{\mathbf{m}}_1 - \boldsymbol{\sigma} : \bar{\mathbf{m}}_2 : \boldsymbol{\xi}}{1 - \boldsymbol{\xi}^2} \tag{3.8}$$

$$\mathbf{T_2} = \frac{\boldsymbol{\sigma} : \bar{\mathbf{m}}_2 - \boldsymbol{\sigma} : \bar{\mathbf{m}}_1 : \boldsymbol{\xi}}{1 - \boldsymbol{\xi}^2} \tag{3.9}$$

For physiological loading conditions, local volume averages of the fibre stresses are calculated for each decomposed volume segment $\mathbf{v}^{\text{mat}}$

$$\mathbf{T_1^{mat}} = \frac{1}{\mathbf{v}^{\text{mat}}} \int \mathbf{T_1} \mathbf{dv} \tag{3.10}$$

$$\mathbf{T_2^{mat}} = \frac{1}{\mathbf{v}^{\text{mat}}} \int \mathbf{T_2} \mathbf{dv} \tag{3.11}$$

With the difference between this mean value and the fibre stresses giving equations 3.12 and 3.13

$$\Delta \mathbf{T_1} = \mathbf{T_1} - \mathbf{T_1^{mat}} \tag{3.12}$$

$$\Delta T_2 = T_2 - T_2^{mat} \tag{3.13}$$

From which, the residual stress can be included:

$$\sigma^{res} = -\Delta P + \Delta T_1 \bar{m}_1 + \Delta T_2 \bar{m}_2 \tag{3.14}$$

By which, ΔP can be calculated from the tensional fibre stress differences from equation 3.12 and 3.13

$$\Delta P = \frac{1}{3}(\Delta T_1 + \Delta T_2) \tag{3.15}$$

Now that residual stress tensor σ^{res} can be calculated, it can be subtracted from the Cauchy stress tensor shown by equation 3.16 to give the actual stress response in the tissue.

$$\sigma = \sigma^* - \sigma_{res} \tag{3.16}$$

The method implemented in this study follows the algorithmic approach detailed in Schroder et al, 2014 [22]. Extended to 3D models, the residual stresses are incorporated by including a tensional fibre stress to homogenize the stress gradient throughout the vessel wall. Implemented via Abaqus UMAT and URDFIL subroutines connected by common blocks to allow the exchange of variables such as section volume, the algorithm is as follows:

(a) Segment the arterial wall into volume sections (see figure 3.4). Done in ANSA pre-processor software.
(b) Define a suitable stress measure (tensional fibre stress).
(c) Compute the local volume averages of the stress measure and the deviation of local and averaged stress measure in a section of interest.
(d) Define the amount of residual stress and apply a proportionate value to the equilibrium stress state (state at which geometry is loaded and not considering the residual stresses).
(e) Iterate until convergence of the stress measure is observed.

Like Schroder et al, 2014, steps (c-e) are denoted as a "smoothing loop"; by which the smoothing loop is repeated until convergence of the solution is reached when no significant changes in the residual stresses are observed.
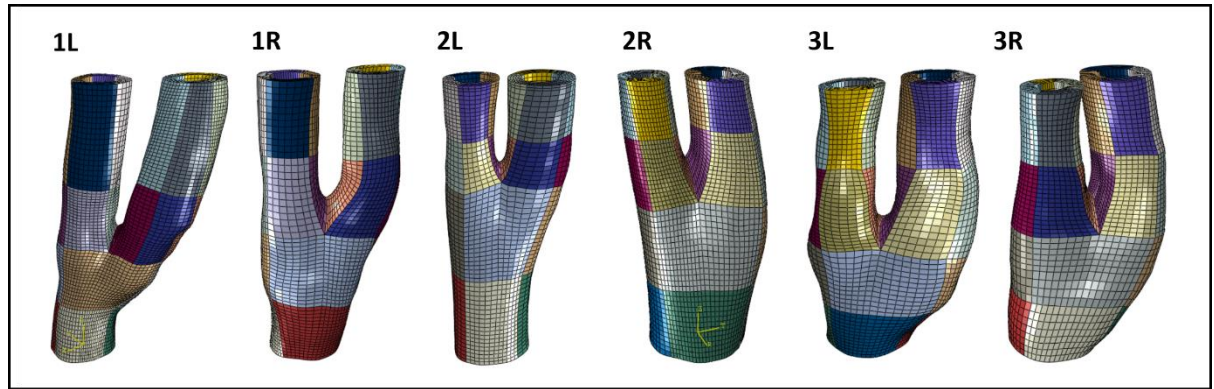
Figure 3.4: Defining volume sections throughout the bifurcation models. The material is defined in each section and volumes are calculated. L denotes that the bifurcation is on the left side while R denotes that the bifurcation is on the right side.

3.2.6 Inverse material parameter estimation

The method of parameter estimation in this study is adapted from the implementation in Liu et al, 2017 [25]. The following statements are made to provide clarity in the method implemented:

(a) *In-vivo* loaded geometries are extracted from two known phases in the cardiac cycle (. e.g., diastole and systole)

(b) Finite element meshes at the two phases are constructed to ensure they have mesh correspondence. i.e., consistent number of elements and connectivity. This ensures that the displacement field can be obtained correctly

(c) Thickness of the vessel wall can be directly inferred from MR Images.

(d) Assuming that the vessel is statically determinant, assigning linear elastic properties ($E = 2 \times 10^4$ GPa and $v = 0.49$ [25]) will give the "almost true" stress state of the vessel, within 10% of the actual true stress experienced by the vessel

The inverse finite element algorithm workflow for material parameter estimation is illustrated by the algorithmic workflow in figure 3.5 and is performed in Isight (Dassault Systemes Simulia corporations, Velizy-Villacoublay, France). This approach leverages that the "almost true" stress field of the vessel wall can be approximately determined using linear elastic properties.
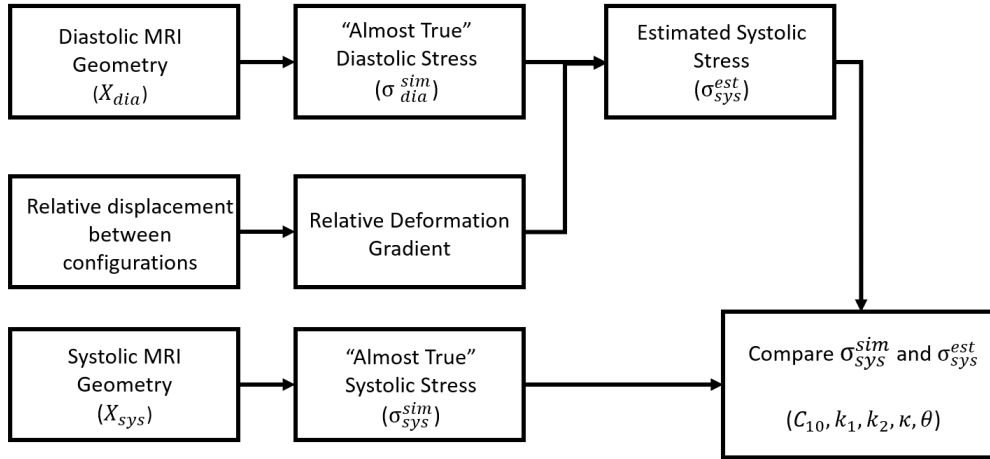
Figure 3.5: Algorithmic workflow of the implemented inverse FE algorithm for material calibration of the carotid artery in Isight.

Different parameterized Abaqus input files have been designated accounting for the diastolic, systolic and zero pressure configuration cases. The input files are imported into the Abaqus component of Isight with the material parameters set as optimization variables. The optimization process is then formulated as follows: the objective is to find a set of constitutive parameters $(C_{10}, k_1, k_2, \kappa, \theta)$, for the element type C3D8H in Abaqus. The square stress at all integration points was calculated and summed together as the value of the objective function as stated in the equation:

$$g_{err} = \sum_{m=1}^{N} \sum_{i=1}^{6} [\sigma_{sys}^{sim} - \sigma_{sys}^{est}(C_{10}, k_1, k_2, \kappa, \theta)]^2 \qquad (3.17)$$

Where σ_{sys}^{sim} is the "almost true" stress state and σ_{sys}^{est} is the estimated stress state with assigned material parameters. N is the number of elements used in the optimization. Upper and lower bounds stated in table 3.4 are set for all parameters and are based on previous studies [17,25].

Table 3.4: Lower and higher bounds set for material parameter estimations [17,25].

Parameters	C_{10} (kPa)	k_1 (kPa)	k_2	κ	θ (deg)
Lower Bound	0	0	0	0	0
Initial Input Parameters	6.56	1482	561	0.16	37
Higher Bound	20	2000	1000	0.33	45

To test the effect of including the zero-pressure configuration and residual stress on estimated material parameters and the overall stress distribution throughout the bifurcation, a number of cases are considered:

Case 1: Models extracted at diastole are simulated with literature material parameters

Case 2: Models are simulated with estimated material parameters from diastole to systole

Case 3: Models start in the zero-pressure configuration with estimated parameters going from this zero-pressure configuration to diastole and systole

Case 4: Residual stress is included at zero-pressure configuration and simulated with estimated material parameters from the zero-pressure configuration to diastole and systole.

To further investigate the effect of including the zero-pressure configuration and residual stress on the stress response, a single element attributed with estimated material parameters is simulated in uniaxial tension for each case. Furthermore, percentage volume plots are extracted from the bifurcation models to observe the effect these implemented methods have on the stress distribution.

3.3 Results

3.3.1 Effect of image resolution on stress calculations

To demonstrate the sensitivity of these finite element models to stresses calculated, it is important to perform a mesh convergence analysis. This is important as it allows for stress calculations to be performed in the least amount of computational time without compromising the accuracy of the result. In this mesh convergence analysis, the location of highest stress was the location of interest, and like the literature and from these biomechanical models, highest stresses were observed at the location of the apex of the bifurcation.
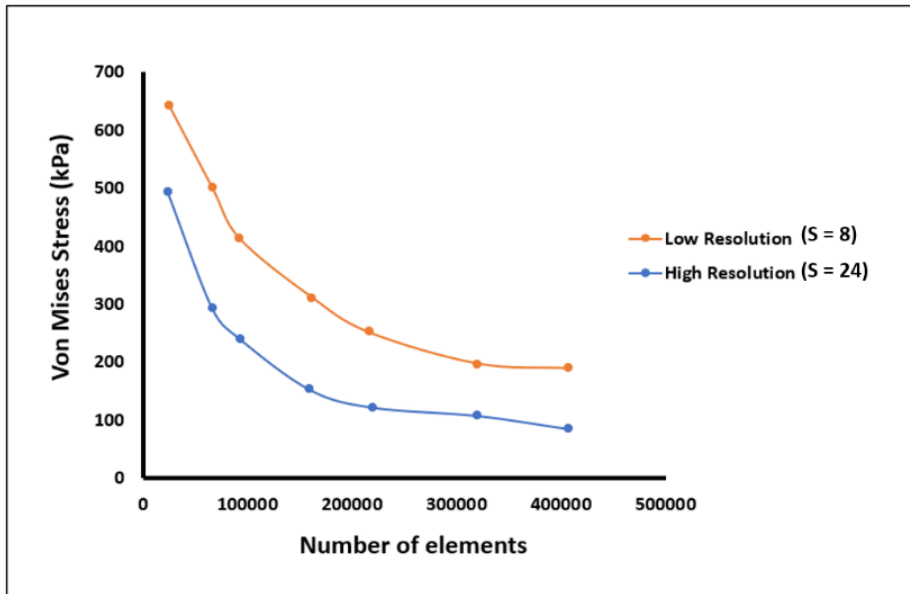
Figure 3.6: Mesh convergence results for bifurcation geometry 2L at two different resolutions. Low resolution model where S = 8 and high-resolution model where S = 24. S represents the number of images slices in this case.

For robust mesh convergence analysis, it would be logical to argue that for models of similar geometry, then the same level of mesh refinement would be suitable to obtain the same level of accuracy. Therefore 250,000 elements are deemed enough for this analysis as values do not change by more than 5% of the previous value, see figure 3.6. Interestingly, it is observed that convergence of stress results is independent of the model resolution. For the low-resolution model, the convergence is observed at a stress value of 286 kPa while for the high-resolution model the convergence is observed at stress values of 145 kPa. The sensitivity difference between these two observed values was calculated to be 49%, which is a significant increase and would lead to an overestimation of the stresses at the apex location.

3.3.2   Optimization of the zero-pressure configuration

3.3.2.1 Cylinder model

For the estimation of the zero-pressure configuration, an idealized cylinder model is first used to test the robustness of the implemented algorithm. In the idealized model, the wall thickness was set to be 0.75mm with an inner diameter of 2mm. An internal pressure was also assigned to be 16kPa. As demonstrated by figure 3.7A, the estimated zero pressure configuration comprises of a lower luminal radius and larger wall thickness when compared to the initial loaded configuration. This is expected and follows results demonstrated in Raghavan et al, 2006 [18].

3.3.2.2 Bifurcation Model

As shown by figure 3.7B, the algorithm shows convergence of the used scaling parameter K to be in between 0.9 and 1 for all 6 bifurcation models, which is similar to results obtained in

Raghavan et al, 2006 for an aneurysmal model. After finding the optimal zero-pressure configuration, the wall thickness of the bifurcation models increased with a decrease in luminal radius. It is important to note that lower increments <0.05 increase the accuracy of the estimated zero pressure configuration. However, due to a new simulation being needed after each iteration, this would increase the computational time needed.
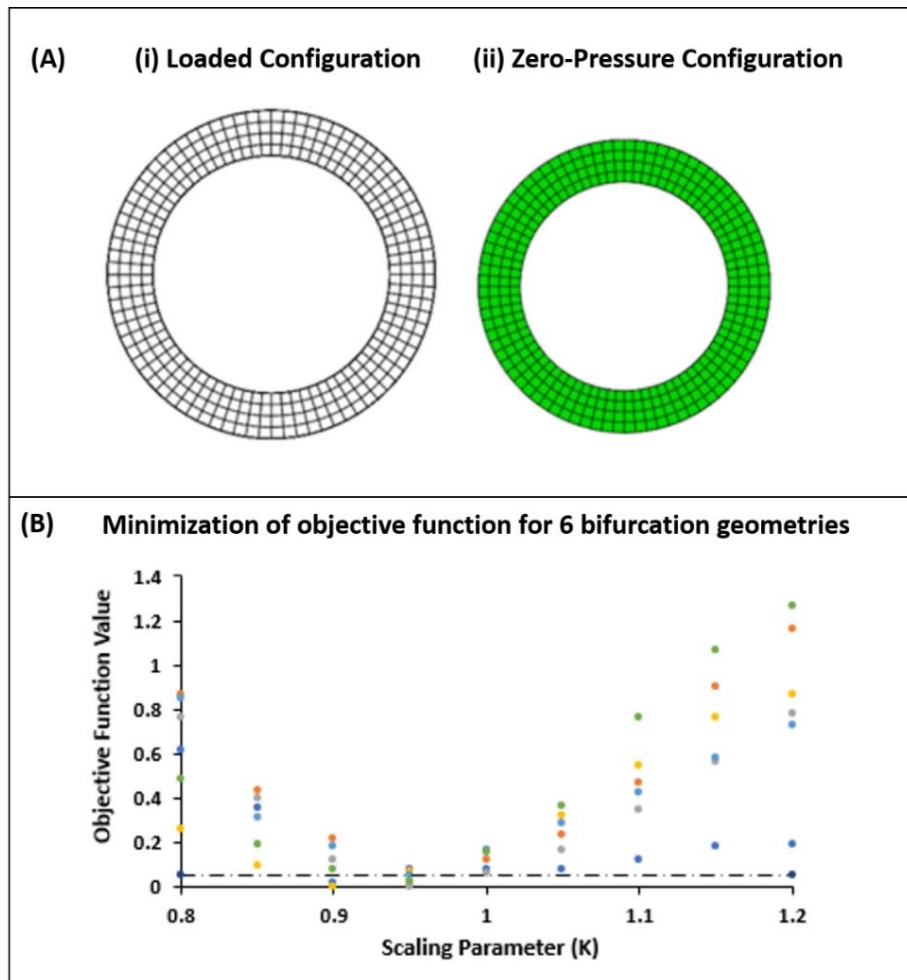
Figure 3.7: Optimization of the zero-pressure configuration for an idealized cylinder model. The wireframe shown in (i) depicts the initial geometry while the green geometry shown in (ii) shows the estimated zero pressure configuration. (B) Optimization of the zero-pressure configuration for patient specific carotid bifurcation models

3.3.3 Optimization of residual stress inclusion

To validate the accuracy of the implemented algorithm, a theoretical calculation is obtained from a simplified cylindrical model. The reason for this is to have an approximate value of stress to optimize towards otherwise a complete smoothing of the gradient would be achieved. Using classical mechanics, it was possible to calculate the expected stress manually before simulation

and validate the calculated stresses observed in the model. By assuming that the model is a thin-walled cylinder, the circumferential stress can be calculated by:

$$\sigma_{cir} = \frac{Pd}{2t}$$

(3.18)

Where P is the pressure imposed, d is the inner diameter of the model and t is the wall thickness. For the cylindrical model, the wall thickness was 0.75mm with an inner diameter of 2mm. Pressure imposed for the model was set to be 120mmHg which corresponds to approximately 16 kPa. The circumferential stress calculated for this cylindrical model was 21.3 kPa, see figure 3.8A.

3.3.3.1 Cylinder model

Using the same dimensions as the theoretical model, both the tensional fibre stresses T_1, T_2 and maximum principal stress gradients decrease when imposing an increased number of smoothing loops. Residual stress was deemed to be incorporated into the model when the tensional fibre stress T_1 converged but preserved the small gradient of maximum principal stress from the inner to outer wall, as shown by figure 3.8B. Tensional fibre stress T_2 is equal to T_1. 10 smoothing loops was determined to be enough to incorporate residual stresses into the cylindrical model as the tensional fibre stress converged when the tensional fibre stress from inner to outer wall was within 10%. For the cylindrical models, the maximum principal stress from outer to inner wall goes from 25 kPa to 21 kPa with the inclusion of residual stresses as illustrated in figure 3.8C. This is in the range of the theoretical calculation that the vessel wall experiences a stress of approximately 21.3kPa.
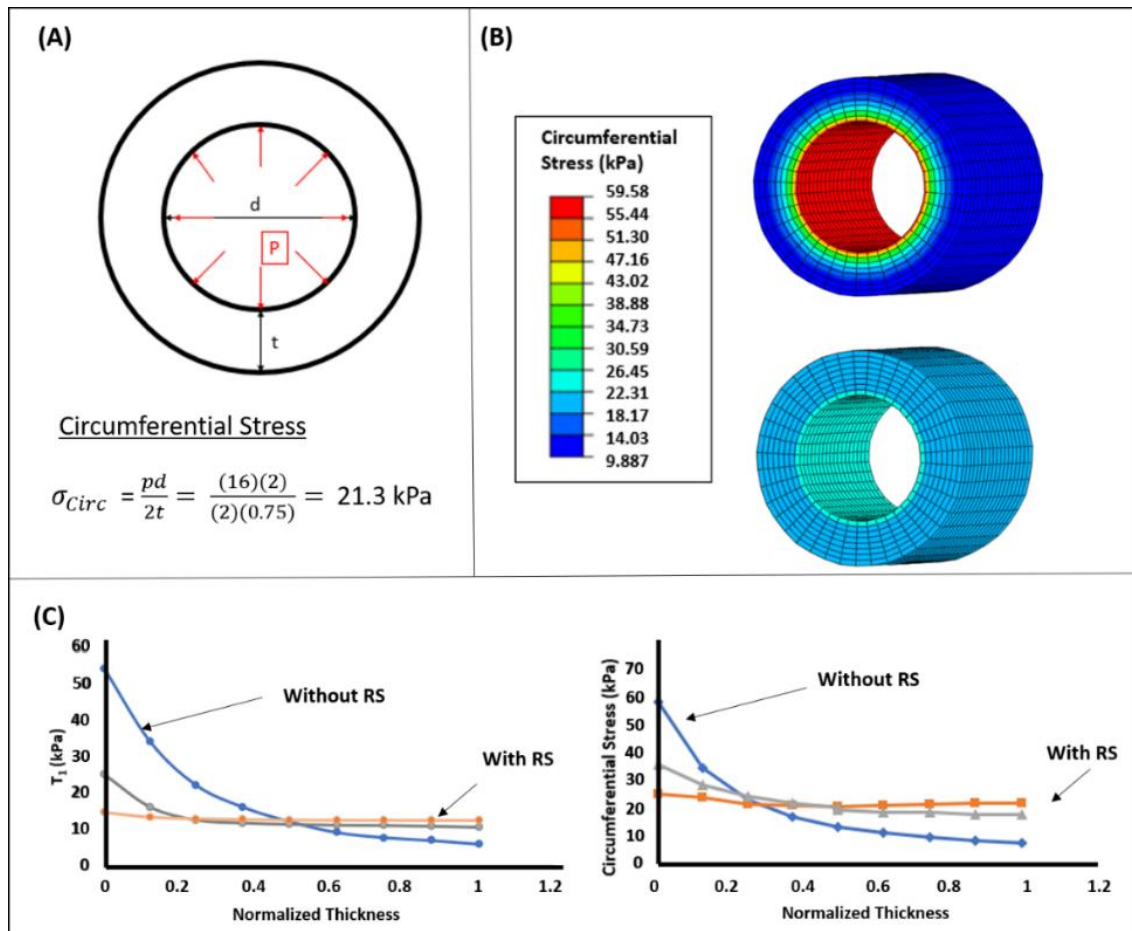
Figure 3.8: Inclusion of residual stresses in a cylindrical model (A) Theoretical calculation of the circumferential stress (B) Circumferential stress contour plots showing (i) without the inclusion of residual stress and (ii) with the inclusion of residual stress (C) (i) Fibre stress T1 (kPa) over the normalized radius (mm) after applying 0,5 and 10 smoothing loops (ii) Impact of inclusion of residual stresses on the maximum principal stress (kPa) after applying 0, 5 and 10 smoothing loops

3.3.3.2 Bifurcation Model

To determine the optimum number of smoothing loops needed for the bifurcation models, the process was extended to include additional smoothing loops until the values of less than 5 kPa is seen in the tensional fibre convergence. The location of interest is the bifurcation apex, where the largest gradient of stress is observed through the vessel wall.
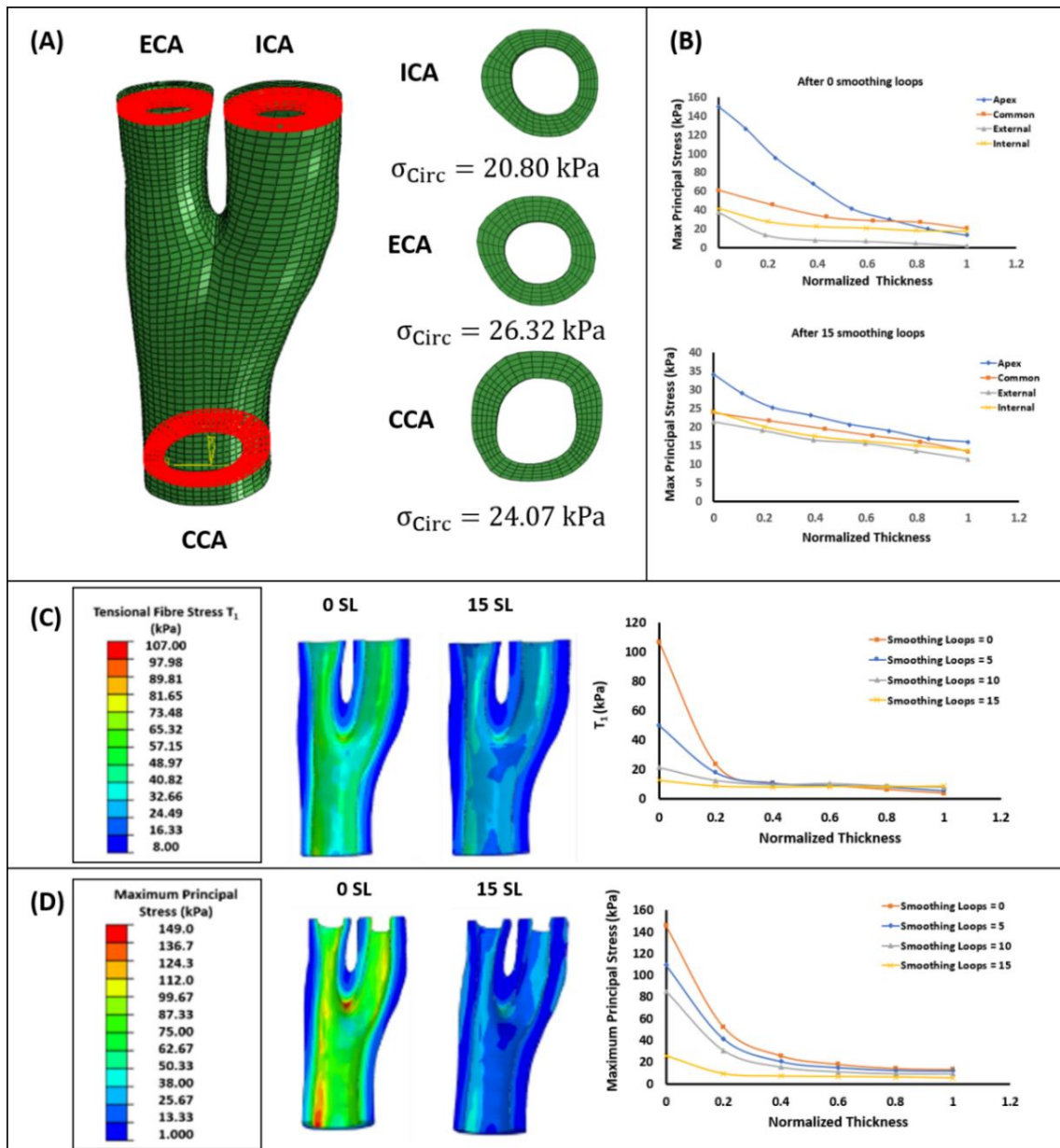
Figure 3.9: (A) Set definition at locations across the bifurcation for theoretical approximation of the circumferential stress (B) Inclusion of the residual stress at the common, external and internal carotid (C) Inclusion of residual stresses in the bifurcation model looking at the Fibre stress T1 (kPa) over the normalized radius (mm) after applying 0,5,10 and 15 smoothing loops (D) Impact of inclusion of residual stresses on the maximum principal stress (kPa) after applying 0,5,10 and 15 smoothing loops

Like the results obtained in the cylinder model. Both the tensional fibre stress T_1 and maximum principal stress gradients decrease when imposing an increased number of smoothing loops, see figure 3.9C and figure 3.9D. The gradient of stress seen initially is considerably larger than the cylindrical model and therefore requires more smoothing loops for the tensional fibre stress to converge to the pre-set criterion. Furthermore, the gradient of stress is preserved from inner to

outer wall, demonstrating the inclusion of the residual stress in the computational models. Again theoretically, the predicted stress at locations such as the common, internal and external carotid are similar to the predicated values after the inclusion of the residual stress, see figure 3.9A and 3.9B.

3.3.4 Estimation of material parameters and calculation of the stress distribution in arterial bifurcations

Presented in figure 3.10 are the results obtained after simulating each case for one geometry. 6 geometries were simulated in total, and the reader is directed to the supplementary documentation provided for the simulation results on the other 5 geometries.

Table 3.5: Implemented material properties after optimization in each case for one geometry.

Parameters	C_{10} (kPa)	k_1 (kPa)	k_2	κ	θ (deg)
Case 1	6.56	1482	561	0.16	37
Case 2	9.36	1639	528	0.16	37
Case 3	6.72	1836.93	817.22	0.13	35
Case 4	11.68	1468.93	512.62	0.23	39
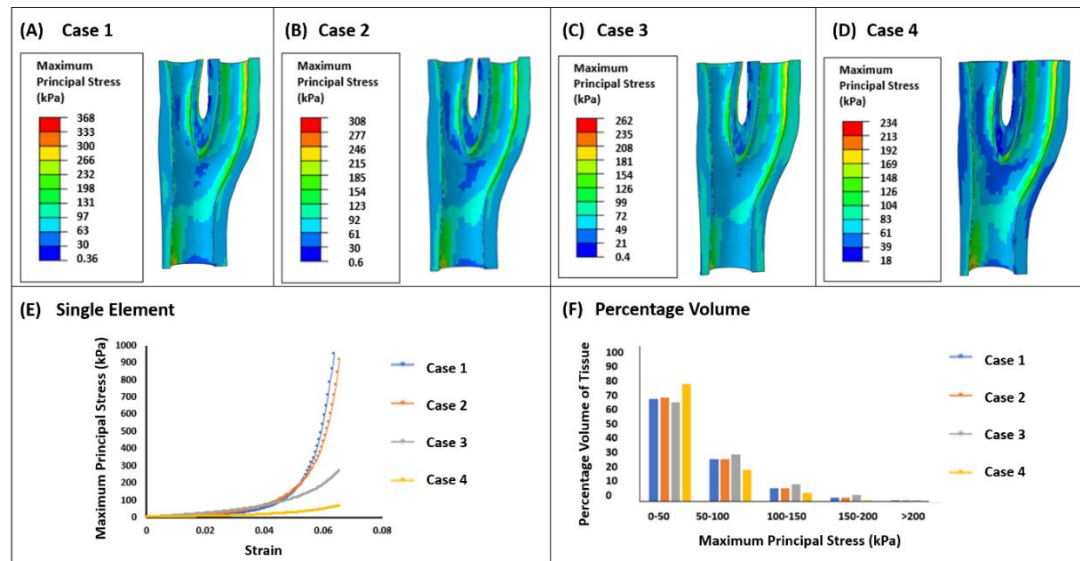
Figure 3.10: (A) Simulated stress result for case 1 (B) Simulated stress result for case 2 (C) Simulated stress result for case 3 (D) Simulated stress result for case 4 (E) Single element test of estimated material parameters under uniaxial tension (F) Percentage of volume graph for the 4 cases showing the stress distribution throughout the vessel wall

Figure 3.10 (A-D) demonstrates that the peak stress values are different in all cases considered. In all models presented here and in the supplementary documentation, the stress is highest with material parameters taken from literature (case 1) and the lowest when taking account of both the

zero-pressure configuration and residual stress (case 4). In case 2 material parameter estimations, the geometry extracted from diastole is attributed literature material parameters that need to be optimized. It is observed that due to the small deformation from diastole to systole that the most significant parameter change comes from C_{10}, which describes the isotropic ground matrix of the tissue and is responsible for its elastic response. In case 3 material parameter estimations, when the zero-pressure configuration of the geometry is incorporated and then loaded to both diastole and systole, due to the greater deformation of the geometry to the desired phases, the material parameters now start to alter more significantly. In this estimation, the parameters C_{10} , k_1 and k_2 differ significantly from the original input parameters. κ and θ alter slightly but not significantly from the original input parameters. In case 4 material parameter estimations, where the zero-pressure configuration and residual stress is included, it is observed that loading this to both diastole and systole, not only do they alter C_{10} , k_1, and k_2 parameters, but also the dispersion parameter κ. These results could be due to the fibres becoming more disperse when residual stress is included, and this ultimately leads to a decrease of the peak stress values observed in all regions of the bifurcation. The single element results shown in Figure 3.10E, highlight the effects of the estimated material parameters with the inclusion of the zero-pressure configuration and residual stress. In all cases, the parameters taken directly from literature show a stiffer response than what is seen when models have optimized patient specific parameters. Furthermore, it is observed that the inclusion of the zero-pressure configuration and residual stress has a distinctly less stiff response. Lastly, the decrease in peak stress values and the stress distribution is further validated by the percentage volume plots, see figure 3.10F. It is observed that there is an increase in the percentage volume of the lower stress value band (0-50kPa) when the zero-pressure configuration and residual stress is included in the model (Case 4), depicting a less stiff response and lower peak stress values when compared to literature parameters (Case 1).

3.4 Discussion

3.4.1 Impact of image axial resolution on the stress calculated in patient specific finite element models of the carotid bifurcation.

As observed in section 3.1 results, the high-resolution model with an "apparent" image slice thickness of 1mm and a total of 24 slices reduced the calculated stress at the apex of the bifurcation models. This agrees with previous research undertaken by Nieuwstadt et al, 2014, by which on a simulated MRI dataset they determined that lower stresses are predicted with higher resolution models [166]. To the authors knowledge, this investigation is the first to look at whether this holds true for *in-vivo* MRI datasets. In terms of the created geometries, convergence of stress values at the bifurcation apex was observed at a mesh density of approximately 250,000 elements. Convergence was deemed enough when the stress values did not differ by more than 5% of the previous value. Interestingly, it was observed that for both the higher and lower

resolution models, convergence is observed at different stress values. This can be solely attributed to the geometries that are created with one being at a higher resolution than the other. A limitation that must be considered is scanning duration, as acquiring a desired high resolution would require longer scan times that is not suitable for clinical practice. Furthermore, longer scan times would also lead to more image artifacts, such as bulk motion that can affect the segmentation accuracy and therefore a compromise must be made. Overall, a robust technique for creating carotid bifurcation geometries from MRI has been established. From segmentation, preparation and meshing, these techniques can be translated to other arterial geometries if required. The sensitivity of stresses calculated is dependent on the resolution of the acquisition that is used; therefore, a higher resolution scan is desirable.

3.4.2   Inclusion of the zero-pressure configuration

Using the method presented in section 3.2.4, the zero-pressure configuration can be extracted for idealized models and arterial bifurcations. For the idealized cylinder model, the robustness of the algorithm was demonstrated by recovering the estimated zero pressure configuration after inputting a known pressure state. The scaling parameter K was optimized at 0.90 to 1 in the idealized case. For the bifurcation models, the algorithm successfully estimated the zero-pressure configuration from geometries at a known phase in the cardiac cycle. Due to the geometry not being idealized, the scaling parameter needed to be optimized to determine the optimum incrementation to be used for robust estimation, and this was observed to be in the region of 0.9 and 0.95 for all geometries tested here, see figure 3.7. It was determined that an incrementation of 0.05 for new guesses of the zero pressure geometry delivered sufficient accuracy and proved to be most time effective for the computational models and is also the incrementation implemented in Raghavan et al, 2006 [18]. Although, it can be suggested that lower incrementations along with higher computational power will be able to perform this analysis. The inclusion of the zero-pressure configuration will alter estimations of stress throughout the vessel wall and compromise the time for the analysis to complete. However, if stress is to be used as a clinical vulnerability indicator, the zero-pressure configuration must be included in the simulation of the arterial bifurcation.

3.4.3   Inclusion of the residual stress

The algorithm presented in this study shows the homogenization of the gradient of stress in the radial direction to represent the presence of residual stress in both the idealized cylinder model and the bifurcation models, see figure 3.8 and 3.9. The idealized cylinder model shows the robustness of this method and can be compared to the 2D simulations in Schroder et al, 2014, where the gradient of stress is homogenized in the radial direction to a reasonable degree after 10 smoothing loops. The circumferential stress values observed through the wall thickness also

falls in the range of the theoretically calculated value of 21.3kPa, further validating its implementation. The method presented here extends the method demonstrated in Schroder et al, 2014 to three-dimensional patient specific models of the carotid bifurcation. Including residual stress into the patient specific bifurcation geometry shows a homogenization of the gradient of stress observed throughout the bifurcation but does not completely remove it. This is noticeably seen at the bifurcation apex, where the highest change in peak stress values occur when residual stress is included. The preservation of this gradient through the thickness is important and observed in the work of Delfino et al, 1999 and Raghavan et al, 2003 to name a few a couple [21,56]. It is important to remember that the residual stress inclusion shown in these studies used the opening angle approach, something that was not used in this implementation. The reason for this is because the opening angle varies through the bifurcation and cannot be quantified *in-vivo*. Therefore, using the approach presented here, the opening angle is neglected, but the residual stress of the vessel can be incorporated in the computational models.

3.4.4 Effect of implemented methods on the estimated material parameters and stress distribution in patient specific finite element models of the carotid bifurcation.

From the results presented here, the estimated material parameters alter with each geometry even without considering both the zero-pressure configuration and residual stress. This is due solely to the fact that the geometries are all different, therefore, validating the need to have patient specific material parameters. Looking at each geometry individually, it is observed that from diastole to systole (Case 2) that changes in the material parameters are mainly governed by the C_{10} parameter, meaning the response is mostly in the low strain region. It is observed when the zero-pressure configuration is included in these estimations, the geometry has to undergo further deformation to reach the diastolic and systolic phases, which effects the overall stress that is calculated. The introduction of the zero-pressure configuration also shows larger changes in the k, k_2 parameters along with an observed change in C_{10}. It can be stated with the inclusion of the zero-pressure configuration that the contribution of the collagen fibres in the stress distribution are now being observed. Lastly, the inclusion of the zero-pressure configuration and residual stress alter the C_{10} , k_1, k_2 and the dispersion parameter κ. Furthermore, the literature and the results presented here shows that the presence of residual stress throughout the arterial wall homogenizes the gradient of stress through the wall thickness. This homogenization effects the parameter estimation and depicts the fibres to be more dispersed, therefore decreasing the overall stress of the model. This decrease in the stress gradient from inner to outer wall is seen in all models that includes the residual stress of the vessel. It is also observed that the maximum principal stress for each model is overestimated when simulated with material parameters taken from the literature as there is a clear decrease in the stress values when the zero-pressure configuration and residual stress are included. This is important as it demonstrates the need for

tailoring the analysis to be patient specific, which in this context means the incorporation of the zero-pressure configuration, residual stress and estimated material parameters in the computational models. Clearly, an overestimation of the stress with literature parameters and exclusion of the zero-pressure configuration and residual stress would lead to a mischaracterization of the vulnerability of the vessel if stress was to be used as a vulnerability measure. Therefore, in order for individually created geometries to be patient specific in this context, the inclusion of the zero-pressure configuration, residual stress and estimated material properties is required.

3.4.5 Limitations

The work presented here shows the impact of excluding the zero-pressure configuration and residual

stresses in the estimation of material parameters and stresses at the carotid bifurcation. The first limitation of the study is that the carotid wall is assumed to be made of one material. This is not the case as arterial tissue is composed of three distinct layers, the tunica intima, the tunica media, and tunica adventitia. All of these layers would independently have their own opening angle and therefore, residual stresses. The protocol for geometry segmentation and meshing has been extended to include the meshing of multiple layers and plaque components and will be future work. The second limitation of the study is exclusion of diseased vessel bifurcations in the analysis of the effect of the zero-pressure configuration and residual stresses. Although the residual stress does not have a major influence in atherosclerotic plaque tissue, the exclusion of the residual stress from the vessel wall with plaque tissue may alter the calculated stress values. The reason for this is because if you consider plaque tissue and the vessel wall to be separate entities, the role of residual stress can be quite different. As stated before, the general procedure to quantify the amount of residual stress in the vessel wall is via the opening angle experiment, whereby once axially cut the vessel springs open releasing the strain energy within the tissue. However, when the same is done for atherosclerotic plaque tissue this springing open of the tissue does not occur, suggesting no residual stress is present. For this reason and for accurate simulation, it is important to take out the plaque, include the residual stress in the vessel wall and re-incorporate the plaque back into the model. Lastly, the angle of fibres does not show considerable change in all estimations undertaken here. This could be from the fact that different ranges of axial strain were not implemented in the material parameter estimation and kept constant for all models. It is expected that if higher levels of axial strain are imposed, the angle of fibres would alter and will start to play a more significant role in the stress distribution and peak stress values.

Chapter 4 An investigation into the critical role of fibre orientation in the ultimate tensile strength and stiffness of human carotid plaque caps

4.1 Introduction

The development and subsequent rupture of atherosclerotic plaques in human carotid arteries is a major cause of ischaemic stroke. Mechanical characterization of atherosclerotic plaques can aid understanding of plaque rupture risk. Despite this however, experimental studies on human atherosclerotic carotid plaques, and fibrous plaque caps in particular, are very limited. This study aims to provide further insights into atherosclerotic plaque rupture by mechanically testing human fibrous plaque caps, the region of the atherosclerotic lesion most often attributed the highest risk of rupture. The results obtained highlight the variability in the ultimate tensile stress, strain and stiffness experienced in atherosclerotic plaque caps. By pre-screening all samples using small angle light scattering (SALS) to determine the dominant fibre direction in the tissue, along with supporting histological analysis, this work suggests that the collagen fibre alignment in the circumferential direction plays the most dominant role for determining plaque structural stability. The work presented in this study could provide the basis for new diagnostic approaches to be developed, which non-invasively identify carotid plaques at greatest risk of rupture.

4.2 Methods

4.2.1 Sample preparation

Carotid plaque specimens were obtained from 20 symptomatic carotid endarterectomy (CEA) patients at St James Hospital Dublin. These patients were aged from between 50 and 85 years of age and had been diagnosed with a percent stenosis of greater than 50%. Ethical approval for obtaining the plaques in this study was obtained from St. James Hospital ethical committee in compliance with the declaration of Helsinki. These carotid plaque specimens were firstly washed in phosphate-buffered saline (PBS) to remove residual blood and then stored in tissue-freezing medium (RPMI-60 Media, 1.8 M DMSO; and 0.1 M sucrose), placed into a Mr. Frosty cryosystem containing 2-proponol and cryopreserved at −80 °C until the day of testing. Cryopreservation has been shown to have a nonsignificant effect on the tissue and there- fore is the method of storage. On the day of testing, samples were defrosted in PBS at ambient temperature and then sectioned as shown in Fig. 4.1. The location of the plaque cap was first located by finding the location of high stenosis and observing where the cap was covering over a lipid core region. The plaque cap was carefully delineated and dissected up to the plaque shoulders by using tweezers, as shown in Fig. 4.1 A. Plaque cap samples were dissected to yield

circumferential strip samples with a 4:1 (length: width) ratio, as recommended in [26]. Furthermore, dimensions of each plaque cap were recorded (width and thickness) using a light microscope. The plaque cap was first placed on a glass slide on the stage of the microscope and brought into focus, by which the stage was then moved using two digital micrometres that allow for measurements to be recorded. For thickness measurements, the sample was orientated on its side. Three measurements were taken, and the mean width and thickness were used for calculation of the cross-sectional area. For accurate analysis of UT stress, UT strain and stiffness, only samples that failed in the centre were included. To prevent sample slippage, Velcro was used on the grips.
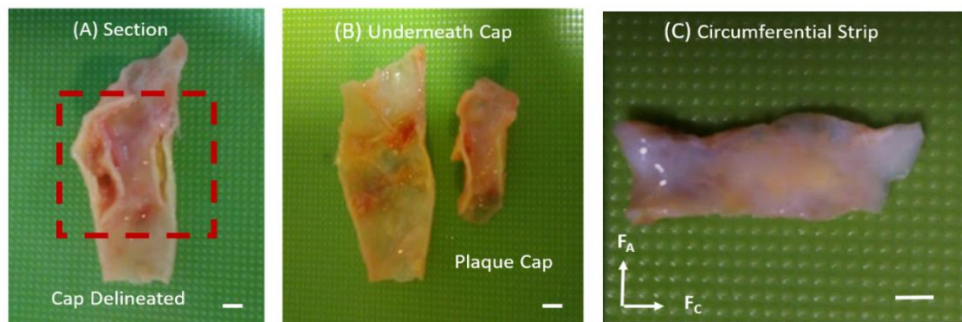
Figure 4.1: (A) Section of atherosclerotic plaque - Red box indicates the delineation of the fibrous plaque cap from the underlying tissue. (B) Separated plaque cap and underlying tissue (C) Circumferential strip sample of the atherosclerotic plaque cap; scalebar = 1 mm. The circumferential direction is in the same direction as F_C.

4.2.2 Small Angle Light Scattering (SALS)

Using an in-house SALS system [32], the dominant fibre orientation of these excised atherosclerotic plaque cap test specimens could be determined before testing. Using a purpose-built MATLAB (MathWorks, Cambridge, UK) code allowing for the pre-dominant direction to be determined, the centroid of the scattered light pat- tern was established before cycling through all angles from 1 to 360, computing the light intensity at each angle. In SALS, the light is scattered perpendicular to the dominant fibre direction. Placing the sample on a glass slide within the SALS system, raster scanning was performed over a set region of interest and the dominant direction in each region was established. The scattered light profile can either be an elliptical shape if a dominant direction is observed or a circular shape if no dominant direction is observed. This is described by the eccentricity (E), which provides the light distribution at a given interrogation point as a ratio based on the major and minor axes, i.e.

$$E = 2 \frac{\sqrt{\left(\frac{\text{Major Axis}}{2}\right)^2 - \left(\frac{\text{Minor Axis}}{2}\right)^2}}{\text{Major Axis}} \qquad (4.1)$$

An eccentricity of 1 corresponds to perfect fibre alignment in one dominant direction, while an eccentricity of 0 corresponds to an isotropic distribution of fibres [32], see Fig. 4.2 . During the pre-screening procedure and due to the variable sample sizes, a 3 mm x 1 mm region of interest was selected in the centre of each sample, with the SALS resolution being set at 0.25 mm x 0.25 mm, thereby allowing a more accurate determination of the dominant fibre direction in the sample in the location of expected failure. After analysis, each sample was then characterized by its dominant fibre orientation, whereby a predominantly axial fibre orientation (F_A) had fibres perpendicular to the direction of loading (θ from 45 °to 90 °and −45 °to −90 °) and a predominately circumferential fibre orientation (F_C) had fibres parallel to the direction of loading (θ from 0 °to ±45 °).
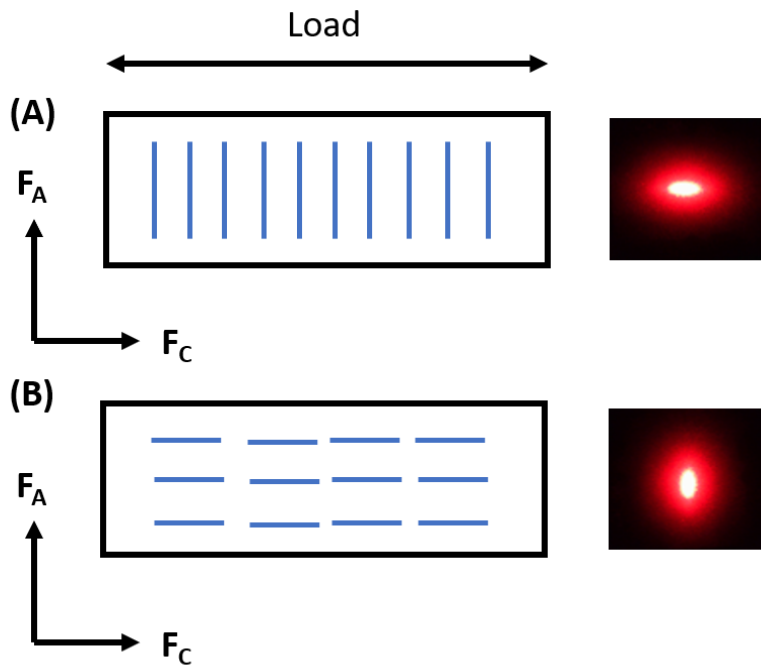
Figure 4.2: Schematic illustration of the specimen fibre orientation and the resulting scattered ellipse. (A) Fibres in predominantly axial direction (F_A). (B) Fibres in predominantly circumferential direction (F_C).

4.2.3 DIC and mechanical testing

Uniaxial tensile tests to complete failure were performed using a uniaxial test machine (Zwick Z005, Zwick GmbH & Co. Ulm, Germany). All tests were performed in a water bath of PBS solution at 37 °C, to simulate the physiological environment. The testing procedure was similar

to that outlined in Ghasemi et al. [16], whereby, a sequence of cyclic loading steps was imposed on the tissue at a constant displacement rate (30 mm/min) with strain limits set for each loading step (10%, 20% and 30%). This displacement rate allowed for easy matching of the DIC acquisition time to the zwick testing time. Preload was set to be at 0.01 N to remove any slack in the tissue before preconditioning and testing and was subsequently zeroed before testing began. Five preconditioning cycles at 10% strain were performed before the loading steps to remove viscoelastic effects in the tissue. None of the samples included in this analysis failed in preconditioning. Digital Image Correlation (DIC) was used to track local strain deformations in the area of failure during testing and was set to a region of 12mm^2. Furthermore, the DIC was set up to record the entire experiment at a rate of two frames per second. Cameras were calibrated and focused before data acquisition to ensure robust results are obtained. A stochastic pattern was applied using spray paint which allowed displacement of the tissue to be tracked, see Fig. 4.3 . Loading continued in each sample until failure of the tissue occurred and the final force-deformation cycle prior to failure was evaluated to establish the stress-strain behaviour of the samples. Only samples that failed approximately in the centre of the sample were considered for analysis to ensure only robust ultimate tensile stress, strain and stiffness measures were obtained. Ultimate tensile stress and ultimate tensile strain values were then extracted at the point of failure of the sample. Stiffness (E) was also calculated for each sample by taking 10 data points and calculating the slope of the final linear region observed in the stress-strain curves but ending before the final 20% of the curve to ensure consistency across samples [33].
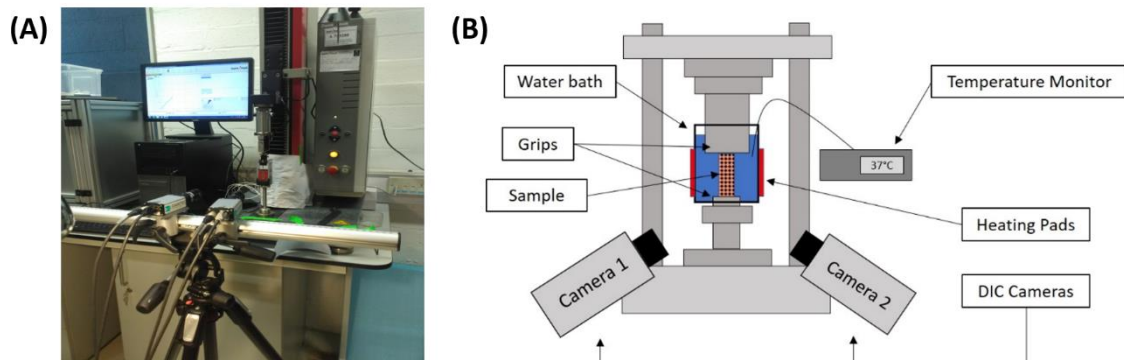
Figure 4.3: (A) Experimental setup as seen in the lab (B) Schematic showing the experimental setup used for the uniaxial tensile tests.

4.2.4 Histology

The use of histology with certain tissue stains such as Haematoxylin and Eosin (H&E) and Picrosirius red (PSR) enables quantitative analysis of the tissue microstructure along with microscopy techniques such as polarized light microscopy (PLM) which can extract information

on the collagen content and collagen fibre orientation [27,30,167]. After testing, carotid plaque cap samples were fixed in 10% formalin at 4 °C for 24 h. The samples were then dehydrated (Leica TP1020, Semi-enclosed benchtop tissue processor, Germany) and embedded in paraffin wax blocks. Following this, 8 μm cross sections were cut from the paraffin blocks using C35 microtome blades and floated on distilled water at 37 °C before being mounted on glass slides. The slides were left to dry overnight. Staining of the samples was done by using a Leica Autostainer (Leica ST5010, Autostainer XL, Germany), that incorporated the de- paraffinization and rehydration of the samples. Slides were stained with PSR to visualize and quantify the collagen fibre alignment and collagen content [168]. Once stained, the slides were imaged using a brightfield and polarized light microscope (Leica, Wetzlar, Germany) at a range of magnifications (2x and 4x) to allow for detailed analysis. The results for both content and the orientation analysis were determined from an average across two sections taken through the thickness of each sample.

4.2.5   Content analysis

To determine the content of collagen within tissue samples, post-processing of the PSR stained tissue sections was performed. Content was determined based on the fractional area of birefringence observed. Firstly, an image of the tissue sample was collected in brightfield and the total tissue area was measured. The same slide was then examined with polarized light and an im- age was collected and binarized, see Fig. 4.4. This binarization was kept at a constant value (0.2) for all images as it was sufficient to remove the background and highlight areas in the polarized light to be just collagen. The collagen content of the sample was then calculated from comparing the birefringent area to the total tissue area [27].

$$\text{Collagen Content (\%)} = \frac{\text{Collagen Area}}{\text{Tissue Area}} \times 100 \qquad (4.2)$$

4.2.6   Orientation analysis

For collagen fibre orientation assessment via histology, the method used was similar to that reported in Douglas et al. [29]. A canny edge detection filter was used to isolate the collagen fibres in the image. The filter was applied both horizontally and vertically to remove any noise or speckles in the image and thresholds were set so any small components were removed. Connected adjacent pixels were then found using the *regionprops function* in MATLAB. Delineated fibres containing less than eight or fewer connected pixels were removed, as they were deemed too small to give robust fibre properties [29]. Following this, the code MatFiber

[167] was used to determine the mean fibre angle across the sample. The process for content and orientation analysis is summarized in the workflow illustrated in Fig. 4.4.
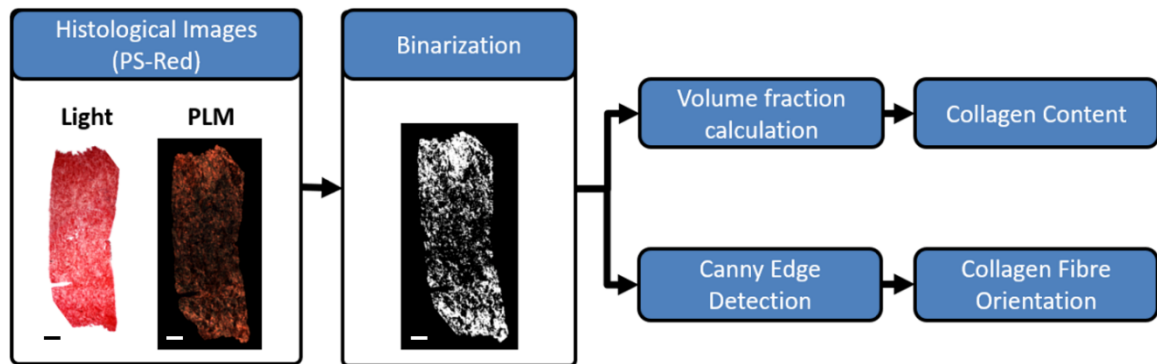
Figure 4.4: Workflow of processing from histological images to obtain both the collagen content and fibre orientation of atherosclerotic plaque caps; scalebar = 1 mm.

4.2.7 Statistical analysis

Statistical analysis was performed with Prism 8 statistical software (GraphPad Software Inc., San Diego, California) and the data for the ultimate tensile (UT) stress, UT strain, stiffness and collagen content were grouped according to the SALS data. Two-tailed unpaired t-tests using Welch's correction were performed on the UT stress, UT strain, stiffness and collagen content values to investigate statistical significance (i.e., $p < 0.05$) between the predominately axial fibre datasets and predominately circumferential fibre datasets due to the uneven sample sizes in each group.

4.3 Results

4.3.1 Width and thickness measurements across atherosclerotic plaques

Three width and thickness measurements were recorded for all atherosclerotic plaque cap samples that underwent testing and are presented in Fig. 4.5. Plotted as mean and standard deviation for each, every individual point corresponds to one measurement. Overall, the width of these samples is in the range of 2.52 mm ± 0.58 mm and the thickness of these samples is in the range 0.54mm ± 0.11 mm, showing the thickness of the plaque cap varies within and between samples, and that this can be attributed to the heterogeneity of the tissue.
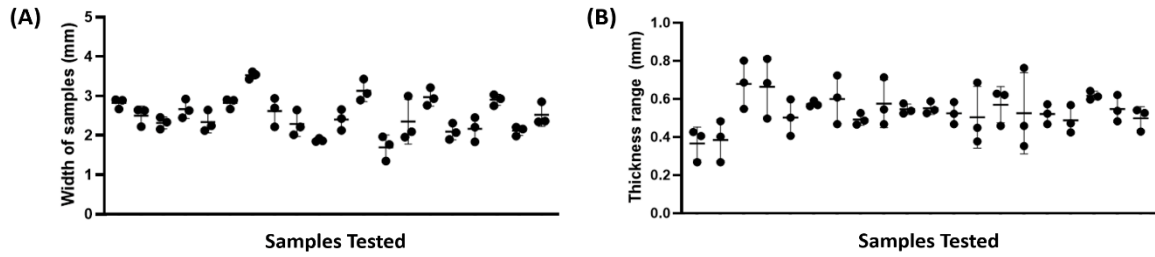
Figure 4.5: (A) Width measurements taken across the atherosclerotic plaque cap samples tested (B) Thickness measurements taken across the atherosclerotic plaque cap samples tested. Plots detail the mean and standard deviation of the measurements taken.

4.3.2 Dominant collagen fibre orientation in carotid plaque caps using SALS.

The mean fibre angle (θ) and standard deviation within samples was determined using SALS and is shown in the order in which samples were tested in Fig. 4.6, where considerable variation in the dominant fibre angle is evident across these plaques harvested from different patients. The samples were therefore grouped in terms of their dominant fibre direction, whereby, predominantly axial fibre orientation (F_A) samples are those where fibre angles, θ from $\pm45°$ to $\pm90°$, and predominantly circumferential fibre orientation (F_C) samples have fibre angles, θ from $0°$ to $\pm 45°$. After determining the respective groupings, a total number of 12 samples with predominately axial fibre orientation and 8 samples with predominately circumferential fibre orientation. Fig. 4.7A and 4.7B show both the SALS eccentricity plots and fibre (elevation) angle distributions for all samples, detailing the sample-to-sample variation in eccentricity values and fibre distributions. The elevation angle is an angular measurement in a spherical coordinate system whereby, for this analysis, an elevation angle at $0°$ corresponds to the circumferential direction and $\pm 90°$ corresponds to the axial direction.
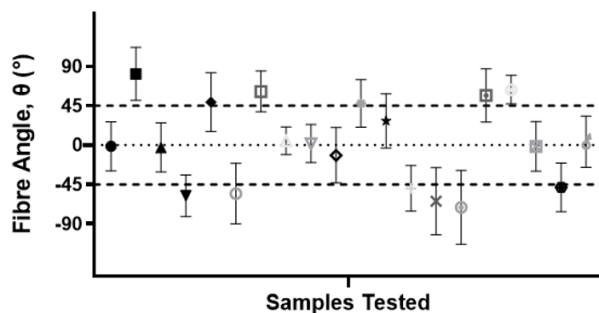
Figure 4.6: Mean Fibre Angle, θ, and standard deviation obtained from samples in the order of testing. Samples where θ is from $\pm 45°$ to $\pm 90°$ are denoted as samples with predominantly axial fibres (F_A) and those with , θ from $0°$ to $\pm 45°$ are denoted as having predominantly circumferential fibres (F_C). Each datapoint is one sample.
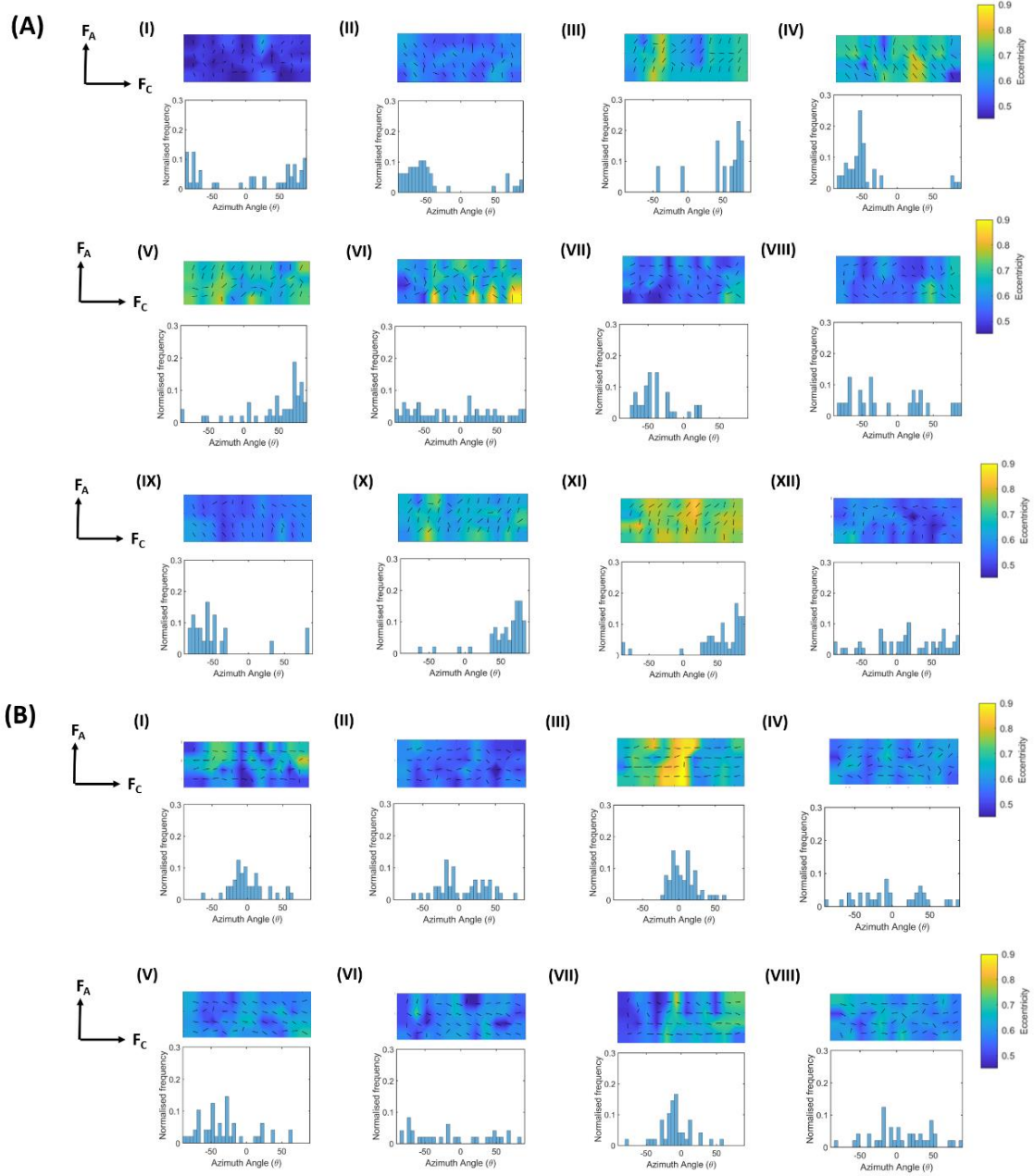
Figure 4.7: SALS eccentricity plots and histograms displaying fibre angle distributions after grouping into (A) predominantly axial fibre dataset (F$_A$) and (B) predominantly circumferential fibre dataset (F$_C$).

4.3.3   Ultimate tensile strength of carotid plaque caps

Data presented here are from samples that failed in the centre of the tissue sample, with a representative sample shown in Fig. 4.9. Stress-strain curves for all samples demonstrated the characteristic non-linear J-shaped curves typical of vascular tissue (Fig. 4.10 A and 4.10 B). Engineering stress was calculated using the Zwick force divided by the original cross-sectional area and engineering strain was calculated using the DIC. Figure 4.8 shows the step-by-step process of a representative sample that has been analysed using DIC. Figure 4.8A shows the speckle pattern and the region of interest selected for data extraction. In this set region, the average value of engineering strain across the tissue is calculated and the stress strain curves are corrected with the engineering strain measured from DIC. Figure 4.8B shows the strain experienced in the atherosclerotic plaque sample after preconditioning while figure 4.8C shows the strain experienced in atherosclerotic plaque sample just before failure. As observed in figure 4.8C, high strains (red) are observed in the failure location.
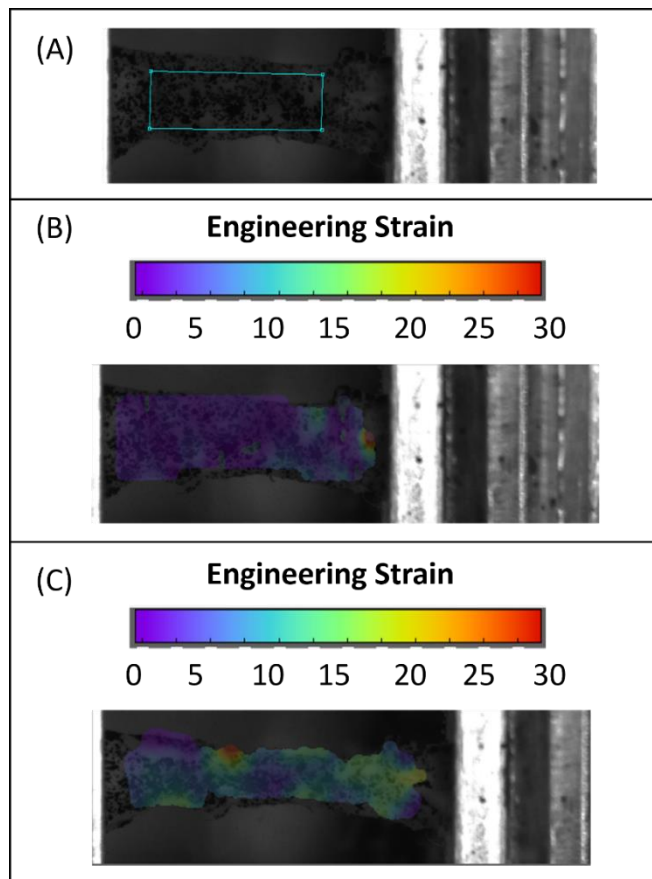
Figure 4.8 Representative example of an atherosclerotic plaque sample analysed with DIC (A) DIC view of the atherosclerotic plaque sample with speckle pattern and region of interest set for calculation of the engineering strain in region, (B) Sample at start of test, (C) Sample just before point of rupture where peak strain (red) is evident at the location of rupture

To observe the effect of fibre orientation, the uniaxial test results were again grouped according to the predominant fibre direction, namely axial fibres and circumferential fibres based on the SALS results, see Fig. 4.10A and 4.10B, respectively. Fig. 4.10 C–E demonstrate significantly different results between the samples with predominantly axial and circumferential fibres for UT stress, strain and stiffness. The mean UT strain is significantly higher (0.13 ± 0.04 versus 0.09 ± 0.04), and mean UT stress significantly lower (0.31 ± 0.18 MPa versus 0.87 ± 0.63 MPa) in predominately axial fibre datasets, whilst the mean stiffness of samples with predominately axial fibres is also considerably lower than samples with predominately circumferential fibres (0.05 ± 0.03 MPa versus 0.19 ± 0.07 MPa), see Fig. 4.10E.
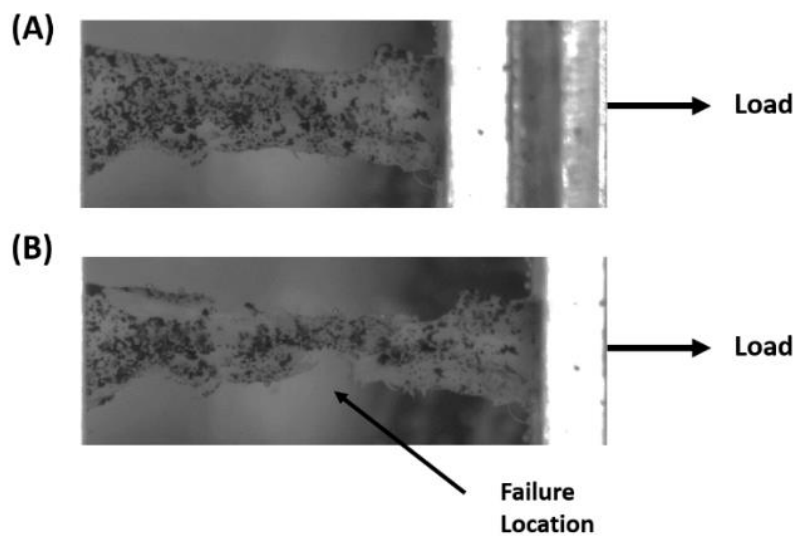
Figure 4.9: DIC view of plaque cap with speckle pattern undergoing uniaxial test showing (A) initial sample setup and (B) failure at centre of sample.
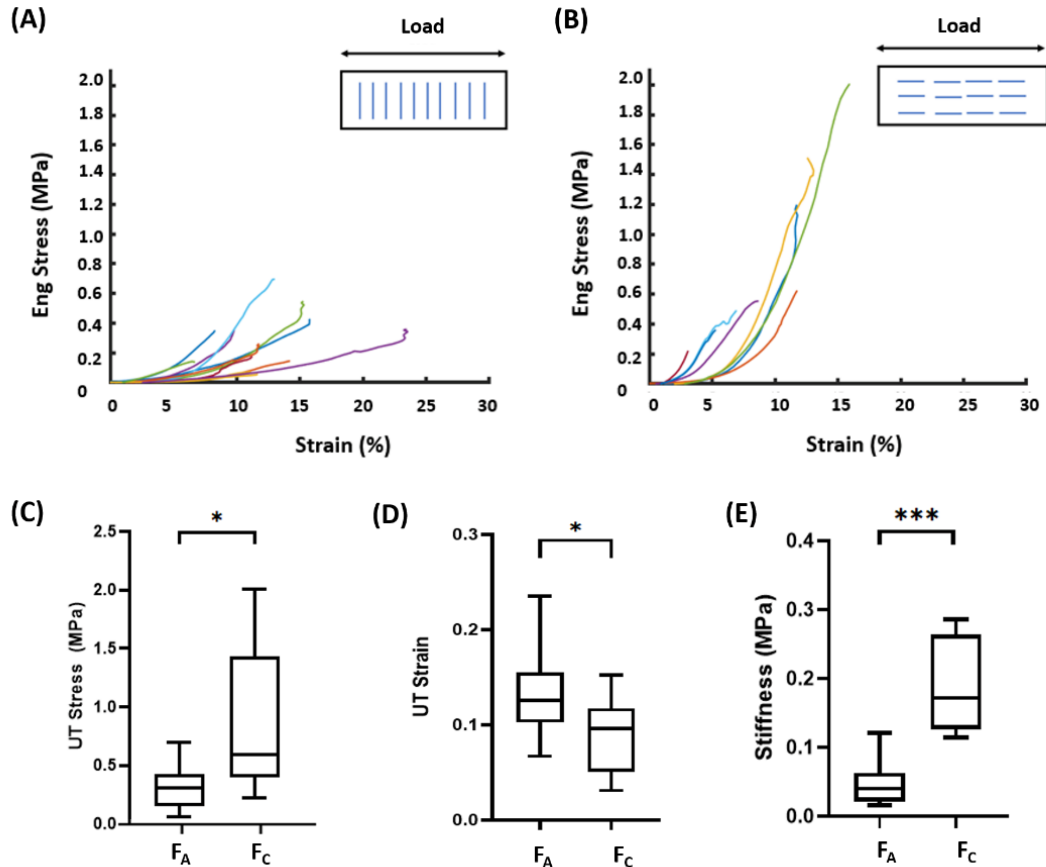
Figure 4.10: Engineering stress-strain curves for A) predominantly axial fibre datasets (F_A) and (B) predominantly circumferential fibre datasets (F_C). Statistical analysis detailing the significant difference between (C) Ultimate tensile stress, (D) Ultimate tensile strain and (E) Stiffness between the groupings, $*p < 0.05$, $***p < 0.0005$.

4.3.4 Histological analysis of carotid plaque caps

4.3.4.1 Histological evaluation of collagen fibre orientation and content in atherosclerotic plaque cap samples.

Fig. 4.11A shows output images from both the light and polarized light and after histological analysis (content and orientations). Collagen content for samples with fibres predominantly in the axial direction was found to have a wider range of content values when compared to samples with predominantly circumferential fibres, see Fig. 4.11C. No significant difference in collagen content was identified between the datasets, however, suggesting that collagen content does not play a significant role in determining the UT stress, UT strain and stiffness of the tissue. From these results, it is shown that the histological fibre angle, shown in Fig. 4.11B is quite different to the SALS fibre angles shown in Fig. 4.6. A Pearson correlation analysis performed between the two datasets, however, showed a good degree of correlation between the SALS fibre angle measurements and the histological fibre angle calculated, with an $R^2 = 0.61$, see Fig. 4.11D.

Whilst SALS obtains an average fibre angle from the laser light passing through the tissue prior to testing, histology is performed on only a limited number of thin sections of the tissue and it is also performed after mechanical testing. In addition, histology requires a number of processing steps before final analysis which can induce sample shrinkage. The process also relies on obtaining a flat cross section of tissue during sectioning to ensure robust fibre angle calculations. Fig. 4.12A and 4.12B show a poor correlation between collagen content and UT stress ($R^2 = -0.02$) and UT strain ($R^2 = 0.02$), respectively. These findings are independent of fibre orientation.
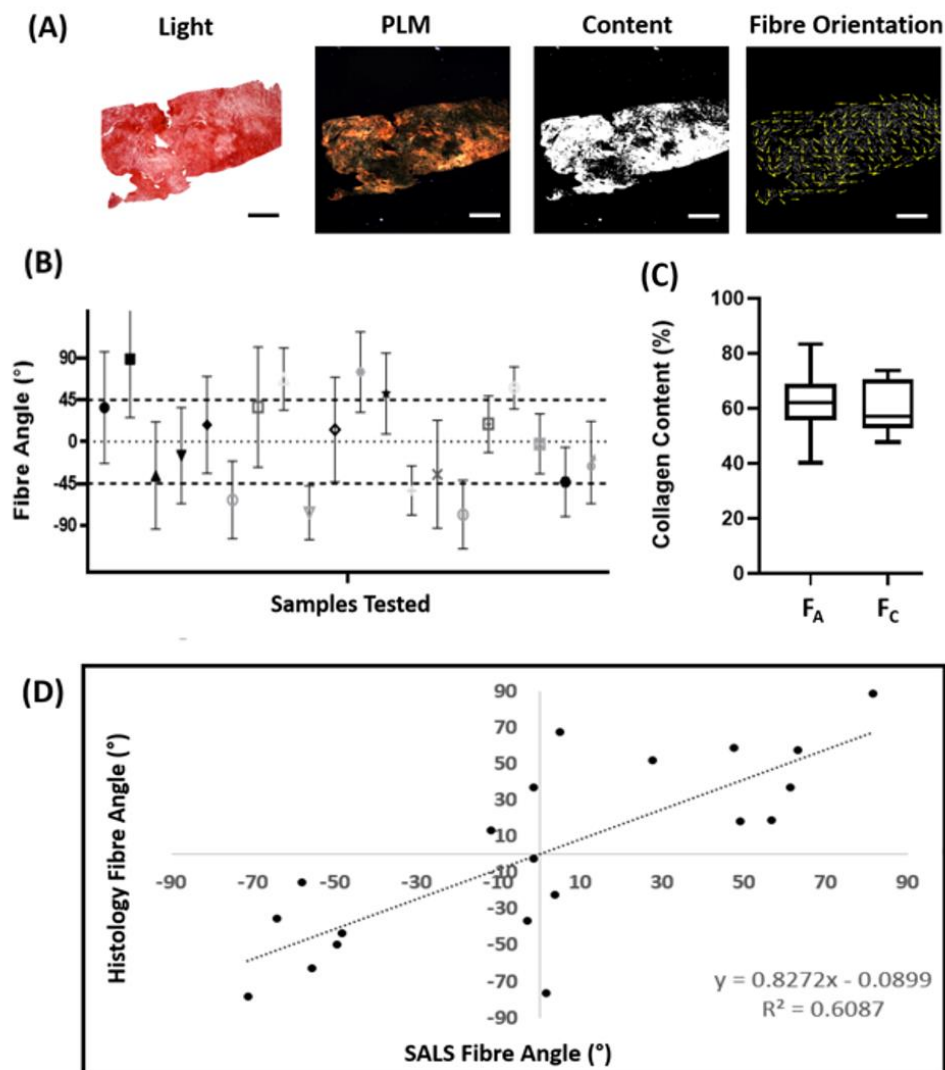
Figure 4.11: (A) Representative images detailing the post-processing of tested plaque cap tissue after histological staining with PSR; scalebar = 1 mm. (B) Mean fibre angle and standard deviation extracted from samples in the order of testing. (C) Collagen content comparing the predominately axial fibre group and predominately circumferential group. (D) Pearson correlation test between SALS fibre angle and calculated fibre angle from histology.
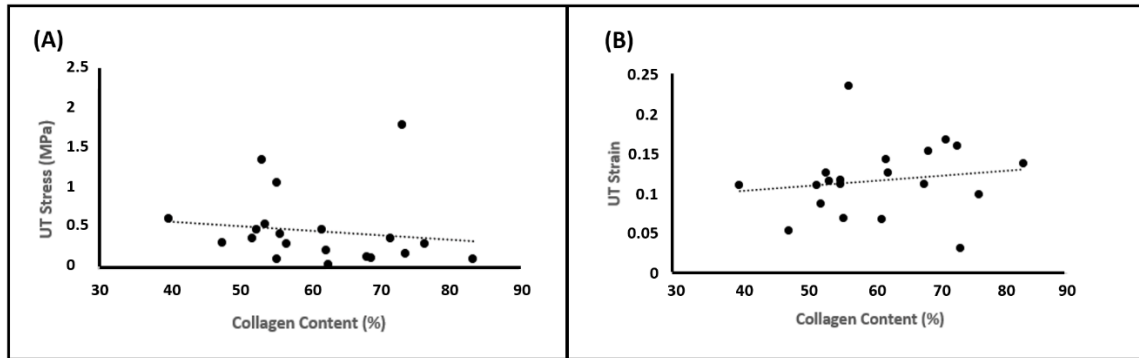
Figure 4.12: Correlation plots for (A) collagen content and ultimate tensile stress and (B) collagen content and ultimate tensile strain, when not considering fibre angle groupings.

4.4 Discussion

The highly variable nature of the mechanical properties of atherosclerotic plaques has been observed in these samples, validating the observations seen in previous studies. Throughout the study, SALS was used as a pre-screening tool to determine the dominant fibre orientation of these samples, thereby determining the anisotropic nature of the atherosclerotic plaque cap. The eccentricity in these samples was low at approximately 0.6 (Fig. 4.7) which would suggest that whilst the cap has an anisotropic collagen structure, it may not be coherently aligned in a particular direction. Thickness variability in the samples can also contribute to this low SALS eccentricity measure. Despite the eccentricity values, once samples were grouped based on SALS fibre angle measurements into those with predominantly axial fibres and predominantly circumferential fibres, these results demonstrate that the orientation of the collagen fibres in the plaque caps plays a significant role in determining the ultimate tensile strength and strain in the plaque caps. The plaque caps with predominantly circumferential fibres demonstrate superior load bearing capacity with higher stresses borne before failure when compared to the predominantly axially aligned fibre samples. It is important to note that throughout the preconditioning phase of the test, there was no evidence of failure or micro-failure in the samples. Whilst it is possible that micro failures could go undetected, it is worth noting that the preconditioning strain level was lower than the strain at which ultimate failure was observed in all samples. When comparing the SALS fibre angle to the histology fibre angle, there can be a huge variation in the fibre angle observed. Although this may suggest a significant methodological issue, its moreover a limitation of histological analysis. The SALS fibre angle is measured as an average through the thickness of the tissue whilst the histology fibre angle is the average angle from 3 cross-sections across the thickness. Interestingly, the histological results suggest that collagen content alone does not play a dominant role in the strength and stability of atherosclerotic plaque cap tissue given that no significant difference was observed in collagen

content between the two plaque cap groupings. Furthermore, when looking at the correlation of collagen content to the ultimate tensile stress and strain, independent of groupings, there is not a correlation between the collagen content and ultimate tensile stress and strain, suggesting that collagen content alone does not play a significant a role in the load bearing capacity of the tissue. A particularly interesting finding from this work is the failure of samples with fibres in predominantly the axial direction at lower UT stress and higher strains than the samples with a predominantly circumferential fibre arrangement. This key finding offers potential mechanistic insight into the results demonstrated in previous in vivo imaging studies such as Huang et al. [146], where vulnerable plaques were found to have a higher maximum value of absolute strain rate from diastole to systole. Without knowing the mechanical structure of the plaque and vessels in the Huang et al. [146] study, the results here would suggest that these vulnerable plaques could possibly have fibres more axially aligned which would consequently fail at lower UTS and thereby make them more vulnerable to rupture. This hypothesis clearly warrants further investigation using in vivo imaging studies on potentially vulnerable plaques, but it could possibly open up new diagnostic techniques with a clear mechanical origin. Finally, as outlined in Davis et al. [27], the use of stress as a rupture metric, as used in many computational studies [87,169], may not be the most appropriate mechanical measure to use when trying to determine plaque rupture vulnerability. This is since plaque caps with collagen orientated in the dominant load bearing direction can withstand higher stresses, however, without this microstructural insight, the stress alone does not offer a robust rupture index, especially as this study highlights that collagen content alone does not correlate with the UT stress and UT strain. Stress can only act as a true rupture measure when it can be determined accurately and compared to a known tissue rupture strength. In contrast, tissue strain measures may offer insights into the underlying microstructure, particularly when considered in the context of the data presented here where higher strains are consistently associated with tissue of lower fracture strength. Characterizing locations across a plaque cap where the deformation of the tissue is increased compared to normal arterial deformation values would suggest microstructural changes to the tissue and overall structural weakness. Furthermore, the current study addresses the limitations stated in Davis et al. [27] and includes the fracture behaviour of fibrous plaques with respect to their underlying fibre orientation, finding that plaque caps with axially aligned fibres would strain more and fail at lower UT stress. Whilst this study provides critical new insights into the mechanical behaviour of atherosclerotic plaque caps, there are some limitations in the study; firstly, only fibrous plaque caps were tested and other components that could contribute to the overall mechanical response of the plaque were not considered here. Akyildiz et al. [38] demonstrated using ex-vivo MRI that the fibre orientation varies throughout an atherosclerotic plaque, and that pre-screening and subsequent testing of entire atherosclerotic plaque specimens should be explored as this can provide further insight into the mechanical strength of the plaque and the importance of collagen

fibre orientation within them. Furthermore, using other novel imaging methods, such as polarization-sensitive optical coherence tomography demonstrated Nadkarni et al. [170], it would be possible to quantify both the collagen fibre orientation and collagen content with corresponding mechanical data similar to the methods in this study and further validate these observations. Calcifications can lead to localized stress concentrations and can even potentially alter the fibre orientation within the plaque cap [171,172] and would therefore be of interest in future investigations. Secondly, plaque caps were only tested in the circumferential direction due to the challenge of working with such small tissue explants, however additional axial or biaxial loading may provide further insight into the mechanical response of the tissue. Lastly, the influence of macrophages was not investigated in this study. Macrophages are known to infiltrate the plaque cap during inflammation and can potentially degrade the matrix of the tissue, thereby weakening the mechanical integrity of the plaque [173]. Whilst macrophage content was not directly explored, the influence of matrix degradation was investigated by quantifying collagen content within the plaques.

4.5 Conclusion

Carotid plaque cap rupture is a local mechanical event in the vessel wall, whereby the stress exerted on the plaque exceeds its mechanical strength causing it to rupture. Parameters such as the percent stenosis do not provide robust metrics for determining plaque vulnerability especially for lower grades of stenosis as they do not consider the underlying mechanical strength of the plaque tissue. The current study demonstrates that the mechanical integrity of the plaque cap is governed by collagen fibres and that collagen content alone may not be a robust predictor of plaque rupture. The critical role of collagen fibre orientation relative to the dominant loading direction in the vessel shows, that for maximum strength, collagen fibres should be in the load bearing circumferential direction. When collagen fibres are predominantly in the circumferential direction, the tissue exhibits a higher ultimate tensile strength and overall stiffer behaviour with lower strains, as compared to plaque tissue with collagen fibres orientated in a predominantly axial direction. This is important as being able to characterize the strain, using *in-vivo* imaging techniques, could potentially aid in the identification of fibre orientations and the overall mechanical strength of the tissue and thereby offer a more mechanistic basis for a clinical indicator of carotid plaque rupture risk.

Chapter 5 A computational investigation to establish a sensitive plaque rupture vulnerability measure using patient specific finite element models informed by *ex-vivo* diffusion tensor imaging and mechanical data.

5.1 Introduction

The collagen fibres are known to be the major load bearing component within the arterial vessel wall and atherosclerotic plaques. It has been established that the orientation of these collagen fibres significantly determines the overall mechanical response of the tissue. Atherosclerotic plaque tissue is known to be heterogenous in nature and comprises of many components such as the fibrotic media, plaque cap, calcification and the lipid pool, all of which contribute to the tissues overall mechanical response. Patient specific finite element (FE) models have the capability to estimate the stresses and strains that the tissue is experiencing *in-vivo* and allows for the development of new diagnostic measures that are able to characterize structural weaknesses within the vessel. In this study, the aim is to investigate the role of fibre orientation in the mechanical strength of atherosclerotic plaques. By assessing the influence of changing the directionality of the fibres on observed computational results, the focus here is to establish a novel indicator to characterize how far the fibres are from the optimal load bearing configuration within the tissue. Due to computational complexity and the aim of this study, the methods established in chapter 3 of this thesis were excluded in this analysis. Firstly, volunteers and patients were scanned using *in-vivo* MRI to establish both the structure of the vessel wall and atherosclerotic plaque and allow for patient specific geometries to be created from these scans. In order to establish the dominant fibre orientation within these atherosclerotic plaques, *ex-vivo* diffusion tensor imaging (DTI) was performed, and the dominant fibre angle was then used to inform the FE models. These imaged atherosclerotic plaques were then uniaxially tested to establish the mechanical behaviour of the tissues. Lastly, a local stress modulated remodelling algorithm is proposed to characterize the mechanical response of the tissue to the re-orientation of collagen fibres. It is suggested that arterial tissue should have its optimum stiffness and strength when the collagen fibres are aligned in the optimum configuration established from the ratio of the maximum and intermediate principal stresses. The continuum damage model (CDM) implemented here establishes a novel remodelling metric (RM) which characterises how far the fibre distribution is from the optimum distribution for the fibres to have their maximum strength. A fibre distribution which is far from the optimum distribution results in a weaker mechanical structure and in the vessel wall this can increase the possibility of atherosclerotic plaque rupture.

The results presented here initially highlight the variability in the mechanical responses of atherosclerotic plaque tissue, which can be attributed to the highly variable orientation of the collagen fibres within the tissue. Interestingly, in the majority of the samples tested in this study, it was observed that there were multiple failure points in atherosclerotic plaque tissue, with there being an initial failure followed by an uptake of load before final failure. This is an interesting observation which shows rupture not only occurs mostly on the luminal side but from the DTI it is observed that this is probably due to the fibres being in the non-load bearing axial direction. Furthermore, this work again supports observations seen in Ghasemi et al (2021), where larger remodelling values were obtained when fibres were further away from the optimum configuration, indicating that the remodelling capability of the plaque is not optimized. Extending on this previous work, it is observed that when models with atherosclerotic plaques are informed with *ex-vivo* fibre angles extracted from DTI, the RM is higher than the circumferential fibre cases but lower than the axial fibre cases. This suggests that these plaques are quite vulnerable to rupture, especially at localized regions where the RM is high. The workflow for this study is presented in Fig 5.1.
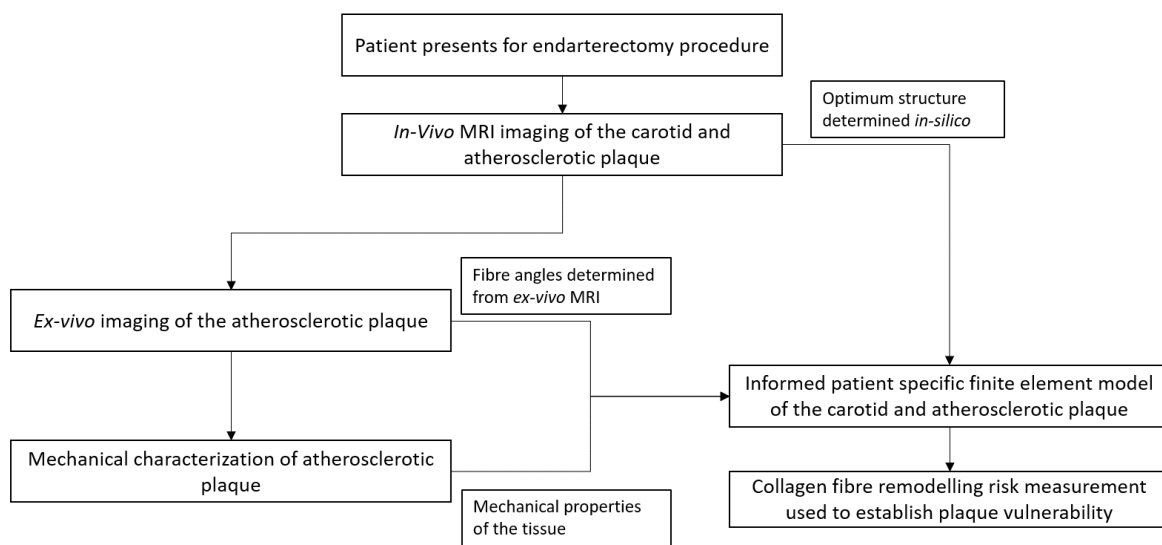
Figure 5.1: Workflow of experiments performed in this study.

5.2 Methods

5.2.1 *In-vivo* MRI and sample collection

In-vivo MRI scans of the carotid arteries were obtained from healthy volunteers using a 3T whole body MRI scanner (Achieva, Phillips Medical Systems, Best, Netherlands) combined with an 8-channel dedicated bilateral carotid artery coil (Shanghai Chenguang Medical Technologies, Shanghai, China). Imaging parameters used in acquisition are stated in Table 3.2, with the field of view centred on the carotid bifurcation after localization to the region of interest using the time

of flight (TOF) imaging sequence. For each patient volunteer in this study, ECG was used to allow for cardiac triggering to be performed. This was done in order to acquire images at known phases of the cardiac cycle.

5.2.2 *Ex-vivo* DTI of atherosclerotic plaque tissue

Using previous established protocols stated in Tornifoglio et al (2020), a small bore (35 cm) horizontal 7 T Bruker BioSpec 70/30 USR system (Bruker, Ettlingen Germany) equipped with a receive only 8-channel surface array coil, birdcage design transmit coil, shielded gradients (maximum strength 770 mT/m) and Paravision 6 software was used for imaging all atherosclerotic plaques. All atherosclerotic plaques were positioned using a custom-made 3D printed holder placed in a 50ml falcon tube and immersed in fresh PBS prior to imaging at room temperature. A 3D DTI sequence with the following parameters was used: TE/TR: 17.682/1000 ms; image size: 64x64x64, field of view: 16x16x16 mm, isotropic resolution 250x250x250 µm, b-values: 0, 800 s/mm^2, 10 b-directions, with fat suppression and acquisition time: 12 hours and 30 minutes. After imaging, the sample was cryopreserved again to ensure no degradation occurs in the tissue as cryopreservation is known to have no effect on the mechanical properties of the tissue [26]

5.2.2.1 Data reconstruction and establishing the helical angle.

All raw data was denoised [174] and corrected for Gibb's ringing [175] in MRtrix3 [176] (http://www.mrtrix3.org) prior to the mono-exponential tensor model fitting in ExploreDTI [177]. The mono-exponential equation expands to incorporate the diffusion tensor and b-matrix which characterises the diffusion sensitivity from the effects of the diffusion gradients, imaging gradients and cross-terms. From the tensor, the mean diffusivity (MD), fractional anisotropy (FA) and first-eigenvector (FE) were calculated and exported from ExploreDTI. The MD represents the total diffusion within a voxel, while FA is indicative of the degree of anisotropic diffusion occurring within a voxel on a scale of 0–1 [178,179]. This is undertaken for the imaging aspect of this study and is not included in this thesis.

In order to import *ex-vivo* DTI-derived fibre orientation information, the helical angle was calculated in order to be incorporated into the finite element models. Here, the FE was used to calculate the helical angle, the angle of the predominant direction of diffusion, with respect to the plane normal to the main magnetic field, B0. The ex-vivo imaging set-up ensured that B0 aligned with the longitudinal axis of the plaques. The FE gives directional information on the dominant orientation of water diffusion within the microstructure [180]. For calculation of the helical angle (α), the reader is referred to figure 5.2;
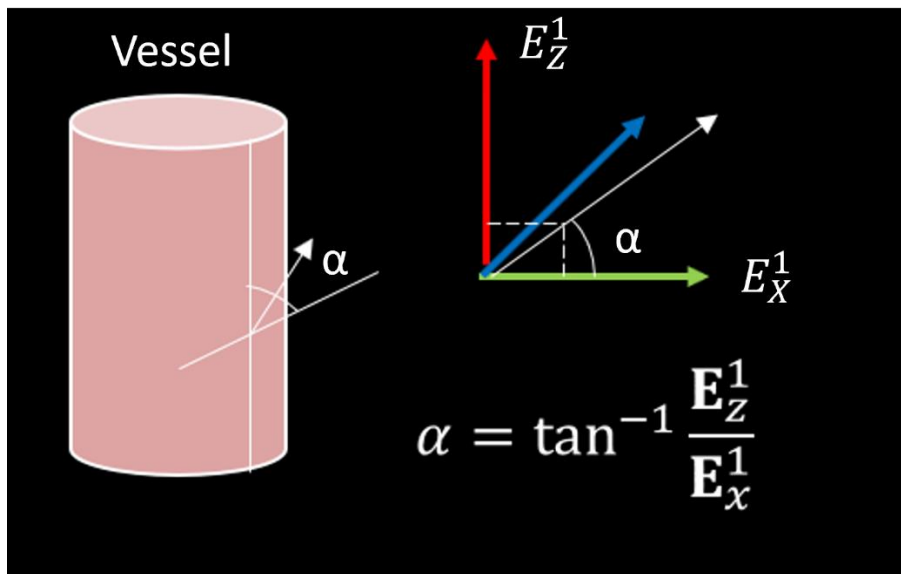
Figure 5.2: Establishment of the helical angle (α) from ex-vivo DTI.

where α is the helical angle, E_{1z} is the z-component of the first eigenvector and E_{1x} is the x-component as shown in Fig. 5.2. The helical angle was calculated on a voxel wise basis, but then a mean value in a region of interest within the atherosclerotic plaque sample was incorporated into the computational model. This allowed for the incorporation of different helical angles into different plaque layers; for example – the luminal edge versus a more medial section of the plaque wall. The directionality of the structure was also visualised using first eigenvector-fractional anisotropy maps (FEFA). These maps show the directionality of the FE which is visualised by hue (red, green or blue), while the FA weights the intensity. For clarity, the blue regions in the image would represent a dominant direction in the z direction whilst green/red regions would represent the x/y direction.

5.2.3   Sample preparation

Using previously established protocols stated in chapter 4 of this thesis, carotid plaque specimens were obtained from 4 symptomatic carotid endarterectomy (CEA) patients at St James Hospital Dublin. These patients were aged from between 50 and 85 years of age and had been diagnosed with a percent stenosis of greater than 50%. Ethical approval for obtaining the plaques in this study was obtained from St. James Hospital ethical committee in compliance with the declaration of Helsinki. Similar to the previous study, carotid plaque specimens were firstly washed in phosphate-buffered saline (PBS) to remove residual blood and then stored in tissue-freezing medium (RPMI-60 Media, 1.8 M DMSO; and 0.1 M sucrose), placed into a Mr. Frosty cryosystem containing 2-propanol and cryopreserved at −80 °C until the day of testing. On the day of testing, samples were defrosted in PBS at ambient temperature and then cut into circumferential strip samples using a custom-made cutting tool as shown in Fig. 5.3.
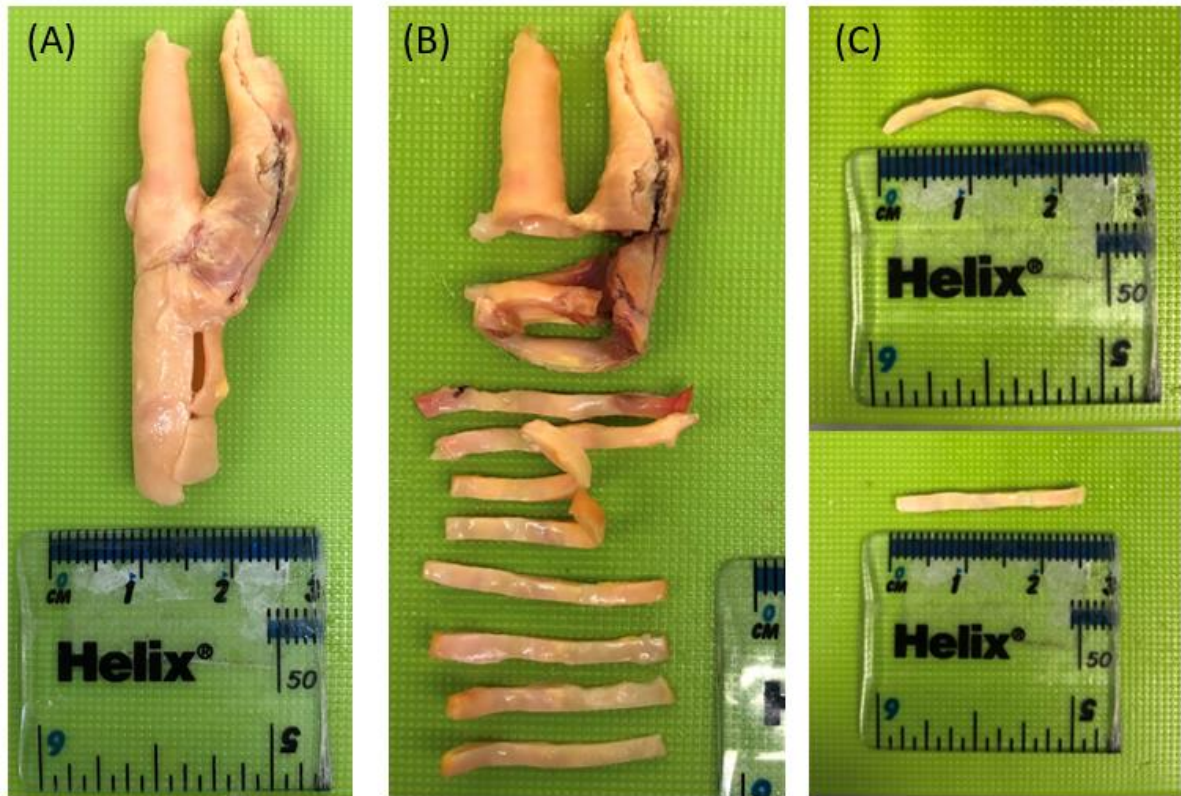
Figure 5.3: (A) Atherosclerotic plaque sample (B) Preparing circumferential strip samples for uniaxial mechanical testing (C) Thickness and width measurements are taken from images of strip samples for calculation of the cross-sectional area.

5.2.4   DIC and Mechanical characterization

Stated in chapter 4 of this thesis, uniaxial tensile tests to complete failure were performed using a uniaxial test machine (Zwick Z005, Zwick GmbH & Co. Ulm, Germany). All tests were performed in a water bath of PBS solution at 37 °C, to simulate the physiological environment. Five preconditioning cycles at 5% strain were performed before the loading steps to remove viscoelastic effects in the tissue. None of the samples included in this analysis failed in preconditioning. Loading continued in each sample until failure of the tissue occurred and the final force-deformation cycle after preconditioning and prior to failure was evaluated to establish the stress-strain behaviour of the samples. Only samples that failed approximately in the centre of the sample were considered for analysis to ensure only robust ultimate tensile stress, strain and stiffness measures were obtained. Furthermore, any samples that showed signs of slippage were also excluded from the end analysis. Digital Image Correlation (DIC) was used to track local strain deformations in the area of failure during testing. Furthermore, the DIC was set up to record the entire experiment at a rate of 5 Hz. Cameras were calibrated and focused before data acquisition to ensure robust results were obtained. A stochastic pattern was applied using spray paint which allowed displacement of the tissue to be tracked.
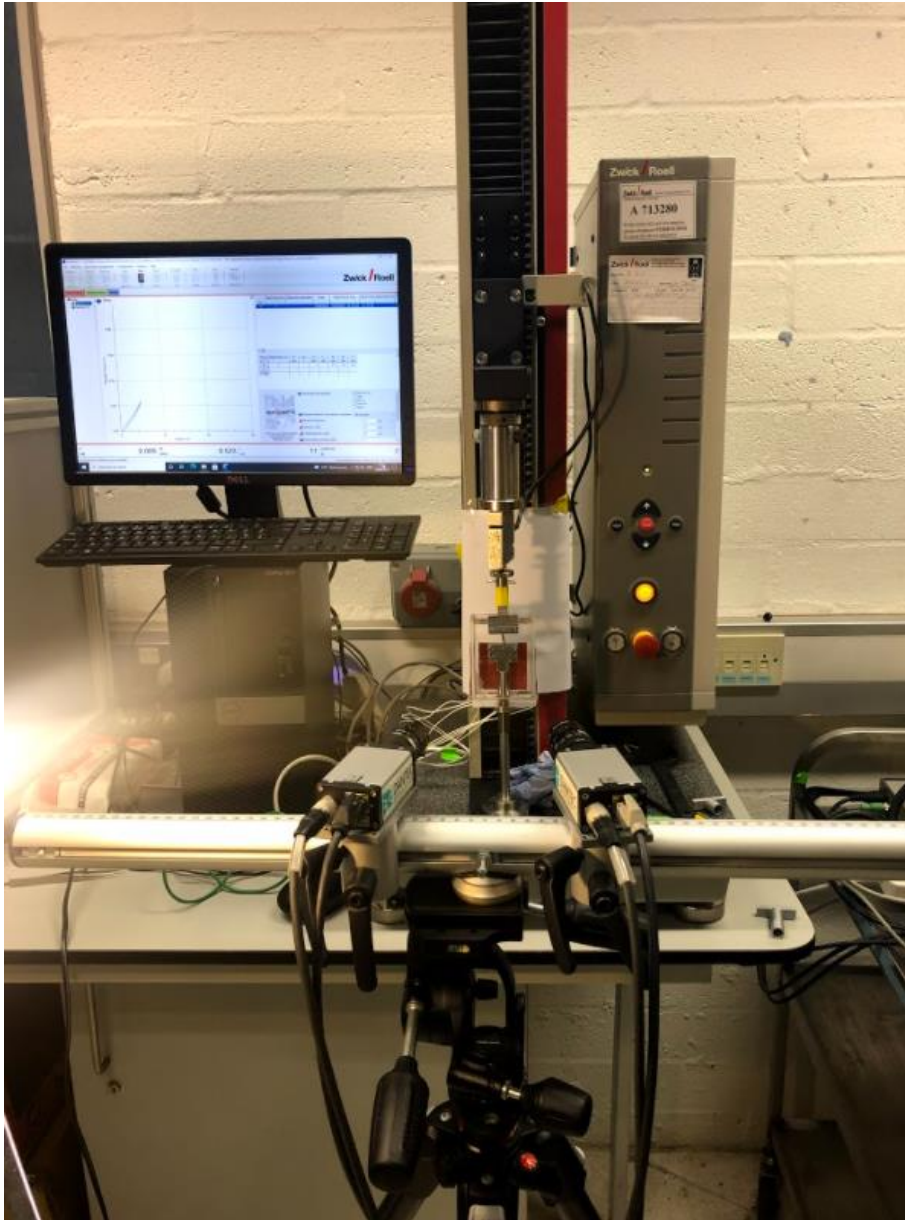
Figure 5.4: Experimental setup in the lab with sample placed in grips and DIC cameras focused on sample. This setup is exactly the same as demonstrated in Johnston et al, 2021 [164]

5.2.5 DTI informed patient specific finite element model

Patient specific finite element (FE) models are created from structural *in-vivo* MRI images using the protocol established in chapter 3. To ensure the capability of increasing the specificity of the created patient specific finite element model to the results obtained from DTI, the plaque is separated into two layers that allowed for independent angles to be inputted as shown by figure 5.5. The inner layer of the plaque includes all elements from the lumen to the edge of the lipid pool. If no lipid is present, the mesh is split into two to account for the inner and outer layers of the plaque.
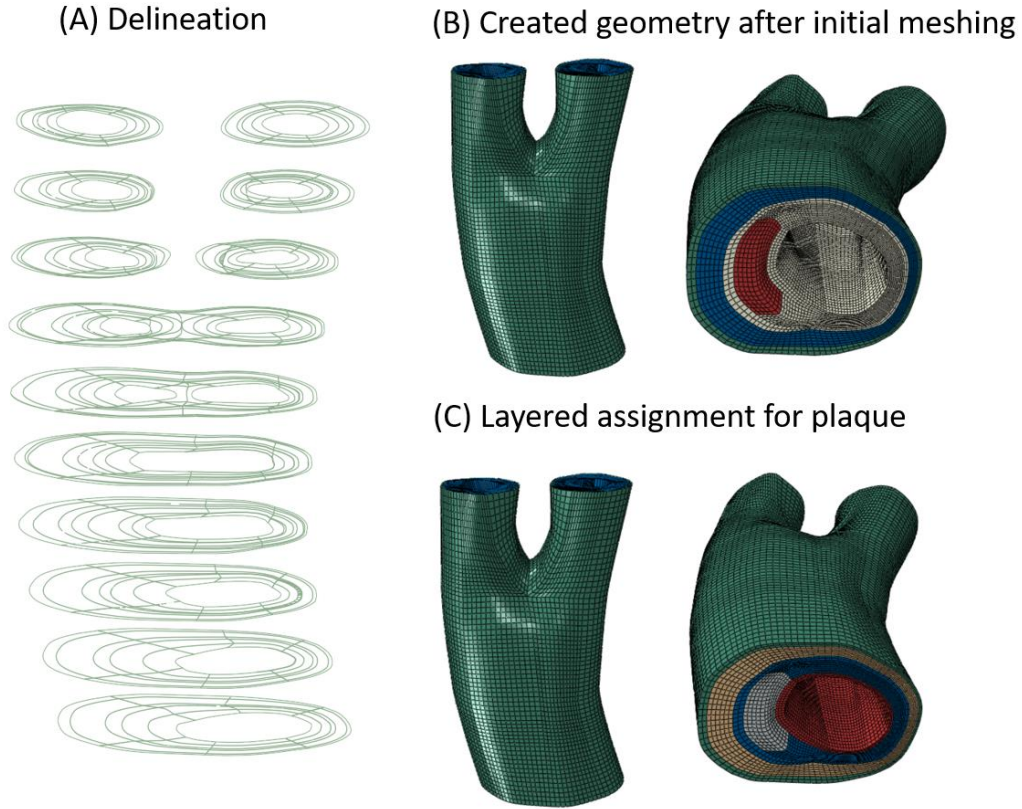
Figure 5.5: Creation of the DTI informed patient specific finite element model. (A) Delineation of artery and atherosclerotic plaque (B) Created geometry after initial mesh creation (C) Layered plaque mesh in patient specific to allow for independent fibre angles to be incorporated into each layer.

5.2.6 Constitutive Modelling

In this study, the anisotropic hyperelastic constitutive model proposed in Gasser et al (2006) was used to capture the mechanical behaviour of both the healthy and diseased components in both the healthy and diseased patient specific arterial geometries and similar to Ghasemi et al. (2021) [16,181]. This constitutive model captures the mechanical behaviour of the tissue by additively decomposing the response of the tissue into its respective components.

$$\psi = \psi_{vol} + \bar{\psi}_{iso} + \bar{\psi}_{cf} \tag{5.1}$$

The response of the non-collagenous tissue was captured using the neo-Hookean material model ($\psi_{vol} + \bar{\psi}_{iso}$). The response of the collagenous tissue was captured by postulating two symmetric families of collagen fibres, $\bar{\psi}_{cf}$. The volumetric free energy function (ψ_{vol}) can be expressed as follows;

$$\psi_{vol}(J) = \frac{1}{2}\kappa_0(J-1)^2 \qquad (5.2)$$

where κ_0 serves as a penalty parameter that controls the compressibility of biological soft tissue. The isotropic strain energy function (SEF), ($\bar{\psi}_{iso}$), can be written as follows;

$$\bar{\psi}_{iso}(\bar{\mathbf{C}}) = \frac{1}{2}\mu(\bar{I}_1 - 3) \qquad (5.3)$$

where μ is the shear modulus of the ground matrix. The SEF to capture the mechanical behaviour of the collagenous tissue can be written as follows;

$$\bar{\psi}_{cf}(\bar{\mathbf{C}}) = \sum_{M_{cf}=M_{4,6}} \frac{k_1}{2k_2} (\exp{(k_2(\kappa\bar{I}_1 + (1-3\kappa)\bar{I}_M - 1)^2)} - 1) \qquad (5.4)$$

where k_1 and k_2 are material parameters and $\bar{I}_{M_4}$ and $\bar{I}_{M_6}$ are the square of the stretch in the direction of collagen fibres and correspond to two unit vectors, $\mathbf{M}_4$ and $\mathbf{M}_6$, respectively. For further information on this constitutive model the reader is referred to Gasser et al. (2006) [181]. Having these SEFs, Cauchy stress can then be defined as follows;

$$\boldsymbol{\sigma} = \frac{2}{J}\mathbf{F}\frac{\partial\psi}{\partial\mathbf{C}}\mathbf{F}^T \qquad (5.5)$$

5.2.7 Remodelling algorithm

Collagen fibre directions re-orient *in-vivo* in order to maximise the load bearing capacity of the tissue. Following established methods demonstrated in Hariton et al. (2006) [14] and Fausten et al (2016) [15] it was assumed that the collagen fibres are located in the plane made by the eigenvectors of the two largest principal stresses σ_1 and σ_2. The spectral decomposition of this stress tensor can be written as follows:

$$\sigma = \sigma_1\vec{e}_1 \otimes \vec{e}_1 + \sigma_2\vec{e}_2 \otimes \vec{e}_2 + \sigma_3\vec{e}_3 \otimes \vec{e}_3 \qquad (5.6)$$

where $\sigma_1 \geq \sigma_2 \geq \sigma_3$. In the first step of this re-orientation algorithm, the influence of collagen fibres on the mechanical response of the tissue is neglected. The stress values in this step are therefore calculated using the isotropic hyperelastic neo-Hookean material model. This is a valid assumption and has been performed in previous re-orientation algorithms. The reason for this assumption is that the anisotropic behaviour of the soft tissue develops due to tissue remodelling and adaptation to mechanical loads and that the behaviour of the tissue in the neonatal stage of development is isotropic [182].

In this implementation of collagen fibre re-orientation, the ratio between the magnitude of the two largest principal stresses was used to define the angle of alignment of the collagen fibres with respect to the direction of the maximum principal stress, as follows.

$$tan(\alpha) = \sigma_2/\sigma_1 \qquad (5.7)$$

Using this equation, two-unit vectors defining the optimum directions of two families of collagen fibres in the spatial configuration were obtained as follows.

$$\overrightarrow{m_{4op}} = \cos(\alpha)\,\vec{e}_1 + \sin(\alpha)\,\vec{e}_2 \qquad (5.8)$$

$$\overrightarrow{m_{6op}} = \cos(\alpha)\,\vec{e}_1 - \sin(\alpha)\,\vec{e}_2 \qquad (5.9)$$

To calculate the stress in the current configuration, the distribution of collagen fibres in undeformed configuration needed to be determined. For this purpose, the vector $\overrightarrow{m_{4op}}$ and $\overrightarrow{m_{6op}}$ were pulled back to the reference configuration as follows:

$$\overrightarrow{M_{4op}} = \frac{\mathbf{F}^{-1}\overrightarrow{m_{4op}}}{\left|\mathbf{F}^{-1}\overrightarrow{m_{4op}}\right|} \qquad (5.10)$$

$$\overrightarrow{M_{6op}} = \frac{\mathbf{F}^{-1}\overrightarrow{m_{6op}}}{\left|\mathbf{F}^{-1}\overrightarrow{m_{6op}}\right|} \qquad (5.11)$$

In this study, the dispersion of collagen fibres was also subjected to these remodelling rules. Following the method established in Driessen et al. (2006) [129], the ratio of the maximum and intermediate principal stress was used to define the optimum dispersion of the collagen fibres in the spatial configuration, as follows;

$$b = \frac{\sigma_1}{\sigma_2} - 1 \qquad (5.12)$$

Where b is the concentration parameter which can be attributed to the von-Mises periodic distribution function as follows:

$$\rho(\alpha, b) = 4\sqrt{\frac{b}{2\pi}}\exp[bcos(2\alpha) + 1]\,/erfi(\sqrt{2b}) \qquad (5.13)$$

The von-Mises distribution has been used to define the distribution of embedded collagen fibres within the tissue. The concentration parameter b was correlated with the dispersion parameter κ as follows;

$$\kappa = \frac{1}{4}\int_{-\pi}^{\pi} \rho(\alpha, b)\sin^3(\alpha) \qquad (5.14)$$

To calculate the optimum dispersion of fibres in the undeformed configuration a generalized structure tensor was firstly made in the deformed configuration using both the optimum fibre direction and dispersion of fibres. This structure tensor **h** was then pulled back to the undeformed configuration as follows;

$$\mathbf{H} = \mathbf{F}^{-1}\mathbf{h}\mathbf{F}^{-T} \tag{5.15}$$

The spectral decomposition of the tensor **H** was calculated to determine the eigenvalues of the structure tensor **H** in the undeformed configuration. The ratio of the maximum and intermediate eigenvalues in the undeformed configuration was then used to calculate the dispersion of fibres in the undeformed configuration, the reader is referred to Ghasemi et al (2021) for the mathematical derivation.

Once the optimum direction and dispersion of fibres was calculated, both vectors and dispersion of fibres remodelled toward this preferred configuration. The vector of fibres was remodelled incrementally in the undeformed configuration toward its optimum direction by adding a fraction (τ) of the total difference between the optimum direction and initial direction of fibres. This process also established the next initial direction of the fibres for the next remodelling step, see figure 5.6. A similar approach was used in Fausten et al (2016) [15]
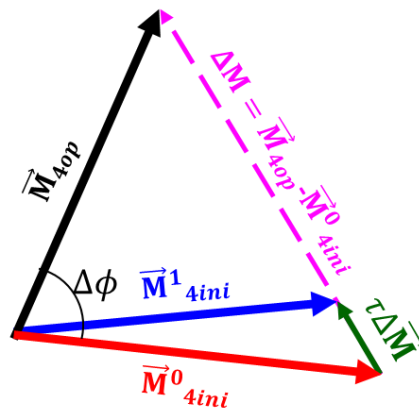
Figure 5.6 A schematic presentation of the remodelling process. Once the vector presenting the optimum direction of the fibres was calculated ($\vec{M}_{4op}$) a fraction of the total difference between optimum fibre configuration and the initial configuration ($\tau\Delta\vec{M}$) was added to the initial configuration of the fibres ($\vec{M}^0{}_{4ini}$) resulting in the initial configuration for the next iteration of the remodelling process $\overrightarrow{(\boldsymbol{M}^1{}_{4ini})}$. In this figure, $\Delta\phi$ indicates the angle between the optimum fibre direction and initial direction of fibres. Schematic here is taken from Ghasemi et al (2021)

The dispersion of fibres was remodelled toward its optimum value using a linear rate equation as follows;

$$\frac{d\kappa}{dt} = \frac{1}{\tau_\kappa}(\Delta\kappa) = \frac{1}{\tau_\kappa}\left(\kappa - \kappa^{ini}\right) \tag{5.16}$$

5.2.8   Remodelling metric

The stiffness of arterial and atherosclerotic plaque tissue has directly been associated with the orientation of fibres. Using the established method in Ghasemi et al, 2021 [16]. The concept of the continuous damage model (CDM) was employed to correspond to the stiffness of the arterial tissue to the distribution of the collagen fibres. Arterial tissue is assumed to have its optimum stiffness where the collagen fibres are aligned with the predicted optimum configuration of fibres. The lack of orientation from this optimum configuration results in softening and weakening of the tissue. In this implementation and like Ghasemi et al (2018), two internal variables, γ_{RM} and β_{RM} were used to capture the softening that is associated with orientation of the fibres away from their optimal configuration [59]. Physically, γ_{RM} and β_{RM} describes the continuous and discontinuous damage experienced within the tissue. Furthermore, these parameters develop as the fibres begin to reorientate as set in the simulation. Therefore, the further away the fibres are from the optimal configuration would lead to an increase in these values (which would suggest softening induced damage) and therefore increase the RM value observed in the tissue. Therefore, these two internal variables together are denoted as the remodelling metric (RM), which is dependent on the change of the collagen fibre orientation and the evolution of these internal variables when the arterial vessel is subjected to load. A brief inclusion overview of the mathematical derivations is detailed below.

Evolution of the internal variable γ during the re-orientation ([0,T]) can be written as follows.

$$\gamma_{RM} = \max_{t\in[0,T]} \langle \bar{I}_M^* - \bar{I}_M^{*ini} \rangle \tag{5.17}$$

Where $\bar{I}_M^*$ is a pseudo invariant associated with each family of fibres (**M**) and can be written as follows.

$$\bar{I}_M^* = \kappa\bar{I}_1 + (1 - 3\kappa)\bar{I}_M \tag{5.18}$$

$\bar{I}_M^{*ini}$ is the value of $\bar{I}_M^*$ defined at the beginning of the re-orientation process. The internal variable β_{RM} can be defined as follows.

$$\beta_{RM} = \langle \tilde{\beta}_{RM} - \tilde{\beta}_{RM}^{ini} \rangle \tag{5.19}$$

Where $\tilde{\beta}_{RM}^{ini}$ are the values of the variable $\tilde{\beta}_{RM}$ at the initial increment of the re-orientation step in the arterial tissue. The variable $\tilde{\beta}_{RM}$ can be written as follows.

$$\tilde{\beta}_{RM} = \int_0^T \langle \bar{I}_M^* \rangle ds \tag{5.20}$$

In equations 5.17, 5.19 and 5.20, $\langle (\bullet) \rangle$ are Macaulay brackets that filter out the negative values. A similar form for the evolution of internal variables was used in studies as Miehe (1995), Balzani et al. (2012) and Ghasemi et al. (2018) [16,183,184]

These two internal variables were then attributed to a softening function as follows;

$$RM = RM_\infty [1 - \exp{(-\frac{\gamma}{\gamma_\infty})}] \left[1 - \exp{\left(-\frac{\beta}{\beta_s}\right)}\right], RM \in [0,1] \tag{5.21}$$

Where, γ_∞ and β_s are material properties. RM_∞ denotes a predefined maximum softening level for this function ($RM_\infty = 0.99$).

5.2.9 Finite Element (FE) implementation

The algorithm was implemented into the commercial FE solver Abaqus, where a user subroutine (UMAT) was used to define the behaviour of different components of healthy and diseased arterial wall whereby the definition of both the Cauchy stress and tangent modulus was required [183].

The arterial bifurcations were segmented into two parts: healthy arterial wall (consisting of the adventitia and media) and the fibrous plaque (composed of plaque atheroma and lipid pool); both of which were observed in the MRI images. Material parameters were taken from Balzani et al, 2012 and are stated in Table 3.3 [17]. Material parameters for the adventitia, media and lipid pool were kept constant throughout the entire study.

Four diseased bifurcations were analysed in this study. The analysis was performed in three main steps.

1. The artery was subjected to axial displacements using and isotropic material model.
2. The artery was subjected to known systolic blood pressure taken from measurements during MRI acquisition. At this stage, the optimum vector and dispersion of collagen fibres were calculated at the end of this step. This step also uses and isotropic material model.
3. Both vector and dispersion of collagen fibres were subjected to remodelling rules as stated in section 5.2.7 using the anisotropic hyperelastic material model. To analyse the models presented here, three different cases were postulated as the initial configuration of fibres in the plaque tissue, where fibres are located at: (i) parallel to the direction of the intermediate principal stress (ii) DTI informed helical angle with respect to the maximum principal stress. (iii) parallel to the direction of maximum principal stress
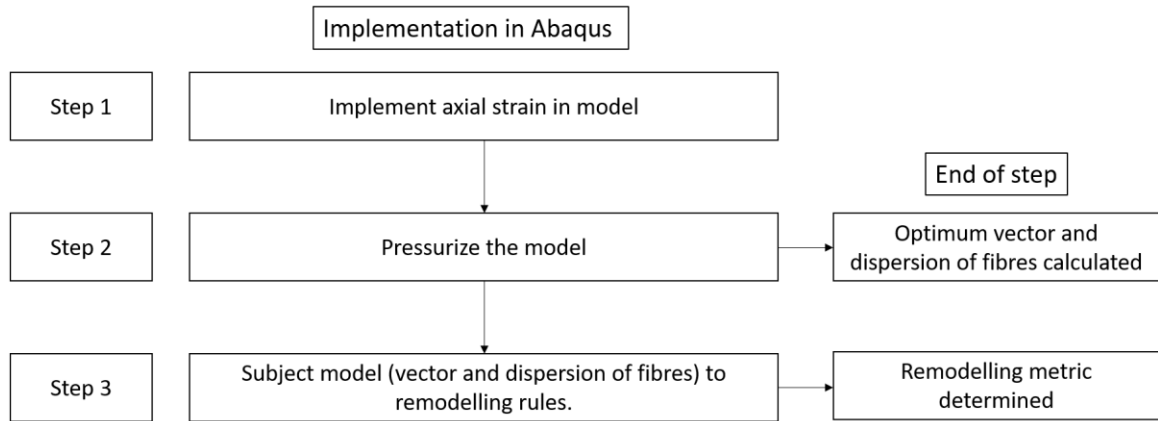
Figure 5.7: Workflow depicting the finite element implementation of the remodelling and CDM algorithm in Abaqus.

5.3 Results

5.3.1 *Ex-vivo* DTI of atherosclerotic plaque tissue and establishment of the microstructural orientation.

Four atherosclerotic plaques were imaged in this study and the dominant microstructural orientation within the tissue was established. As shown by figure 5.8, FEFA maps show the directionality of the FE, controlling hue and fractional anisotropy controlling brightness. For clarity, the blue regions in the image would represent a dominant direction in the z direction whilst green/red regions would represent the x/y direction. Qualitatively, it can be observed that in samples 2 and 3 there is a trend of more axial alignment with a sudden change in the orientation to represent a circumferential alignment through the thickness of the samples. The helical angles for each specimen were established using the method stated in section 5.2.2.1 and is reported in figure 5.8. Furthermore, extracted helical angles for two datasets that represent the inner and outer layers are also reported here showing that plaques can have mixed (sample 1 and 4) or layered (sample 2 and 3) fibre orientation. The effect of this layered fibre orientation response is investigated further using specified patient specific computational models.
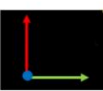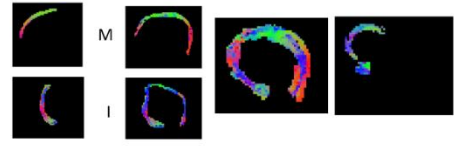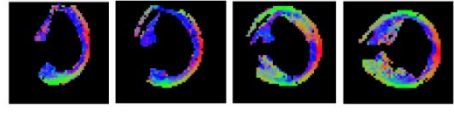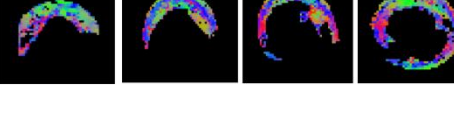
Figure 5.8: First eigenvector fractional anisotropy maps (FEFA) showing directionality of the microstructure in atherosclerotic plaque strip samples for N=4 and extracted helical angles for (A) Sample 1 (M represents the outer layer of specimen, I represent the inner layer of specimen) (B) Sample 2 (C) Sample 3 (D) Sample 4

5.3.2 Mechanical characterization of atherosclerotic plaques

Data presented here are the circumferential strip samples that failed in approximately the centre of the tissue sample. Stress-strain curves for all samples exhibited the characteristic non-linear J-shaped curve, which is indicative of arterial and atherosclerotic plaque tissue, see figure 5.9. Engineering stress was calculated using the Zwick force displacement divided by the original cross-sectional area and the strain was extracted directly from the Zwick. Each sample is plotted individually as shown in figure 5.9A,B,C,D and altogether in figure 5.9E. Data presented here shows the processed data up to the initial failure point where rupture was observed.
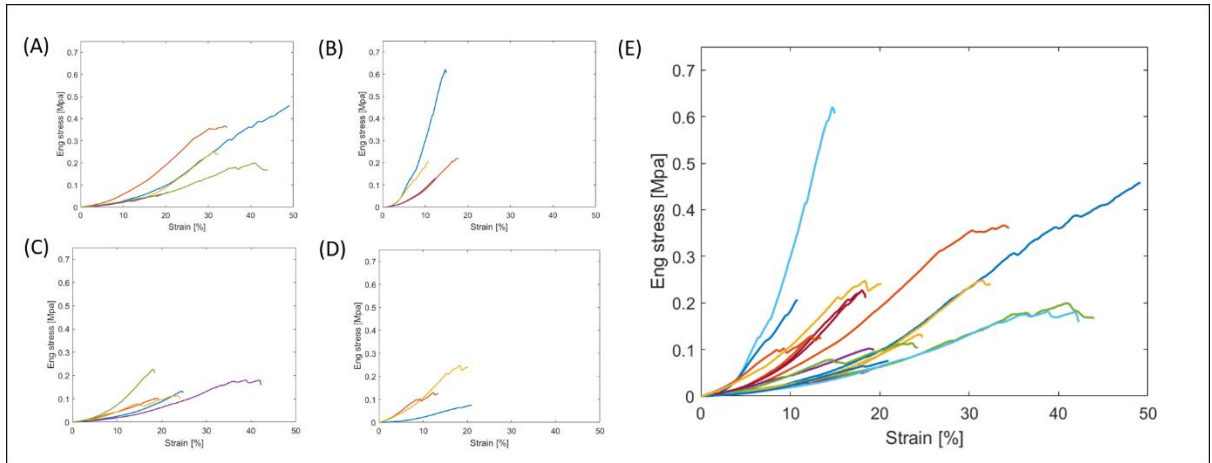
Figure 5.9: Engineering stress vs strain results for atherosclerotic plaque samples where each curve represents one circumferential strip sample tested (A) Sample 1 (B) Sample 2 (C) Sample 3 (D) Sample 4 (E) All samples plotted together.

In total, 19 strip samples were tested from four atherosclerotic plaques. An interesting observation in these samples is the layered failure observed in the majority of tests as shown by a representative example of the raw data in figure 5.10 A. A number of samples exhibit this behaviour whereby an initial failure is observed on the inner side of the strip sample followed by further up taking of the load before final failure as shown by figure 5.10 B,C and D.
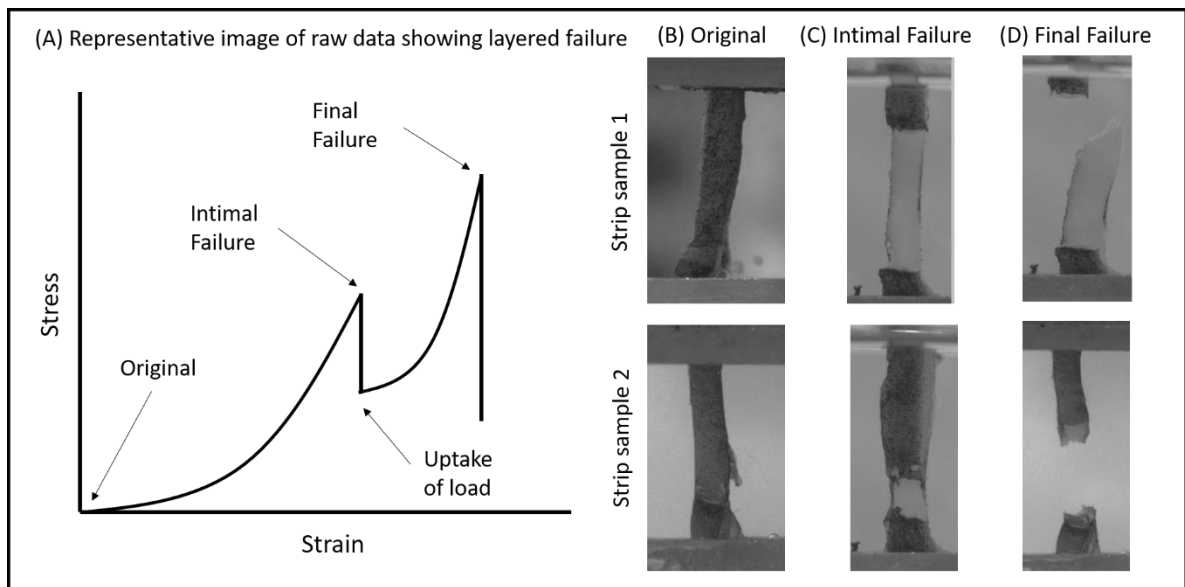
Figure 5.10: (A) Representative stress vs strain curve showing what has been observed in the raw data for 19 samples during testing. Note the uptake of load after significant failure of the strip sample on the inner layer (B) Visual representation of two samples (C) Visual representation of first failure from DIC for two samples (D) Visual representation of final failure from DIC for two samples

113

5.3.3   Patient specific finite element models informed by *ex-vivo* and i*n-vivo* DTI.

5.3.3.1   Remodelling in healthy carotid artery

To validate the use of 5% axial strain used in previous studies in these simulations, three cases are simulated to observe the effect this boundary condition has on the direction of the maximum principal stress. This is especially important as the reorientation algorithm implemented here depends on the ratio between the magnitude of the two largest principal stresses and was used to define the angle of alignment of the collagen fibres with respect to the direction of the maximum principal stress. As shown by figure 5.11, the imposed boundary condition has a significant impact on the magnitude and directionality of stress. It is observed that a 5% axial strain preserves the circumferential orientation of the maximum principal stress which is vital for accurate implementation of the remodelling algorithm. Higher levels of axial strain, as seen in the 10% case would alter this so the maximum principal stress in now in the axial direction. This is not correct as the circumferential orientation of collagen fibres within the vessel is known to be the load bearing orientation [32,181] and deviation of this would significantly affect the prediction of the optimum fibre direction and the fibre remodelling algorithm implemented. It is for this reason, an axial strain of 5% is used in all models presented here.
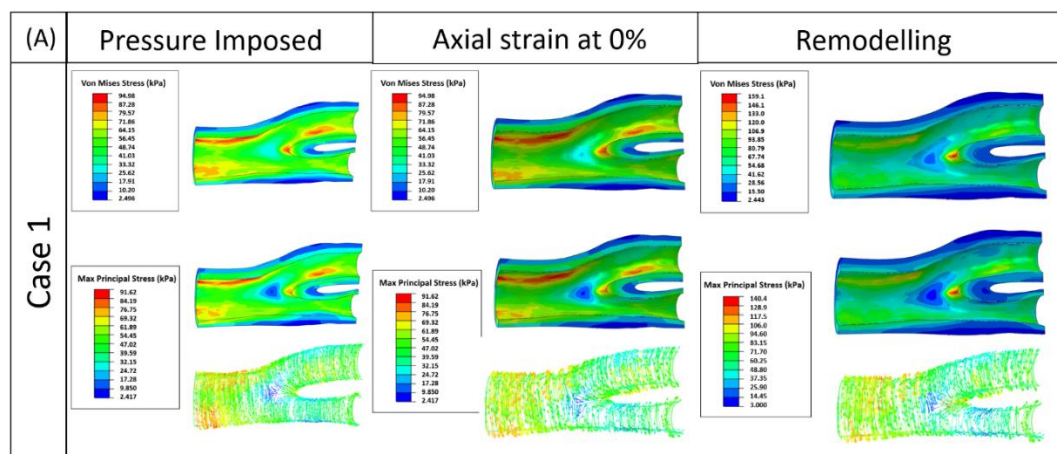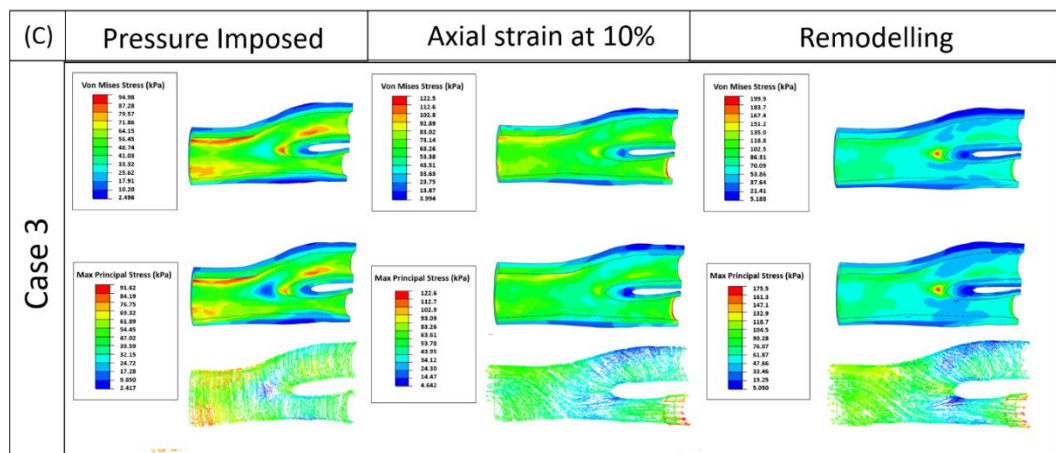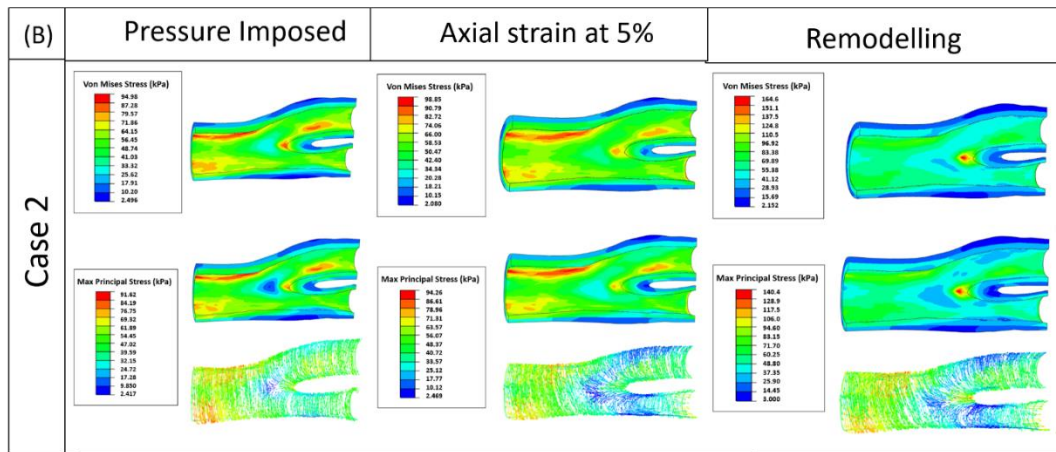
Figure 5.11: Arterial remodelling implemented in a healthy geometry undergoing three different levels of axial strain (A) 0% axial strain (B) 5% axial strain (C) 10% axial strain. Direction of the maximum principal stress after each case is also shown.

5.3.3.2   Remodelling in diseased atherosclerotic carotid artery and remodelling metric to determine plaque vulnerability

Figure 5.12 shows the remodelling algorithm implemented in a diseased geometry with a specific focus on the atherosclerotic plaque. Similar to the results observed in the healthy case, when axial strain is imposed on the model it changes the directionality of the maximum principal stress and when pressure is imposed the directionality then changes back to the circumferential direction as expected. Again, the level of axial strain would change this directionality but for consistency with the result found in the healthy datasets, this was set to 5%.
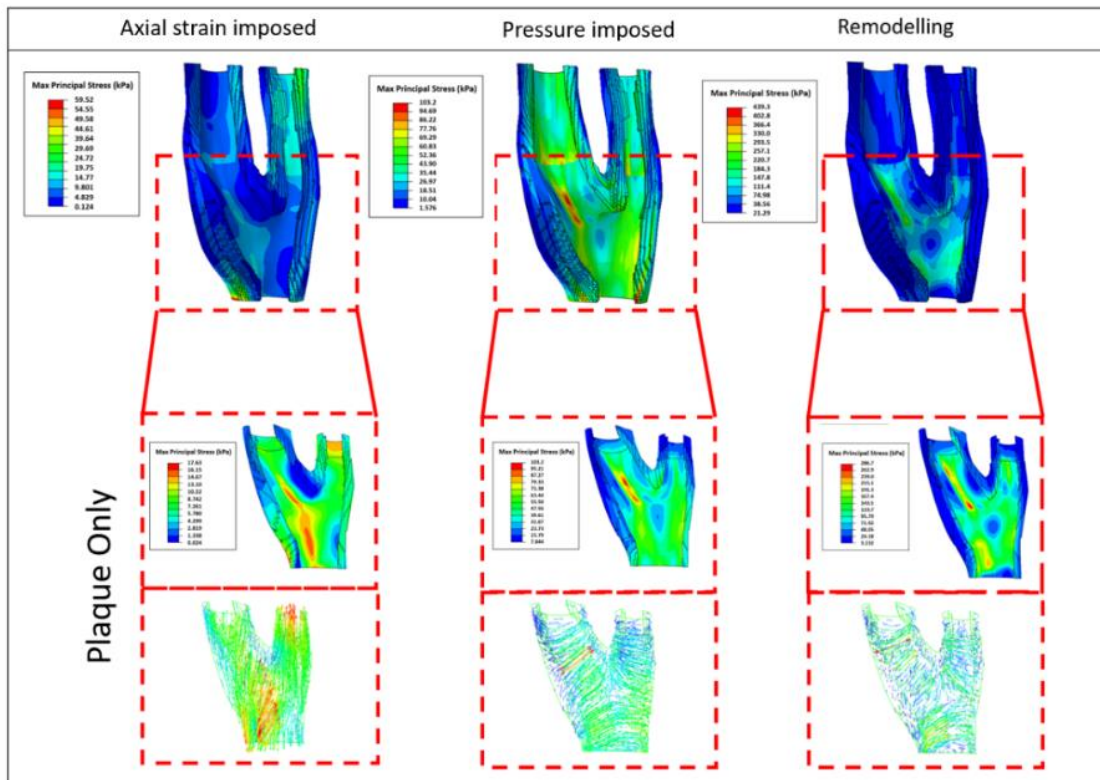
Figure 5.12: Arterial remodelling algorithm implemented in a diseased geometry with atherosclerotic plaque also observing the maximum principal stress after each step in the implementation of the algorithm.

Figure 5.13 shows the remodelling metric being implemented in 4 diseased vessels in which atherosclerotic plaques are present. In each geometry, similar trends are observed whereby, fibres set in the circumferential orientation show the smallest amount of remodelling needed for maximum load bearing capacity while fibres set in the axial orientation show a significant need of remodelling in order for the vessel to be in the optimum orientation. This inability to remodel when the fibres are not in the load bearing configuration is important to characterize as this can demonstrate which plaques are more likely to be vulnerable to rupture as it is structurally weak. Interestingly, models that have been informed by DTI extracted fibre angles depict a response that is very much that is in between both the cases where fibres are set in the axial or circumferential directions. This is important as plaque with a higher RM present within them can suggest which ones are more vulnerable to rupture. In all DTI fibre models, there is an increase in the RM observed when compared to the circumferential fibre models, suggesting that the fibres are not in the load bearing configuration and an intervention should take place.

116
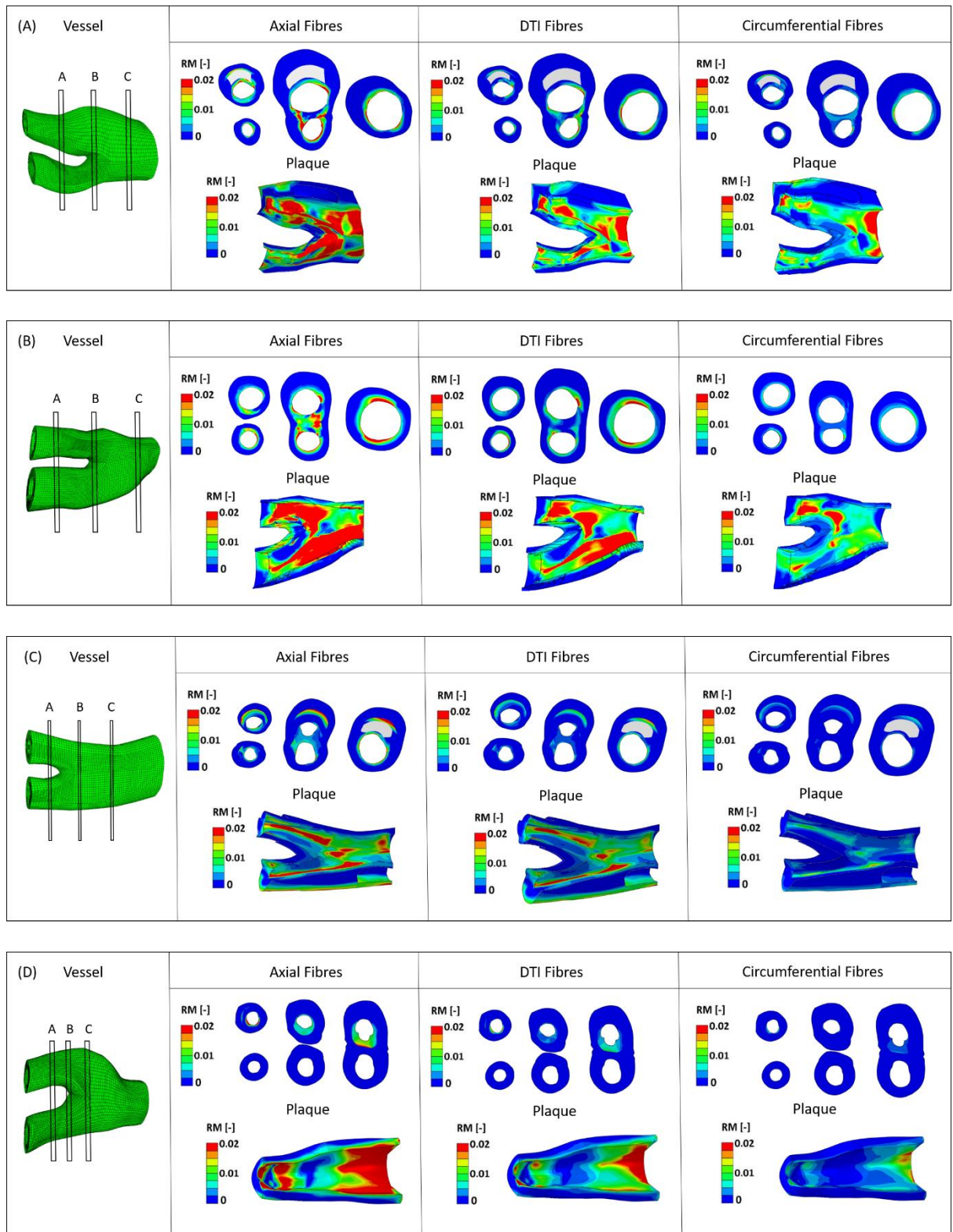
Figure 5.13: Remodelling metric in diseased arterial bifurcations (N=4). (A) Geometry 1 with axial, DTI and circumferential fibres set (B) Geometry 2 with axial, DTI and circumferential fibres set (C) Geometry 3 with axial, DTI and circumferential fibres set (D) Geometry 4 with axial, DTI and circumferential fibres set.

To investigate the layered failure responses observed from the mechanical data, figure 5.14 shows the response obtained from layered models from two cases with the atherosclerotic plaque having hypothesised fibre orientations set in axial and circumferential orientations in respective layers and finally with fibre angles calculated from *ex-vivo* DTI for each layer. Interestingly, in the DTI datasets it is observed that due to the presence of the fibres being more axial on the inner layer, there is a greater RM value on the inner wall then observed in the previous cases shown figure 5.13, where the average fibre angle was implemented across the entire thickness of the plaque. This is important as it suggests the need to further specify created patient specific FE models to be sensitive to the microstructure that is being modelled as its only then can you capture the true mechanical response of the tissue. Lastly, it is observed in the mechanical tests that there is failure on the intimal side first for the majority of the samples tested here. At high RM in the computational models is due to the fact fibres are not in the load bearing orientation and tend to be more axially aligned, possibly suggesting that it's the collagen fibre orientation that governs the structural integrity of the tissue.
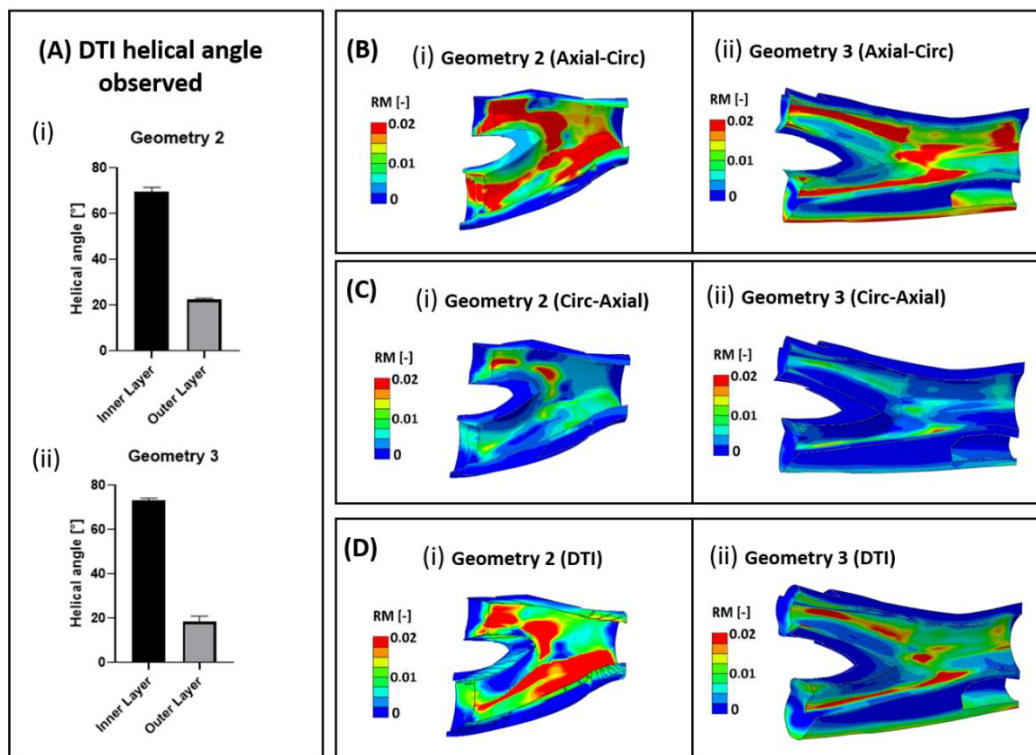
Figure 5.14: Investigating the response after setting fibre orientation in independent layers within the plaque fibrotic media for N=2 models (A) Difference in helical angle observed for 2 models depicting layers in the fibrotic media (B) Computational model with inner layer set with fibres with axial orientation and outer layer set with fibres with circumferential orientation (C) Computational model with inner layer set with fibres in circumferential orientation and outer layer set with fibres in axial orientation (D) Computational model with layers informed from DTI

5.4 Discussion

Similar to previous results shown in chapter 4, the highly variable mechanical nature of atherosclerotic plaques has been observed in all the samples tested, again verifying results from the results shown in chapter 3 and in previous studies [26,164,185]. Throughout this study, these atherosclerotic plaque samples were imaged using *ex-vivo* DTI in order to establish the microstructural orientation of the tissue and by observing the first eigenvector maps. It is important to note that cells align with collagen in the vessel wall, therefore the establishment of the fibre angle can be directly related to the directionality of the collagen fibres [39], allowing this to be incorporated into the computational models. The first observation from ex-vivo MRI measurements is the highly variable nature of the microstructural orientation in each sample, see figure 5.8. Furthermore, this variability is also observed from specimen to specimen in the same samples. For incorporation into computational models, the value of the averaged helical angle across the specimen is used. Interestingly, in samples 2 and 3 there is a similar trend where the fibres are more axially aligned on the luminal side with an abrupt change to more circumferential through the thickness of the samples. An interesting observation that has not been documented in the literature to the authors knowledge is the layered failure of the atherosclerotic plaque strip samples. This was observed in the majority of the samples tested as shown by representative samples in figure 5.10 and provides a very interesting insight into the mechanical behaviour of atherosclerotic plaque tissue. A hypothesis from this research is that this initial failure is due to the fibres on the luminal side of this tissue being in the axial direction. This would also agree with previous work as it is observed when collagen fibres are aligned in the non-load bearing direction, the samples fail at a lower stress and higher strain and would be deemed more vulnerable [42].

The distribution of collagen fibres in healthy tissues are known to evolve *in vivo* in order to maximize the load bearing capacity of the arterial tissue [186,187]. To-date, many studies suggest different forms of constitutive laws that incorporate the distribution of collagen fibres to capture the mechanical behaviour of the arterial tissue such as stress or strain in both axial and circumferential directions respectively. The anisotropic behaviour of the tissue in both the circumferential and axial directions is due to the orientation of the collagen fibres [188]. The remodelling metric (RM) presented here, which is based on the evolution of internal variables during the reorientation process was able to characterize the how far from the optimal distribution the fibres are when set in the axial, circumferential and when informed by DTI directions respectively. Firstly, these results verified observations previously stated in Ghasemi et al (2021), whereby a higher RM is needed for fibres in the axial direction while lower RM values is required for fibres in the circumferential direction. More interestingly though is that when the models have been informed by *ex-vivo* DTI the values of the RM fall very much in between that of both axial

and circumferential cases but certain locations within the plaque do exhibit high RM values. What this means is that for the two idealized cases where the fibres are set in the axial and circumferential directions respectively, this represents the two extreme cases and the RM values expected when the fibres are in the non-load bearing and load bearing respectively. When models have been informed with DTI fibre angles it is observed that the RM values are no longer at the extremes seen in the idealized cases. In all cases, the DTI informed models show a trend away from the circumferential arrangement and towards the axial arrangement. This high RM could suggest that the structure at these locations is possibly weaker due to fibres not being in the load bearing configuration. It is suggested to further investigate this observation; pressure inflation testing of these plaques after establishment of the RM values when informed by DTI should be performed. This will allow for the capability to observe localized rupture of the tissue in a mechanical environment similar to that experienced *in-vivo* and will verify the locations of high RM predicted to have fibres in the non-load bearing orientation. Furthermore, the reason for collagen fibres in the non-load bearing configuration in atherosclerotic plaque tissue is still unknown but a few reasons can be suggested that contribute to this behaviour. Firstly, atherosclerotic plaque tissues are extremely heterogenous tissues that comprise of many components such as calcifications and lipid pools that effect the stress distribution throughout the vessel wall. Collagen fibres typically align in the circumferential load bearing direction; however, the presence of these components can alter the dominant load direction, causing fibres to be deposited in a configuration not typically to be load bearing. Secondly, the degradation observed in arterial tissue is known to be strain dependent [189]. Locations which experience higher strains could have increased degradation of the collagen fibres within these locations due to the presence of matrix metalloproteases (MMPs) within the tissue. Lastly, in atherosclerotic plaque tissue there has been a reported decrease of vascular smooth muscle cells and these cells would be needed in the tissue to sufficiently produce new collagen oriented in the load bearing configuration [190]. This lack of new collagen production would inherently affect the remodelling capability of the tissue and there would be a lack of reorientation of the fibres to the optimum load bearing configuration as the geometry changes, which in turn could weaken the vessel wall and increase the likelihood of rupture at these locations.

Overall, the computational results of plaques informed with DTI fibre angles suggest that all plaques show locations of structural weakness and should be deemed as vulnerable plaques. However, some plaques are more structurally weak than others due to higher values of the RM present across a larger area of the model. It would be suggested that these plaques that would be deemed to be more vulnerable to plaque rupture and an intervention should take place sooner. Although, a higher sample number and correlation with mechanical data would be required to fully support this association. Lastly, MRI and mechanical results highlighted the interesting

phenomenon of multiple layers within the atherosclerotic plaque. To investigate this further, two computational models of atherosclerotic plaques that exhibited this trend were created and respective fibre angles calculated from DTI were imported into each layer respectively, with the inner layer being more axially oriented and the outer layer being more circumferentially oriented. Interestingly, the observed RM value in these cases were higher than the RM value observed when the averaged fibre angle was used across the entire plaque. This would suggest that in order to have increased accuracy of the RM to establish locations of structural weakness, the computational model itself must include the microstructural orientation of the tissue being modelled

Overall, this preliminary work has demonstrated the capability of using the remodelling metric (RM) to characterize plaque vulnerability when being informed with patient specific fibre angles from *ex-vivo* DTI. This remodelling metric is sensitive to when fibres are not in the load bearing configuration and can characterize which plaques are more vulnerable to rupture, aiding in diagnosis and eventual treatment options.

5.4.1   Limitations

A number of limitations that must be mentioned as a part of this study. Firstly, computational models in this study do not include the zero-pressure configuration, residual stress or patient specific material parameters except for the changing of the fibre angles once informed with DTI. The reason for this is that it allows for direct understanding of the impact of varying the fibre angle has on the simulation and the estimated RM values. To ensure a more patient specific response, these methods should be included in future simulations. However, because this study solely is focused on the fibre orientation and the incorporation of DTI fibre angles and the effect this has on the calculated remodelling metric, these methods were excluded. Another limitation of this study is the inability to use DIC to correct the strain data obtained from the zwick for my data. Due to the samples exhibiting this layered failure and the speckle pattern being administered on the luminal side it was not possible to obtain robust results of the local tissue strain using DIC, so the Zwick strain is used in this analysis. Lastly, it must be stated that the rate of remodelling and the production and degradation of collagen that are involved in the remodelling process is neglected in this work. However, what we do know is this "snapshot" in time and what the predicted optimum fibre angles should be and therefore at that moment in time how vulnerable the plaque could be.

5.5 Conclusion

This study establishes that the microstructural orientation, which is governed by the direction of collagen and cells within the tissue, can be incorporated into a patient specific finite element model and the remodelling metric can establish locations within the plaque where fibres are not in the load bearing configuration, suggesting structural weakness and possible rupture locations.

Chapter 6 Establishing a sensitive imaging indicator capable of differentiating atherosclerotic plaques more vulnerable to rupture based on its strain environment using *in-vivo* MRI: Verified using patient specific finite element models.

6.1 Introduction

Establishing a sensitive plaque rupture vulnerability measure has been the focus of many studies in the literature. This is due to the fact that atherosclerotic plaque rupture in the carotid arteries can directly lead to stroke, is one of the major contributors to CVDs and a major cause of death worldwide. Current diagnostic measures to assess vulnerable plaques at risk of rupture are mostly based on general risk factors (hypertension, age, and family history) and geometrical plaque features (degree of stenosis, intima-media thickness, and irregular plaque morphology). The most common geometrical measure used for diagnosis is the degree of stenosis, a measure based solely on luminal narrowing. It is insufficient in establishing plaque vulnerability to rupture as rupture can occur below the clinical threshold set. Rupture of atherosclerotic plaques can be observed purely as a mechanical event, where the forces imposed on the tissue exceeds its overall mechanical strength. Therefore, using mechanically sensitive imaging indicators or image-based patient specific finite element (FE) models that can estimate the stress and strain environment may be useful for plaque vulnerability assessments and prediction of future clinical events.

In this study, the aim is to characterize the strain environment across atherosclerotic plaques using *in-vivo* MRI and establish a sensitive mechanical imaging indicator that could aid in determining which plaques are more vulnerable to rupture. This study excludes the inclusion of the zero-pressure configuration and residual stress methods established in chapter 3 of this work. To do this, the circumferential strain was calculated from images taken at both diastole and systole over several slices across the entire bifurcation and plaque. The variation of the strain was also established. To verify these measurements biomechanical models that were informed from structural magnetic resonance imaging (MRI) and ex-vivo DTI were used, and the circumferential strain and the variation was calculated using set path definition to represent regions at similar intervals as the *in-vivo* MRI data. A statistical comparison was then made to establish the robustness of the techniques and if they can be used to verify the measurements obtained. Furthermore, in the imaging data a comparison between the healthy and diseased cases (both contralateral and ipsilateral sides) is performed and this comparison is similarly done for the computational models for healthy and diseased cases.

6.2 Methods

6.2.1 *In-vivo* imaging and characterizing the circumferential strain and the variation of strain across atherosclerotic plaques.

In-vivo MRI scans of the carotid arteries were obtained from healthy volunteers using a 3T whole body MRI scanner (Achieva, Phillips Medical Systems, Best, Netherlands) combined with an 8-channel dedicated bilateral carotid artery coil (Shanghai Chenguang Medical Technologies, Shanghai, China). In total, four healthy volunteers and nine patients were scanned, with both left and right side of healthy volunteers grouped as healthy datasets and diseased datasets were split into contralateral (opposite side to symptomatic location) and ipsilateral (side of symptomatic location) groups. Similar to the protocol explained in chapter 3 of this thesis, structural MRI images were acquired at two cardiac phases which allowed for the calculation of the circumferential strain across healthy vessels and diseased vessels with atherosclerotic plaques present from the delineated boundaries of the vessel, see figure 6.1.
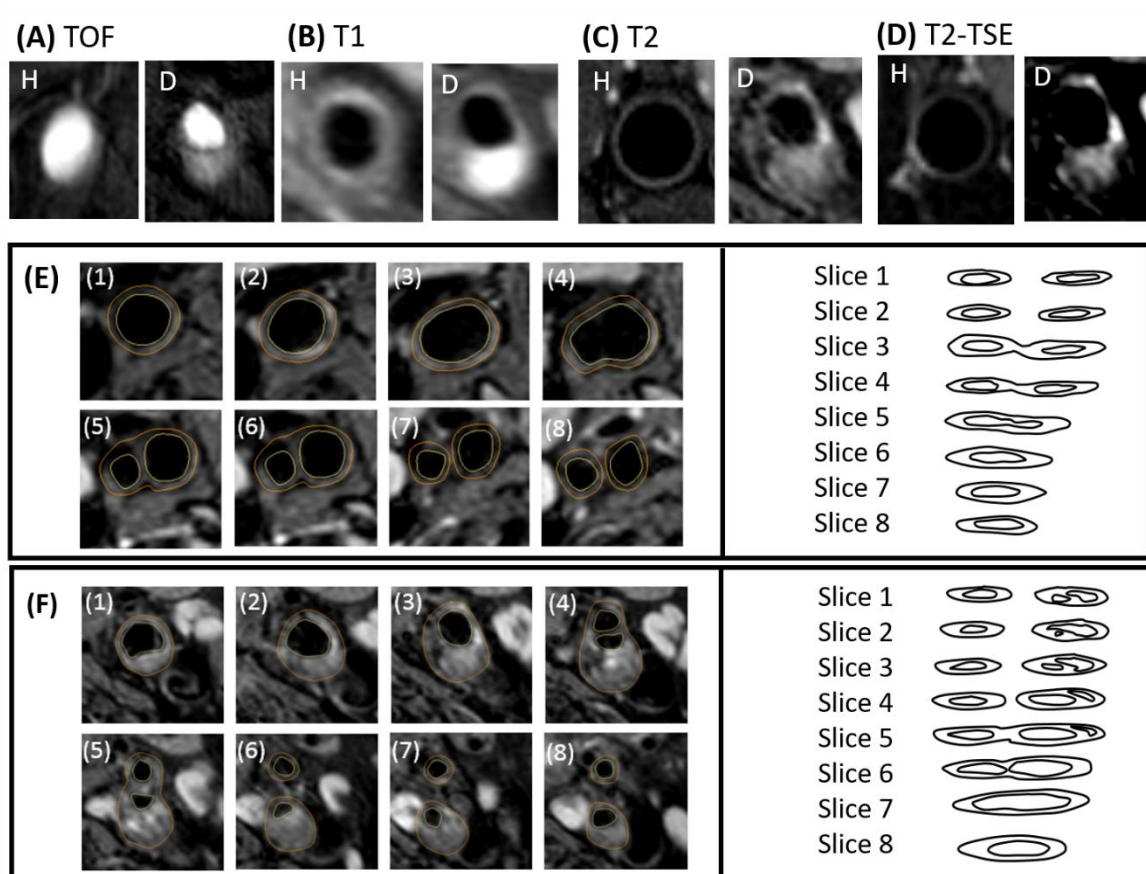
Figure 6.1: 2D structural MRI images showing different contrast weightings visualising the carotid bifurcation (A) Time of flight (TOF) (B) T1 weighting (C) T2 weighting (D) Turbo spin echo. (E) and (F) show delineation of bifurcation from structural T2 images for healthy and patient volunteers respectively, allowing calculation of the circumferential strain.

The circumferential strain was calculated for every imaging slice and is recorded so the coefficient of variation across healthy vessels and atherosclerotic plaques can be calculated using the following equation:

$$Coefficient\ of\ variation\ (COV) = \frac{\sigma}{\mu}$$ (6.1)

Where σ = standard deviation of the population and μ = mean of the population.

6.2.2   Patient specific model creation

Similar to the procedure discussed in chapter 3, section 3.2.2 the patient specific finite element geometries were created from structural *in-vivo* MRI images of the carotid bifurcation and atherosclerotic plaque. Differing from the previous protocol, one element thick models were also created from the delineated curves as shown by figure 6.2. To create these models, a quadrilateral surface mesh was created for each layer of the vessel wall and the plaque. After this, the offset function in ANSA (v17.0, BETA CAE Systems, Thessaloniki, Greece) was used to create 1 element thick models. To do this, the size of the single element in the z-direction was set to the slice thickness of the scan with a similar segmentation for the components in the vessel and atherosclerotic plaque. This allows for more accurate representation of the *in-vivo* data obtained. In total, four healthy and four diseased geometries were analysed in this study.
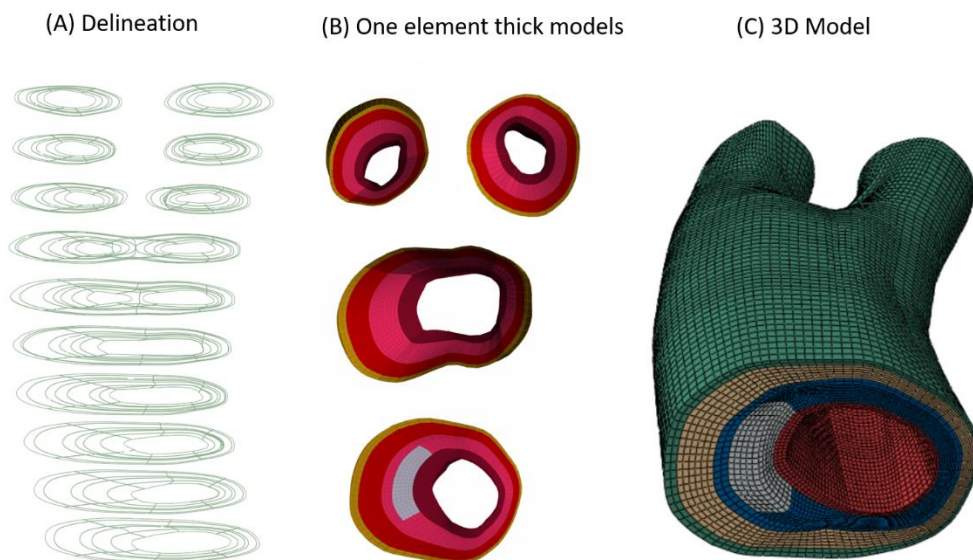
Figure 6.2: One element thick and 3D model creation of the diseased vessel wall with atherosclerotic plaque present. (A) delineation of plaque and vessel wall (B) One element thick models with plaque components (fibrotic media and intima) (C) Corresponding 3D model.

6.2.3   Statistical analysis

Firstly, in comparing the ipsilateral, contralateral and healthy *in-vivo* imaging datasets, two-tailed unpaired t-tests using Welch's correction was performed with Prism 8 statistical software (GraphPad Software Inc., San Diego, California). This allowed for direct comparisons just for the imaging datasets. Secondly, the level of agreement between the circumferential strain measurements and the coefficient of variation of circumferential strain calculated using MRI and patient specific finite element models was assessed using the Bland-Altman technique and was performed using GraphPad Prism Software. Confidence intervals in the Bland-Altman analysis were set at 95% of the bias, whereby the bias is the difference between the means of the measurement from both methods. Lastly, two-tailed unpaired t-tests using Welch's correction were performed to compare the coefficient of variation of circumferential strain extracted from MRI and FE for both healthy and diseased datasets.

6.3 Results

6.3.1   *In-vivo* circumferential strain across healthy and diseased vessels.

Extracting circumference measurements from structural images of the bifurcation at diastole and systole allowed for the calculation of circumferential strain in these vessels. Circumferential strains ranged from 8-12% in healthy carotid arteries with the values of circumferential strain and apparent elastic modulus consistent in each dataset, see figure 6.3A. In the diseased vessels, it was observed that higher strains (>12%) occurred at locations proximal and distal to plaque build-up (see figure 6.3B). Lower strains and increased stiffness were observed at locations where plaque inwardly remodels occluding the lumen diameter (see figure 6.3B i,ii and iii). There was high variability in all datasets diagnosed as symptomatic atherosclerotic plaques, with larger differences observed in dataset 3 compared with dataset 1, perhaps suggesting that the vessel in dataset 3 may be more vulnerable to rupture than the vessel in dataset 1or 2, see figure 6.3B. Furthermore, as shown by figure 6.3C, the variation of circumferential strain of the ipsilateral side was significantly different to both the contralateral side of the same patient and healthy volunteers. Interestingly, the contralateral side and the healthy were not significantly different from each other but the variation of circumferential strain was greater on the contralateral side, suggesting plaque development although not as severe as the ipsilateral side.
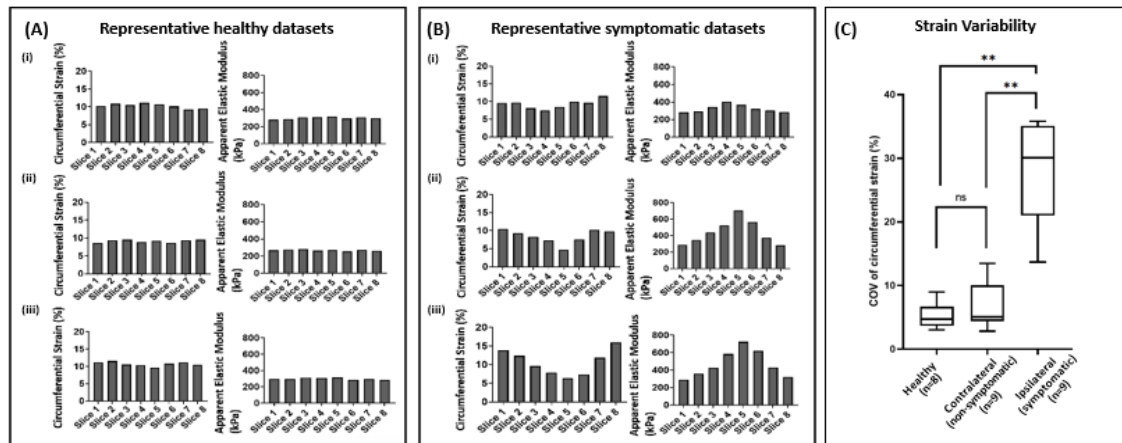
Figure 6.3: (A) Representative circumferential strain and apparent elastic modulus across healthy (n=3) datasets. (B) Representative circumferential strain and apparent elastic modulus across patient (n=3) datasets. (C) Coefficient of variation of circumferential strain across healthy (n=8) and patient (n=9) datasets. Diseased datasets were split looking at contralateral and ipsilateral sides. (**p<0.01)

6.3.2   Characterizing the circumferential strain from patient specific finite element models.

Similar to the results obtained in section 6.3.1, circumference measurements were extracted via path definitions set in the computational model at both diastole and systole that allowed for the circumferential strain to be calculated in a similar fashion to the MRI data. Like the imaging data, the representative healthy datasets showed a consistent strain range from 9-11%. In diseased vessels, again, similar to the imaging cases, there was a larger variability in the strain observed from 4-12%, with lower strains again highlighting locations where plaque inwardly remodels and occludes the lumen diameter, see figure 6.4B. The variation in the circumferential strain from healthy to diseased FE models showed a significant difference, see figure 6.4C, similar to the observations in MRI cases.
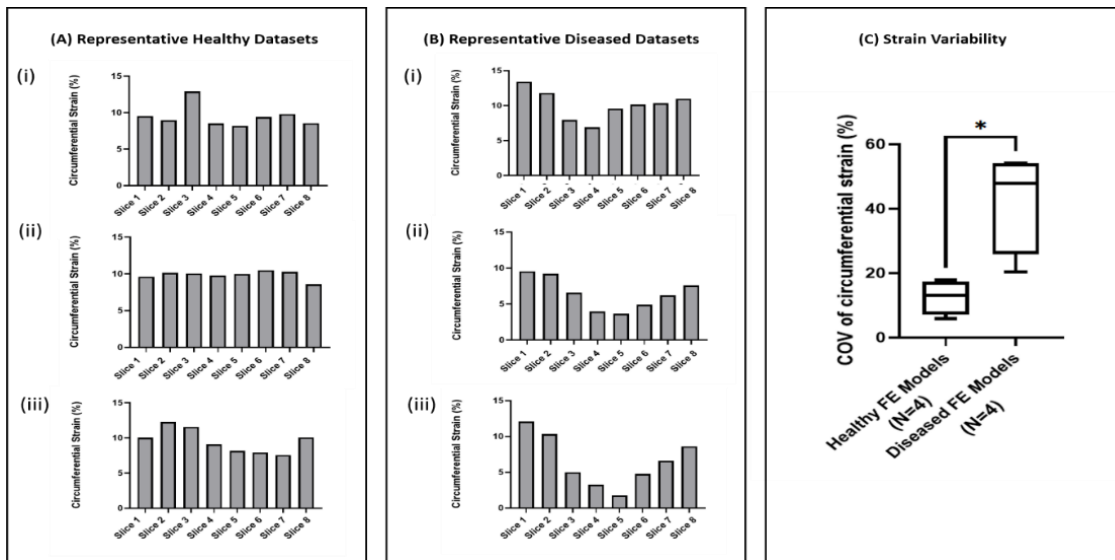
Figure 6.4: Characterizing the circumferential strain in finite element models (A) Representative circumferential strains across healthy (n=3) datasets. (B) Representative circumferential strains across patient (n=3) datasets. (C) Coefficient of variation of circumferential strain across healthy (n=4) and patient datasets (n=4), *p < 0.05

6.3.3 Statistical Analysis

Bland Altman analyses show the agreement between calculated circumferential strain measurements from both *in-vivo* MRI and patient specific computational models. Relatively, a good agreement was observed between the MRI and FE measurements, with all points falling within the confidence intervals set, see figure 6.5. It must be stated however that this comparison can be improved further especially on the computational side as it is expected that with tailored material properties (not just the fibre angles as implemented here) it could be possible to exactly match the deformation seen *in-vivo*.
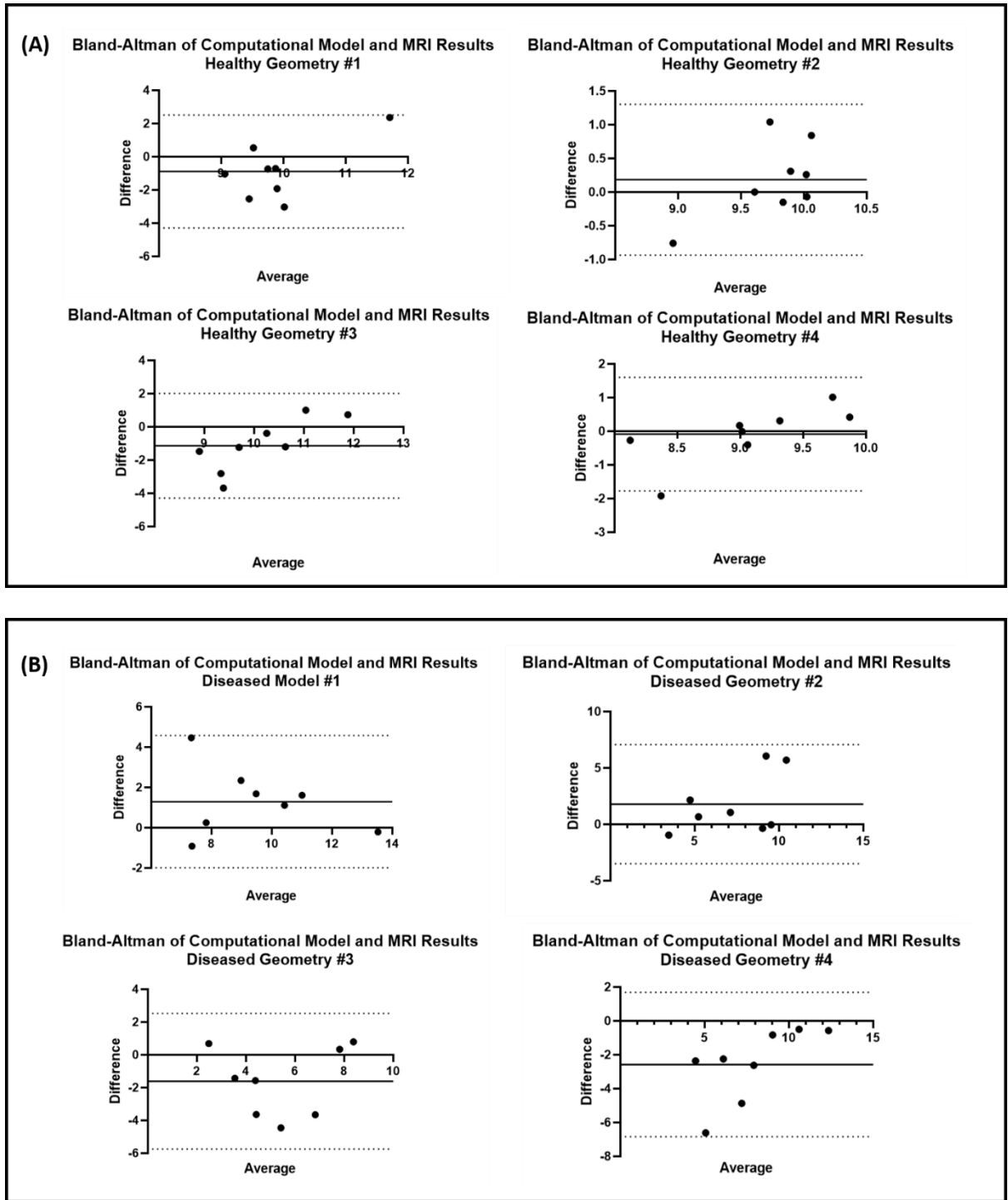
Figure 6.5: Bland Altman analyses comparing circumferential strain measurements extracted from in-vivo MRI and patient specific finite element models for all (A) healthy and (B) diseased cases examined. Each data point represents the difference in circumferential strain between an image slice in MRI and the created one element thick model.

Furthermore, comparing the coefficient of variation of circumferential strain for both FE and MRI measurements, figure 6.6 shows that there was no statistically significant difference between the healthy MRI to the corresponding healthy FE models or the diseased MRI to the

corresponding diseased FE models. This suggests that the FE models accurately capture the response expected *in-vivo*. Lastly, figure 6.6 also shows that healthy MRI measurements were significantly different than both the diseased MRI measurement and the FE measurements, showing that the variation in the circumferential strain can be used to characterize the difference between healthy and diseased.
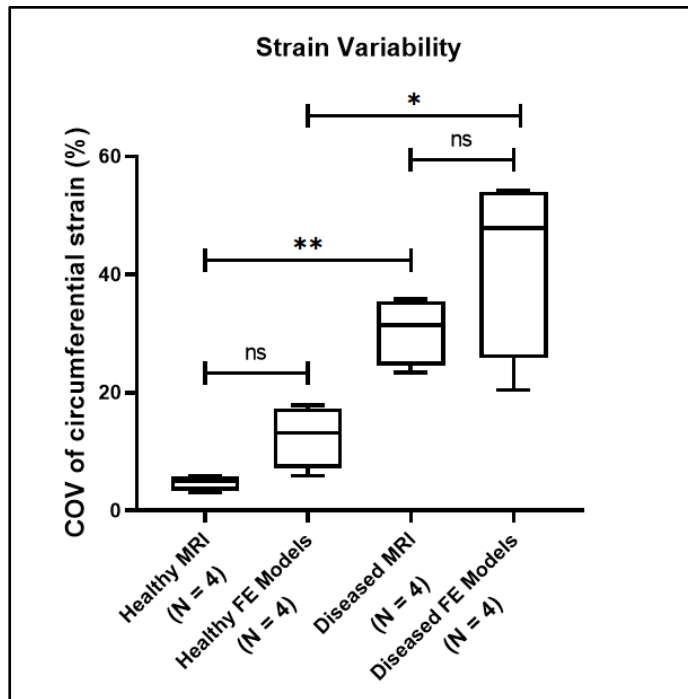
Figure 6.6: Unpaired t-test comparing the coefficient of variation of circumferential strain estimated from finite element models and In-vivo MRI across healthy and diseased datasets, *p < 0.05, **p < 0.005

6.4 Discussion

This study shows that characterizing the strain environment of atherosclerotic plaques *in-vivo* can offer a key mechanical insight into the mechanical integrity of the tissue and that patient specific finite element models can verify the results obtained and allow for further characterization of the vulnerability of atherosclerotic plaques to rupture. Ultrasound studies have shown the capability of differentiating between vulnerable and stable plaques by observing the strain environment of them *in-vivo* [146]. The method demonstrated here shows that characterizing the variation in the circumferential strain across atherosclerotic plaque *in-vivo* using MRI also has the capability of distinguishing between healthy and diseased atherosclerotic arteries. It was observed in figure 6.3, that in healthy vessels there was a consistent strain across the bifurcation with small variability. However, in diseased vessels it was observed that higher strains (>12%) occur at locations proximal and distal to the location of highest stenosis and lower strains and increased stiffness were observed at locations where plaque inwardly remodels occluding the lumen

diameter. This an important observation, as previous work presented earlier in this thesis would suggest that the reason for this high strain would be due to the collagen fibres at these locations being disorganised and orientated more axially then in the load bearing circumferential direction. Therefore, this indicates that the vessel has structural weakness and could be vulnerable to rupture. Another interesting point to note from the literature is that collagen degradation has been established as a strain driven process [189]. This suggests that in atherosclerotic plaques where a higher variability in and magnitude of the strain environment is observed there could be increased collagen degradation in the tissue. This effectively alters the capability of the tissue to remodel effectively to bear the load and remain structurally stable.

A question put forward in this study is how reliable the patient specific computational models were in estimating the circumferential strain and its variability across healthy and diseased vessels respectively. When comparing the computational measurements for the circumferential strain to the MRI, it was observed that there was an overprediction of the coefficient of variation of circumferential strain observed in the computational models for both healthy and diseased cases, see figure 6.6. Although, all circumferential strain measurements fall between the confidence intervals set in the Bland Altman analyses for comparing between the methods, see figure 6.5 and show no significant difference between MRI and FE in establishing the coefficient of variation of the circumferential strain, see figure 6.6. There could be several reasons for this overprediction of the circumferential strain observed in the FE models. One main reason would be that the material parameters were kept constant throughout every model except for alteration of the fibre angles as informed by DTI. In order to perfectly match the deformation observed *in-vivo* other material parameters need to be optimized. Most importantly though, is that even though the variation does not match exactly, there was a no significant difference observed in the values of variation of the circumferential strain when comparing MRI to the patient specific FE models. This is important as clinically FE can possibly be used as a verification tool for relevant imaging measures, such as the variation in circumferential strain. It must be noted that this is being suggested to be used as a clinical diagnosis measure involving patients whereby the relevant diagnostic scans take a significant amount of time. FE in this instance offers the choice to significantly decrease scan time but offer the same measure that can be used to aid diagnosis and treatment options. However, until this is established, and the FE protocols become more automated, it is still some way off clinical use.

6.4.1   Limitations

As stated previously, computational models in this study do not include the zero-pressure configuration, residual stress or patient specific material parameters except for the changing of the fibre angles once informed with DTI. Inverse FE analysis in conjunction with imaging

techniques can be used to obtain the undeformed configuration of real vessel geometries and characterise the patient specific material properties. It is expected that with the inclusion of these methods, a more accurate model will be created that can match the deformation experienced *in-vivo*. Another limitation is the small sample size tested for both imaging and computational analysis. To further prove the validity of the variation of circumferential strain to predict more vulnerable plaques at risk of rupture, a larger dataset would be required. Furthermore, a sensitive threshold in which a level of variation in circumferential strain would need to be established in order to become a clinically sensitive measure. Although it can be said that initial observations are extremely promising.

6.5 Conclusion

In conclusion, this study supports characterising the circumferential strain *in-vivo* in diseased carotid arteries via imaging or computational analysis to determine the plaques at greatest risk of rupture, as by knowing the strain environment, it can be predicted whether the collagen fibres are no longer aligned in the load bearing circumferential direction and consequently the risk of tissue failure may be increase.

Chapter 7 Final Discussion

Cardiovascular diseases (CVDs) are known to be one of the leading causes of death worldwide. Furthermore, CVDs were noted to be responsible for an estimated 17.8 million deaths in 2017, representing 32% of deaths globally and an increase of 21% from 2007 [1]. A contributing factor to these deaths is the development of atherosclerotic plaques in the carotid arteries. Furthermore, the presence of atherosclerotic plaques in this region is known to be a key contributor to ischaemic stroke cases. The presence of atherosclerotic plaques alters both the mechanical behaviour and the geometry of the arterial wall. Therefore, an increased understanding of the mechanical behaviour of healthy and diseased arterial tissue can enhance not only the treatment option but aid in the development of new metrics for diagnosing vulnerable plaques at risk of rupture. Remodelling encompasses the reorientation, production and degradation of collagen, with the reorientation of fibres and the inability of fibres to remodel playing a major role in the tissue's mechanical integrity. Despite the importance of the fibre orientation within these tissues, no diagnostic measure has been able to be directly associated with the microstructure. Therefore, the overall objective of this thesis was to establish the role of collagen fibres in the mechanical response of atherosclerotic plaque tissue and suggest new diagnostic measures that can infer what is happening in the microstructure. To achieve this, a combination of experimental, imaging and computational investigations was conducted to establish new sensitive indicators that indicate vulnerable plaques at risk of rupture.

The first objective of this thesis was to develop patient specific finite element models extracted from *in-vivo* MRI and establish the importance of including the zero-pressure configuration, residual stress and estimated material parameters to accurately estimate the stress experienced *in-vivo*. The reason for this is because many studies in the literature have associated the risk of atherosclerotic plaque rupture with locations subjected to high stresses in the arterial wall [88,191]. According to studies, plaques subjected to stresses in the range of 300-500 kPa generally would suggest they are vulnerable to rupture [192]. However, the robustness of computational models to accurately estimate the stress and for it to be used as a robust indicator of plaque rupture vulnerability is still up for question. From this work, stress cannot be a robust rupture vulnerability indicator without inclusion of the zero-pressure configuration, residual stress and estimated material parameters. Firstly, it is known that geometries extracted from *in-vivo* scans are already in a loaded configuration [18], therefore, simulation of a geometry at this configuration would not mimic what is occurring *in-vivo* and the resulting stress would be higher as the imposing luminal pressure will be exerted over a smaller area. Correct simulation would be to predict the zero-pressure configuration and restore the cross-sectional area as done in this thesis to then pressurize the vessel and capture the actual stress response experienced *in-vivo*. This is generally not considered in studies and therefore stress values are overpredicted and

would be in the "vulnerable" 300-500 kPa range. Secondly, residual stress is neglected which also has a major effect on the distribution of stress throughout the vessel wall. Residual stress is important as it homogenises the gradient of stress and this effectively removes peak stresses at more vulnerable locations [21,22]. Therefore, exclusion of this would again overpredict the stresses estimated. Lastly, the exclusion of patient specific material parameters would also impact the final stress calculation and should be estimated. It was observed in these results that the material properties change for each geometry, and this was done for a number of factors, such as the geometry and pressure exerted. Using literature values that are specific only to that tissue/geometry it estimated values from other geometries would not be correct as every geometry and its corresponding mechanical properties are different, even in the same person. It is observed in these simulations, using literature values would again overpredict the stress experienced in the vessel and only after estimation of patient specific properties can we better characterize these values. Overall, results shown in chapter 3 highlight that for accurate patient specific analysis of arterial bifurcations and to mimic *in-vivo* conditions the zero-pressure configuration, residual stresses and patient specific material parameters are of utmost importance and would need to be included for any patient specific analysis.

Having established that stress is not a robust indicator for measuring the level of plaque rupture vulnerability, the second objective of this thesis was to explore the influence of the collagen fibre orientation in determining the ultimate tensile strength and strain of atherosclerotic plaque tissue, specifically looking at the location deemed the most vulnerable to rupture, which is the atherosclerotic plaque cap. In chapter 4 of this thesis, the highly variable nature of the mechanical properties of atherosclerotic plaques was observed in these samples, supporting the observations seen in previous studies [7]. SALS, a non-destructive imaging technique, was used as a pre-screening tool to determine the dominate fibre orientation in these samples, thereby determining the anisotropic nature of the atherosclerotic plaque cap. These results demonstrate that the collagen fibre orientation plays the most significant role in determining the mechanical strength of the atherosclerotic plaque cap. From this data, it appears that for a given load plaque cap tissue with fibres that are aligned in the axial direction would experience higher strains and lower stresses at failure when compared to plaque cap tissue with fibres aligned in the circumferential direction. Furthermore, when we look at the correlation of collagen content to the ultimate tensile stress and strain, independent of fibre groupings, the correlation was poor, suggesting that collagen content alone does not play a significant role in the tissue's mechanical stability.

These variations in the distribution of the collagen fibres in the atherosclerotic plaque caps may be explained by looking at remodelling the diseased tissues. Bennett et al. (1999) showed that apoptosis can change the architecture of the arterial wall and lead to positive or negative remodelling of the artery during atherosclerotic plaque development [190]. Bennett et al. (1999)

also showed that apoptosis of the vascular smooth muscle cells (VSMCs) can be a major contributor to vulnerable atherosclerotic plaque rupture, where a paucity of VSMCs was observed - particularly at plaque shoulders [190]. The lack of VSMCs in the atherosclerotic atheroma can also result in lack of remodelling as new collagen fibres cannot be produced in the preferred direction to maximize the load bearing capacity of the tissue. An inability of fibres to remodel back to the load bearing configuration can lead to weakening of the arterial wall and potentially result in plaque rupture. Alongside apoptosis, studies have shown that collagen degradation is a strain dependent process [61]. Higher strains observed at locations with fibres aligned in the non-load bearing axial direction would suggest increased collagen degradation alongside this lack of new collagen deposition due to the lack of cells present.

From the knowledge obtained in chapter 4 of this thesis, the third and fourth objective of this thesis was to establish sensitive computational and imaging indicators that could aid in establishing structural weakness in atherosclerotic plaque tissue. Having observed the critical role of the collagen fibres in the mechanical response of atherosclerotic plaque caps, the distribution of the collagen fibres in healthy and diseased carotid bifurcations was investigated in Chapter 5 of this thesis. To date many constitutive laws have been proposed in the literature to incorporate the distribution of collagen fibres to accurately capture the mechanical behaviour of arterial tissue [10,181]. However, these models generally assume collagen fibre orientation from histological means [30]. The results from chapter 5, demonstrate that the remodelling metric (RM) presented here, which is based on the evolution of internal variables during the reorientation process, was able to characterize the deviation of fibres from the optimal configuration when fibres are set in the axial, circumferential and DTI-informed directions respectively. The results presented here verified previously observations stated in Ghasemi et al (2021), whereby a higher RM was estimated for fibres in the axial direction while a lower RM value was required for fibres in the circumferential direction. More interestingly though, is that in the models that have been informed by *ex-vivo* DTI, the values of the RM fall very much in between that of both axial and circumferential cases but certain locations within the plaque do exhibit a higher RM value and would be deemed vulnerable. This would suggest that the structure at these locations is weaker due to fibres not being in the load bearing configuration and that the fibre alignment is significantly different to the optimum configuration. The most important output from this work is that the RM can characterize locations where collagen fibres are not in the load bearing configuration and it is expected from the mechanical results observed in chapter 4, that these locations of high RM would also be experiencing higher strain.

Lastly, the mechanical results from chapter 4 offer potential mechanistic insights into the imaging results and computational results shown in chapter 6, which suggest that when a plaque is present, the variation of the circumferential strain experienced is significantly higher than when no plaque

is present. In diseased datasets, both MRI and FE showed that higher strains were experienced at the "shoulder" regions of the plaque and the lowest strain where the plaque showed the highest level of stenosis. This is important to note as these studies would suggest that these vulnerable plaques more than likely have fibres aligned more axially in these higher strain regions, which would subsequently fail at a lower UTS and thereby make them at higher risk of rupture. Furthermore, this study supports characterising the circumferential strain *in-vivo* in diseased carotid arteries via imaging or computational analysis to determine the plaques at greatest risk of rupture. By knowing the strain environment, it can be predicted whether the collagen fibres are no longer aligned in the load bearing circumferential direction and consequently the risk of tissue failure may be increased. Furthermore, computational analysis allows for the use of other metrics to measure plaque rupture vulnerability, such as the remodelling metric presented in chapter 5.

Chapter 8 Concluding Remarks

8.1 Summary of key findings

The overall objective of this thesis is to investigate the role of the collagen fibres in atherosclerotic plaque tissue and how it determines the tissue's overall mechanical strength. Key insights from these findings can then be used to interpret results and establish sensitive mechanical plaque rupture indicators which was achieved through structural, imaging and computational analysis. The key contributions this research has made in the field of arterial and plaque biomechanics are summarised below.

- A robust geometry creation protocol was established alongside a novel meshing technique that delivers high quality hexahedral meshes for healthy and diseased bifurcations also accounting for the atherosclerotic plaque and its components. This process can be altered for other vessels such as the aortic arch and heart valve leaflets.

- Correct simulation of the carotid bifurcation and any patient specific geometry is of utmost importance in order to establish accurate measurement of the stress and strain. In this research a robust zero pressure configuration, residual stress and inverse finite element material parameter estimation algorithm was presented on a number of geometries and can be extended to atherosclerotic plaques and its components. Each method impacts the estimated stress and strain observed in the finite element models and for accurate simulation, should be included.

- It is the opinion after this research that stress in not a robust indicator of the rupture risk and there are several reasons for this: Firstly, stress as an entity is not an easy thing to measure *in-vivo*. It is possible to do strain-based imaging or either elastography to establish the strain or stiffness respectively and it is why circumferential strain is suggested in later chapters. Secondly, without use of the methods established in chapter 3 of this thesis, the specificity of the stress measurement comes into question. As previously stated, the geometry acquired at imaging is already in a loaded configuration, so without going back to the unloaded configuration first the stress predicted will not be what it is *in-vivo*. Furthermore, the arterial wall has residual stress that homogenises the stress gradient and this is generally neglected. Lastly estimated material parameters are needed to correctly map the deformation observed *in-vivo*, and these factors all effect the estimated stress and therefore increase the difficulty for it to be used as a robust indicator of rupture risk

- The collagen fibre orientation plays a critical role in the mechanical strength of atherosclerotic plaque cap tissue. The study presented in chapter 4 demonstrates that the mechanical integrity of the plaque cap is governed by collagen fibres and that collagen content alone may not be a robust predictor of plaque rupture. The critical role of collagen fibre orientation relative to the dominant loading direction in the vessel shows, that for maximum strength, collagen fibres should be in the load bearing circumferential direction. When collagen fibres are predominantly in the circumferential direction, the tissue exhibits a higher ultimate tensile strength and overall stiffer behaviour with lower strains, as compared to plaque tissue with collagen fibres orientated in a predominantly axial direction.

- Using a previously established remodelling metric based on a continuum damage model that involves the evolution of internal variables, it is established that computational models with collagen fibres orientated in the axial direction require a larger degree of remodelling to be in the optimal configuration while the opposite trend is observed for computational models with fibres in the circumferential direction. Furthermore, models that have been informed with DTI fibre angles have RM values that fall very much in between both axial and circumferential cases with locations of higher RM observed at more vulnerable locations such as plaque shoulders. Furthermore, the severity of each plaque analysed here is quite different to each other as certain plaques have higher RM present. Overall, these high RM values would suggest that these plaques are more likely to be structurally weak as fibres are not in the load bearing configuration and therefore would be deemed more vulnerable

- The variation of circumferential strain observed across atherosclerotic plaques on the ipsilateral side is significantly different from both healthy and contralateral sides. Larger strains observed at plaque shoulders (regions proximal and distal to higher stenosis) would suggest that the collagen fibres at this location are not in the load bearing configuration and ultimately would fail at lower stress. This suggests that not only can characterizing the strain variation differentiate between vulnerable and more stable plaques but it can also infer information on the expected fibre orientation within these plaques, whereby a larger strain would suggest more axially aligned fibres and in turn structural weakness.

- Patient specific finite element models informed by ex-vivo DTI fibre angles can accurately capture the strain variation observed in the *in-vivo* MRI data. The results shown highlight that patient specific finite element models can be used in conjunction with imaging data to estimate the strain environment accurately but can also give information on other measures of relevance such as the remodelling metric presented here.

8.2 Future perspectives

Whilst this thesis makes considerable advancement in terms of assessing the risk of atherosclerotic plaque rupture by understanding more of the mechanics of the tissue, the following recommendations are proposed for future investigations:

- Results shown in chapter 3 highlight that for accurate simulation of patient specific geometries it is important to estimate the zero-pressure configuration, residual stress and material parameters for every individual case. It is suggested that the inclusion of these methods become standard practice for future computational models looking into developing diagnostic measures.

- Results shown in chapter 4 demonstrate that the collagen fibre orientation plays a critical role in determining the mechanical strength of atherosclerotic plaque tissue. It is expected that increased sample numbers would strengthen this relationship further and is suggested as future work. An area that is neglected in this work is to quantify the calcification content and the number of microcalcifications within these atherosclerotic plaque caps. Microcalcifications can act as stress concentrators within the tissue and depending on their location within the cap can promote fracture. A suggestion would be to also group tested plaque cap samples by calcification content or microcalcification number in order to establish which plaques are more fibrous, which ones are more calcified and their corresponding mechanical response.

- Results shown in chapter 5 suggest the DTI shows great promise in establishing the dominant microstructural orientation within arterial and plaque tissue and can be used to directly inform patient specific computational models for more accurate estimation of the stress-strain environment of the tissue. Furthermore, the results in chapter 5 also demonstrate that the remodelling metric implemented could possibly be used as an indicator of whether plaques have fibres in the load bearing or non-load bearing configurations respectively. To further validate the robustness of this indicator, a larger dataset is recommended but initial observations are promising. In addition, a sensitive threshold for the RM presented here could be calibrated using *in vitro* inflation tests.

- Results from chapter 6 show the highly variable strain environment that atherosclerotic plaques experience *in-vivo* and that these measurements can accurately be predicted using patient specific finite element models that are informed by the collagen fibre angles. Future work should look at increasing the total number of datasets analysed to further prove the robustness of both techniques.

- In this thesis, the influence of cells on the mechanical behaviour of arterial tissue and atherosclerotic plaques was neglected in these simulations. Cells are known to contribute to the production and growth of the collagen fibres in arterial tissue. However, in atherosclerotic plaque tissue there may be reduced vascular smooth muscle cells in the tissue limiting the production of new collagen oriented in the load bearing configuration. Future work should look to include the influence of cells on the mechanical behaviour of the tissue. Moreover, the active contribution cells play in terms of contractility of the tissue should be investigated further.

- Another aspect not addressed in this thesis is the degradation of collagen in arterial tissue and atherosclerotic plaques. It is known that matrix metalloproteases (MMPs) degrade the extracellular matrix of the tissue and previous research has shown that collagen degradation in arterial tissue is strain dependent. Degradation would have significant influence on the artery and the atherosclerotic plaque's ability to remodel sufficiently and cause weakening at locations experiencing high strain variability. A study to investigate which MMPs drive this degradation response would be of key interest.

References

[1]   S.S. Virani, A. Alonso, E.J. Benjamin, M.S. Bittencourt, C.W. Callaway, A.P. Carson, A.M. Chamberlain, A.R. Chang, S. Cheng, F.N. Delling, L. Djousse, M.S.V. Elkind, J.F. Ferguson, M. Fornage, S.S. Khan, B.M. Kissela, K.L. Knutson, T.W. Kwan, D.T. Lackland, T.T. Lewis, J.H. Lichtman, C.T. Longenecker, M.S. Loop, P.L. Lutsey, S.S. Martin, K. Matsushita, A.E. Moran, M.E. Mussolino, A.M. Perak, W.D. Rosamond, G.A. Roth, U.K.A. Sampson, G.M. Satou, E.B. Schroeder, S.H. Shah, C.M. Shay, N.L. Spartano, A. Stokes, D.L. Tirschwell, L.B. VanWagner, C.W. Tsao, S.S. Wong, D.G. Heard, Heart disease and stroke statistics—2020 update: A report from the American Heart Association, 2020. https://doi.org/10.1161/CIR.0000000000000757.

[2]   C.D. Mathers, D. Loncar, Projections of Global Mortality and Burden of Disease from 2002 to 2030, 3 (2015). https://doi.org/10.1371/journal.pmed.0030442.

[3]   A. Timmis, N. Townsend, C.P. Gale, A. Torbica, M. Lettino, S.E. Petersen, E.A. Mossialos, A.P. Maggioni, D. Kazakiewicz, H.T. May, D. De Smedt, M. Flather, L. Zuhlke, J.F. Beltrame, R. Huculeci, L. Tavazzi, G. Hindricks, J. Bax, B. Casadei, S. Achenbach, L. Wright, P. Vardas, L. Mimoza, G. Artan, D. Aurel, M. Chettibi, N. Hammoudi, H. Sisakian, S. Pepoyan, B. Metzler, P. Siostrzonek, F. Weidinger, T. Jahangirov, F. Aliyev, Y. Rustamova, N.M.A. Mrochak, P. Lancellotti, A. Pasquet, M. Claeys, Z. Kusljugic, L.D. Hudic, E. Smajic, M.P. Tokmakova, P.M. Gatzov, D. Milicic, M. Bergovec, C. Christou, H.H. Moustra, T. Christodoulides, A. Linhart, M. Taborsky, M. Abdelhamid, K. Shokry, P. Kampus, M. Viigimaa, E. Ryödi, M. Niemela, T.T. Rissanen, J.Y. Le Heuzey, M. Gilard, A. Aladashvili, A. Gamkrelidze, M. Kereselidze, A. Zeiher, H. Katus, K. Bestehorn, C. Tsioufis, J. Goudevenos, Z. Csanádi, D. Becker, K. Tóth, P.J. Hrafnkelsdóttir, J. Crowley, P. Kearney, B. Dalton, D. Zahger, A. Wolak, D. Gabrielli, C. Indolfi, S. Urbinati, G. Imantayeva, S. Berkinbayev, G. Bajraktari, A. Ahmeti, G. Berisha, M. Erkin, A. Saamay, A. Erglis, I. Bajare, S. Jegere, M. Mohammed, A. Sarkis, G. Saadeh, R. Zvirblyte, G. Sakalyte, R. Slapikas, K. Ellafi, F. El Ghamari, C. Banu, J. Beissel, T. Felice, S.C. Buttigieg, R.G. Xuereb, M. Popovici, A. Boskovic, M. Rabrenovic, S. Ztot, S. Abir-Khalil, A.C. Van Rossum, B.J.M. Mulder, M.W. Elsendoorn, E. Srbinovska-Kostovska, J. Kostov, B. Marjan, T. Steigen, O.C. Mjølstad, P. Ponikowski, A. Witkowski, P. Jankowski, V.M. Gil, J. Mimoso, S. Baptista, D. Vinereanu, O. Chioncel, B.A. Popescu, E. Shlyakhto, R. Oganov, M. Foscoli, M. Zavatta, A.D. Dikic, B. Beleslin, M.R. Radovanovic, P. Hlivak, R. Hatala, G. Kaliska, M. Kenda, Z. Fras, M. Anguita, A. Cequier, J. Muniz, S. James, B. Johansson, P. Platonov, M.J. Zellweger, G.B. Pedrazzini, D. Carballo, H.E. Shebli, S. Kabbani, L. Abid, F. Addad, E. Bozkurt, M. Kayikçioğlu, M.K. Erol, V. Kovalenko, E. Nesukay, A. Wragg, P. Ludman, S. Ray, R. Kurbanov, D. Boateng, G. Daval, V. De Benito Rubio, D. Sebastiao, P.T. De Courtelary, I. Bardinet, European society of cardiology: Cardiovascular disease statistics 2019, Eur. Heart J. 41 (2020) 12–85. https://doi.org/10.1093/eurheartj/ehz859.

[4]   D. Mozaffarian, E.J. Benjamin, A.S. Go, D.K. Arnett, M.J. Blaha, M. Cushman, S.R. Das, S. De Ferranti, J. Després, H.J. Fullerton, V.J. Howard, M.D. Huffman, C.R. Isasi, M.C. Jiménez, S.E. Judd, B.M. Kissela, J.H. Lichtman, L.D. Lisabeth, S. Liu, R.H. Mackey, D.J. Magid, D.K. Mcguire, E.R.M. Iii, C.S. Moy, P. Muntner, M.E. Mussolino, K. Nasir, R.W. Neumar, G. Nichol, L. Palaniappan, D.K. Pandey, M.J. Reeves, C.J. Rodriguez, W. Rosamond, P.D. Sorlie, J. Stein, A. Towfighi, T.N. Turan, S.S. Virani, D. Woo, R.W. Yeh, M.B. Turner, AHA Statistical Update Heart Disease and Stroke Statistics — 2016 Update A Report From the American Heart Association WRITING GROUP MEMBERS, 2016. https://doi.org/10.1161/CIR.0000000000000350.

[5]   E.J. Benjamin, M.J. Blaha, S.E. Chiuve, M. Cushman, S.R. Das, R. Deo, S.D. De Ferranti,

J. Floyd, M. Fornage, C. Gillespie, C.R. Isasi, M.C. Jim'nez, L.C. Jordan, S.E. Judd, D. Lackland, J.H. Lichtman, L. Lisabeth, S. Liu, C.T. Longenecker, R.H. MacKey, K. Matsushita, D. Mozaffarian, M.E. Mussolino, K. Nasir, R.W. Neumar, L. Palaniappan, D.K. Pandey, R.R. Thiagarajan, M.J. Reeves, M. Ritchey, C.J. Rodriguez, G.A. Roth, W.D. Rosamond, C. Sasson, A. Towfghi, C.W. Tsao, M.B. Turner, S.S. Virani, J.H. Voeks, J.Z. Willey, J.T. Wilkins, J.H.Y. Wu, H.M. Alger, S.S. Wong, P. Muntner, Heart Disease and Stroke Statistics 2017 Update: A Report from the American Heart Association, 2017. https://doi.org/10.1161/CIR.0000000000000485.

[6]   WHO, Global status report on noncommunicable diseases 2010, World Heal. Organ. (2011) 176. https://doi.org/ISBN 978 92 4 156422 9.

[7]   G.A. Roth, C. Johnson, A. Abajobir, F. Abd-Allah, S.F. Abera, G. Abyu, M. Ahmed, B. Aksut, T. Alam, K. Alam, F. Alla, N. Alvis-Guzman, S. Amrock, H. Ansari, J. Ärnlöv, H. Asayesh, T.M. Atey, L. Avila-Burgos, A. Awasthi, A. Banerjee, A. Barac, T. Bärnighausen, L. Barregard, N. Bedi, E. Belay Ketema, D. Bennett, G. Berhe, Z. Bhutta, S. Bitew, J. Carapetis, J.J. Carrero, D.C. Malta, C.A. Castañeda-Orjuela, J. Castillo-Rivas, F. Catalá-López, J.Y. Choi, H. Christensen, M. Cirillo, L. Cooper, M. Criqui, D. Cundiff, A. Damasceno, L. Dandona, R. Dandona, K. Davletov, S. Dharmaratne, P. Dorairaj, M. Dubey, R. Ehrenkranz, M. El Sayed Zaki, E.J.A. Faraon, A. Esteghamati, T. Farid, M. Farvid, V. Feigin, E.L. Ding, G. Fowkes, T. Gebrehiwot, R. Gillum, A. Gold, P. Gona, R. Gupta, T.D. Habtewold, N. Hafezi-Nejad, T. Hailu, G.B. Hailu, G. Hankey, H.Y. Hassen, K.H. Abate, R. Havmoeller, S.I. Hay, M. Horino, P.J. Hotez, K. Jacobsen, S. James, M. Javanbakht, P. Jeemon, D. John, J. Jonas, Y. Kalkonde, C. Karimkhani, A. Kasaeian, Y. Khader, A. Khan, Y.H. Khang, S. Khera, A.T. Khoja, J. Khubchandani, D. Kim, D. Kolte, S. Kosen, K.J. Krohn, G.A. Kumar, G.F. Kwan, D.K. Lal, A. Larsson, S. Linn, A. Lopez, P.A. Lotufo, H.M.A. El Razek, R. Malekzadeh, M. Mazidi, T. Meier, K.G. Meles, G. Mensah, A. Meretoja, H. Mezgebe, T. Miller, E. Mirrakhimov, S. Mohammed, A.E. Moran, K.I. Musa, J. Narula, B. Neal, F. Ngalesoni, G. Nguyen, C.M. Obermeyer, M. Owolabi, G. Patton, J. Pedro, D. Qato, M. Qorbani, K. Rahimi, R.K. Rai, S. Rawaf, A. Ribeiro, S. Safiri, J.A. Salomon, I. Santos, M. Santric Milicevic, B. Sartorius, A. Schutte, S. Sepanlou, M.A. Shaikh, M.J. Shin, M. Shishehbor, H. Shore, D.A.S. Silva, E. Sobngwi, S. Stranges, S. Swaminathan, R. Tabarés-Seisdedos, N. Tadele Atnafu, F. Tesfay, J.S. Thakur, A. Thrift, R. Topor-Madry, T. Truelsen, S. Tyrovolas, K.N. Ukwaja, O. Uthman, T. Vasankari, V. Vlassov, S.E. Vollset, T. Wakayo, D. Watkins, R. Weintraub, A. Werdecker, R. Westerman, C.S. Wiysonge, C. Wolfe, A. Workicho, G. Xu, Y. Yano, P. Yip, N. Yonemoto, M. Younis, C. Yu, T. Vos, M. Naghavi, C. Murray, Global, Regional, and National Burden of Cardiovascular Diseases for 10 Causes, 1990 to 2015, J. Am. Coll. Cardiol. 70 (2017) 1–25. https://doi.org/10.1016/j.jacc.2017.04.052.

[8]   S. Carr, A. Farb, W.H. Pearce, R. Virmani, J.S.T. Yao, H.S. Bassiouny, P. Gloviczki, Atherosclerotic plaque rupture in symptomatic carotid artery stenosis, J. Vasc. Surg. 23 (1996) 755–766. https://doi.org/10.1016/S0741-5214(96)70237-9.

[9]   W. Insull, The Pathology of Atherosclerosis: Plaque Development and Plaque Responses to Medical Treatment, Am. J. Med. 122 (2009) S3–S14. https://doi.org/10.1016/j.amjmed.2008.10.013.

[10]   G.A. Holzapfel, T.C. Gasser, R.W. Ogden, A new constitutive framework for arterial wall mechanics and a comparative study of material models, J. Elast. 61 (2000) 1–48. https://doi.org/10.1023/A:1010835316564.

[11]   T.C. Gasser, R.W. Ogden, G.A. Holzapfel, Hyperelastic modelling of arterial layers with distributed collagen fibre orientations, (2006) 15–35. https://doi.org/10.1098/rsif.2005.0073.

[12]   A. Creane, E. Maher, S. Sultan, N. Hynes, D.J. Kelly, C. Lally, Prediction of fibre

architecture and adaptation in diseased carotid bifurcations, Biomech. Model. Mechanobiol. 10 (2011) 831–843. https://doi.org/10.1007/s10237-010-0277-8.

[13]   A. Creane, E. Maher, S. Sultan, N. Hynes, D.J. Kelly, C. Lally, A remodelling metric for angular fibre distributions and its application to diseased carotid bifurcations, (2011). https://doi.org/10.1007/s10237-011-0358-3.

[14]   I. Hariton, G. DeBotton, T.C. Gasser, G.A. Holzapfel, Stress-driven collagen fiber remodeling in arterial walls, Biomech. Model. Mechanobiol. 6 (2007) 163–175. https://doi.org/10.1007/s10237-006-0049-7.

[15]   S. Fausten, D. Balzani, J. Schröder, An algorithmic scheme for the automated calculation of fiber orientations in arterial walls, Comput. Mech. 58 (2016) 861–878. https://doi.org/10.1007/s00466-016-1321-z.

[16]   M. Ghasemi, D.R. Nolan, C. Lally, An investigation into the role of different constituents in damage accumulation in arterial tissue and constitutive model development, Biomech. Model. Mechanobiol. (2018). https://doi.org/10.1007/s10237-018-1054-3.

[17]   D. Balzani, S. Brinkhues, G.A. Holzapfel, Constitutive framework for the modeling of damage in collagenous soft tissues with application to arterial walls, Comput. Methods Appl. Mech. Eng. 213–216 (2012) 139–151. https://doi.org/10.1016/j.cma.2011.11.015.

[18]   M.L. Raghavan, B. Ma, M.F. Fillinger, Non-invasive determination of zero-pressure geometry of arterial aneurysms, Ann. Biomed. Eng. 34 (2006) 1414–1419. https://doi.org/10.1007/s10439-006-9115-7.

[19]   S. de Putter, B.J.B.M. Wolters, M.C.M. Rutten, M. Breeuwer, F.A. Gerritsen, F.N. van de Vosse, Patient-specific initial wall stress in abdominal aortic aneurysms with a backward incremental method, J. Biomech. 40 (2007) 1081–1090. https://doi.org/10.1016/j.jbiomech.2006.04.019.

[20]   C.J. Chuong, Y.C. Fung, Three-dimensional stress distribution in arteries., J. Biomech. Eng. 105 (1983) 268–74. http://www.ncbi.nlm.nih.gov/pubmed/6632830.

[21]   A. Delfino, N. Stergiopulos, J.E. Moore, J.J. Meister, Residual strain effects on the stress field in a thick wall finite element model of the human carotid bifurcation, J. Biomech. 30 (1997) 777–786. https://doi.org/10.1016/S0021-9290(97)00025-0.

[22]   J. Schröder, S. Brinkhues, A novel scheme for the approximation of residual stresses in arterial walls, Arch. Appl. Mech. 84 (2014) 881–898. https://doi.org/10.1007/s00419-014-0838-x.

[23]   A. Wittek, K. Karatolios, P. Bihari, T. Schmitz-rixen, R. Moosdorf, S. Vogt, C. Blase, In vivo determination of elastic properties of the human aorta based on 4D ultrasound data, J. Mech. Behav. Biomed. Mater. 27 (2013) 167–183. https://doi.org/10.1016/j.jmbbm.2013.03.014.

[24]   A. Wittek, W. Derwich, K. Karatolios, P. Fritzen, S. Vogt, T. Schmitz-rixen, C. Blase, A fi nite element updating approach for identi fi cation of the anisotropic hyperelastic properties of normal and diseased aortic walls from 4D ultrasound strain imaging, J. Mech. Behav. Biomed. Mater. 58 (2016) 122–138. https://doi.org/10.1016/j.jmbbm.2015.09.022.

[25]   M. Liu, L. Liang, W. Sun, A new inverse method for estimation of in vivo mechanical properties of the aortic wall, J. Mech. Behav. Biomed. Mater. 72 (2017) 148–158. https://doi.org/10.1016/j.jmbbm.2017.05.001.

[26]   M.T. Walsh, E.M. Cunnane, J.J. Mulvihill, A.C. Akyildiz, F.J.H. Gijsen, G.A. Holzapfel, Uniaxial tensile testing approaches for characterisation of atherosclerotic plaques, J.

Biomech. 47 (2014) 793–804. https://doi.org/10.1016/j.jbiomech.2014.01.017.

[27] L.A. Davis, S.E. Stewart, C.G. Carsten, B.A. Snyder, M.A. Sutton, S.M. Lessner, Characterization of fracture behavior of human atherosclerotic fibrous caps using a miniature single edge notched tensile test, Acta Biomater. 43 (2016) 101–111. https://doi.org/10.1016/j.actbio.2016.07.027.

[28] Z. Teng, Y. Zhang, Y. Huang, J. Feng, J. Yuan, Q. Lu, M.P.F. Sutcliffe, A.J. Brown, Z. Jing, J.H. Gillard, Material properties of components in human carotid atherosclerotic plaques: A uniaxial extension study, Acta Biomater. 10 (2014) 5055–5063. https://doi.org/10.1016/j.actbio.2014.09.001.

[29] C. Pagiatakis, R. Galaz, J.C. Tardif, R. Mongrain, A comparison between the principal stress direction and collagen fiber orientation in coronary atherosclerotic plaque fibrous caps, Med. Biol. Eng. Comput. 53 (2015) 545–555. https://doi.org/10.1007/s11517-015-1257-z.

[30] G.R. Douglas, A.J. Brown, J.H. Gillard, M.R. Bennett, M.P.F. Sutcliffe, Z. Teng, Impact of Fiber Structure on the Material Stability and Rupture Mechanisms of Coronary Atherosclerotic Plaques, Ann. Biomed. Eng. 45 (2017) 1462–1474. https://doi.org/10.1007/s10439-017-1827-3.

[31] S. Ghazanfari, A. Driessen-Mol, G.J. Strijkers, F.M.W. Kanters, F.P.T. Baaijens, C.V.C. Bouten, A comparative analysis of the collagen architecture in the carotid artery: Second harmonic generation versus diffusion tensor imaging, Biochem. Biophys. Res. Commun. 426 (2012) 54–58. https://doi.org/10.1016/j.bbrc.2012.08.031.

[32] R.T. Gaul, D.R. Nolan, C. Lally, Collagen fibre characterisation in arterial tissue under load using SALS, J. Mech. Behav. Biomed. Mater. 75 (2017) 359–368. https://doi.org/10.1016/j.jmbbm.2017.07.036.

[33] A. Whelan, J. Duffy, R.T. Gaul, D. O'Reilly, D.R. Nolan, P. Gunning, C. Lally, B.P. Murphy, Collagen fibre orientation and dispersion govern ultimate tensile strength, stiffness and the fatigue performance of bovine pericardium, J. Mech. Behav. Biomed. Mater. 90 (2019) 54–60. https://doi.org/10.1016/j.jmbbm.2018.09.038.

[34] M.C. Robitaille, R. Zareian, C.A. DiMarzio, K.T. Wan, J.W. Ruberti, Small-angle light scattering to detect strain-directed collagen degradation in native tissue, Interface Focus. 1 (2011) 767–776. https://doi.org/10.1098/rsfs.2011.0039.

[35] M.S. Sacks, D.B. Smith, E.D. Hiester, A small angle light scattering device for planar connective tissue microstructural analysis, Ann. Biomed. Eng. 25 (1997) 678–689. https://doi.org/10.1007/BF02684845.

[36] V. Flamini, C. Kerskens, K.M. Moerman, C.K. Simms, C. Lally, Imaging arterial fibres using diffusion tensor imaging-feasibility study and preliminary results, EURASIP J. Adv. Signal Process. 2010 (2010) 6–8. https://doi.org/10.1155/2010/904091.

[37] V. Flamini, C. Kerskens, C. Simms, C. Lally, Fibre orientation of fresh and frozen porcine aorta determined non-invasively using diffusion tensor imaging, Med. Eng. Phys. (2012). https://doi.org/10.1016/j.medengphy.2012.08.008.

[38] A.C. Akyildiz, C.K. Chai, C.W.J. Oomens, A. van der Lugt, F.P.T. Baaijens, G.J. Strijkers, F.J.H. Gijsen, 3D Fiber Orientation in Atherosclerotic Carotid Plaques, J. Struct. Biol. 200 (2017) 28–35. https://doi.org/10.1016/j.jsb.2017.08.003.

[39] B. Tornifoglio, A.J. Stone, R.D. Johnston, S.S. Shahid, C. Kerskens, C. Lally, Diffusion tensor imaging and arterial tissue: establishing the influence of arterial tissue microstructure on fractional anisotropy, mean diffusivity and tractography, Sci. Rep. 10

(2020) 1–12. https://doi.org/10.1038/s41598-020-77675-x.

[40] J.L. Mas, Internal carotid artery revascularization, Rev. Esp. Cardiol. 60 (2007) 861–871. https://doi.org/10.1157/13109000.

[41] H. Gray, Anatomy of the Human Body, 20th ed., 1918.

[42] L.R. Fiedler, Cardiovascular Research: Past, Present and Future, Hear. Res. - Open J. 2 (2015) 70–81. https://doi.org/10.17140/hroj-2-112.

[43] J.A.G. Rhodin, Architecture of the Vessel Wall, in: John Wiley & Sons (Ed.), Compr. Physiol., Hoboken, NJ, USA, 1980: pp. 1–31. https://doi.org/10.1002/cphy.cp020201.

[44] A. Milutinović, D. Šuput, R. Zorc-Pleskovič, Pathogenesis of atherosclerosis in the tunica intima, media, and adventitia of coronary arteries: An updated review, Bosn. J. Basic Med. Sci. 20 (2020) 21–30. https://doi.org/10.17305/bjbms.2019.4320.

[45] H.M. den Ruijter, S.A. Peters, T.J. Anderson, Common Carotid Intima-Media Thickness Measurements in Cardiovascular Risk Prediction: A Meta-Analysis, J. Vasc. Surg. 56 (2012) 1810. https://doi.org/10.1016/j.jvs.2012.10.058.

[46] D.E. Grobbee, M.L. Bots, Carotid artery intima-media thickness as an indicator of generalized atherosclerosis, J. Intern. Med. 236 (1994) 567–573. https://doi.org/10.1111/j.1365-2796.1994.tb00847.x.

[47] C. Burton, Relation of Structure of the Wall, Physiol. Rev. 34 (1954) 619–642.

[48] A.J.A. Leloup, C.E. Van Hove, A. Heykers, D.M. Schrijvers, G.R.Y. De Meyer, P. Fransen, Elastic and muscular arteries differ in structure, basal NO production and voltage-gated Ca2+-channels, Front. Physiol. 6 (2015) 1–9. https://doi.org/10.3389/fphys.2015.00375.

[49] P.B. Canham, H.M. Finlay, Morphometry of medial gaps of human brain artery branches, Stroke. 35 (2004) 1153–1157. https://doi.org/10.1161/01.STR.0000124926.76836.df.

[50] G. Holzapfel, Collagen in Arterial Walls: Biomechanical Aspects. In: FRATZL, P. (ed.) Collagen Structure and Mechanics, Collagen Struct. Mech. Springer V (2008) Heidelberg, Germany.

[51] A.P. Ebrahimi, Mechanical properties of normal and diseased cerebrovascular system., J. Vasc. Interv. Neurol. 2 (2009) 155–62. http://www.ncbi.nlm.nih.gov/pubmed/22518247%0Ahttp://www.pubmedcentral.nih.gov/articlerender.fcgi?artid=PMC3317338.

[52] K.M. Erickson, D.J. Cole, Carotid artery disease: stenting vs endarterectomy, Br. J. Anaesth. 105 (2010) i34–i49. https://doi.org/10.1093/bja/aeq319.

[53] G.A. Holzapfel, G. Sommer, C.T. Gasser, P. Regitnig, Determination of layer-specific mechanical properties of human coronary arteries with nonatherosclerotic intimal thickening and related constitutive modeling, Am. J. Physiol. - Hear. Circ. Physiol. 289 (2005) 2048–2058. https://doi.org/10.1152/ajpheart.00934.2004.

[54] R.A. Macrae, K. Miller, B.J. Doyle, Methods in Mechanical Testing of Arterial Tissue: A Review, Strain. 52 (2016) 380–399. https://doi.org/10.1111/str.12183.

[55] D. Balzani, D. Gross, Simulation of discontinuous damage incorporating residual stresses in circumferentially overstretched atherosclerotic arteries, 2 (2006) 609–618. https://doi.org/10.1016/j.actbio.2006.06.005.

[56] M.L. Raghavan, S. Trivedi, A. Nagaraj, D.D. McPherson, K.B. Chandran, Three-dimensional finite element analysis of residual stress in arteries, Ann. Biomed. Eng. 32

(2004) 257–263. https://doi.org/10.1023/B:ABME.0000012745.05794.32.

[57]   G.A. Holzapfel, R.W. Ogden, Modelling the layer-specific three-dimensional residual stresses in arteries, with an application to the human aorta, J. R. Soc. Interface. 7 (2010) 787–799. https://doi.org/10.1098/rsif.2009.0357.

[58]   G.A. Holzapfel, G. Sommer, M. Auer, P. Regitnig, R.W. Ogden, Layer-specific 3D residual deformations of human aortas with non-atherosclerotic intimal thickening, Ann. Biomed. Eng. 35 (2007) 530–545. https://doi.org/10.1007/s10439-006-9252-z.

[59]   G. Sommer, P. Regitnig, L. Költringer, G.A. Holzapfel, Biaxial mechanical properties of intact and layer-dissected human carotid arteries at physiological and supraphysiological loadings, Am. J. Physiol. - Hear. Circ. Physiol. 298 (2010) 898–912. https://doi.org/10.1152/ajpheart.00378.2009.

[60]   G. Sommer, G.A. Holzapfel, 3D constitutive modeling of the biaxial mechanical response of intact and layer-dissected human carotid arteries, J. Mech. Behav. Biomed. Mater. 5 (2012) 116–128. https://doi.org/10.1016/j.jmbbm.2011.08.013.

[61]   R.T. Gaul, D.R. Nolan, T. Ristori, C.V.C. Bouten, S. Loerakker, C. Lally, Pressure-induced collagen degradation in arterial tissue as a potential mechanism for degenerative arterial disease progression, J. Mech. Behav. Biomed. Mater. 109 (2020) 103771. https://doi.org/10.1016/j.jmbbm.2020.103771.

[62]   A.C. Akyildiz, H.H.G. Hansen, H.A. Nieuwstadt, L. Speelman, C.L. De Korte, A.F.W. van der Steen, F.J.H. Gijsen, A Framework for Local Mechanical Characterization of Atherosclerotic Plaques: Combination of Ultrasound Displacement Imaging and Inverse Finite Element Analysis, Ann. Biomed. Eng. 44 (2016) 968–979. https://doi.org/10.1007/s10439-015-1410-8.

[63]   R. V. Luepker, Cardiovascular disease: Rise, fall, and future prospects, Annu. Rev. Public Health. 32 (2011) 1–3. https://doi.org/10.1146/annurev-publhealth-112810-151726.

[64]   P.A. VanderLaan, C.A. Reardon, G.S. Getz, Site Specificity of Atherosclerosis: Site-Selective Responses to Atherosclerotic Modulators, Arterioscler. Thromb. Vasc. Biol. 24 (2004) 12–22. https://doi.org/10.1161/01.ATV.0000105054.43931.f0.

[65]   H.C. Stary, Natural history and histological classification of atherosclerotic lesions an update, Arterioscler. Thromb. Vasc. Biol. 20 (2000) 1177–1178. https://doi.org/10.1161/01.ATV.20.5.1177.

[66]   H. Stary, A. Chandler, S. Glagov, G. Jr, W. Insull, M.J. Rosenfeld, S. Schaffer, C. Schwartz, W. Wagner, R. Wissler, A Definition of Initial , Fatty Streak , and Intermediate Lesions of Atherosclerosis, Circulation. 89 (1994) 2462–2478.

[67]   H.C. Stary, A.B. Chandler, R.E. Dinsmore, V. Fuster, S. Glagov, W. Insull, M.E. Rosenfeld, C.J. Schwartz, W.D. Wagner, R.W. Wissler, A definition of advanced types of atherosclerotic lesions and a histological classification of atherosclerosis: A report from the Committee on Vascular Lesions of the council on arteriosclerosis, American heart association, Circulation. 92 (1995) 1355–1374. https://doi.org/10.1161/01.CIR.92.5.1355.

[68]   M. Naghavi, P. Libby, E. Falk, S.W. Casscells, S. Litovsky, J. Rumberger, J.J. Badimon, C. Stefanadis, P. Moreno, G. Pasterkamp, Z. Fayad, P.H. Stone, S. Waxman, P. Raggi, M. Madjid, A. Zarrabi, A. Burke, C. Yuan, P.J. Fitzgerald, D.S. Siscovick, C.L. De Korte, M. Aikawa, K.E.J. Airaksinen, G. Assmann, C.R. Becker, J.H. Chesebro, A. Farb, Z.S. Galis, C. Jackson, I.K. Jang, W. Koenig, R.A. Lodder, K. March, J. Demirovic, M. Navab, S.G. Priori, M.D. Rekhter, R. Bahr, S.M. Grundy, R. Mehran, A. Colombo, E. Boerwinkle, C. Ballantyne, W. Insull, R.S. Schwartz, R. Vogel, P.W. Serruys, G.K.

Hansson, D.P. Faxon, S. Kaul, H. Drexler, P. Greenland, J.E. Muller, R. Virmani, P.M. Ridker, D.P. Zipes, P.K. Shah, J.T. Willerson, From vulnerable plaque to vulnerable patient: A call for new definitions and risk assessment strategies: Part I, Circulation. 108 (2003) 1664–1672. https://doi.org/10.1161/01.CIR.0000087480.94275.97.

[69]   M. Naghavi, P. Libby, E. Falk, S.W. Casscells, S. Litovsky, J. Rumberger, J.J. Badimon, C. Stefanadis, P. Moreno, G. Pasterkamp, Z. Fayad, P.H. Stone, S. Waxman, P. Raggi, M. Madjid, A. Zarrabi, A. Burke, C. Yuan, P.J. Fitzgerald, D.S. Siscovick, C.L. De Korte, M. Aikawa, K.E.J. Airaksinen, G. Assmann, C.R. Becker, J.H. Chesebro, A. Farb, Z.S. Galis, C. Jackson, I.K. Jang, W. Koenig, R.A. Lodder, K. March, J. Demirovic, M. Navab, S.G. Priori, M.D. Rekhter, R. Bahr, S.M. Grundy, R. Mehran, A. Colombo, E. Boerwinkle, C. Ballantyne, W. Insull, R.S. Schwartz, R. Vogel, P.W. Serruys, G.K. Hansson, D.P. Faxon, S. Kaul, H. Drexler, P. Greenland, J.E. Muller, R. Virmani, P.M. Ridker, D.P. Zipes, P.K. Shah, J.T. Willerson, From Vulnerable Plaque to Vulnerable Patient: A Call for New Definitions and Risk Assessment Strategies: Part II, Circulation. 108 (2003) 1772–1778. https://doi.org/10.1161/01.CIR.0000087481.55887.C9.

[70]   H. Ota, K. Takase, H. Rikimaru, M. Tsuboi, T. Yamada, A. Sato, S. Higano, T. Ishibashi, S. Takahashi, Quantitative vascular measurements in arterial occlusive disease, Radiographics. 25 (2005) 1141–1158. https://doi.org/10.1148/rg.255055014.

[71]   G.G. Ferguson, M. Eliasziw, H.W.K. Barr, G.P. Clagett, R.W. Barnes, M.C. Wallace, D.W. Taylor, R.B. Haynes, J.W. Finan, V.C. Hachinski, H.J.M. Barnett, The North American Symptomatic Carotid Endarterectomy Trial, Stroke. 30 (2015) 1751–1758.

[72]   S. Störk, A.W. Van Den Beld, C. Von Schacky, C.E. Angermann, S.W.J. Lamberts, D.E. Grobbee, M.L. Bots, Carotid artery plaque burden, stiffness, and mortality risk in elderly men: A prospective, population-based cohort study, Circulation. 110 (2004) 344–348. https://doi.org/10.1161/01.CIR.0000134966.10793.C9.

[73]   J. Gariepy, J. Salomon, N. Denarié, F. Laskri, J.L. Mégnien, J. Levenson, A. Simon, Sex and topographic differences in associations between large-artery wall thickness and coronary risk profile in a French working cohort: The AXA Study, Arterioscler. Thromb. Vasc. Biol. 18 (1998) 584–590. https://doi.org/10.1161/01.ATV.18.4.584.

[74]   J.N. Cameron, O.H. Mehta, M. Michail, J. Chan, S.J. Nicholls, M.R. Bennett, A.J. Brown, Exploring the relationship between biomechanical stresses and coronary atherosclerosis, Atherosclerosis. 302 (2020) 43–51. https://doi.org/10.1016/j.atherosclerosis.2020.04.011.

[75]   G.L. Basatemur, H.F. Jørgensen, M.C.H. Clarke, M.R. Bennett, Z. Mallat, Vascular smooth muscle cells in atherosclerosis, Nat. Rev. Cardiol. 16 (2019) 727–744. https://doi.org/10.1038/s41569-019-0227-9.

[76]   E. Maher, A. Creane, S. Sultan, N. Hynes, C. Lally, D.J. Kelly, Tensile and compressive properties of fresh human carotid atherosclerotic plaques, J. Biomech. 42 (2009) 2760–2767. https://doi.org/10.1016/j.jbiomech.2009.07.032.

[77]   M.G. Lawlor, M.R. O'Donnell, B.M. O'Connell, M.T. Walsh, Experimental determination of circumferential properties of fresh carotid artery plaques, J. Biomech. 44 (2011) 1709–1715. https://doi.org/10.1016/j.jbiomech.2011.03.033.

[78]   E.M. Cunnane, J.J.E. Mulvihill, H.E. Barrett, D.A. Healy, E.G. Kavanagh, S.R. Walsh, M.T. Walsh, Mechanical, biological and structural characterization of human atherosclerotic femoral plaque tissue, Acta Biomater. 11 (2015) 295–303. https://doi.org/10.1016/j.actbio.2014.09.024.

[79]   Z. Teng, D. Tang, J. Zheng, P.K. Woodard, A.H. Hoffman, An experimental study on the ultimate strength of the adventitia and media of human atherosclerotic carotid arteries in circumferential and axial directions, J. Biomech. 42 (2009) 2535–2539.

https://doi.org/10.1016/j.jbiomech.2009.07.009.

[80] J.J. Mulvihill, M.T. Walsh, On the mechanical behaviour of carotid artery plaques: The influence of curve-fitting experimental data on numerical model results, Biomech. Model. Mechanobiol. 12 (2013) 975–985. https://doi.org/10.1007/s10237-012-0457-9.

[81] A.C. Akyildiz, L. Speelman, F.J.H. Gijsen, Mechanical properties of human atherosclerotic intima tissue, J. Biomech. 47 (2014) 773–783. https://doi.org/10.1016/j.jbiomech.2014.01.019.

[82] C.K. Chai, L. Speelman, C.W.J. Oomens, F.P.T. Baaijens, Compressive mechanical properties of atherosclerotic plaques - Indentation test to characterise the local anisotropic behaviour, J. Biomech. 47 (2014) 784–792. https://doi.org/10.1016/j.jbiomech.2014.01.018.

[83] S.R.H. Barrett, M.P.F. Sutcliffe, S. Howarth, Z.Y. Li, J.H. Gillard, Experimental measurement of the mechanical properties of carotid atherothrombotic plaque fibrous cap, J. Biomech. 42 (2009) 1650–1655. https://doi.org/10.1016/j.jbiomech.2009.04.025.

[84] E. Maher, A. Creane, S. Sultan, N. Hynes, C. Lally, D.J. Kelly, Inelasticity of human carotid atherosclerotic plaque, Ann. Biomed. Eng. 39 (2011) 2445–2455. https://doi.org/10.1007/s10439-011-0331-4.

[85] C.K. Chai, A.C. Akyildiz, L. Speelman, F.J.H. Gijsen, C.W.J. Oomens, M.R.H.M. van Sambeek, A. van der Lugt, F.P.T. Baaijens, Local anisotropic mechanical properties of human carotid atherosclerotic plaques - Characterisation by micro-indentation and inverse finite element analysis, J. Mech. Behav. Biomed. Mater. 43 (2014) 59–68. https://doi.org/10.1016/j.jmbbm.2014.12.004.

[86] A.C. Akyildiz, L. Speelman, B. Van Velzen, R.R.F. Stevens, A.F.W. Van Der Steen, W. Huberts, F.J.H. Gijsen, Intima heterogeneity in stress assessment of atherosclerotic plaques, Interface Focus. 8 (2018). https://doi.org/10.1098/rsfs.2017.0008.

[87] D. Tang, Z. Teng, G. Canton, T.S. Hatsukami, L. Dong, X. Huang, C. Yuan, Local critical stress correlates better than global maximum stress with plaque morphological features linked to atherosclerotic plaque vulnerability: An in vivo multi-patient study, Biomed. Eng. Online. 8 (2009) 1–9. https://doi.org/10.1186/1475-925X-8-15.

[88] D. Tang, Z. Teng, G. Canton, C. Yang, M. Ferguson, X. Huang, J. Zheng, P.K. Woodard, C. Yuan, Sites of Rupture in Human Atherosclerotic Carotid Plaques Are Associated With High Structural Stresses, Stroke. 40 (2009) 3258–3263. https://doi.org/10.1161/STROKEAHA.109.558676.

[89] K.K.L. Wong, P. Thavornpattanapong, S.C.P. Cheung, Z. Sun, J. Tu, Effect of calcification on the mechanical stability of plaque based on a three-dimensional carotid bifurcation model, BMC Cardiovasc. Disord. 12 (2012). https://doi.org/10.1186/1471-2261-12-7.

[90] L.H. Arroyo, R.T. Lee, Mechanisms of plaque rupture: Mechanical and biologic interactions, Cardiovasc. Res. 41 (1999) 369–375. https://doi.org/10.1016/S0008-6363(98)00308-3.

[91] T.C. Gasser, M. Auer, F. Labruto, J. Swedenborg, J. Roy, Biomechanical Rupture Risk Assessment of Abdominal Aortic Aneurysms : Model Complexity versus Predictability of Finite Element Simulations, Eur. J. Vasc. Endovasc. Surg. 40 (2010) 176–185. https://doi.org/10.1016/j.ejvs.2010.04.003.

[92] M.F. Fillinger, M.L. Raghavan, S.P. Marra, J.L. Cronenwett, F.E. Kennedy, In vivo analysis of mechanical wall stress and abdominal aortic aneurysm rupture risk, J. Vasc.

Surg. 36 (2002) 589–597. https://doi.org/10.1067/mva.2002.125478.

[93] T.C. Gasser, A. Nchimi, J. Swedenborg, J. Roy, N. Sakalihasan, D. Böckler, A. Hyhlik-Dürr, A novel strategy to translate the biomechanical rupture risk of abdominal aortic aneurysms to their equivalent diameter risk: Method and retrospective validation, Eur. J. Vasc. Endovasc. Surg. 47 (2014) 288–295. https://doi.org/10.1016/j.ejvs.2013.12.018.

[94] M.S. Heng, M.J. Fagan, J.W. Collier, G. Desai, P.T. McCollum, I.C. Chetter, Peak wall stress measurement in elective and acute abdominal aortic aneurysms, J. Vasc. Surg. 47 (2008) 17–22. https://doi.org/10.1016/j.jvs.2007.09.002.

[95] D. Tang, C. Yang, J. Zheng, P.K. Woodard, J.E. Saffitz, G.A. Sicard, T.K. Pilgram, C. Yuan, Quantifying effects of plaque structure and material properties on stress distributions in human atherosclerotic plaques using 3D FSI models, J. Biomech. Eng. 127 (2005) 1185–1194. https://doi.org/10.1115/1.2073668.

[96] D.R. Nolan, J.P. McGarry, On the Compressibility of Arterial Tissue, Ann. Biomed. Eng. 44 (2016) 993–1007. https://doi.org/10.1007/s10439-015-1417-1.

[97] Z. Teng, J. Yuan, J. Feng, Y. Zhang, A.J. Brown, S. Wang, Q. Lu, J.H. Gillard, The influence of constitutive law choice used to characterise atherosclerotic tissue material properties on computing stress values in human carotid plaques, J. Biomech. 48 (2015) 3912–3921. https://doi.org/10.1016/j.jbiomech.2015.09.023.

[98] T. Schmidt, D. Pandya, D. Balzani, Influence of isotropic and anisotropic material models on the mechanical response in arterial walls as a result of supra-physiological loadings, Mech. Res. Commun. 64 (2015) 29–37. https://doi.org/10.1016/j.mechrescom.2014.12.008.

[99] A.C. Akyildiz, L. Speelman, H. van Brummelen, M.A. Gutiérrez, R. Virmani, A. van der Lugt, A.F.W. van der Steen, J.J. Wentzel, F.J.H. Gijsen, Effects of intima stiffness and plaque morphology on peak cap stress, Biomed. Eng. Online. 10 (2011) 1–13. https://doi.org/10.1186/1475-925X-10-25.

[100] Z.Y. Li, S. Howarth, R.A. Trivedi, J.M. U-King-Im, M.J. Graves, A. Brown, L. Wang, J.H. Gillard, Stress analysis of carotid plaque rupture based on in vivo high resolution MRI, J. Biomech. 39 (2006) 2611–2622. https://doi.org/10.1016/j.jbiomech.2005.08.022.

[101] T.Y. Tang, Z.Y. Li, S.R. Miller, M.J. Graves, R.A. Trivedi, S.R. Walsh, A.P. Brown, P.J. Kirkpatrick, M.E. Gaunt, J.H. Gillard, Correlation of carotid atheromatous plaque in inflammation with biomechanical stress: Utility of USPIO enhanced MR imaging and finite element analysis, Atherosclerosis. 196 (2008) 879–887. https://doi.org/10.1016/j.atherosclerosis.2007.02.004.

[102] D. Tang, C. Yang, G. Canton, Z. Wu, T. Hatsukami, C. Yuan, Correlations between carotid plaque progression and mechanical stresses change sign over time: A patient follow up study using MRI and 3D FSI models, Biomed. Eng. Online. 12 (2013) 1–12. https://doi.org/10.1186/1475-925X-12-105.

[103] H.M. Loree, R.D. Kamm, R.G. Stringfellow, R.T. Lee, Effects of fibrous cap thickness on peak circumferential stress in model atherosclerotic vessels, Circ. Res. 71 (1992) 850–858. https://doi.org/10.1161/01.RES.71.4.850.

[104] J. Ohayon, G. Finet, A.M. Gharib, D.A. Herzka, P. Tracqui, J. Heroux, G. Rioufol, M.S. Kotys, A. Elagha, R.I. Pettigrew, Necrotic core thickness and positive arterial remodeling index: Emergent biomechanical factors for evaluating the risk of plaque rupture, Am. J. Physiol. - Hear. Circ. Physiol. 295 (2008) 717–727. https://doi.org/10.1152/ajpheart.00005.2008.

[105] H.A. Nieuwstadt, A. van der Lugt, Z.A.M. Kassar, M. Breeuwer, A.F.W. van der Steen, F.J.H. Gijsen, Atherosclerotic plaque fibrous cap assessment under an oblique scan plane orientation in carotid MRI., Quant. Imaging Med. Surg. 4 (2014) 216–24. https://doi.org/10.3978/j.issn.2223-4292.2014.07.05.

[106] X. Huang, Z. Teng, G. Canton, M. Ferguson, C. Yuan, D. Tang, Intraplaque hemorrhage is associated with higher structural stresses in human atherosclerotic plaques: An in vivo MRI-based 3d fluid-structure interaction study, Biomed. Eng. Online. 9 (2010) 1–12. https://doi.org/10.1186/1475-925X-9-86.

[107] Y. Huang, Z. Teng, U. Sadat, M.J. Graves, M.R. Bennett, J.H. Gillard, The influence of computational strategy on prediction of mechanical stress in carotid atherosclerotic plaques: Comparison of 2D structure-only, 3D structure-only, one-way and fully coupled fluid-structure interaction analyses, J. Biomech. 47 (2014) 1465–1471. https://doi.org/10.1016/j.jbiomech.2014.01.030.

[108] D. Tang, Z. Teng, G. Canton, C. Yang, M. Ferguson, X. Huang, J. Zheng, P.K. Woodard, C. Yuan, Sites of rupture in human atherosclerotic carotid plaques are associated with high structural stresses: An in Vivo MRI-based 3D fluid-structure interaction study, Stroke. 40 (2009) 3258–3263. https://doi.org/10.1161/STROKEAHA.109.558676.

[109] X. Huang, Z. Teng, G. Canton, M. Ferguson, C. Yuan, D. Tang, Intraplaque hemorrhage is associated with higher structural stresses in human atherosclerotic plaques : an in vivo MRI-based 3d fluid-structure interaction study, Biomed. Eng. Online. 9 (2010) 86. https://doi.org/10.1186/1475-925X-9-86.

[110] L. Antiga, B. Ene-Iordache, L. Caverni, G.P. Cornalba, A. Remuzzi, Geometric reconstruction for computational mesh generation of arterial bifurcations from CT angiography, Comput. Med. Imaging Graph. 26 (2002) 227–235. https://doi.org/10.1016/S0895-6111(02)00020-4.

[111] Seung Lee, N. Piersol, F. Loth, P. Fischer, G. Leaf, B. Smith, R. Yedevalli, A. Yardimci, N. Alperin, L. Schwartz, Automated mesh generation of an arterial bifurcation based upon in vivo MR images, (2002) 719–722. https://doi.org/10.1109/iembs.2000.900848.

[112] G. De Santis, P. Mortier, M. De Beule, P. Segers, P. Verdonck, B. Verhegghe, Patient-specific Computational Fluid Dynamics: Structured mesh generation from coronary angiography, Med. Biol. Eng. Comput. 48 (2010) 371–380. https://doi.org/10.1007/s11517-010-0583-4.

[113] G. De Santis, M. De Beule, K. Van Canneyt, P. Segers, P. Verdonck, B. Verhegghe, Medical Engineering & Physics Full-hexahedral structured meshing for image-based computational vascular modeling, Med. Eng. Phys. 33 (2011) 1318–1325. https://doi.org/10.1016/j.medengphy.2011.06.007.

[114] B.J.B.M. Wolters, M.C.M. Rutten, G.W.H. Schurink, U. Kose, J. De Hart, F.N. Van De Vosse, A patient-specific computational model of fluid-structure interaction in abdominal aortic aneurysms, Med. Eng. Phys. 27 (2005) 871–883. https://doi.org/10.1016/j.medengphy.2005.06.008.

[115] A. Creane, E. Maher, S. Sultan, N. Hynes, D.J. Kelly, C. Lally, Finite element modelling of diseased carotid bifurcations generated from in vivo computerised tomographic angiography, Comput. Biol. Med. 40 (2010) 419–429. https://doi.org/10.1016/j.compbiomed.2010.02.006.

[116] J. Tarjuelo-Gutierrez, B. Rodriguez-Vila, D.M. Pierce, T.E. Fastl, P. Verbrugghe, I. Fourneau, G. Maleux, P. Herijgers, G.A. Holzapfel, E.J. Gomez, High-quality conforming hexahedral meshes of patient-specific abdominal aortic aneurysms including their intraluminal thrombi, Med. Biol. Eng. Comput. 52 (2014) 159–168.

https://doi.org/10.1007/s11517-013-1127-5.

[117] F. Riveros, S. Chandra, E.A. Finol, T.C. Gasser, J.F. Rodriguez, A pull-back algorithm to determine the unloaded vascular geometry in anisotropic hyperelastic AAA passive mechanics, Ann. Biomed. Eng. 41 (2013) 694–708. https://doi.org/10.1007/s10439-012-0712-3.

[118] S. Chandra, F. Riveros, J.F. Rodriguez, A Methodology for the Derivation of Unloaded Abdominal Aortic Aneurysm Geometry With Experimental Validation, 138 (2016) 1–11. https://doi.org/10.1115/1.4034425.

[119] J. Bols, J. Degroote, B. Trachet, B. Verhegghe, P. Segers, J. Vierendeels, A computational method to assess the in vivo stresses and unloaded configuration of patient-specific blood vessels, J. Comput. Appl. Math. 246 (2013) 10–17. https://doi.org/10.1016/j.cam.2012.10.034.

[120] C.J. Chuong, Y.C. Fung, On Residual Stresses in Arteries, J. Biomech. 108 (1986) 189–192.

[121] M.L. Raghavan, B. Ma, M.F. Fillinger, Three-Dimensional Finite Element Analysis of Residual Stress in Arteries, 32 (2004) 257–263.

[122] Y.C. Fung, What Are the Residual Stresses Doing in Our Blood Vessels?, Ann. Biomed. Eng. 19 (1991) 237–249.

[123] V. Alastrué, E. Peña, M.Á. Martínez, M. Doblaré, Assessing the use of the "opening angle method" to enforce residual stresses in patient-specific arteries, Ann. Biomed. Eng. 35 (2007) 1821–1837. https://doi.org/10.1007/s10439-007-9352-4.

[124] M. Kroon, G.A. Holzapfel, Estimation of the Distributions of Anisotropic , Elastic Properties and Wall Stresses of Saccular Cerebral Aneurysms by Inverse Analysis Estimation elastic of the distributions and wall properties cerebral aneurysms by of anisotropic , of saccular analysi, Proc. R. Soc. 464 (2008) 807–825. https://doi.org/10.1098/rspa.200.7.0332.

[125] S. Avril, P. Badel, A. Duprey, Anisotropic and hyperelastic identification of in vitro human arteries from full-field optical measurements, J. Biomech. 43 (2010) 2978–2985. https://doi.org/10.1016/j.jbiomech.2010.07.004.

[126] K. Genovese, Y. Lee, A.Y. Lee, J.D. Humphrey, An improved panoramic digital image correlation method for vascular strain analysis and material characterization, J. Mech. Behav. Biomed. Mater. 27 (2013) 132–142. https://doi.org/10.1016/j.jmbbm.2012.11.015.

[127] A.C. Akyildiz, H.H.G. Hansen, H.A. Nieuwstadt, L. Speelman, C.L. De Korte, A.F.W. van der Steen, F.J.H. Gijsen, A Framework for Local Mechanical Characterization of Atherosclerotic Plaques: Combination of Ultrasound Displacement Imaging and Inverse Finite Element Analysis, Ann. Biomed. Eng. 44 (2016) 968–979. https://doi.org/10.1007/s10439-015-1410-8.

[128] C.K. Chai, A.C. Akyildiz, L. Speelman, F.J.H. Gijsen, C.W.J. Oomens, M.R.H.M. van Sambeek, A. van der Lugt, F.P.T. Baaijens, Local anisotropic mechanical properties of human carotid atherosclerotic plaques - Characterisation by micro-indentation and inverse finite element analysis, J. Mech. Behav. Biomed. Mater. 43 (2015) 59–68. https://doi.org/10.1016/j.jmbbm.2014.12.004.

[129] N.J.B. Driessen, C.V.C. Bouten, F.P.T. Baaijens, A Structural Constitutive Model For Collagenous Cardiovascular Tissues Incorporating the Angular Fiber Distribution, J. Biomech. Eng. 127 (2005) 494. https://doi.org/10.1115/1.1894373.

[130] N.J.B. Driessen, R.A. Boerboom, J.M. Huyghe, C.V.C. Bouten, F.P.T. Baaijens, Computational analyses of mechanically induced collagen fiber remodeling in the aortic heart valve, J. Biomech. Eng. 125 (2003) 549–557. https://doi.org/10.1115/1.1590361.

[131] A. Creane, E. Maher, S. Sultan, N. Hynes, D.J. Kelly, C. Lally, Prediction of fibre architecture and adaptation in diseased carotid bifurcations, (2010). https://doi.org/10.1007/s10237-010-0277-8.

[132] I. Hariton, G. deBotton, T.C. Gasser, G.A. Holzapfel, Stress-modulated collagen fiber remodeling in a human carotid bifurcation, J. Theor. Biol. 248 (2007) 460–470. https://doi.org/10.1016/j.jtbi.2007.05.037.

[133] D.E. Kiousis, S.F. Rubinigg, M. Auer, G.A. Holzapfel, A methodology to analyze changes in lipid core and calcification onto fibrous cap vulnerability: The human atherosclerotic carotid bifurcation as an illustratory example, J. Biomech. Eng. 131 (2009) 1–9. https://doi.org/10.1115/1.4000078.

[134] P. Mortier, G.A. Holzapfel, M. De Beule, D. Van Loo, Y. Taeymans, P. Segers, P. Verdonck, B. Verhegghe, A novel simulation strategy for stent insertion and deployment in curved coronary bifurcations: Comparison of three drug-eluting stents, Ann. Biomed. Eng. 38 (2010) 88–99. https://doi.org/10.1007/s10439-009-9836-5.

[135] M. Ghasemi, Mechanical Assessment of the Risk of Atherosclerotic Plaque Rupture in Carotid Arteries with a Focus on Damage Accumulation, (2019).

[136] P.B. Canham, H.M. Finlay, J.G. Dixon, D.R. Boughner, A. Chen, Measurements from light and polarised light microscopy of human coronary arteries fixed at distending pressure, Cardiovasc. Res. 23 (1989) 973–982. https://doi.org/10.1093/cvr/23.11.973.

[137] A.J. Schriefl, G. Zeindlinger, D.M. Pierce, P. Regitnig, G.A. Holzapfel, Determination of the layer-specific distributed collagen fibre orientations in human thoracic and abdominal aortas and common iliac arteries, J. R. Soc. Interface. 9 (2012) 1275–1286. https://doi.org/10.1098/rsif.2011.0727.

[138] T.C. Gasser, S. Gallinetti, X. Xing, C. Forsell, J. Swedenborg, J. Roy, Spatial orientation of collagen fibers in the abdominal aortic aneurysm's wall and its relation to wall mechanics, Acta Biomater. 8 (2012) 3091–3103. https://doi.org/10.1016/j.actbio.2012.04.044.

[139] R. Rezakhaniha, A. Agianniotis, J.T.C. Schrauwen, A. Griffa, D. Sage, C.V.C. Bouten, F.N. Van De Vosse, M. Unser, N. Stergiopulos, Experimental investigation of collagen waviness and orientation in the arterial adventitia using confocal laser scanning microscopy, Biomech. Model. Mechanobiol. 11 (2012) 461–473. https://doi.org/10.1007/s10237-011-0325-z.

[140] H. Chen, Y. Liu, M.N. Slipchenko, X. Zhao, J.X. Cheng, G.S. Kassab, The layered structure of coronary adventitia under mechanical load, Biophys. J. 101 (2011) 2555–2562. https://doi.org/10.1016/j.bpj.2011.10.043.

[141] S. Ghazanfari, A. Driessen-Mol, G.J. Strijkers, F.M.W. Kanters, F.P.T. Baaijens, C.V.C. Bouten, A comparative analysis of the collagen architecture in the carotid artery: Second harmonic generation versus diffusion tensor imaging, Biochem. Biophys. Res. Commun. 426 (2012) 54–58. https://doi.org/10.1016/j.bbrc.2012.08.031.

[142] C.L. De Korte, M.J. Sierevogel, F. Mastik, C. Strijder, J.A. Schaar, E. Velema, G. Pasterkamp, P.W. Serruys, A.F.W. Van der Steen, Identification of atherosclerotic plaque components with intravascular ultrasound elastography in vivo: A Yucatan pig study, Circulation. 105 (2002) 1627–1630. https://doi.org/10.1161/01.CIR.0000014988.66572.2E.

[143] R.A. Wain, R.T. Lyon, F.J. Veith, G.L. Berdejo, J.G. Yuan, W.D. Suggs, T. Ohki, L.A. Sanchez, R.G. Zierler, Accuracy of duplex ultrasound in evaluating carotid artery anatomy before endarterectomy, J. Vasc. Surg. 27 (1998) 235–244. https://doi.org/10.1016/S0741-5214(98)70354-4.

[144] M.R. Jaff, G. V. Goldmakher, M.H. Lev, J.M. Romero, Imaging of the carotid arteries: The role of duplex ultrasonography, magnetic resonance arteriography, and computerized tomographic arteriography, Vasc. Med. (United Kingdom). 13 (2008) 281–292. https://doi.org/10.1177/1358863X08091971.

[145] D.P. Slovut, J.M. Romero, K.M. Hannon, J. Dick, M.R. Jaff, Detection of common carotid artery stenosis using duplex ultrasonography: A validation study with computed tomographic angiography, J. Vasc. Surg. 51 (2010) 65–70. https://doi.org/10.1016/j.jvs.2009.08.002.

[146] C. Huang, X. Pan, Q. He, M. Huang, L. Huang, X. Zhao, C. Yuan, J. Bai, J. Luo, Ultrasound-Based Carotid Elastography for Detection of Vulnerable Atherosclerotic Plaques Validated by Magnetic Resonance Imaging, Ultrasound Med. Biol. 42 (2016) 365–377. https://doi.org/10.1016/j.ultrasmedbio.2015.09.023.

[147] A. Gupta, H. Baradaran, H. Kamel, A. Pandya, A. Mangla, A. Dunning, R.S. Marshall, P.C. Sanelli, Evaluation of computed tomography angiography plaque thickness measurements in high-grade carotid artery stenosis, Stroke. 45 (2014) 740–745. https://doi.org/10.1161/STROKEAHA.113.003882.

[148] B. et Al, Quantification of carotid stenosis on CT angiography, Am. J. Neuroradiol. 27 (2006) 1601.

[149] M.J.W. Koelemay, P.J. Nederkoorn, J.B. Reitsma, C.B. Majoie, Systematic review of computed tomographic angiography for assessment of carotid artery disease, Stroke. 35 (2004) 2306–2312. https://doi.org/10.1161/01.STR.0000141426.63959.cc.

[150] T. Shearer, R.S. Bradley, L.A. Hidalgo-Bastida, M.J. Sherratt, S.H. Cartmell, Three-dimensional visualisation of soft biological structures by X-ray computed micro-tomography, J. Cell Sci. 129 (2016) 2483–2492. https://doi.org/10.1242/jcs.179077.

[151] E. Pauwels, D. Van Loo, P. Cornillie, L. Brabant, L. Van Hoorebeke, An exploratory study of contrast agents for soft tissue visualization by means of high resolution X-ray computed tomography imaging, J. Microsc. 250 (2013) 21–31. https://doi.org/10.1111/jmi.12013.

[152] S. De Bournonville, S. Vangrunderbeeck, G. Kerckhofs, Contrast-enhanced microCT for virtual 3D anatomical pathology of biological tissues: A literature review, Contrast Media Mol. Imaging. 2019 (2019). https://doi.org/10.1155/2019/8617406.

[153] M. Nierenberger, Y. Rémond, S. Ahzi, P. Choquet, Assessing the three-dimensional collagen network in soft tissues using contrast agents and high resolution micro-CT: Application to porcine iliac veins, Comptes Rendus - Biol. 338 (2015) 425–433. https://doi.org/10.1016/j.crvi.2015.04.009.

[154] S.T. Robinson, R.E. Levey, R. Beatty, D. Connolly, E.B. Dolan, N.H. Osborne, P. Dockery, P.K. Henke, G.P. Duffy, A versatile technique for high-resolution three-dimensional imaging of human arterial segments using microcomputed tomography, JVS Vasc. Sci. 2 (2021) 13–19. https://doi.org/10.1016/j.jvssci.2020.08.001.

[155] Bartlett et al, Quantification of Carotid Stenosis on CT Angiography, Am J Neuroradiol. 27 (2006) 13–19. https://doi.org/27/1/13 [pii].

[156] L.P. Smits, D.F. Van Wijk, R. Duivenvoorden, D. Xu, C. Yuan, E.S. Stroes, A.J.

Nederveen, Manual versus automated carotid artery plaque component segmentation in high and lower quality 3.0 tesla MRI scans, PLoS One. 11 (2016) 1–12. https://doi.org/10.1371/journal.pone.0164267.

[157] J. Cai, T.S. Hatsukami, M.S. Ferguson, W.S. Kerwin, T. Saam, B. Chu, N. Takaya, N.L. Polissar, C. Yuan, In vivo quantitative measurement of intact fibrous cap and lipid-rich necrotic core size in atherosclerotic carotid plaque: Comparison of high-resolution, contrast-enhanced magnetic resonance imaging and histology, Circulation. 112 (2005) 3437–3444. https://doi.org/10.1161/CIRCULATIONAHA.104.528174.

[158] T. Saam, M.S. Ferguson, V.L. Yarnykh, N. Takaya, D. Xu, N.L. Polissar, T.S. Hatsukami, C. Yuan, Quantitative evaluation of carotid plaque composition by in vivo MRI, Arterioscler. Thromb. Vasc. Biol. 25 (2005) 234–239. https://doi.org/10.1161/01.ATV.0000149867.61851.31.

[159] T. Saam, T.S. Hatsukami, N. Takaya, B. Chu, H. Underhill, W.S. Kerwin, J. Cai, M.S. Ferguson, C. Yuan, The Vulnerable, or High-Risk, Atherosclerotic Plaque: Noninvasive MR Imaging for Characterization and Assessment, Radiology. 244 (2007) 64–77. https://doi.org/10.1007/978-1-4020-5558-4_7.

[160] M.E. Porambo, J.K. DeMarco, MR imaging of vulnerable carotid plaque, Cardiovasc. Diagn. Ther. 10 (2020) 1019–1031. https://doi.org/10.21037/cdt.2020.03.12.

[161] M. Honda, N. Kitagawa, K. Tsutsumi, I. Nagata, M. Morikawa, T. Hayashi, High-resolution magnetic resonance imaging for detection of carotid plaques, Neurosurgery. 58 (2006) 338–344. https://doi.org/10.1227/01.NEU.0000195097.31033.66.

[162] L. Saba, M. Anzidei, B.C. Marincola, M. Piga, E. Raz, P.P. Bassareo, A. Napoli, L. Mannelli, C. Catalano, M. Wintermark, Imaging of the carotid artery vulnerable plaque, Cardiovasc. Intervent. Radiol. 37 (2014) 572–585. https://doi.org/10.1007/s00270-013-0711-2.

[163] P. O'Priessnig, G. Silbernagel, S. Krassnig, G. Reishofer, Magnetic resonance microscopy diffusion tensor imaging of collagen fibre bundles stabilizing an atherosclerotic plaque of the common carotid artery, Eur. Heart J. 39 (2018) 3337. https://doi.org/10.1093/eurheartj/ehy146.

[164] R.D. Johnston, R.T. Gaul, C. Lally, An investigation into the critical role of fibre orientation in the ultimate tensile strength and stiffness of human carotid plaque caps, Acta Biomater. (2021). https://doi.org/10.1016/j.actbio.2021.02.008.

[165] P. Opriessnig, H. Mangge, R. Stollberger, H. Deutschmann, G. Reishofer, In vivo cardiovascular magnetic resonance of 2D vessel wall diffusion anisotropy in carotid arteries, J. Cardiovasc. Magn. Reson. 18 (2017) 81. https://doi.org/10.1186/s12968-016-0304-8.

[166] H.A. Nieuwstadt, L. Speelman, M. Breeuwer, A. van der Lugt, A.F.W. van der Steen, J.J. Wentzel, F.J.H. Gijsen, The Influence of Inaccuracies in Carotid MRI Segmentation on Atherosclerotic Plaque Stress Computations, J. Biomech. Eng. 136 (2014) 021015. https://doi.org/10.1115/1.4026178.

[167] G.M. Fomovsky, J.W. Holmes, Evolution of scar structure, mechanics, and ventricular function after myocardial infarction in the rat, Am. J. Physiol. - Hear. Circ. Physiol. 298 (2010) 221–228. https://doi.org/10.1152/ajpheart.00495.2009.

[168] B. Vogel, H. Siebert, U. Hofmann, S. Frantz, Determination of collagen content within picrosirius red stained paraffin-embedded tissue sections using fluorescence microscopy, MethodsX. 2 (2015) 124–134. https://doi.org/10.1016/j.mex.2015.02.007.

[169] D. Tang, Z. Teng, G. Canton, C. Yang, M. Ferguson, X. Huang, J. Zheng, P.K. Woodard, C. Yuan, Sites of rupture in human atherosclerotic carotid plaques are associated with high structural stresses: An in Vivo MRI-based 3D fluid-structure interaction study, Stroke. 40 (2009) 3258–3263. https://doi.org/10.1161/STROKEAHA.109.558676.

[170] S.K. Nadkarni, M.C. Pierce, B.H. Park, J.F. de Boer, P. Whittaker, B.E. Bouma, J.E. Bressner, E. Halpern, S.L. Houser, G.J. Tearney, Measurement of Collagen and Smooth Muscle Cell Content in Atherosclerotic Plaques Using Polarization-Sensitive Optical Coherence Tomography, J. Am. Coll. Cardiol. 49 (2007) 1474–1481. https://doi.org/10.1016/j.jacc.2006.11.040.

[171] H.E. Barrett, K. Van der Heiden, E. Farrell, F.J.H. Gijsen, A.C. Akyildiz, Calcifications in atherosclerotic plaques and impact on plaque biomechanics, J. Biomech. 87 (2019) 1–12. https://doi.org/10.1016/j.jbiomech.2019.03.005.

[172] F.J.H. Gijsen, B. Vis, H.E. Barrett, A.A. Zadpoor, H.J. Verhagen, D. Bos, A.F.W. Van Der Steen, A.C. Akyildiz, Morphometric and Mechanical Analyses of Calcifications and Fibrous Plaque Tissue in Carotid Arteries for Plaque Rupture Risk Assessment, IEEE Trans. Biomed. Eng. 68 (2021) 1429–1438. https://doi.org/10.1109/TBME.2020.3038038.

[173] D. Tang, C. Yang, S. Huang, V. Mani, J. Zheng, P.K. Woodard, P. Robson, Z. Teng, M. Dweck, Z.A. Fayad, Cap inflammation leads to higher plaque cap strain and lower cap stress: An MRI-PET/CT-based FSI modeling approach, J. Biomech. 50 (2017) 121–129. https://doi.org/10.1016/j.jbiomech.2016.11.011.

[174] J. Veraart, D.S. Novikov, D. Christiaens, B. Ades-aron, J. Sijbers, E. Fieremans, Denoising of diffusion MRI using random matrix theory, Neuroimage. 142 (2016) 394–406. https://doi.org/10.1016/j.neuroimage.2016.08.016.

[175] E. Kellner, B. Dhital, V.G. Kiselev, M. Reisert, Gibbs-ringing artifact removal based on local subvoxel-shifts, Magn. Reson. Med. 76 (2016) 1574–1581. https://doi.org/10.1002/mrm.26054.

[176] J.D. Tournier, R. Smith, D. Raffelt, R. Tabbara, T. Dhollander, M. Pietsch, D. Christiaens, B. Jeurissen, C.H. Yeh, A. Connelly, MRtrix3: A fast, flexible and open software framework for medical image processing and visualisation, Neuroimage. 202 (2019) 116137. https://doi.org/10.1016/j.neuroimage.2019.116137.

[177] A. Leemans, B. Jeurissen, J. Sijbers, D.K. Jones, ExploreDTI: a graphical toolbox for processing, analyzing, and visualizing diffusion MR data, Proc. Int. Soc. Magn. Reson. Med. 17 (2009) 3537.

[178] J.M. Soares, P. Marques, V. Alves, N. Sousa, A hitchhiker ' s guide to diffusion tensor imaging, 7 (2013) 1–14. https://doi.org/10.3389/fnins.2013.00031.

[179] P.J. Basser, J. Mattiello, D. Lebihan, Estimation of the Effective Self-Diffusion Tensor from the NMR Spin Echo, J. Magn. Reson. Ser. B. 103 (1994) 247–254. https://doi.org/10.1006/jmrb.1994.1037.

[180] S.S. Shahid, R.T. Gaul, C. Kerskens, V. Flamini, C. Lally, Quantifying the ultrastructure of carotid arteries using high-resolution micro-diffusion tensor imaging - Comparison of intact versus open cut tissue, Phys. Med. Biol. 62 (2017) 8850–8868. https://doi.org/10.1088/1361-6560/aa9159.

[181] T.C. Gasser, R.W. Ogden, G.A. Holzapfel, Hyperelastic modelling of arterial layers with distributed collagen fibre orientations, J. R. Soc. Interface. 3 (2006) 15–35. https://doi.org/10.1098/rsif.2005.0073.

[182] E. Kuhl, K. Garikipati, E.M. Arruda, K. Grosh, Remodeling of biological tissue: Mechanically induced reorientation of a transversely isotropic chain network, J. Mech. Phys. Solids. 53 (2005) 1552–1573. https://doi.org/10.1016/j.jmps.2005.03.002.

[183] C. Miehe, Numerical computation of algorithmic (consistent) tangent moduli in large-strain computational inelasticity, Comput. Methods Appl. Mech. Eng. 134 (1996) 223–240. https://doi.org/10.1016/0045-7825(96)01019-5.

[184] D. Balzani, S. Brinkhues, G.A. Holzapfel, Constitutive framework for the modeling of damage in collagenous soft tissues with application to arterial walls, Comput. Methods Appl. Mech. Eng. 213–216 (2012) 139–151. https://doi.org/10.1016/j.cma.2011.11.015.

[185] L.A. Davis, S.E. Stewart, C.G. Carsten, B.A. Snyder, M.A. Sutton, S.M. Lessner, Characterization of fracture behavior of human atherosclerotic fibrous caps using a miniature single edge notched tensile test, Acta Biomater. 43 (2016) 101–111. https://doi.org/10.1016/j.actbio.2016.07.027.

[186] F. Baaijens, C. Bouten, N. Driessen, Modeling collagen remodeling, J. Biomech. 43 (2010) 166–175. https://doi.org/10.1016/j.jbiomech.2009.09.022.

[187] N.J.B. Driessen, M.A.J. Cox, C.V.C. Bouten, F.P.T. Baaijens, Remodelling of the angular collagen fiber distribution in cardiovascular tissues, Biomech. Model. Mechanobiol. 7 (2008) 93–103. https://doi.org/10.1007/s10237-007-0078-x.

[188] G. Sommer, P. Regitnig, L. Költringer, G.A. Holzapfel, Biaxial mechanical properties of intact and layer-dissected human carotid arteries at physiological and supraphysiological loadings, (2018) 898–912. https://doi.org/10.1152/ajpheart.00378.2009.

[189] R.T. Gaul, D.R. Nolan, T. Ristori, C.V.C. Bouten, S. Loerakker, C. Lally, Strain mediated enzymatic degradation of arterial tissue: Insights into the role of the non-collagenous tissue matrix and collagen crimp, Acta Biomater. 77 (2018) 301–310. https://doi.org/10.1016/j.actbio.2018.06.037.

[190] M.R. Bennett, Apoptosis of vascular smooth muscle cells in vascular remodelling and atherosclerotic plaque rupture, Cardiovasc. Res. 41 (1999) 361–368. https://doi.org/10.1016/S0008-6363(98)00212-0.

[191] Z.Y. Li, S.P.S. Howarth, T. Tang, M.J. Graves, J. U-King-Im, R.A. Trivedi, P.J. Kirkpatrick, J.H. Gillard, Structural analysis and magnetic resonance imaging predict plaque vulnerability: A study comparing symptomatic and asymptomatic individuals, J. Vasc. Surg. 45 (2007) 768–775. https://doi.org/10.1016/j.jvs.2006.12.065.

[192] B.R. Kwak, M. Bäck, M.L. Bochaton-Piallat, G. Caligiuri, M.J.A.P. Daemen, P.F. Davies, I.E. Hoefer, P. Holvoet, H. Jo, R. Krams, S. Lehoux, C. Monaco, S. Steffens, R. Virmani, C. Weber, J.J. Wentzel, P.C. Evans, Biomechanical factors in atherosclerosis: Mechanisms and clinical implications, Eur. Heart J. 35 (2014) 3013–3020. https://doi.org/10.1093/eurheartj/ehu353.

A   Protocol for meshing arterial bifurcations.

These instructions give a demonstrate the of meshing complex arterial geometries after initial segmentation and reconstruction from clinical MRI or CT images. The software used for this is the ANSA BETA pre-processor. This process is simpler for more cylindrical geometries.

For a simple demonstration of meshing, please view the attached video in this development.

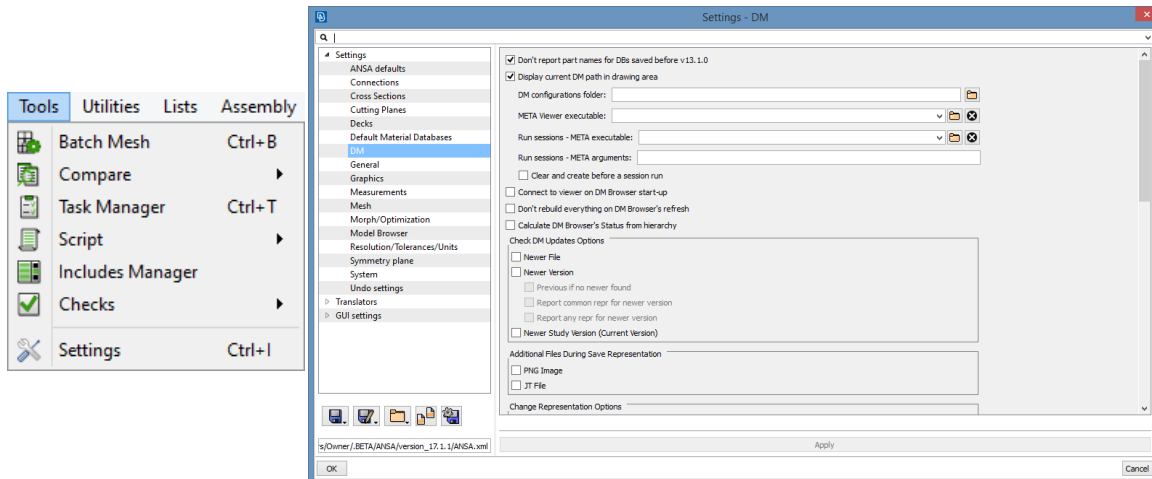## *Process*

Initial ANSA window – Ensure selection of the Abaqus module deck (Top right corner)
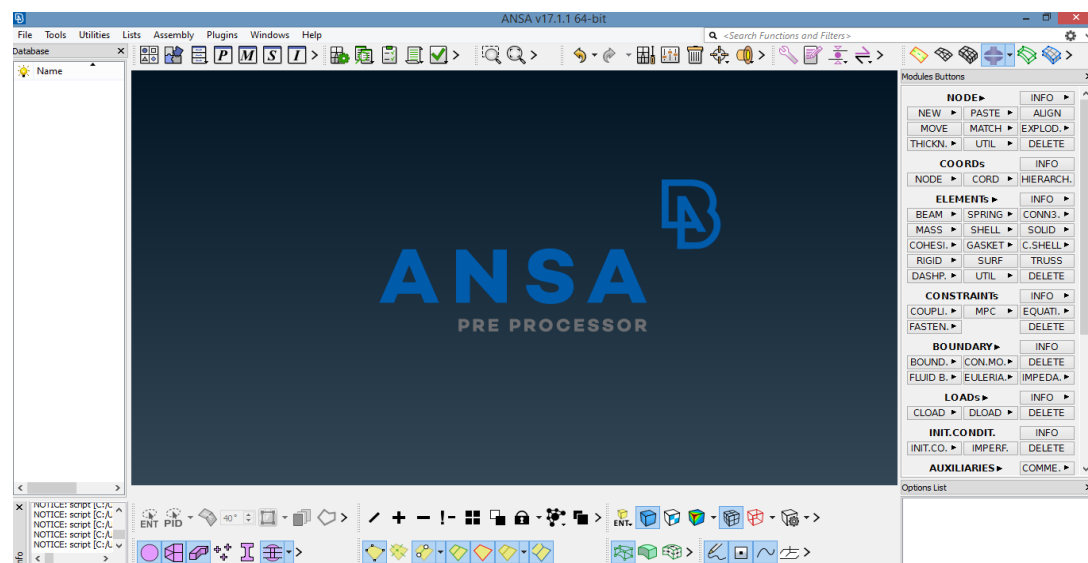
Preliminary Steps

This section deals with the initial settings of geometry import and meshing parameters that must be fixed before geometry

1. **Set the initial scale of the geometry.**

Tools → Settings

This opens the window for the ANSA settings. Select Resolution/Tolerances/Units to set the input dimensions.
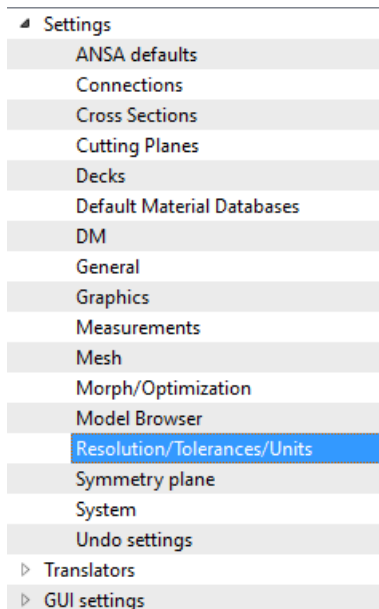
Scaled model dimensions is important so the model that you are working on is realistic.

2. <u>Import the geometry – common inputs</u>

For importation of the geometry we have two methods depending on the file type.

- For VDA, IGES and CATIA inputs

  File → Open → "Choose file"

- For STL, INP inputs

  `   File → Input → "Choose desired input"

File Tools Utilities Lists Assembly

- Open — Ctrl+O
- Open recent ▸
- Auto
- Merge
- New — Ctrl+N
- Input ▸
- Input recent ▸
- Output ▸
- Output CAD ▸
- Save
- Save as — Ctrl+S
- Save as v16
- Save visible as
- Save All
- Output connections ▸
- Read connections ▸
- Read model definition ▸
- Read session file
- Quit — Ctrl+Q

ABAQUS
NASTRAN
LS-DYNA
PAM-CRASH
RADIOSS
ANSYS
PERMAS
MOLDEX3D
SESTRA
CFD++
FLUENT
OPENFOAM
STAR
UH3D
SC/TETRA
RADTHERM
THESEUS
TAU
More ▸

CFX
CGNS
MEDINA
Tosca Structure
ONF
PATRAN
I-DEAS
SONATE
FREE FORM
OFF FORM
SHL FORM
BETA TANK
WAVE FRONT
INVENTOR
ST-LITHGRP
VRML
FiberSim metadata
ADAMS/View
ANSA Thickness
MOLDFLOW
OPTISTRUCT
SIMULAYT

More inputs can be imported into the software using these two methods. The inputs addressed here are the most common.

3. Setting of mesh thresholds

For mesh parameters – find the following toolbar

For mesh parameters

For Quality criteria

Mesh Parameters

Name:

Basic | Perimeters | Features | Fix Quality | Volume Mesh

- Maximum growth rate (1-3) 1.2
- Maximum element length 0
- ABAQUS min. shape factor 1.
- Coordinate system 0
- Buffer zones 3
- Frozen entities 0
- ☑ Create pyramids
- ☐ Force 2 rows in thin walls
- ☑ Transition point offset

Fix Quality:
- ☑ Fix violating solid elements
- ☐ Freeze non visible shells
- External bounds movement Constrained
- Maximum distance from external bounds 0.1*local
- PID bounds movement Unconstrained
- Maximum distance from PID bounds 0.1*local

OK   Cancel

Quality Criteria - Presentation Parameters

Name:

Shells | Solids | Graph Parameters | Presentation Parameters

Criteria	Calculation	Color	Weight	Best	Good	Failed	Worst
Percentage				0.	60.	95.	100.
Penalty values				0.	0.	1.	10.
☑ aspect ratio	ABAQUS		1.	1.	3.	8.	15.
☐ skewness	FLUENT		1.	0.	0.25	0.5	1.
☐ warping	IDEAS		1.	0.	5.	10.	90.
☐ crash time step	LS-DYN		1.	1.	1.4E-6	1.E-6	0.
☐ squish			1.	0.	0.15	0.3	1.
☐ jacobian	ANSA		1.	1.	0.8	0.7	0.
☐ min length			1.	0.5	0.	0.	0.
☐ max length			1.	0.5	0.	0.	0.
☐ min angle tetras	ABAQUS		1.	60.	40.	20.	0.
☐ max angle tetras	ABAQUS		1.	60.	90.	120.	180.
☑ min angle pentas	ABAQUS		1.	60.	45.	30.	0.
☑ max angle pentas	ABAQUS		1.	60.	90.	120.	180.
☑ min angle hexas	ABAQUS		1.	90.	60.	30.	0.
☑ max angle hexas	ABAQUS		1.	90.	110.	140.	180.
☐ stretch			1.	1.	0.75	0.5	0.
☐ collapse			1.	1.	0.9	0.75	0.
☐ mid point deviation %			1.	0.	25.	33.3	100.
☐ mid point alignment %			1.	50.	40.	33.3	0.
☐ multi violation			1.	0.	1.	2.	4.
☐ non orthogonality	OPENFC		1.	0.	50.	70.	80.
☐ growth ratio	ANSA		1.	0.8	1.	1.2	2.
☐ negative volume	PARTIAL		1.				
☐ incomplete element			1.				
☐ left handed			1.				
☐ min height			1.	0.5	0.	0.	0.

☑ Enable Ranges   Edit Criteria Visibility

OK   Apply   Cancel

Values inputted here from windows

Meshing Procedure

4. After Importation of the geometry we now must assign boxes via the hexa box module.

Boxes → New   A window should now pop up.

FE Entities – STL imports

Geometry – VDA, IGES imports

Select all the geometry in the window
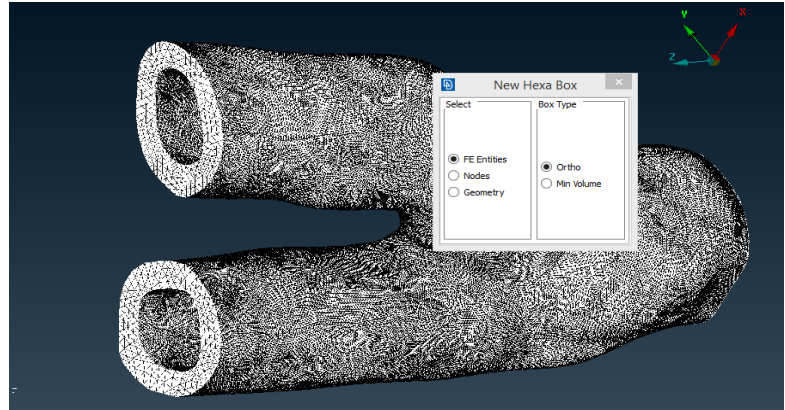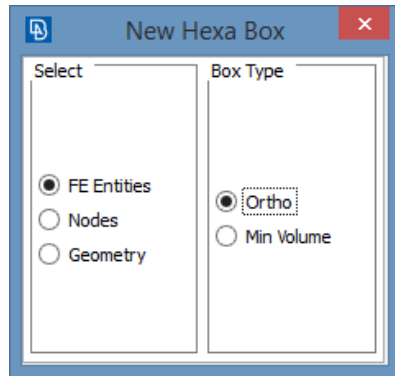
Ortho or min volume can be chosen here as this gives the general shape of the hexablock

5. For IGES and VDA inputs we must set the perimeter lengths accordingly, so we can get the correct shape of the geometry

IGES Import and VDA Import

For refinement of geometry before hexa box

Mesh Module → Perimeters → Number
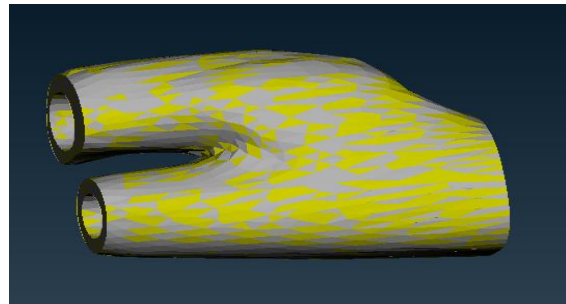
Then we can define hexa box on these geometries

6. Now I have the hexa box – refine so we have more blocks to fit to the geometry.

Boxes → Split

Number – Select box edge
and set number

User – Select box edge
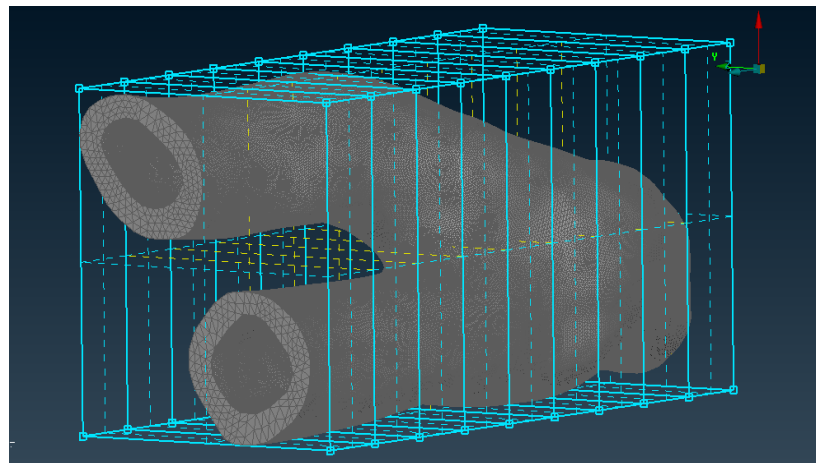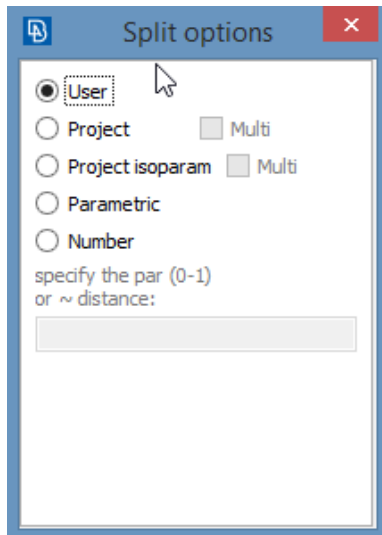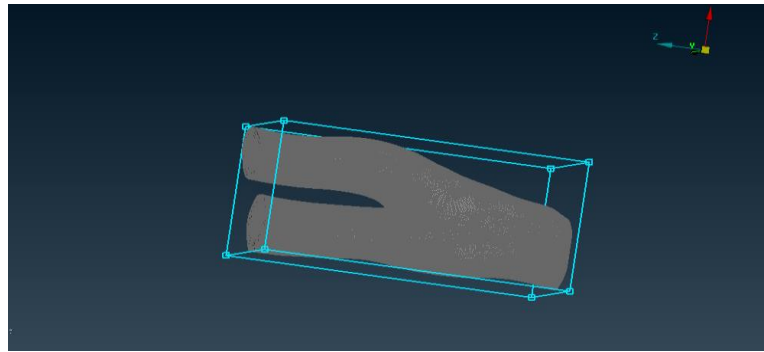
As a preference – it is easier to work on STL geometries. I would recommend that if possible that stl imports are used

7. **Split the hexa boxes until it gets to the bifurcation**.

Turn on box hatches as shown – this allows for us to pick box faces
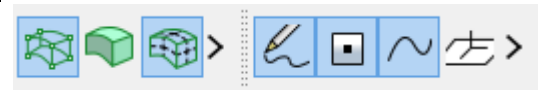
Boxes → Release – Select centre box faces

This disconnects the hexa boxes.
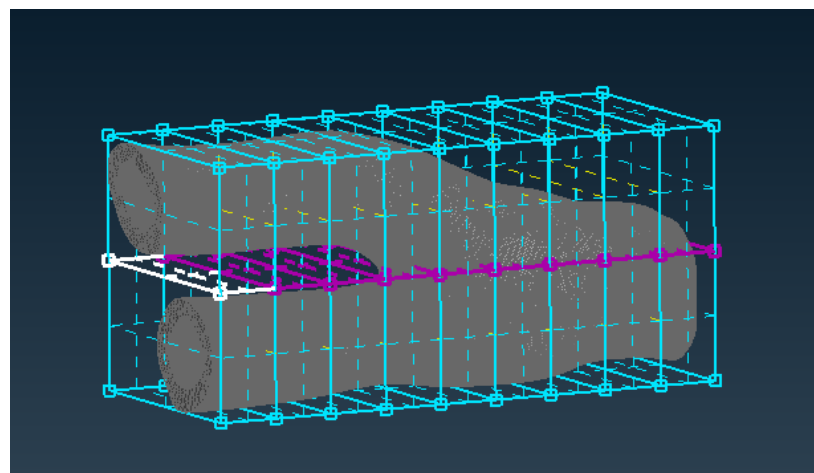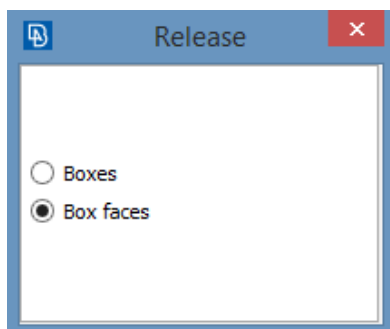
Move boxes accordingly – centre points should split to create new separate boxes.

Modification → Move – Select points
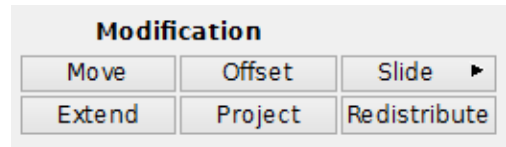
Do this until boxes are split to resemble bifurcation
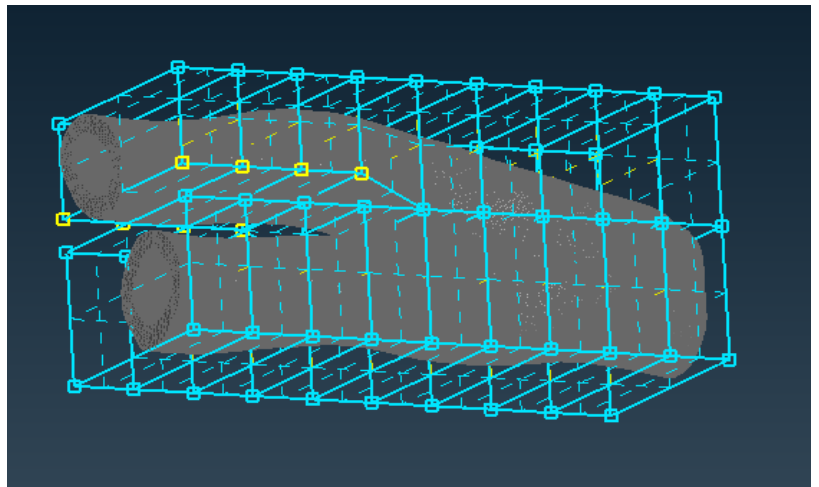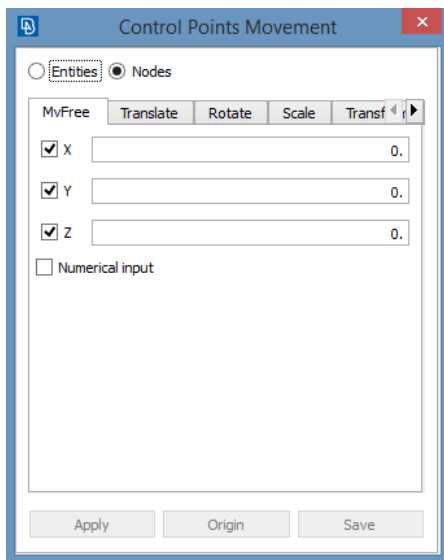
Boxes can be adjusted until we obtain a good mapping of the geometry.

Once we have the boxes we must apply topology, so boxes do not split when we move them.

Boxes →Topo – Select all boxes

We now have the boxes over the geometry as shown. Now we need to map the boxes to the geometry
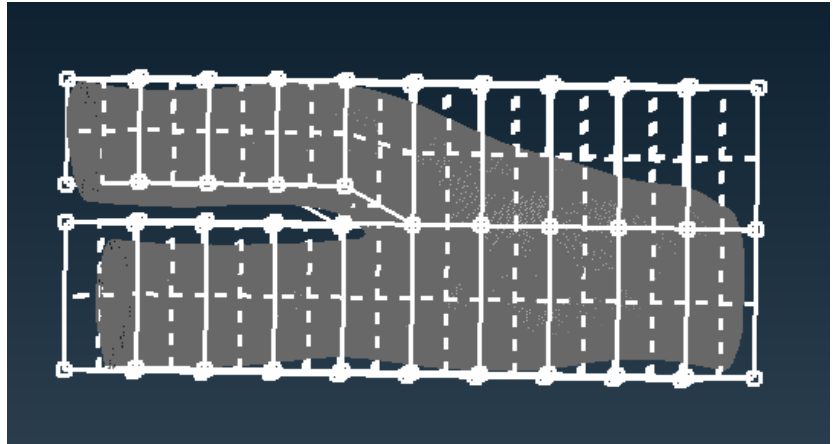
8. Map the boxes to the geometry

Three methods of mapping:

Association → Points

"Project to points"

Select point in box and then point on the geometry

Association → Edges

"Project to Edges"

Select box edge then select geometry edge

Association → Edges

"Project to Surfs"

Select entire the boxes and the entire geometry for quick association.

Can use alternative methods of association of boxes to geometry. These seem to be the most efficient.

163
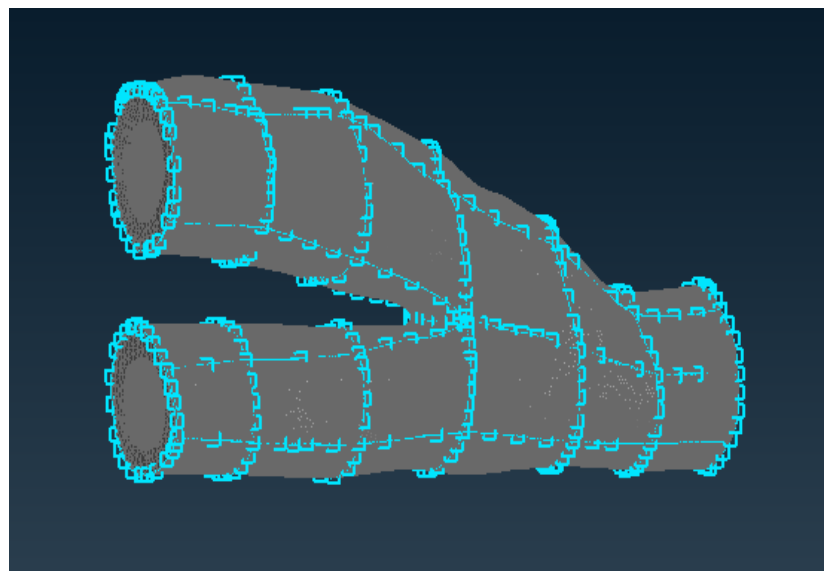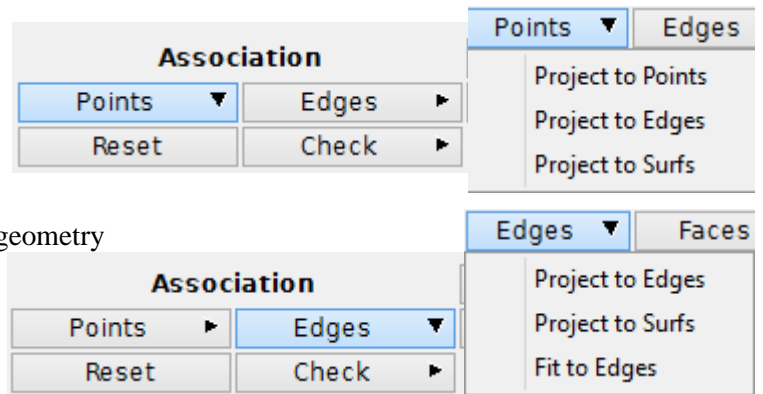
9. Creation of Internal radius using OGRID

Boxes → OGRID

A new window should pop up with OGRID topology

- Click the action symbol
- New

Another window should pop up. Here we select all the boxes. Then continue
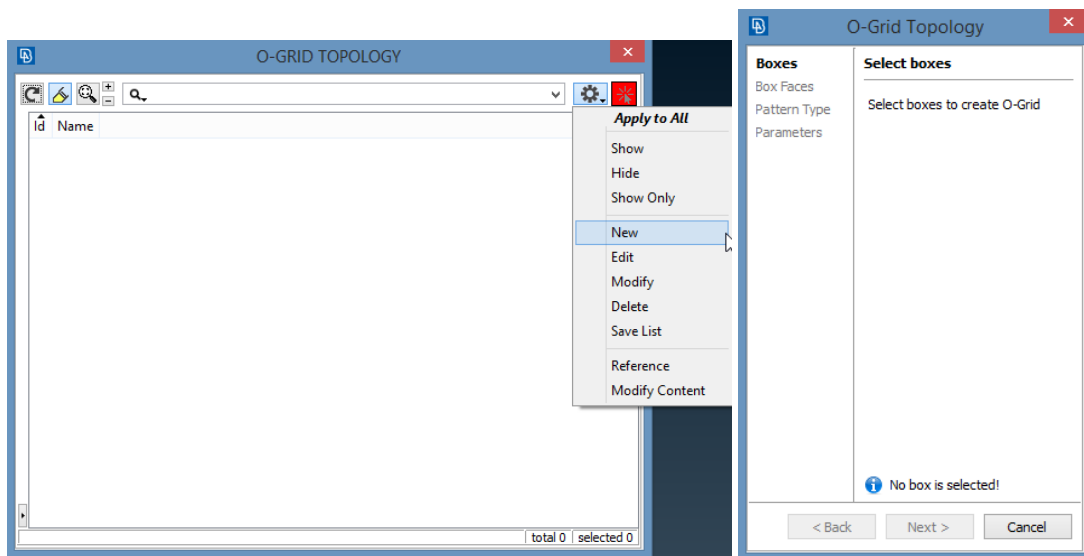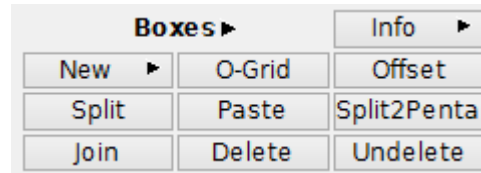
For box faces we select the proximal and distal surfaces of the geometry
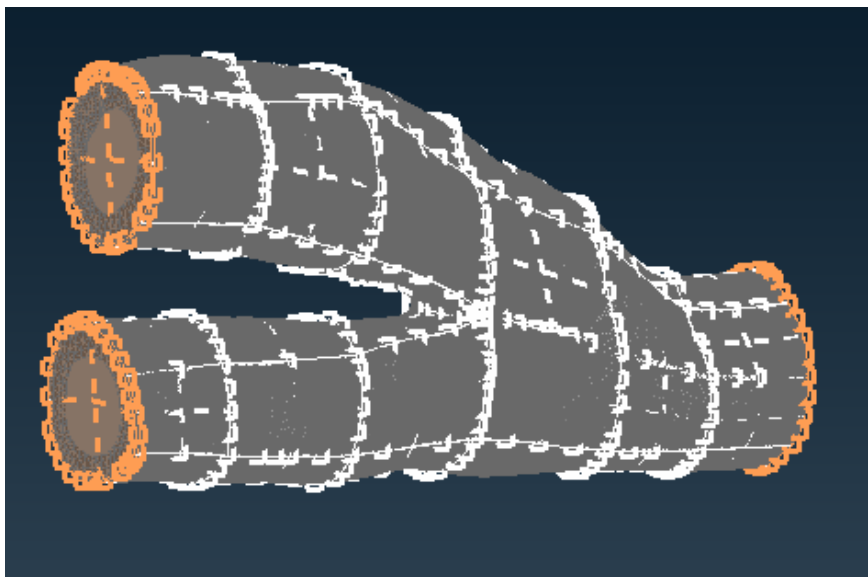
Continue when we have completed this operation

164

Now we must define the pattern type

Pipe → Branches – Select the box faces
up to bifurcation
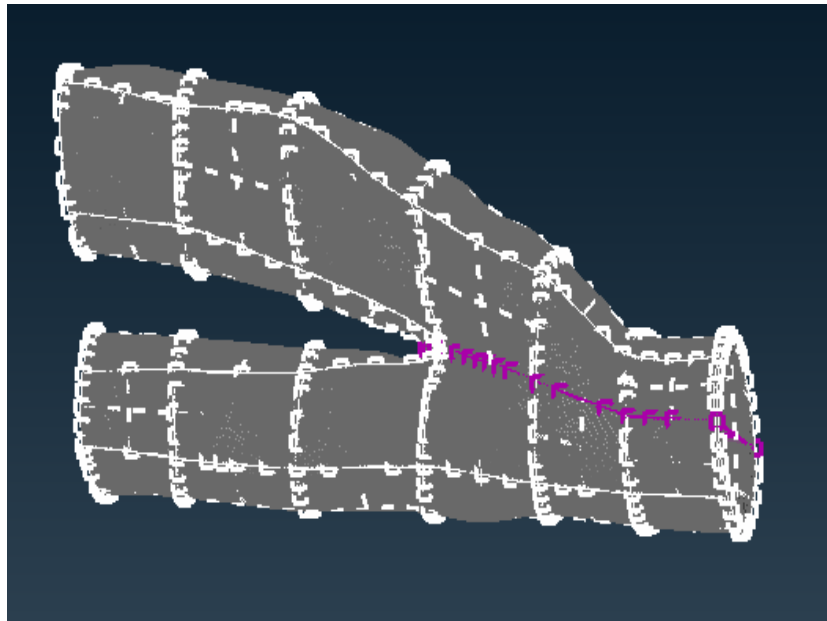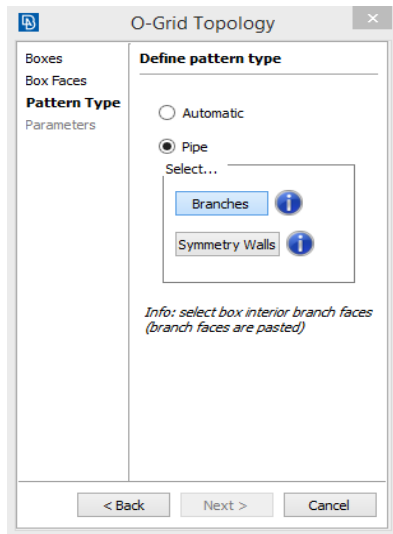
Define the OGRID parameters

Value = 1.000 → Absolute offset value

Pattern – Set = 1.000
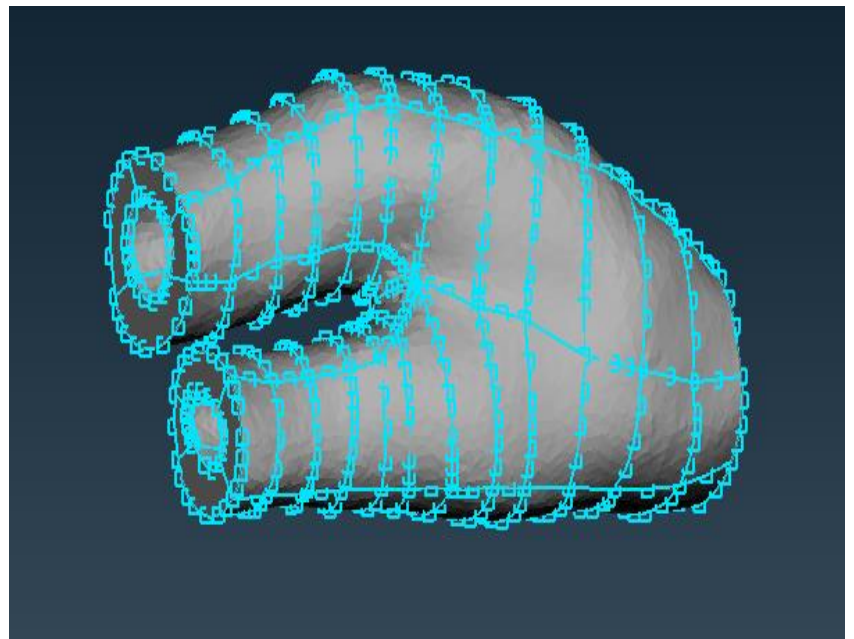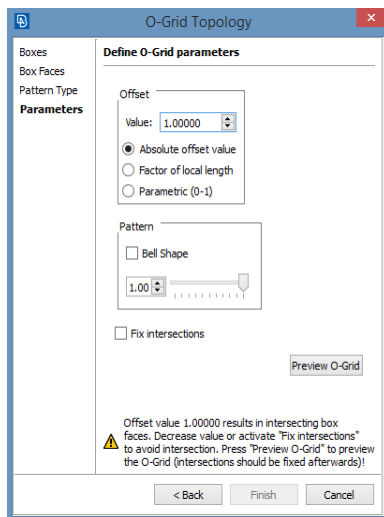
This creates inner boxes from the assigned outer boxes. This gives the uniform thickness to the
geometry

To assign the inner boxes to the inner surfaces of the geometry we must hide the outer assigned boxes and geometry

Select the not option → " – " on the toolbar

Select the feature edge on the toolbar – Can change the degrees to select boxes / geometry
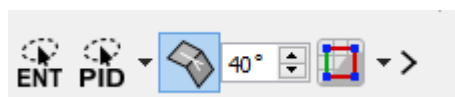
Now we can select the outer assigned boxes and geometry.

10. Assign the inner boxes and the inner surface of geometry.

Use the same tools as addressed in step (8) to assign the boxes to the inner surface
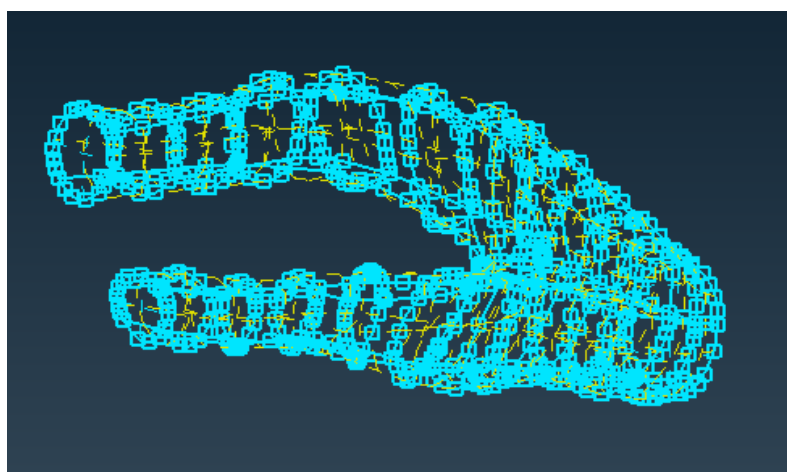
To double check that we have assigned both outer and inner surfaces we can bring back all geometry

Select the " ▦ " on the toolbar

To take away the centre of OGRID so we have the lumen. From inner surface assigned only – see image.

Boxes → Delete
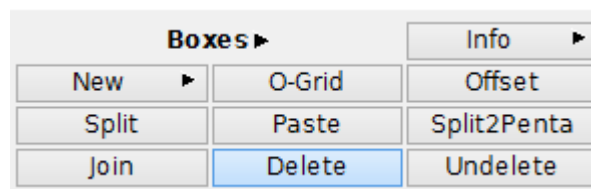
This leaves us the hexa boxes mapped to the geometry (outer and inner surfaces) with variable thickness.

Boxes ►		Info ►
New ►	O-Grid	Offset
Split	Paste	Split2Penta
Join	Delete	Undelete

11. Hexahedral Meshing

Volume Mesh → Pure Hexa

Volume Mesh ►		
Pure Hexa	Map	Erase
Ortho Smooth	Preview Section	
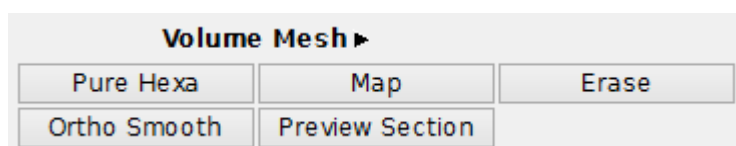
Project on geometry

Tolerance set

Project not associated boxes

Can create multiple properties if geometry is segmented and meshed accordingly
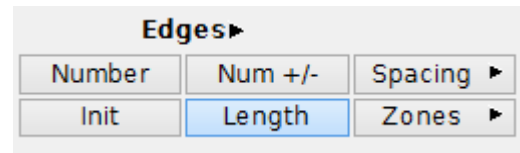

To increase the density of the mesh
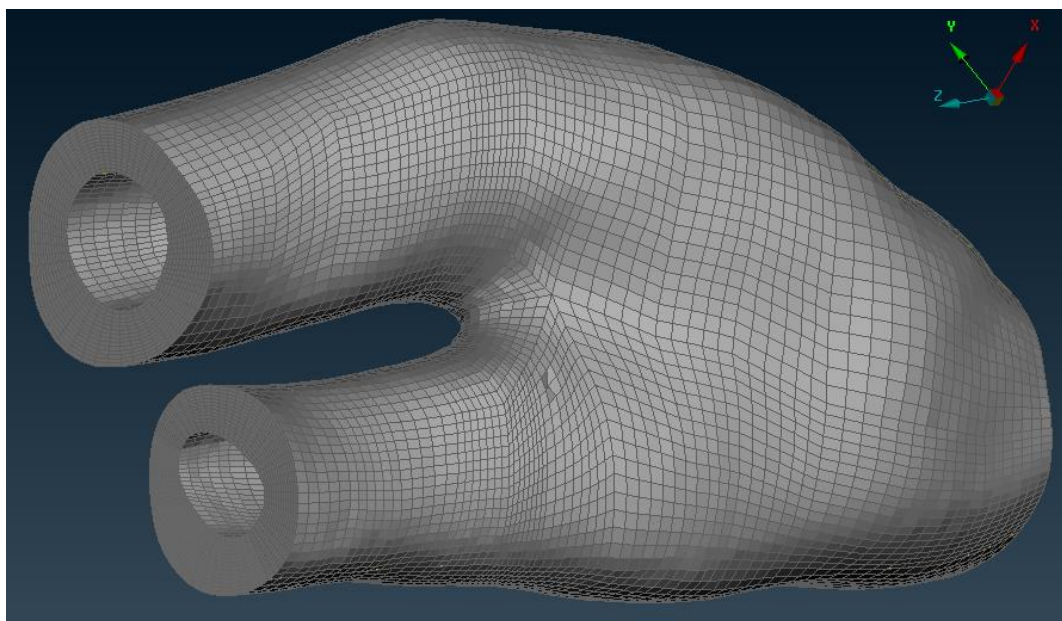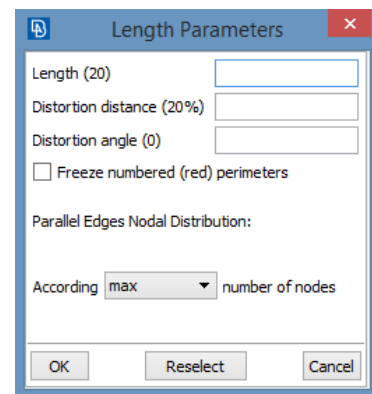
Edges → Length

Edges → Number – Set Number

Can control distortion here by adjusting the distance
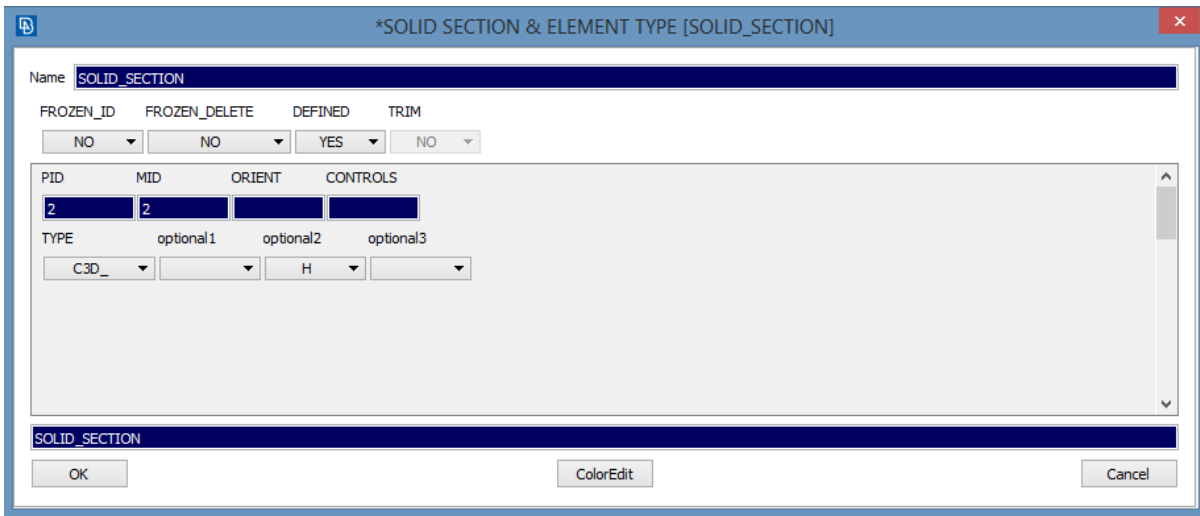
Once set with the parameters set

Meshed geometry

Window should pop up to defined whether this is a solid mesh.

Define Solid_Section → Type "Element Type" → Optional "Select element criteria"
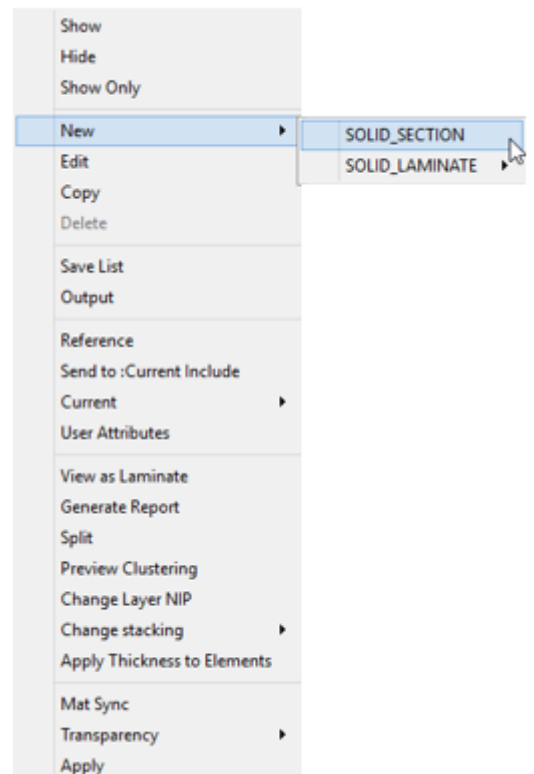

To look at the parts, materials, sets and includes can be done by selecting the icons on the toolbar

To create more sections, materials. Etc.

- Select the following parameter on toolbar
- Select settings icon
- New
- Solid Section / Material

This can be attributed to have multiple sections and multiple material properties assigned in the same geometry

12. Output the geometry to Abaqus

File → Output → Abaqus
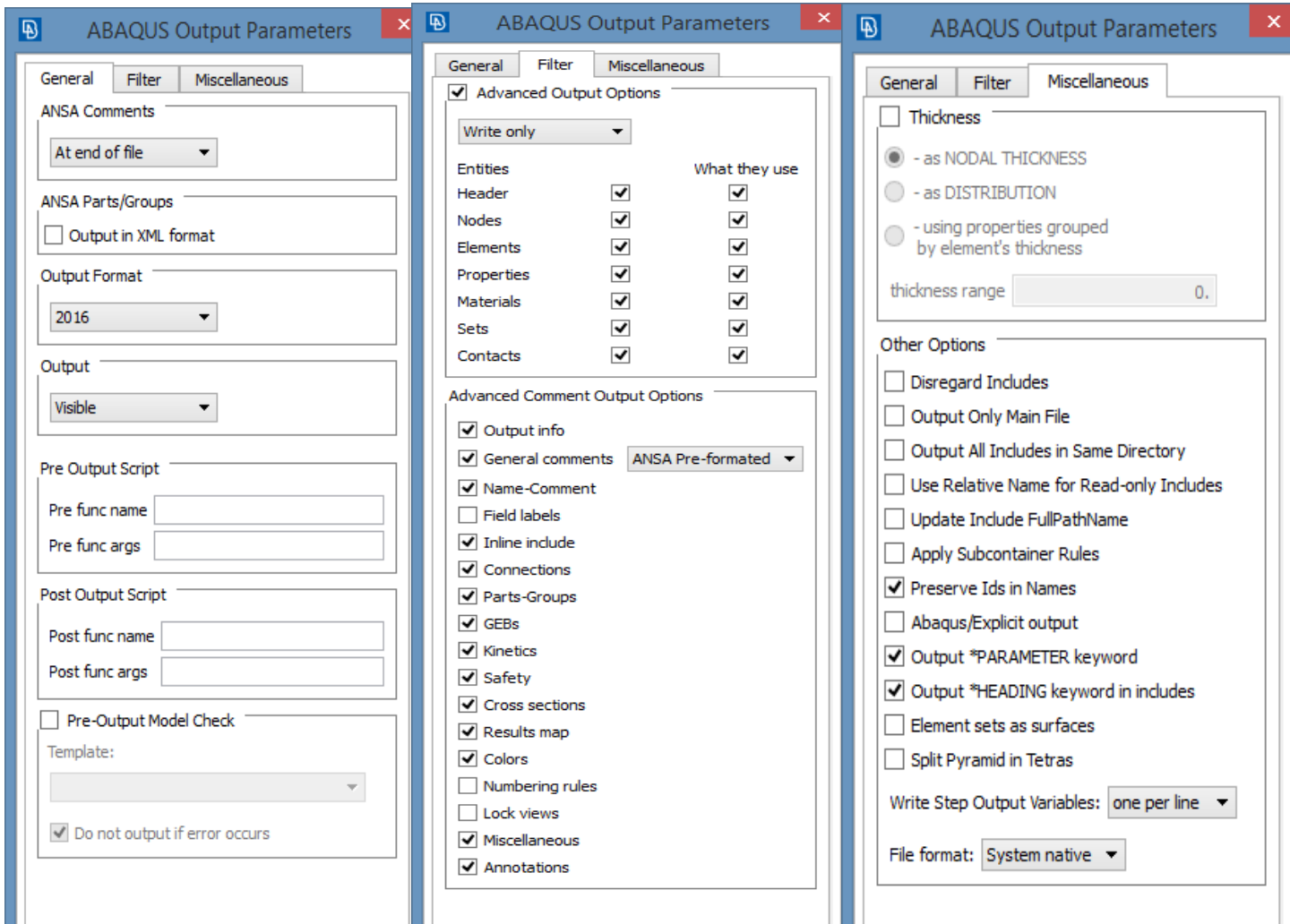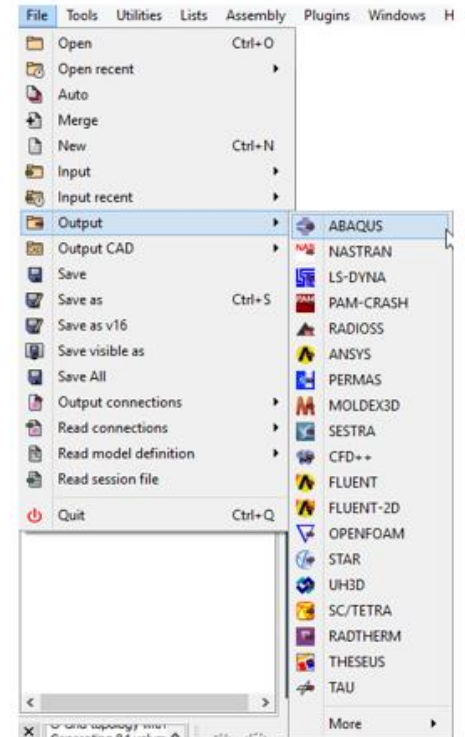
ABAQUS output parameter windows pop up

- General Tab - Select Output format to version of Abaqus

Then OK

- Filter Tab - Advanced Output Options. Select desired outputs. All the rest stays the same

Then OK

- Miscellaneous Tab – All predefined settings

B   Supplementary information for chapter 3.

Table 1: Material parameters used for each case for simulation of the stress for geometry 2. Case 2, 3 and 4 have been optimized under certain conditions previously stated in the text

| Parameters	C_{10} (kPa)	k_1 (kPa)	k_2	κ	θ (deg)
Case 1	6.56	1482	561	0.16	37
Case 2	5.82	1512	522	0.16	37
Case 3	8.35	1428.61	941.13	0.12	38
Case 4	9.42	1489.1	385.61	0.20	37
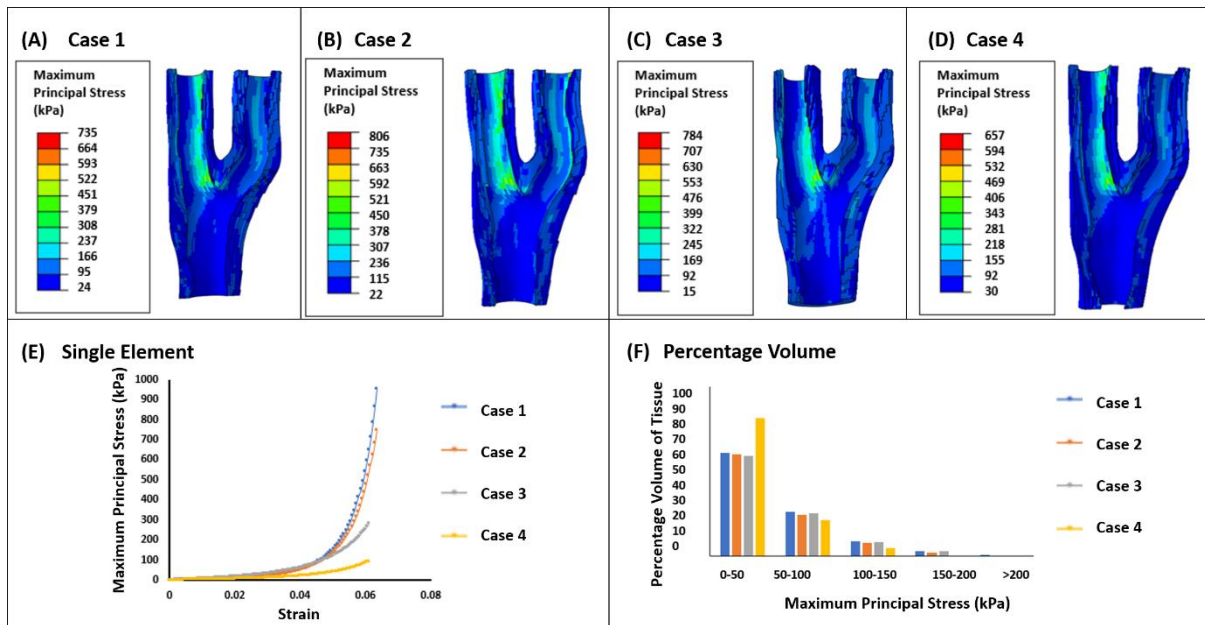
Figure B1: Maximum Principal Stress (kPa) observed in geometry 2 with (i) material parameters taken from literature (Case 1) (ii) optimized parameters without the inclusion of zero pressure configuration and residual stress (Case 2) (iii) optimized parameters with the inclusion of the zero pressure configuration (Case 3) (iv) optimized parameters with the inclusion of the zero pressure configuration and residual stress (Case 4) (v) Single element test undergoing uniaxial tension looking at stress strain response of each case (vi) Percentage of volume graph for the 4 cases showing the stress distribution throughout the vessel wall

Table 2: Material parameters used for each case for simulation of the stress for geometry 3. Case 2, 3 and 4 have been optimized under certain conditions previously stated in the text

Parameters	C_{10} (kPa)	k_1 (kPa)	k_2	κ	θ (deg)
Case 1	6.56	1482	561	0.16	37
Case 2	3.26	1472	571	0.16	37
Case 3	6.06	1479.29	862.02	0.17	39
Case 4	8.68	1546.92	423.17	0.22	39
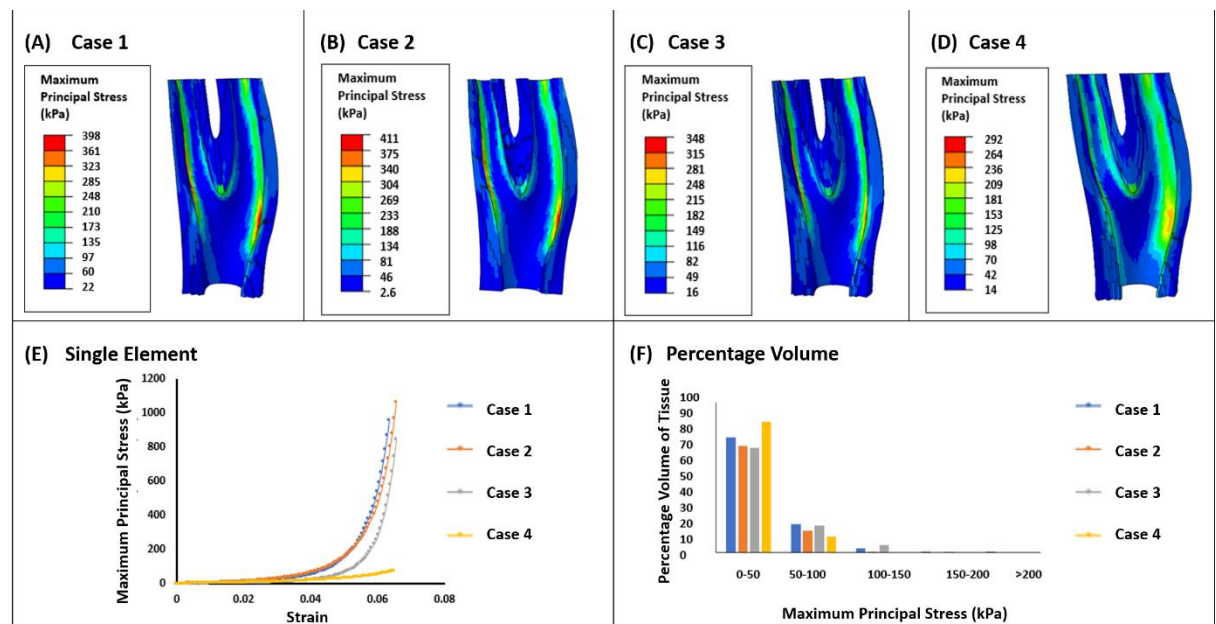
Figure B2: Maximum Principal Stress (kPa) observed in geometry 3 with (i) material parameters taken from literature (Case 1) (ii) optimized parameters without the inclusion of zero pressure configuration and residual stress (Case 2) (iii) optimized parameters with the inclusion of the zero pressure configuration (Case 3) (iv) optimized parameters with the inclusion of the zero pressure configuration and residual stress (Case 4) (v) Single element test undergoing uniaxial tension looking at stress strain response of each case (vi) Percentage of volume graph for the 4 cases showing the stress distribution throughout the vessel wall

Table 3: Material parameters used for each case for simulation of the stress for geometry 4. Case 2, 3 and 4 have been optimized under certain conditions previously stated in the text

Parameters	C_{10} (kPa)	k_1 (kPa)	k_2 (	κ	θ (deg)
Case 1	6.56	1482	561	0.16	37
Case 2	8.82	1568	586	0.16	37
Case 3	7.98	1653.13	616.09	0.15	38
Case 4	9.64	1369.46	224.64	0.24	38
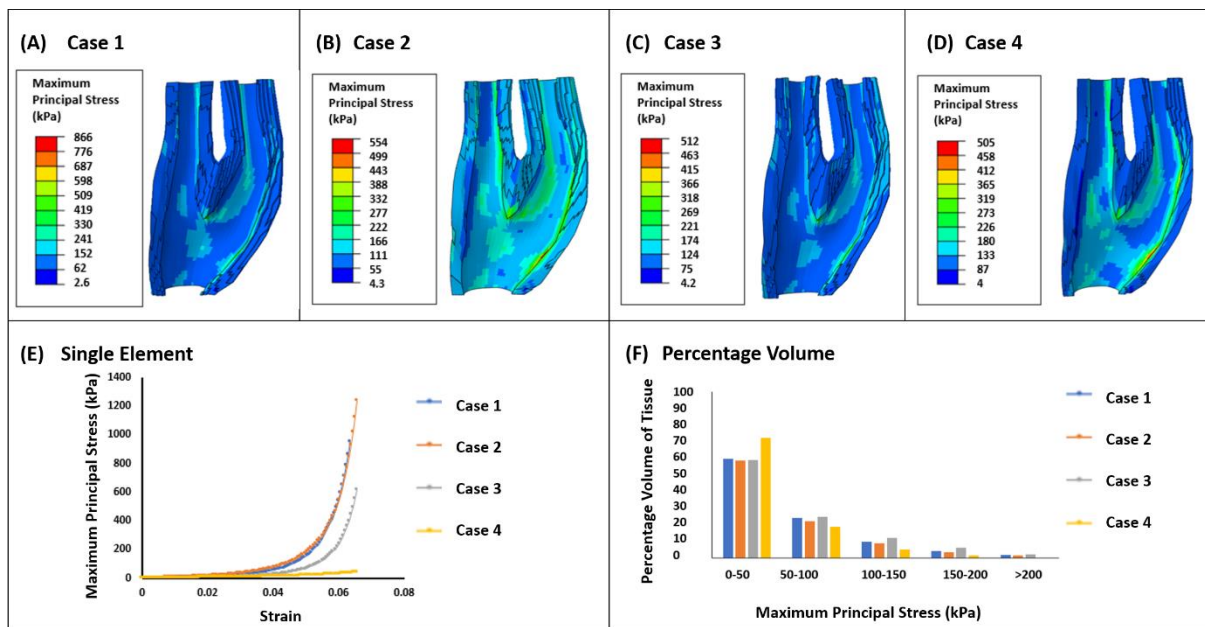
Figure B3: Maximum Principal Stress (kPa) observed in geometry 4 with (i) material parameters taken from literature (Case 1) (ii) optimized parameters without the inclusion of zero pressure configuration and residual stress (Case 2) (iii) optimized parameters with the inclusion of the zero pressure configuration (Case 3) (iv) optimized parameters with the inclusion of the zero pressure configuration and residual stress (Case 4) (v) Single element test undergoing uniaxial tension looking at stress strain response of each case (vi) Percentage of volume graph for the 4 cases showing the stress distribution throughout the vessel wall

Table 4: Material parameters used for each case for simulation of the stress for geometry 5. Case 2, 3 and 4 have been optimized under certain conditions previously stated in the text

Parameters	C_{10} (kPa)	k_1 (kPa)	k_2	κ	θ (deg)
Case 1	6.56	1482	561	0.16	37
Case 2	12.46	1549	561	0.16	37
Case 3	7.75	1722.37	684.81	0.12	37
Case 4	8.76	1682.12	464.21	0.18	38
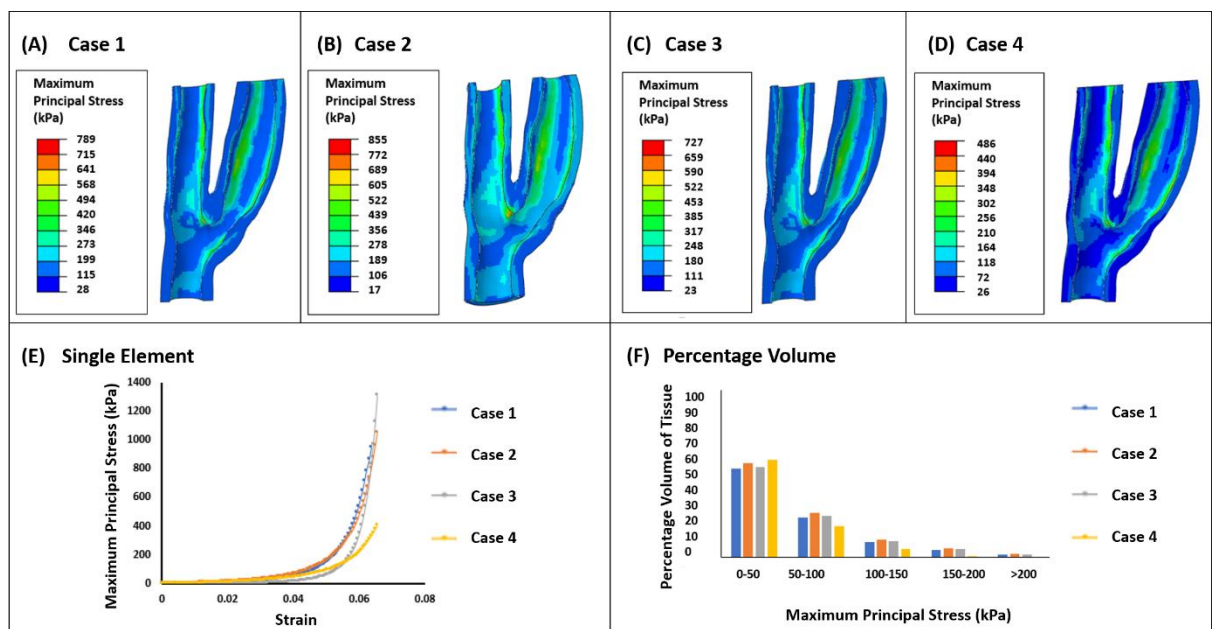
Figure B4: Maximum Principal Stress (kPa) observed in geometry 5 with (i) material parameters taken from literature (Case 1) (ii) optimized parameters without the inclusion of zero pressure configuration and residual stress (Case 2) (iii) optimized parameters with the inclusion of the zero pressure configuration (Case 3) (iv) optimized parameters with the inclusion of the zero pressure configuration and residual stress (Case 4) (v) Single element test undergoing uniaxial tension looking at stress strain response of each case (vi) Percentage of volume graph for the 4 cases showing the stress distribution throughout the vessel wall

Table 5: Material parameters used for each case for simulation of the stress for geometry 6. Case 2, 3 and 4 have been optimized under certain conditions previously stated in the text

Parameters	C_{10} (kPa)	k_1 (kPa)	k_2	κ	θ (deg)
Case 1	6.56	1482	561	0.16	37
Case 2	6.87	1362	486	0.16	37
Case 3	6.43	1280.77	744.01	0.08	38
Case 4	10.24	1864.22	486.46	0.18	37
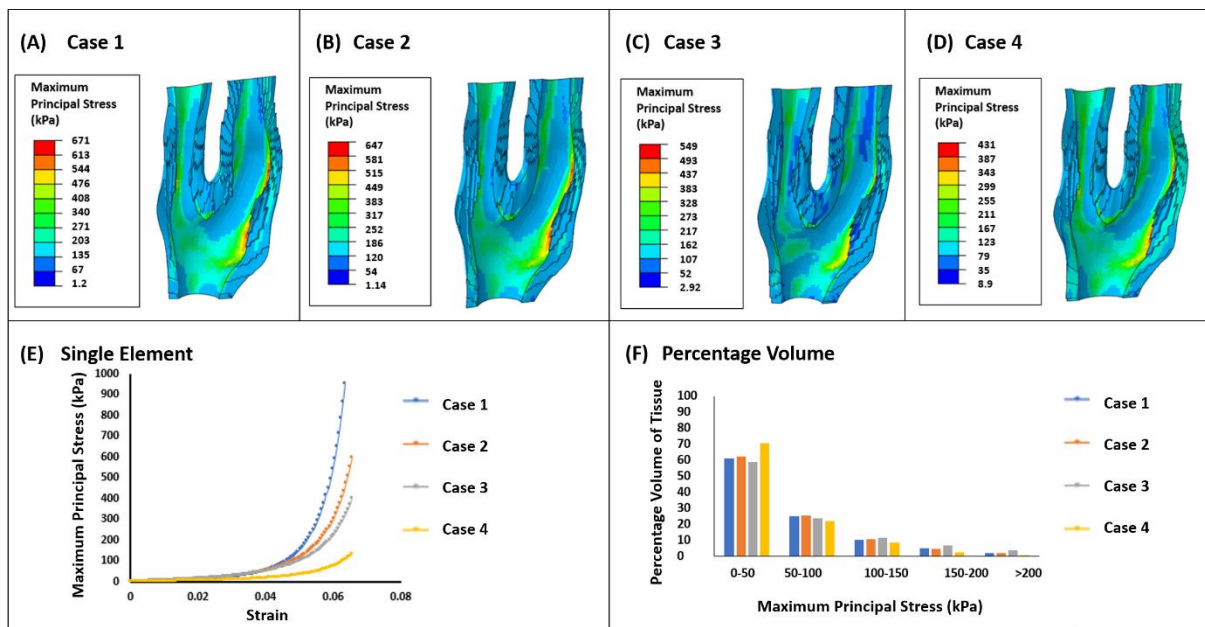
Figure B5: Maximum Principal Stress (kPa) observed in geometry 6 with (i) material parameters taken from literature (Case 1) (ii) optimized parameters without the inclusion of zero pressure configuration and residual stress (Case 2) (iii) optimized parameters with the inclusion of the zero pressure configuration (Case 3) (iv) optimized parameters with the inclusion of the zero pressure configuration and residual stress (Case 4) (v) Single element test undergoing uniaxial tension looking at stress strain response of each case (vi) Percentage of volume graph for the 4 cases showing the stress distribution throughout the vessel wall

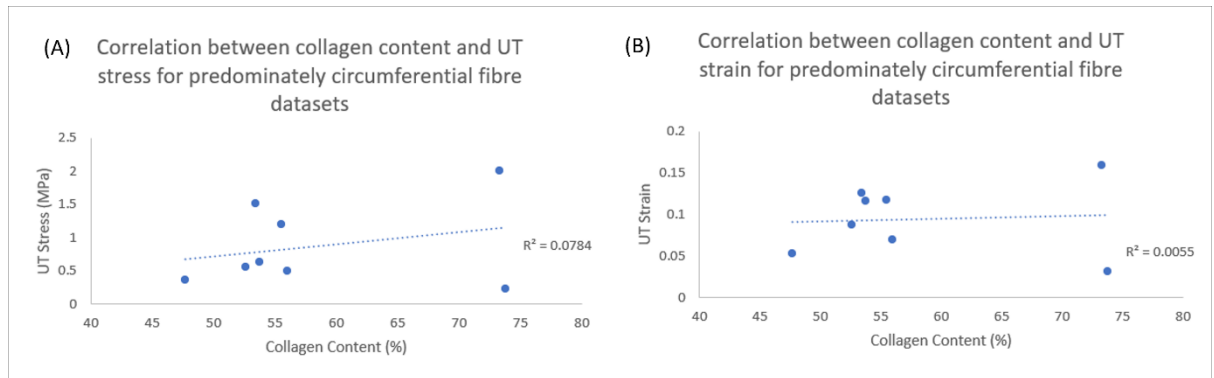# C   Supplementary information for chapter 4.

Figure C1: Correlation analysis for (A) collagen content and UT stress for predominately circumferential fibre datasets and (B) collagen content and UT strain for predominately circumferential fibre datasets.
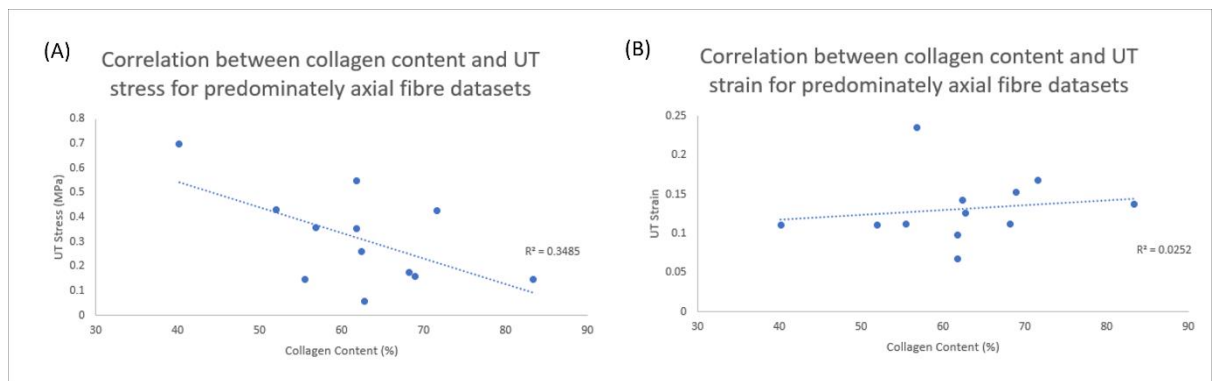

Figure C2: Correlation analysis for (A) collagen content and UT stress for predominately axial fibre datasets and (B) collagen content and UT strain for predominately axial fibre datasets.